NOTE TO USERS

The original manuscript received by UMI contains pages with slanted print. Pages were microfilmed as received.

This reproduction is the best copy available

UMI

STRUCTURAL SETTING, GEOCHEMISTRY, AND TEMPORAL RELATIONSHIPS OF THE LODE GOLD DEPOSITS IN THE STAR LAKE-MCLENNAN LAKE AREA, NORTHERN SASKATCHEWAN

By

Jie He

A thesis
presented to the University of Waterloo
in fulfilment of the
thesis requirement for the degree of
Doctor of Philosophy
in
Earth Sciences

Waterloo, Ontario, Canada, 1997

© Jie He 1997

National Library of Canada
Acquisitions and Bibliographic Services
395 Wellington Street
Ottawa ON K1A 0N4
Canada

Bibliothèque nationale du Canada
Acquisitions et services bibliographiques
395, rue Wellington
Ottawa ON K1A 0N4
Canada

Your file Votre référence

Our file Notre référence

The author has granted a non-exclusive licence allowing the National Library of Canada to reproduce, loan, distribute or sell copies of this thesis in microform, paper or electronic formats.

L'auteur a accordé une licence non exclusive permettant à la Bibliothèque nationale du Canada de reproduire, prêter, distribuer ou vendre des copies de cette thèse sous la forme de microfiche/film, de reproduction sur papier ou sur format électronique.

The author retains ownership of the copyright in this thesis. Neither the thesis nor substantial extracts from it may be printed or otherwise reproduced without the author's permission.

L'auteur conserve la propriété du droit d'auteur qui protège cette thèse. Ni la thèse ni des extraits substantiels de celle-ci ne doivent être imprimés ou autrement reproduits sans son autorisation.

0-612-30616-X

Canada

The University of Waterloo requires the signatures of all persons using or photocopying this thesis. Please sign below, and give address and date.

STRUCTURAL SETTING, GEOCHEMISTRY, AND TEMPORAL RELATIONSHIPS OF THE LODE GOLD DEPOSITS IN THE STAR LAKE-MCLENNAN LAKE AREA, NORTHERN SASKATCHEWAN

ABSTRACT

The gold deposits in the Star Lake-McLennan Lake area, northern Saskatchewan are epigenetic, shear zone-controlled lode gold deposits. The deposits are hosted in the calc-alkaline Star Lake and Island Lake plutons, which intrude the calc-alkaline and low-potassium tholeiitic volcanic rocks of the Central Metavolcanic Belt of the La Ronge Domain, the Paleoproterozoic Trans-Hudson Orogen.

The tectonic fabrics of the area define three phases of deformation. D_1 structures include regional foliation with contained mineral lineation; isoclinal folds with axial surfaces parallel to the foliation; and foliation within the McLennan Lake Tectonic Zone that strikes parallel to the contact between the Central Metavolcanic Belt and the McLennan Group, and dips at shallower angles than the regional foliation. D_2 structures are subvertical, mesoscopic shears and cataclastic zones; and associated steeply plunging mineral lineations. Asymmetric and rotated fabrics indicate that the direction of shearing on the D_2 structures is at a high angle to the mineral lineation. D_{3a} structures are dip-slip gold-bearing shears and shallow-dipping shears that are conjugate to the gold-bearing ones. D_{3b} structures include asymmetric folds of early fabrics and associated shears and quartz veins, which indicate dextral movement on the McLennan Lake Tectonic Zone and the D_{3a} gold-bearing shears. The gold deposits were emplaced into the D_3 shears, synchronously with the D_{3a} dip-slip shearing, and were subsequently deformed by the D_{3b} deformation. The deformations occurred during and following the terminal continent-continent collision of the Trans-Hudson Orogen, and represent progressive strain in a transpressional regime.

The peak of regional metamorphism was coeval with the D_1 deformation, and reached low to middle amphibolite grade. Temperature and pressure of the regional metamorphism were approximately 545° to 575°C and 4.5 to 5.0 kbars. The P-T

conditions of the D_2 deformation were approximately 500° to 550°C and 3.0 to 4.0 kbars. The D_3 deformation, with which the gold mineralization was associated, occurred at a temperature of 480° to 500°C and a pressure of 3.0 to 4.0 kbars.

The hydrothermal alteration associated with the McLennan Lake Tectonic Zone, the D_2 structures and the D_3 gold-bearing shears is characterized by enrichment of $\delta^{18}O$ of silicate minerals in the deformed rocks relative to their precursors. The fluids that infiltrated the D_2 and D_3 structures were possibly of similar composition, and were enriched in Au, K, Rb, Ba, and Cu (+ Pb + Zn) relative to the wall rocks. The water/rock ratio associated with alteration was greater in the D_3 shears than in the McLennan Lake Tectonic Zone and the D_2 structures. The occurrence of gold mineralization in the D_3 structures was probably related to a higher fluid flow.

Vein quartz from the D_1 to D_3 structures, with the exception of the Jasper deposit, defines a narrow range of oxygen isotopic composition of 10.0 to 11.5 per mil, with auriferous quartz showing minor $\delta^{18}O$ enrichment relative to barren quartz. The auriferous quartz in the Jasper deposit is enriched in $\delta^{18}O$ by up to 3 per mil relative to the Jolu, Rush Lake and Star Lake deposits. The calculated oxygen and hydrogen isotopic compositions of hydrothermal fluids that deposited the quartz veins in the D_1 to D_3 structures are 6.8 to 10.3‰ and -89 to -26‰, respectively. The oxygen and hydrogen isotopic values are similar to fluids of metamorphic or magmatic origin, or to fluids that acquired isotopic equilibrium with metamorphic or magmatic rocks at high temperatures.

Hornblendes from the D_1, D_2 and D_3 structures yield the same $^{40}Ar/^{39}Ar$ plateau ages (within error) of *ca.* 1750 Ma. The ages probably reflect the time of cooling through the closure of hornblende to argon loss at 500°C, and approximate the time of the D_3 deformation. In conjunction with previous geochronological studies, the timing of hydrothermal activity linked to the formation of the gold deposits is constrained between 1807 Ma and *ca.* 1750 Ma. This postdates the emplacement of the Star Lake and Island Lake plutons (1855 to 1846 Ma), and the regional metamorphism (1820 to 1798 Ma).

The auriferous hydrothermal fluids were probably not of magmatic origin related to the emplacement of the host plutons. The fluids could have been generated by devolatilization of the lower levels of the crust during prograde metamorphism at the final stages of the Trans-Hudson Orogen. The absence of deep plumbing systems may account for the small size of the gold deposits with respect to Archean counterparts.

ACKNOWLEDGMENTS

My prime acknowledgment is to my supervisor, Dr. R.G. Roberts. He has been a catalyst for this work by consistently encouraging high standards of research and critical thinking, and by providing incisive criticism and illuminating discussions during the course of this study. I have benefited from his willingness to share his thoughts on structural geology and gold deposits, which significantly influenced my own thinking and helped to greatly improve the dissertation. I gratefully acknowledge the enthusiastic support throughout the program of Dr. I.L. Gibson. I would also like to thank Dr. E.C. Appleyard for his valuable comments on the studies of metamorphism and alteration, and Dr. E.C. Jowett for his direction during the earlier stages of the program. The enthusiasm and encouragement of Dr. S.K. Frape are much appreciated.

I am particularly indebted to Dr. T.K. Kyser for his enthusiastic and generous support of the project by providing free and full access to his laboratories in the Department of Geological Sciences, the University of Saskatchewan. He is also thanked for his assistance in completing the Ar^{40}/Ar^{39} age determinations in the Department of Geological Sciences, the Queen's University. This work would not have been possible without his support. I am also grateful to the technical staff in the Department of Geological Sciences, the University of Saskatchewan: David Pezderic, Kerry Klassen and Bonli Thomas, for help with stable isotopic analyses and electron microprobe analyses; and Brian Morgan is thanked for conducting trace element analyses.

I especially wish to thank the graduate officer of the Department, Dr. D.E. Lawson, for his understanding and confidence in my abilities, and for providing continuous financial support through a Teaching Assistantship and a University of Waterloo Graduate Scholarship.

The project was funded by the Saskatchewan Energy and Mines under the Canada-Saskatchewan Partnership Agreement on Mineral Development (1990-95). Dr. T.I.I. Sibbald of the Saskatchewan Geological Survey is greatly acknowledged for initiating this project and for his critical support. Pamela Schwann and Andrew Gracie,

Resident Geologists at La Ronge, are acknowledged for providing logistical assistance during the field work.

I am grateful to Dr. R.L. Sherlock for his kind help in making my stay at the University of Waterloo enjoyable. I benefited from many discussions with Christopher Lee, graduate student at the University of Waterloo. He helped improve sections of an earlier version of the dissertation.

I wish to acknowledge Dr. K.H. Yang of the University of Toronto for help with some of the geochemical analyses.

Dr. K.H. Poulsen of the Geological Survey of Canada and David Thomas of the Saskatchewan Geological Survey are thanked for sharing their invaluable knowledge on the regional geology during the early stages of the project. David Billard of Cameco is acknowledged for his hospitality and for providing valuable information on the geology of the Jasper deposit. John Miedema provided location maps of drill cores at the Jolu Mine. The field assistance of Carol Macdonald and David Bowman is acknowledged with gratitude.

Most of all, I would like to thank my wife and Ph.D. candidate at the University of Waterloo, Min Zhang, for her understanding, encouragement and support throughout this special journey of life.

TABLE OF CONTENTS

Abstract iv
Acknowledgment vii

CHAPTER 1
INTRODUCTION

Introductory Statement 1
Field Work 2
Previous Geological Studies 2
History of Exploration and Development 3

CHAPTER 2
REGIONAL SETTING AND
GEOLOGY OF STAR LAKE-MCLENNAN LAKE AREA

Trans-Hudson Orogen 6
Churchill-Superior Boundary Zone 6
Reindeer Zone 8
Subdivisions and Age Constraints *8*
General Structural Geology *10*
Metamorphism *12*
Wathaman-Chipewyan Batholith 13
Cree Lake Zone 13
La Ronge Domain 14
Subdivisions 14
Crew Lake Belt *14*
Central Metavolcanic Belt *15*
MacLean Lake Belt *15*
La Ronge Horseshoe *16*
Tectonic Evolution of Reindeer Zone 16
Geology of Star Lake-McLennan Lake Area 20
Lithological Subdivisions 20

Metavolcanic Rocks *20*
Pelitic Sedimentary Rocks *22*
Meta-Arkoses and Meta-Conglomerates *22*
Intrusive Rocks *23*
Major Structures and Metamorphism 24
Gold Mineralization 25

CHAPTER 3
STRUCTURAL GEOLOGY

Introduction **27**
D_1 Deformation **27**
Supracrustal Rocks 28
Plutonic Rocks 28
Strain Pattern 31
D_2 Deformation **31**
D_2 Shears 31
Attitude of The D_2 Shears *31*
Sense of Movement *36*
D_2 Cataclastic Zones 39
D_3 Deformation **42**
General Characteristics 42
James-Jasper-Roxy Shears 43
D_{3a} Dip-Slip Shearing *43*
D_{3b} Strike-Slip Shearing *47*
Rod Shear 53
D_{3a} Dip-Slip Shearing *56*
D_{3b} Oblique-Slip Shearing *56*
D_{3b} Strike-Slip Shearing *60*
Megascopic Structures **60**
David Lake Shear 60
Mallard Lake Shear 63
Relationship to D_2 Structures 65
Regional Structures **65**

Definition and Stratigraphic Relationships 65
McLennan Lake Tectonic Zone *65*
Alpat Lake Tectonic Zone *69*
Internal Structures 69
Foliation and Lineation *69*
Finite Strains *72*
Evidence of Dip-Slip Shear Movement *72*
D_{3b} Structures *79*
Discussion 84
Transpression 86
Introduction 86
Tectonic Fabric Development 89
D_1 Deformation *89*
D_2 Deformation *89*
D_{3a} Deformation *92*
D_{3b} Deformation *93*
Concluding Statement 96
Relationship of Gold Mineralization to Deformation 96
Jasper Deposit 96
Jolu Deposit 99
Relative Timing of Mineralization 99
Conclusions 104

CHAPTER 4
METAMORPHISM, METASOMATISM AND WALL-ROCK ALTERATION

Introduction 106
Petrography and Mineral Geochemistry 106
D_1 Deformation 106
Metavolcanic Rocks *106*
Pelitic Rocks *112*
Meta-Arkoses *113*
Plutonic Rocks *114*
McLennan Lake Tectonic Zone 116

D_2 Deformation 119
D_3 Deformation 126
Rod Shear *126*
James-Jasper-Roxy Shears *133*
Relative Timing of Deformation and Metamorphism 134
Temperature and Pressure of M_1 Metamorphism 135
Geothermobarometry 135
Garnet-Biotite Geothermometer *136*
Garnet-Hornblende Geothermometer *138*
Quartz-Hornblende Isotopic Geothermometry *138*
Garnet-Hornblende-Plagioclase-Quartz Geobarometers *139*
Summary 139
Temperature and Pressure of M_2 and M_3 Metamorphism 140
Geothermobarometry 140
Plagioclase-Amphibole Geothermometry *142*
Plagioclase-Hornblende Geothermobarometry *142*
Quartz-Hornblende Isotopic Geothermometry *144*
Discussion 144
Chemistry of Wall-Rock Alteration 150
Chemical Mass Balance 150
Alteration Chemistry 151
McLennan Lake Tectonic Zone *151*
D_2 Mallard Lake Shear *153*
D_3 Gold-Bearing Shears *153*
Discussion 157
Conclusions 160

CHAPTER 5
OXYGEN AND HYDROGEN ISOTOPIC SYSTEMATICS

Introduction 161
Sampling and Analytical Techniques 161
Oxygen and Hydrogen Isotopic Data 162
Oxygen and Hydrogen Isotopic Compositions of Quartz Veins 162

Oxygen Isotopes *162*
Hydrogen Isotopes *172*
Oxygen Isotopic Composition of Deformed Rocks 172
Isotopic Geothermometry **174**
Temperatures Calculated from Quartz Veins 177
Temperatures Calculated from Deformed Rocks 177
Discussion **179**
Diffusion Effect on Oxygen Isotopic Exchange 179
Isotopic Equilibration Temperatures of Deformation and Alteration 183
Isotopic Compositions of Hydrothermal Fluids 187
Estimate of Water-Rock Ratios 188
Controls on The Oxygen Isotopic Composition of Quartz Veins 190
Conclusions **193**

CHAPTER 6
GEOCHRONOLOGY

Introduction **195**
Previous Results **195**
$^{40}Ar/^{39}Ar$ Hornblende Systematics **198**
Sampling and Analytical Method 198
Results 199
Implications of The Age Data **202**
Conclusions **204**

CHAPTER 7
SUMMARY AND CONCLUSIONS

Summary and Contributions to Knowledge **205**
Discussion **208**
Sources of Hydrothermal Fluids 209
Magmatic Hydrothermal Fluids *209*
Metamorphic Fluids *210*
Genesis of Mineralization in The Star Lake-McLennan Lake Area 212

REFERENCES **217**
APPENDIX A **239**
APPENDIX B **257**

LIST OF TABLES

CHAPTER 1

Table 1-1. Ore reserves and gold produced from the Star Lake-McLennan Lake area 4

CHAPTER 2

Table 2-1. Age constraints for igneous, metamorphic, and tectonic events in the Reindeer Zone 18

Table 2-2. Description of gold occurrences in the Star Lake-McLennan Lake area 25

CHAPTER 3

Table 3-1. The mean attitude of each population of D_2 shears and the mean plunge of associated lineation 36

Table 3-2. Strain data measured from meta-conglomerate 73

Table 3-3. Strain data measured from metavolcanic rocks 73

CHAPTER 4

Table 4-1. Mineral assemblages associated with D_1 to D_3 deformation 107

Table 4-2. Temperature and pressure associated with M_1 metamorphism in pelitic rocks southwest of the Jolu Mine 137

Table 4-3. Temperature and pressure of deformation and metamorphism derived from plagioclase-amphibole geothermometry, plagioclase-hornblende geothermobarometry, and quartz-hornblende isotopic geothermometry..... 146

Table 4-4. K/Rb and K/Ba ratios from the MLTZ, D_2 shears and D_3 gold-bearing shears and from the host Star Lake pluton and Island Lake pluton 153

CHAPTER 5

Table 5-1. Oxygen and hydrogen isotopic compositions of vein minerals; calculated temperatures; and oxygen and hydrogen isotopic compositions of hydrothermal fluids 163

Table 5-2. Oxygen isotopic composition of minerals and calculated equilibration temperatures from deformed rocks of the MLTZ and D_1 to D_3 structures; and oxygen isotopic composition of hydrothermal fluids in equilibrium with the quartz 167

Table 5-3. Temperature uncertainties resulting from a ±0.2‰ precision of the $\Delta^{18}O_{quartz\text{-}mineral}$ and $\Delta^{18}O_{hornblende\text{-}biotite}$ measurements 176

Table 5-4. Closure temperatures (T_c) and diffusion rates (D) of ^{18}O in various minerals 182

Table 5-5. Quartz-hornblende oxygen isotopic equilibration temperatures 186

CHAPTER 6

Table 6-1. Summary of geochronological data for volcanism, plutonism, metamorphism and gold mineralization from the Star Lake-McLennan Lake area 197

Table 6-2. Metamorphic zircon ages from the southern portion of the La Ronge Domain 198

Table 6-3. Analytical data for $^{40}Ar/^{39}Ar$ step-heating experiments 200

APPENDIX A

Table A-1. Electron microprobe analyses of amphibole 240

Table A-2. Electron microprobe analyses of plagioclase 248

Table A-3. Electron microprobe analyses of biotite 252

Table A-4. Electron microprobe analyses of garnet 256

APPENDIX B

Table B-1. Major and trace element chemistry 258

Table B-2. Net composition 264

LIST OF FIGURES

CHAPTER 1

Figure 1-1. Geology of the Star Lake-McLennan Lake area, La Ronge Domain, northern Saskatchewan ..... in pocket

CHAPTER 2

Figure 2-1. Lithotectonic domains of the Trans-Hudson orogen and the adjacent Archean Rae, Hearne and Superior provinces 7

Figure 2-2. Tectonostratigraphic subdivisions of the La Ronge Domain 9

Figure 2-3. Schematic diagrams illustrating tectonic evolution of the northwestern Trans-Hudson Orogen 17

Figure 2-4. Geological map of the Star Lake-McLennan Lake area 21

CHAPTER 3

Figure 3-1. Stereographic plots of S_1-L_1 fabrics 29

Figure 3-2. (A) Photograph of D_1 isoclinal folds. (B) Stereographic plot of D_1 fold axes 30

Figure 3-3. Photographs of D_2 shears 32

Figure 3-4. (A) Map of D_2 shears in an outcrop of mafic metavolcanic rock. (B) Map of D_2 shears in an outcrop of meta-arkose 34

Figure 3-5. Stereographic plots of planar and linear fabrics from D_2 shears 37

Figure 3-6. Synoptic diagrams of D_2 shears 38

Figure 3-7. Photomicrographs of deformation features in the D_2 shear 40

Figure 3-8. (A) A horizontal view of a D_2 tabular cataclastic zone in diorite of the Star Lake pluton. (B) Photomicrograph of the cataclastic zone in (A) 41

Figure 3-9. Stereographic plots of shear fabrics from D_{3a} shears 44

Figure 3-10. Surface geological map of shears and veins in the Roxy deposit 45

Figure 3-11. S-C fabric in protomylonite in granite from the James shear indicating D_{3a} dip-slip shearing 46

Figure 3-12. Structural features developed by D_{3b} strike-slip shearing in the James-Jasper-Roxy shears 48

Figure 3-13. Stereographic plots of structural fabrics developed by D_{3b} strike-slip shearing in the James-Jasper-Roxy shears 51

Figure 3-14. Stereographic illustration (A) and Schematic illustration (B) of relationships among structural fabrics related to D_{3b} strike-slip shearing 52

Figure 3-15. Geological map of the Jolu Mine at the 50 m and 75 m levels 54

Figure 3-16. Outcrop map of the Rod shear with stereographic plots of structural data 55

Figure 3-17. (A) S-C fabrics in protomylonite in granodiorite from the Rod shear. (B) S-C fabric from a shallow-dipping shear 57

Figure 3-18. Structural features developed by D_{3b} dextral oblique-slip shearing in the Rod shear near the Jolu Mine 58

Figure 3-19. (A) Quartz vein and aplite dykes deformed during the D_{3b} oblique shearing. (B) Line drawing showing detailed structural fabrics in (A). (C) Stereographic plot of shear fabric and thrust shears from (A) 59

Figure 3-20. Fabrics developed by D_{3b} strike-slip shearing in the central segment of the Rod shear 61

Figure 3-21. (A) Stereographic plot of foliation and lineation from the David Lake Shear. (B) Stereographic plot of foliation and lineation from the Mallard Lake Shear 62

Figure 3-22. Geological map of the Mallard Lake area 64

Figure 3-23. Outcrop map of the Blindman shear zone close to the David Lake Shear 66

Figure 3-24. Extent of the McLennan Lake Tectonic Zone and Alpat Lake Tectonic Zone. Insert: folded unconformity in the Scriver Lake area 67

Figure 3-25. Stereographic plots of internal fabrics in the MLTZ 70

Figure 3-26. Stereographic plots of internal fabrics in the ALTZ 71

Figure 3-27. (A) Flinn diagram for deformed pebbles in meta-conglomerates. (B) Flinn diagram for deformed lapilli in lapilli tuff. (C) Stereographic plot of principal axes of deformed pebbles and lapilli 74

Figure 3-28. (A) Strongly flattened conglomerate pebbles. (B) Photomicrograph of quartz shape fabric in highly deformed alaskite. 75

Figure 3-29. (A) Locations of specimens used to determine quartz c-axis preferred orientations in the McLennan Lake area and Dickens Lake area. (B) Preferred-orientations diagrams of quartz c-axes..... 77

Figure 3-30. D_{3b} structures from the MLTZ and the ALTZ 80

Figure 3-31. Schematic illustrations of the development of asymmetric structures as a result of progressive dextral shear deformation 83

Figure 3-32. The finite strains as a consequence of two increments of decomposed pure-shear and simple-shear components of transpression..... 88

Figure 3-33. (A) Plan view of geometric relations among typical shear fractures formed in a simple shear zone. (B) Expected modification in the orientation of the brittle shear fractures under conditions of dextral transpression. (C) Expected modification in the orientation of the ductile shears under conditions of dextral transpression..... 91

Figure 3-34. (A) Stereographic plot of mean attitudes of D_{3a} gold-bearing shears and shallow-dipping shears, and the MLTZ. (B) Schematic illustration of relationships among the MLTZ, D_{3a} gold-bearing shears and shallow-dipping shears..... 94

Figure 3-35. Schematic diagram illustrating sinistral transcurrent movement on the ALTZ under dextral transpression..... 97

Figure 3-36. Longitudinal section of the Jasper deposit showing the steep northeast pitch of the ore shoots 98

Figure 3-37. Longitudinal section of Rod Main orebody, Jolu Mine 98

Figure 3-38. Stereographic plot illustrating the relationships between the plunge of the Rod Main orebody and the intersection of shears 102

Figure 3-39. Diagrams illustrate how the shape and orientation of the Rod Main orebody in longitudinal section may be obtained by the D_{3b} oblique-slip shearing..... 103

CHAPTER 4

Figure 4-1. Bimodal grain size of D_1 amphibole in moderately foliated mafic metavolcanic rock 109

Figure 4-2. D_1 amphiboles in weakly foliated mafic metavolcanic rock 110

Figure 4-3. Zoning patterns of D_1 amphiboles in the mafic metavolcanic rocks, pelitic rocks and plutonic rocks 111

Figure 4-4. Zoning patterns of D_1 amphiboles in the mafic metavolcanic rocks and granodiorite in the MLTZ 117

Figure 4-5. Photomicrograph of D_{3b} amphiboles growing in the hinge area of a Z-shaped asymmetric fold in the MLTZ 118

Figure 4-6. Progressive syn-kinematic metamorphism and fabric development in a D_2 shear hosted by mafic metavolcanic rock 120

Figure 4-7. Zoning patterns of amphiboles in the D_2 structures 122

Figure 4-8. Variation in the composition of D_2 amphiboles with respect to D_1 amphiboles 123

Figure 4-9. Variation in the composition of plagioclase in D_2 structures with respect to plagioclase in the host rocks 124

Figure 4-10. Variations in the composition of biotite in D_2 structures with respect to biotite in the host rocks 125

Figure 4-11. D_{3b} amphibole porphyroblasts in the central phyllonite zone of the Rod shear zone 128

Figure 4-12. Zoning patterns of D_{3a} and D_{3b} amphiboles associated with the Rod shear zone 129

Figure 4-13. Variation in the composition of D_{3a} and D_{3b} amphiboles in the Rod shear zone with respect to D_1 amphiboles 130

Figure 4-14. Variation in the composition of plagioclase in the Rod shear with respect to plagioclase in the host rocks 131

Figure 4-15. Variation in the composition of biotite in the Rod shear zone with respect to biotite in the host rocks 132

Figure 4-16. Petrogenetic grid for the KFMASH system 141

Figure 4-17. Empirical geothermometer for plagioclase-amphibole exchange equilibrium 143

Figure 4-18. Experimental plagioclase-hornblende geothermobarometer 145

Figure 4-19. Variation in amphibole composition with reference to variation in the host-rock chemistry 149

Figure 4-20. Percent mass flux of selected major and trace elements in the deformed granodiorite of the McLennan Lake Tectonic Zone 152

Figure 4-21. Percent mass flux of selected major and trace elements in the deformed porphyritic diorite of the Mallard Lake Shear 154

Figure 4-22. Geochemical variation diagrams for selected elements from the D_3 gold-bearing shears 155

Figure 4-23. Comparison of percent mass fluxes of selected elements between the porphyritic diorite-hosted D_2 Mallard Lake Shear and D_3 Rod shear 158

CHAPTER 5

Figure 5-1. Plots of oxygen isotopic compositions of minerals from veins with respect to host structures 170

Figure 5-2. Plot of hydrogen isotopic composition of hydrous vein minerals with respect to host structures 173

Figure 5-3. Positive shifts in oxygen isotopic composition of minerals in deformed rocks associated with the MLTZ, D_2 shear and D_3 gold-bearing shears 175

Figure 5-4. Isotherm plots of oxygen isotopic equilibration temperatures for quartz and coexisting minerals 178

Figure 5-5. Diffusion rate of ^{18}O in minerals plotted as a function of temperature ... 181

Figure 5-6. $\delta^{18}O$ - $\delta^{18}O$ plots of coexisting mineral pairs from granodiorite and granite, and the D_3 shear-related protomylonite and mylonite 185

Figure 5-7. Calculated oxygen and hydrogen isotopic compositions of waters involved in the formation of quartz veins 189

Figure 5-8. Fluid/rock oxygen ratio versus $\delta^{18}O$ of infiltrating fluids in the MLTZ, D_2 shear, D_3 Rod and Jasper shears on the basis of quartz $\delta^{18}O$ values 191

CHAPTER 6

Figure 6-1. Schematic diagram outlining the major geological events through time that affected the Star Lake-McLennan Lake area 196

Figure 6-2. $^{40}Ar/^{39}Ar$ incremental-release age spectra and apparent Ca/K spectra of hornblende separates 201

APPENDIX A

Figure A-1. Classification of calcic amphiboles 247

CHAPTER 1

INTRODUCTION

Introductory Statement

The Star Lake-McLennan Lake area is located approximately 120 km northeast of La Ronge, northern Saskatchewan. The area has been the most productive gold camp in the Paleoproterozoic Reindeer Zone of the Trans-Hudson Orogen since the mid-1980's. Although less well documented and considerably smaller in total gold production, structurally controlled gold mineralization in the Reindeer Zone (e.g. Kyser *et al.*, 1986; Ibrahim and Kyser, 1991; Ansdell and Kyser, 1992; Hrdy and Kyser, 1995) exhibits many of the empirical characteristics common to Archean deposits of the Superior province (Card *et al.*, 1989, and references therein) and Yilgarn Block of Western Australia (Groves and Phillips, 1987, and references therein).

Over recent years, the geology, structure, geochemistry, timing and tectonic setting of gold mineralization have been the focus of intensive research. Efforts have concentrated on understanding the origin of gold-bearing fluids. The controversy centres around the timing of initial gold mineralization in relationship to the history of magmatism and regional metamorphism. Considerable emphasis has also been placed on documenting the structural geology of the deposits. However, the history of the gold-bearing structures and the relationships of the gold-bearing structures to the regional deformation and to the regional tectonic zones have not been well demonstrated.

The program undertaken in this study is a continuation of an earlier study of the relationship of the lode gold deposits in the Star Lake and Island Lake plutons to the deformation of the plutons (Roberts, 1993). This program extends the study to an examination of the relationships of the structures in the plutons with those in the supracrustal metavolcanic and metasedimentary rocks, and the structures in regional

high strain zones, such as the McLennan Lake Tectonic Zone and the Alpat Lake Tectonic Zone. The principal objective of this program was to provide better understanding of the relative and absolute timing of the structural and metamorphic events, and the emplacement of gold.

Field Work

Geological mapping on a scale of 1:20,000 was carried out in June to September 1991, followed by a detailed investigation of selected structures in June to September 1992 and in July 1993 (Figure 1-1). Samples were collected for petrological and structural examination and for geochemical and microprobe analyses. Samples were also taken for Ar-Ar geochronometry in an attempt to establish the absolute timing of metamorphic and deformational events.

Previous Geological Studies

Initial geological reconnaissance mapping of the Star Lake-McLennan Lake region was undertaken by the Geological Survey of Canada in the 1930's (see Thomas, 1993). However, extensive studies were not undertaken until the early 1980's. The Star Lake area was mapped by Thomas (1985), and the Star Lake pluton by Ames *et al.* (1987). Watters (1984, 1985) and Janser (1993) undertook lithogeochemical studies of metavolcanic and plutonic rocks. Geochronology of volcanism and plutonism was carried out by Bickford *et al.* (1983, 1986), Van Schmus *et al.* (1987), and Watters and Armstrong (1985). The age of sedimentation in the MacLean Belt was studied by Ansdell and Yang (1995). The regional tectonic and tectonostratigraphic relationships between the metavolcanic rocks of the Central Metavolcanic Belt and the meta-arkoses of the McLennan Lake Belt were described by Lewry (1983, 1986), Schaaf and Schwerdtner (1992), Maxeiner and Sibbald (1995), and Yeo (1996). The most recent summary of the geology and economic geology of the area was provided by Thomas (1993).

Fluid inclusion and stable isotopic studies were carried out on the Star Lake

deposit (Kyser *et al.*, 1986; Ibrahim and Kyser, 1991) and the Jasper deposit (Hrdy and Kyser, 1995). Appleyard (1991) described hydrothermal alteration associated with gold mineralization. The age dating of gold mineralization in the Star Lake deposit, the Jasper deposit and the Jolu deposit was undertaken by Ibrahim and Kyser (1991), Hrdy and Kyser (1995), and Thomas and Heaman (1994), respectively.

The association of gold deposits with shear zones in the plutons was demonstrated by exploration companies in the 1980's, and by work carried out by the Geological Survey of Canada (GSC), under the Canada-Saskatchewan Mineral Development Agreement 1984-89. The objectives of the GSC study were to examine the structural features related to gold mineralization, with detailed descriptions of the structures from selected deposits. The results were published in a series of reports (Poulsen, 1986; Poulsen *et al.*, 1985, 1986a, 1986b; Poulsen *et al.*, 1987; Ames *et al.*, 1987), and were summarized in Poulsen (1989). Subsequent studies of the structural geology were reported in publications by Roberts and Schwann (1989), Roberts (1990, 1993) and He and Roberts (1991).

History of Exploration and Development

The exploration and development history of the Star Lake-McLennan Lake area was summarized by Coombe (1984) and Murphy (1986), and more recently by Thomas (1993) and Roberts (1993). Gold was mainly produced from the Star Lake, the Jolu, and the Jasper deposits, with the combined gold production in excess of 360,000 oz (Table 1-1).

The first significant discovery of gold mineralization was made in 1944 at Mallard Lake, along the northwestern margin of the Star Lake pluton, by prospectors of the Consolidated Mining and Smelting Company of Canada Ltd. A trenching and diamond drill program conducted in 1944-45 outlined a small ore body with initial reserves estimated at 22,000 tons, grading 1.15 oz/ton gold. In 1967, reserves were calculated to be approximately 25,000 tons at a grade of 0.5 oz/ton Au. Between 1973 and 1975, two parallel gold-bearing quartz veins were outlined on the Mallard Lake

property and approximately 5,000 tons of ore were milled at mill head grades of 0.30 oz/ton (10.3g/t).

Table 1-1. Ore reserves and gold produced from the Star Lake-McLennan Lake area

Deposit	Grade and tonnage[1]	Gold produced[1]
Decade	18,350 tons @ 0.66 oz/ton	~ 1,500 oz
Jolu	520,522 tons @ 0.40 oz/ton	203,300 oz
Rush Lake	18,700 ton @ 0.3 oz/ton	N/A
Star Lake	230,000 tons @ 0.50 oz/ton	76,947 oz
Jasper	163,000 tons @ 0.47 oz/ton	82,696 oz

[1] Thomas (1993) and references therein.

In 1984 a new drill program was undertaken by Mahogany Minerals Resources Ltd. at the Mallard Lake property, which resulted in the discovery of a new ore zone lying immediately northwest of the previously discovered veins. The reserves for the Mallard Lake property were updated to 18,350 tons grading of 0.66 oz/ton (22.7 g/t). In 1990 Corona Corporation and Mahogany Minerals Resources Inc. re-evaluated the deposit and a small amount of ore was taken to the Jolu Mill for processing.

The Rod Main and Rod South zones of the Jolu deposit, approximately 500 metres to the south of Mallard Lake were discovered by Mahogany Minerals Resources Inc. in 1984. By 1989 ore reserves to the 450 metre level were estimated to be 377,000 tons at a grade of 0.4 oz/ton (13.7 g/t). Mine development began in June 1988 under the ownership of International Mahogany Corporation and Corona Corporation, and the deposit was mined out by May 1991 with the last ore milled in August 1991. Total production yielded 203,300 oz of gold from 520,522 tons of ore with a mill feed grade of 0.4 oz/ton (13.7 g/t) and an average recovery of 97.4 percent.

The Star Lake mine is located on the northeast shore of David Lake. Gold mineralization in the Star Lake property was initially discovered in 1961 at the south end of Rush Lake by Mary and Eugene Hird, and immediately east of Star Lake by

Eric Partridge. The property was optioned to Athabasca Columbia Mining Ltd. in 1973, and then to Phoenix Canada Oil Ltd. in 1980. Exploration on the property by Saskatchewan Mining and Development Corporation (SMDC), in a joint venture with Phoenix Starrex Mining, a subsidiary of Phoenix Canada, led to the discovery of the 21 Zone in 1983. By the end of 1984, reserves of 230,000 tons at a grade of 0.5 oz/ton (17.1 g/t) had been outlined by an extensive drill program. Construction of the mine began in late 1985 with SMDC as the operator, and partners Starrex Mining Corporation and Uranerz Exploration and Mining Ltd. Underground mining of the 21 Zone was completed by November 1988 after the production of 76,947 oz of gold from 198,747 tons of ore, with an average grade of 0.387 oz/ton and a recovery rate of 93 percent.

Reserves of the Rush Lake deposit, approximately 1300 metres north of the Star Lake deposit, were estimated at 18,700 tons grading 0.3 oz/ton gold in 1988. The ore was taken to the Star Lake mill for processing.

The Jasper zone, in the Island Lake pluton, was discovered by SMDC in 1987 in a shear, southwest of Broeder Lake. The Jasper zone and the James zone to the southwest form a continuous zone of mineralization. Drilling, initiated in 1987, and subsequent underground exploration outlined mineable reserves of approximately 163,000 tons at a grade of 0.47 oz/ton by 1990. Production from the Jasper mine began in April 1990 under the joint ownership of Cameco (80 percent) and Shore Gold Fund (20 percent). The ore was shipped to the Star Lake mill for processing. Before shut-down in December 1991, the Jasper mine had produced a total of 82,696 oz of gold from 140,127 tons of ore, with a grade of 0.55 oz/ton (18.8 g/t).

CHAPTER 2

REGIONAL SETTING AND GEOLOGY OF STAR LAKE-MCLENNAN LAKE AREA

Trans-Hudson Orogen

The Trans-Hudson Orogen is a Paleoproterozoic orogen of the "Pan-American System" (Lewry, 1987), which coincides with a major episode of North American continental accretion and amalgamates Archean provinces to form a Paleoproterozoic supercontinent (Hoffman, 1988, 1990). The Trans-Hudson Orogen is 500 km wide and extends approximately 5000 km from Greenland through Canada into the midwest United States. In northern Saskatchewan and Manitoba, the orogen consists of four composite lithotectonic zones (Lewry and Collerson, 1990) (Figure 2-1): (1) the Churchill-Superior Boundary Zone; (2) the Reindeer Zone; (3) the Wathaman-Chipewyan Batholith; and (4) the Cree Lake Zone. The Reindeer Zone is subdivided into a number of domains; the Star Lake-McLennan Lake area is in the La Ronge Domain. The geology of these lithotectonic zones is summarized in the following sections.

Churchill-Superior Boundary Zone

The Churchill-Superior Boundary Zone is a narrow eastern foreland forming the northwestern margin of the Archean Superior craton, in fault or thrust contact with Proterozoic rocks of the Reindeer Zone. The boundary zone is composed mainly of reworked Archean Pikwitonei gneisses, with subordinate, highly deformed metavolcanic and metasedimentary rocks, interpreted as parautochthonous Proterozoic supracrustal rocks, and dismembered ultramafic bodies (Bleeker, 1990). Unreworked Archean granulite facies gneisses of the Pikwitonei belt, exposed to the southeast of the boundary zone, are representatives of deep level exhumation of the Archean crust (Bleeker, 1990).

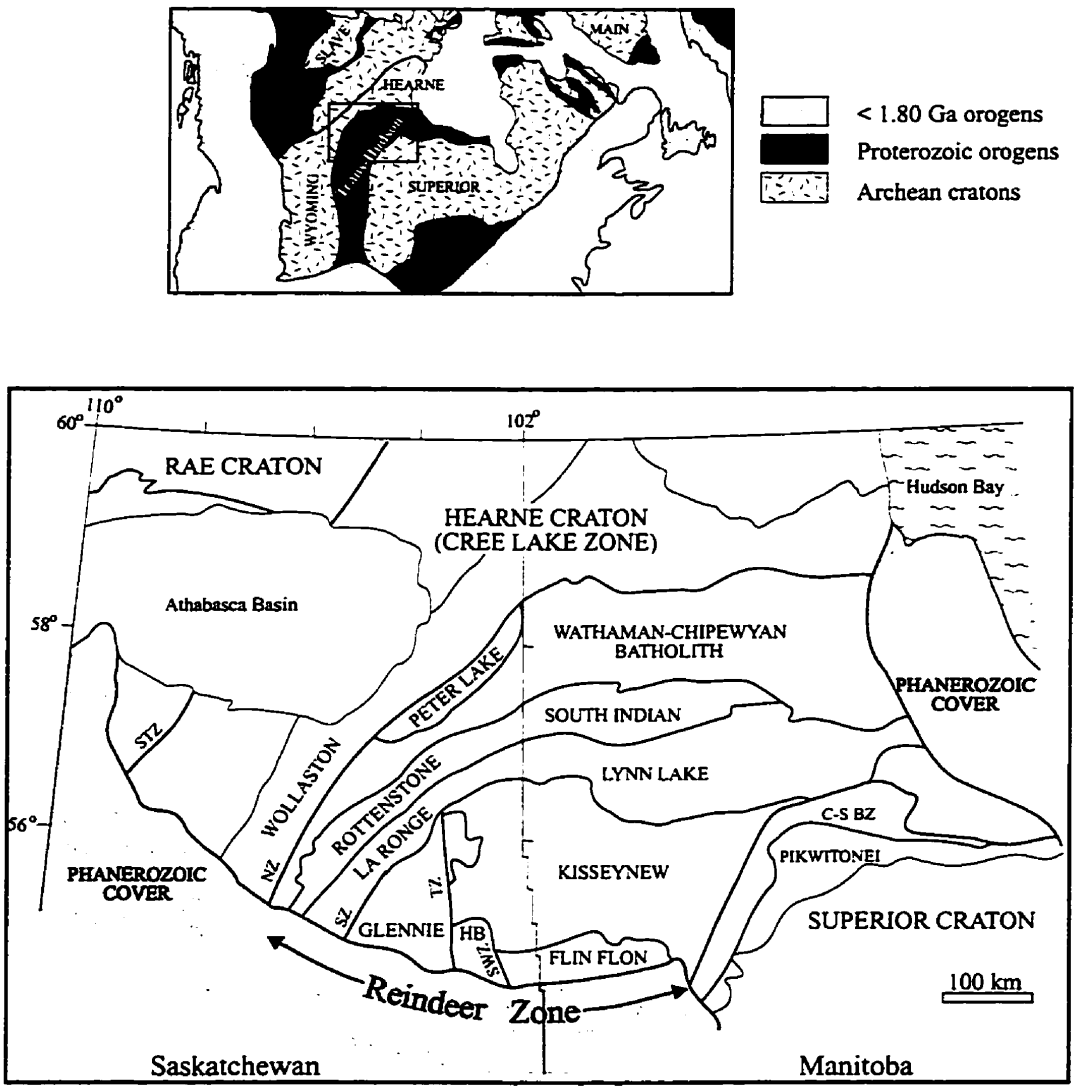

Figure 2-1. Lithotectonic domains of the Trans-Hudson orogen and the adjacent Archean Rae, Hearne and Superior provinces (modified from Lewry *et al.*, 1990). Thick solid line, ductile shear zones/faults; Thin solid line, boundaries between domains; C-S BZ, Churchill-Superior boundary zone; HB, Hanson Lake Block; NZ, Needle Falls-Parker Lake shear zone; STZ, Snowbird tectonic zone; SWZ, Sturgeon Weir shear zone; SZ, Stanley fault/shear zone; TZ, Tabbernor fault zone. Smaller map shows general extent of Trans-Hudson Orogen and adjacent Archean cratons (after Hoffman, 1989).

The Churchill-Superior Boundary Zone has experienced two metamorphic events (Machado, 1990). Peak metamorphism of middle to upper amphibolite facies occurred at 1809 Ma, following the initial phase of granitic magmatism at 1822 Ma. These ages are comparable with peak metamorphism (1815-1810 Ma) in the adjacent Kisseynew Domain (Gordon *et al.*, 1990), which was probably related to thermal relaxation following the initial phase of the Reindeer-Superior collision and crustal thickening. The second event is marked by granitoid intrusion and renewed amphibolite facies metamorphism at 1726-1720 Ma, and may reflect the continuing Reindeer-Superior convergence after initial collision (Machado, 1990).

Reindeer Zone

The Reindeer Zone includes all lithotectonic components lying between the Churchill-Superior Boundary Zone and the Wathaman-Chipewyan Batholith. It is an aggregation of arc-related Proterozoic volcanic and plutonic rocks, coeval volcanogenic sediments, arkosic molasse and late to post-tectonic intrusions (Lewry *et al.*, 1990). The arcs and associated sedimentary basins were intensely reworked during collision between Hearne and Superior cratons. The Proterozoic assemblages of the Reindeer Zone are underlain by an Archean basement terrane (Saskatchewan Craton), as revealed by recent seismic profiles across Saskatchewan and Manitoba (Lucas *et al.*, 1993; Lewry *et al.*, 1994), and across Montana and North Dakota (Nelson *et al.*, 1993; Baird *et al.*, 1996). The reworked Archean basement, exposed in the Hanson Lake Block and in the southwestern Glennie Domain (Figure 2-2), occupy the lowest exposed structural levels of the Reindeer Zone and are separated from overlying Proterozoic assemblages by flat-lying mylonite zones (Lewry *et al.*, 1990).

Subdivisions and Age Constraints

The Reindeer Zone is divided into Rottenstone-South Indian Domain, La Ronge-Lynn Lake Domain, Glennie Domain, Kisseynew Domain, Flin Flon Domain, and Hanson Lake Block (Macdonald, 1987) (Figure 2-1).

The La Ronge-Lynn Lake and Flin Flon domains comprise remnants of island

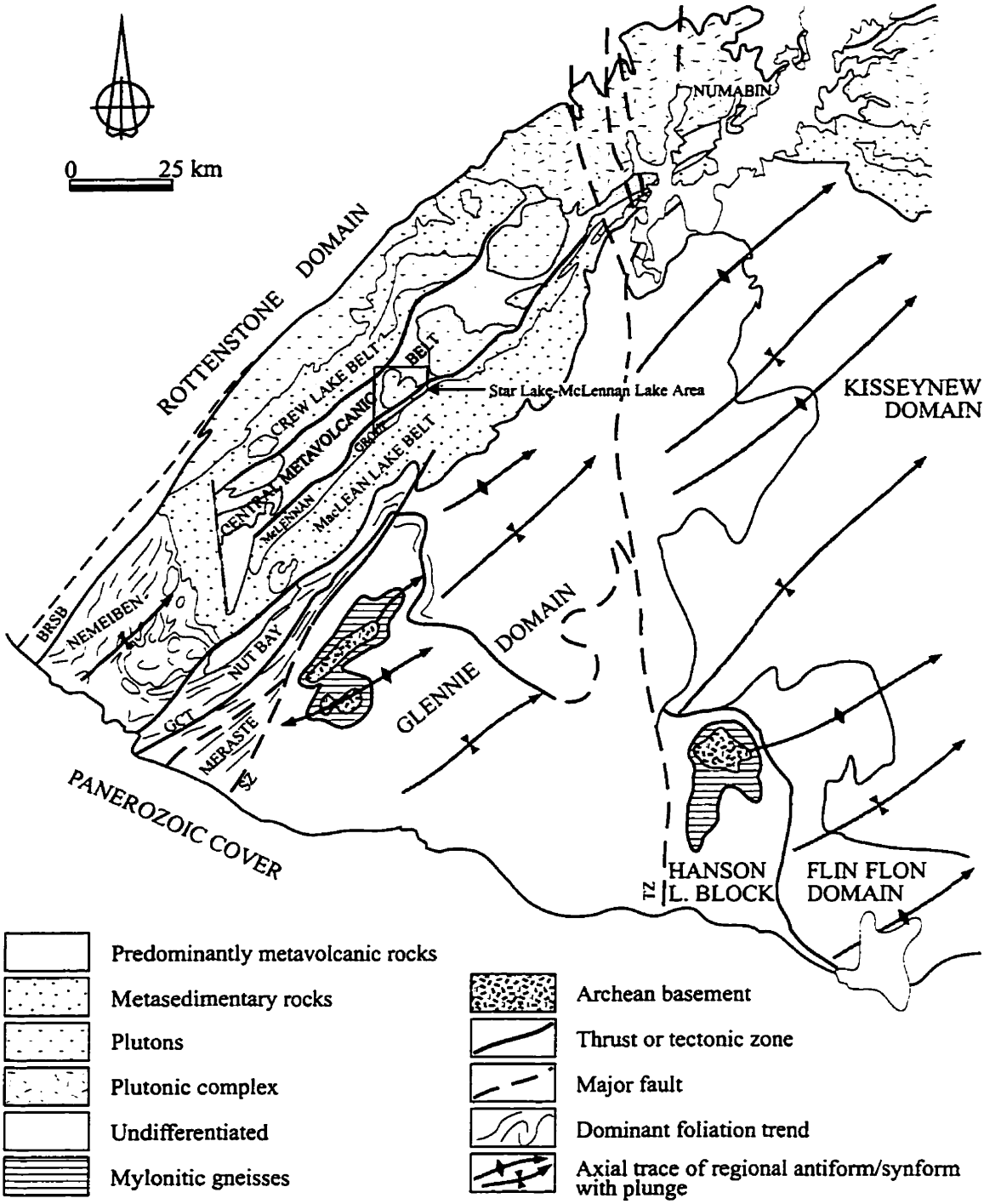

Figure 2-2. Tectonostratigraphic subdivisions of the La Ronge Domain (after Coombe *et al.*, 1986), and the axial traces of the latest regional folds in northern Saskatchewan (after Lewry *et al.*, 1990). BRSB, Birch Rapids straight belt; GCT, Guncoat thrust; SZ, Stanley fault/shear zone; TZ, Tabbernor fault zone.

arc and back-arc assemblages (Syme, 1990; Thom *et al.*, 1990) and alluvial-fluvial sedimentary rocks (Stauffer, 1990). The Kisseynew Domain is dominated by high-grade paragneisses that may be derived from turbiditic greywackes and subordinate volcanic rocks and arkoses, presumably deposited in a basin marginal to the Flin Flon and La Ronge-Lynn Lake arcs (Zwanzig, 1990). The Rottenstone-South Indian Domain consists mainly of tonalitic, granodioritc and granitic plutons and subordinate supracrustal rocks (Lewry and Sibbald, 1980). The Glennie Domain and Hanson Lake Block are dominated by variably deformed granitoid rocks with subordinate to minor supracrustal rocks (Macdonald, 1987).

Precise U-Pb zircon ages indicate that volcanism had begun by 1.91 Ga and was active throughout the Reindeer Zone by 1.88 Ga (Van Schmus *et al.* 1987; Bickford *et al.* 1990; Gordon *et al.* 1990). Plutonism occurred between 1.87 and 1.83 Ga (Bickford *et al.* 1990; Gordon *et al.*, 1990). Post kinematic intrusions, including granitic sheets and pegmatites, were emplaced at 1.79 to 1.77 Ga (Bickford *et al.*, 1990; Sun *et al.*, 1996). Geochemical and isotopic studies indicate that the igneous rocks of 1.91 to 1.30 Ga are juvenile, formed in an oceanic arc or back arc setting as intervening oceanic lithosphere was subducted (Watters and Pearce, 1987; Syme, 1990).

Sedimentation in the Kisseynew Domain probably occurred as early as 1.86 Ga (David *et al.*, 1993). The arc volcanic and plutonic rocks of the Flin Flon Domain and southern Kisseynew Domain are unconformably overlain by Missi Group molasse deposits with ages of ca. 1.85-1.83 Ga (Gordon *et al.*, 1990; Stauffer, 1990). Similar ages were also reported for sedimentation in the eastern La Ronge Domain (Ansdell and Yang, 1995).

General Structural Geology

The structures of the Reindeer Zone can be ascribed, in general terms, to two periods of deformation (Stauffer, 1984; Hoffman, 1988; Lewry *et al.*, 1990). The earlier period of deformation is characterized by tight to isoclinal, upright to inclined folds throughout the Reindeer Zone. In the Central Metavolcanic Belt of the La Ronge Domain (Figure 2-2) and in the Flin Flon Domain, only one set of the folds occurs and

there is little evidence of the development of large-scale isoclinal folds (Stauffer and Mukherjee, 1971; Thomas, 1985; He and Roberts, 1992). Elsewhere, the early deformation is indicated by the superposition of multiple sets of tight to isoclinal folds and associated fabric, and is believed to represent a progressive strain continuum involving extreme crustal shortening (Lewry *et al.*, 1981).

The second period of deformation is characterized by the development of at least two sets of regional scale folds (Lewry *et al.*, 1990). The axial traces of the later regional folds of the second deformation are delineated in Figure 2-2. The folds vary from open to close, with upright to steeply inclined axial surfaces and gentle northeast plunges. They are superimposed on the early folds of the second deformation to produce complex interference patterns in the Glennie, Kisseynew, and Flin Flon domains, the Hanson Lake Block, and the La Ronge Horseshoe of the La Ronge Domain (Lewry *et al.*, 1990 and the references therein). Elsewhere in the La Ronge Domain and in the Rottenstone Domain, the folds of the second deformation were not observed. Lewry (1984) and Lewry *et al.* (1990) suggest that in these areas the second deformation is mainly manifest in regional-scale, rotational oversteepening of the lithostructural elements. The Glennie Domain forms the core of the NE-plunging regional anticlinorium of the second deformation, with the La Ronge Domain and the Rottenstone Domain forming its northwestern limb.

The Reindeer zone is also characterized by a number of ductile high-strain zones of regional extent, defining major boundaries between the lithotectonic domains or subdomains of the Reindeer Zone (Stauffer, 1984). The high-strain structures vary in attitude from subhorizontal to subvertical. Some of them are recognized as the sole thrusts to major allochthonous sheets, and are believed to have been initiated as gently-dipping structures with dominant southeast-vergence, along which major displacement occurred during the early period of deformation (Lewry *et al.*, 1990).

The exposure of the Archean basement in the Glennie Domain and Hanson Lake Block, separated from overlying Proterozoic arc-related igneous rocks and metasedimentary rocks by mylonitic zones (e.g. Chiarenzelli and Lewry, 1988), suggests that the Proterozoic assemblages were stacked above a regional sole thrust with the Archean basement in its footwall (Bickford *et al.*, 1990; Lewry *et al.*, 1990).

The Archean basement is structurally isolated from the Archean Superior and Hearne cratons (Lucas *et al.*, 1993; Lewry *et al.*, 1994), and may therefore be exotic. The early flat-lying complexes and the high-strain soles were refolded during second deformation and oversteepened in regional fold limbs to produce the present tectonostratigraphic systems (Lewry *et al.*, 1990).

Metamorphism

The distribution pattern of metamorphic facies in the Reindeer Zone displays a spatial correlation with the lithotectonic domains and major tectonic discontinuities. Metamorphic grade is relatively uniform within the main lithotectonic domains, with abrupt metamorphic gradients usually coincident with major, domain-bounding high-strain zones (Lewry *et al.*, 1978).

The grade of metamorphism in the Rottenstone Domain is generally within the upper amphibolite facies (Lewry *et al.*, 1978). In the Central Metavolcanic Belt of the La Ronge Domain, the metamorphic grade ranges from the upper greenschist to amphibolite facies, increasing to higher grade in the highly deformed Numabin Complex in the northeast (Coombe *et al.*, 1986). The metamorphic grade shows a general tendency to increase outwards towards the margins of the belt, and reaches middle to upper amphibolite facies conditions in the flanking Crew Lake Belt to the northwest and McLennan Lake Belt to the southeast (Coombe *et al.*, 1986).

In the Glennie Lake Domain there is a general increase in metamorphic grade to the north and northwest into the La Ronge Domain. While middle to upper amphibolite facies metamorphism was attained in the northern part, most of the southern part is within upper greenschist to lower amphibolite facies (Lewry *et al.*, 1978; Thomas, 1988).

The metamorphic grade in the Flin Flon Domain is relatively low, ranging from subgreenschist to upper greenschist facies in the south (Gordon *et al.*, 1990). The grade increases to lower amphibolite facies northward to the contact with the Kisseynew Domain (Gordon *et al.*, 1990), and westward to the Hanson Lake Block (Slimmon, 1992). Upper amphibolite to granulite facies was attained within the

Hanson Lake Block (Abbas-Hasanie *et al.*, 1991), and the central portion of the Kisseynew Domain, where the metamorphic grade is remarkably uniform (Bailes and McRitchie, 1978).

Early peak metamorphism was recognized in the area adjacent to the southeastern edge of the Wathaman Batholith, predating the 1865-to-1850-Ma batholith (see below) (Lewry *et al.*, 1981). Metamorphism peaked at *ca.* 1820-1800 Ma in the La Ronge Domain (Kyser and Stauffer, 1995), coeval with the penetrative fabric of the early period of deformation. In the Flin Flon and Kisseynew domains, metamorphism was accompanied by the folding events of the later deformation (Stauffer and Mukherjee, 1971; Sibbald, 1978; Bailes and McRitchie, 1978), and reached its highest temperatures in the Kisseynew Domain at *ca.* 1815-1810 Ma (Gordon *et al.*, 1990).

Wathaman-Chipewyan Batholith

The Wathaman-Chipewyan Batholith (Meyer *et al.*, 1992) was emplaced between reactivated Archean continental crust of the Hearne craton and juvenile arc terranes of the Reindeer Zone. The batholith is a monzogranitic-granodioritic complex with calc-alkaline geochemical signature (Lewry *et al.*, 1981; Meyer *et al*, 1992), and ages of 1865-1850 Ma (Meyer *et al.*, 1992). The geological relationships and geochemistry of the batholith indicate that it is a continental-margin batholith that was formed when the oceanic crust subducted under the Archean continental crust (Bickford *et al.*, 1990; Meyer *et al.*, 1992).

Cree Lake Zone

The Cree Lake Zone is a broad, highly reactivated southeastern part of the Archean Hearne craton (Lewry and Sibbald, 1980). It consists mainly of amphibolite to granulite facies, granitoid orthogneisses, migmatites and minor mafic gneisses. The Archean basement is overlain by the Wollaston domain (eastern Cree Lake Zone), a

fold belt which includes medium to high grade Proterozoic continental margin metasedimentary rocks.

La Ronge Domain

The La Ronge Domain lies in the western part of the Reindeer Zone (Figure 2-1). It is flanked in the northwest by the Rottenstone Domain and in the southeast by the Kisseynew and Glennie domains. The junction between the La Ronge Domain and Rottenstone Domain is defined in the southwest by the eastern margin of the Birch Rapids Straight Belt, a broad subvertical ductile high-strain zone (Lewry, 1984), and farther north by ductile mylonitic gneisses of the Paul River Shear Zone (Gilboy, 1982). The southeastern margin of the La Ronge Domain is defined by the Stanley Shear Zone, a subvertical belt of protomylonitic-mylonitic gneisses and tectonic schists (Lewry, 1984).

Subdivisions

The La Ronge Domain is subdivided into the Crew Lake Belt, Central Metavolcanic Belt, MacLean Lake Belt, and La Ronge Horseshoe (Nemeiben Zone and Nut Bay Belt) (Coombe *et al.*, 1986) (Figure 2-2).

Crew Lake Belt

The Crew Lake Belt structurally overlies the Central Metavolcanic Belt to the southeast, with the boundary marked largely by a broad zone of high strain (Thomas, 1993; Harper, 1986). It consists mainly of psammitic to psammopelitic metasediments with subordinate intercalated hornblendic gneisses (Lewry, 1984), intruded by tonalitic to granitic plutons (Coombe *et al.*, 1986). The Crew Lake Belt is laterally equivalent to and possibly stratigraphically overlain by the Central Metavolcanic Belt (Thomas, 1993).

Central Metavolcanic Belt

The Central Metavolcanic Belt is an assemblage of predominantly mafic to intermediate and minor felsic metavolcanic rocks with intercalated metasediments, intruded by pre- to late kinematic plutons (Thomas, 1985). Volcanism occurred at 1882-1872 Ma (Van Schmus *et al.*, 1987). The volcanic rocks are essentially calc-alkaline and low potassium tholeiitic lavas similar to those generated from modern volcanic arcs (Harper *et al.*, 1986; Watters and Pearce, 1987).

A younger period of volcanism, which consists of trachytoid intermediate flows, was recently recognized in the MacKay Lake area in the southern La Ronge Domain (Maxeiner and Sibbald, 1995). The volcanism occurred at *ca.* 1850 to 1840 Ma, coeval with the deposition of a sedimentary assemblage that unconformably overlies the volcano-plutonic rocks of the Central Metavolcanic Belt (see below) (Maxeiner and Sibbald, 1995).

The plutons range from uniform to multiphase, and from gabbro to granite (Coombe *et al.*, 1986). They were emplaced between 1874 and 1835 Ma, and may have been episodic at 1870 Ma, 1855 Ma and 1835 Ma (Kyser and Stauffer, 1995). The plutonic rocks have a strong calc-alkaline character and trace element patterns typical of formation in a volcanic arc environment (Harper *et al.*, 1986; Janser, 1993).

The Numabin Complex, situated in the northeastern segment of the Central Metavolcanic Belt, is dominated by pre- to early synkinematic diorite, tonalite and granodiorite. Subordinate metavolcanic and metasedimentary rocks occur along the southeastern margin and as remnants within the plutonic complex (Coombe *et al.*, 1986).

MacLean Lake Belt

The MacLean Lake Belt includes two major lithostratigraphic components: the MacLean Lake Gneisses and the McLennan Group (Lewry, 1983). The MacLean Lake Gneisses are an assemblage of predominantly psammitic-psammopelitic gneisses and subordinate polymictic metaconglomerates, calc-silicate gneisses and volcanogenic

metagreywackes (Coombe *et al.*, 1986). The MacLean Lake Gneisses stratigraphically and structurally underlie the McLennan Group, with the contact between the two sequences marked locally by shear deformation (Thomas, 1993).

The McLennan Group consists of meta-arkosic rocks and minor basal arkosic polymictic meta-conglomerates, which originated from granitic sources and formed as a molasse-like deposit along the northwestern margin of the MacLean Lake Belt (Lewry *et al.*, 1990; Thomas, 1993). Lewry (1986) described that the McLennan Group unconformably overlies the Central Metavolcanic Belt, with the unconformity at the base of the McLennan Group. More recent work carried out by Maxeiner and Sibbald (1995) indicates that the McLennan Group is underlain by a volcano-sedimentary succession (*ca.* 1855 to 1840 Ma), which unconformably overlies the volcano-plutonic rocks of the Central Metavolcanic Belt, and grades to the sediments of the McLennan Group. Along much of its length, the boundary between the Central Metavolcanic Belt and the McLennan Group is defined by the McLennan Lake Tectonic Zone (Lewry, 1983; Thomas, 1985).

La Ronge Horseshoe

The La Ronge Horseshoe, including Nemeiben Zone and Nut Bay Belt, forms the southwestern part of the La Ronge Domain. It is composed mainly of a complex of pre- to syn-kinematic plutons of biotite-bearing granodiorite and granite, and less abundant hornblende quartz diorite, tonalite and granodiorite. Supracrustal rocks are subordinate, and include psammitic to psammopelitic metagreywackes, amphibolitic gneisses and schists of probably volcanic origin, felsic metavolcanic rocks, carbonate rocks and local polymictic metaconglomerates (Coombe *et al.*, 1986).

Tectonic Evolution of Reindeer Zone

Table 2-1 summarizes U-Pb zircon ages on major events of volcanism, plutonism, sedimentation and metamorphism in the Reindeer Zone. Tectonic evolution in the western Reindeer Zone, where the study area is located, is illustrated in a series of schematic diagrams in Figure 2-3.

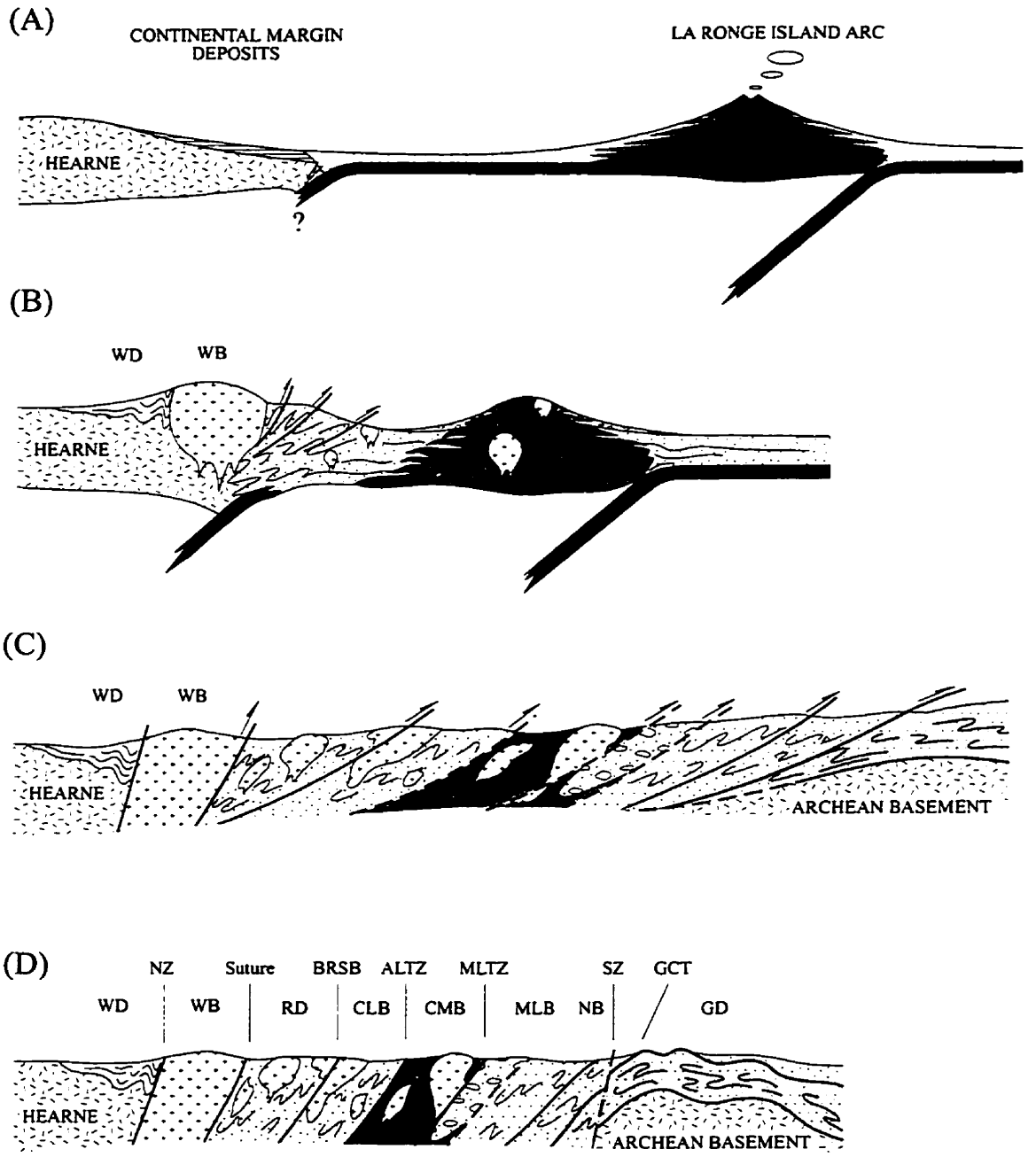

Figure 2-3. Schematic diagrams illustrating tectonic evolution of the northwestern Trans-Hudson Orogen (*ca.* 1.91-1.79 Ga). See text for detail. ALTZ, Alpat Lake Tectonic Zone; BRSB, Birch Rapids straight belt; CLB, Crew Lake Belt; CMB, Central Metavolcanic Belt; GCT, Guncoat thrust; GD, Glennie Domain; MLB, MacLean Lake Belt; MLTZ, McLennan Lake Tectonic Zone; NB, Nut Bay Belt; NZ, Needle Falls-Parker Lake shear zone; RD, Rottenstone Domain; SZ, Stanley fault/shear zone; WB, Wathaman Batholith; WD, Wollaston Domain.

Continental rifting and seafloor spreading, based on data from the Hudson Bay and Ungava segments of the Trans-Hudson Orogen, may have begun at approximately 2.1-2.0 Ga (St-Onge *et al.*, 1992). Early intra-oceanic subduction began at *ca.* 1910 Ma, resulting in subduction-generated oceanic arc volcanism that was active throughout the Reindeer Zone until 1875 Ma (Van Schmus *et al.*, 1987; Bickford *et al.* 1990; Gordon *et al.* 1990). Volcanogenic sedimentary rocks were deposited into adjacent basins. Recent deep seismic investigations indicate that the Reindeer Zone may have been subducted to the west in the western portion of the zone and to the east in the eastern portion (Lucas *et al.*, 1993; Nelson *et al.*, 1993). From this point of view, the La Ronge Domain represents the remnant of one of the Proterozoic juvenile volcanic arcs (Figure 2-3A).

Table 2-1. Age constraints for igneous, metamorphic, and tectonic events in the Reindeer Zone.

Age (Ga)	Geological event	Reference
To 1.72	Post-collision deformation	Machado (1990)
1.83-1.79	Reindeer-Superior collision; major deformation and emplacement of nappe-sheets; peak metamorphism	Bickford *et al.* (1990) Gordon *et al.* (1990)
1.88-1.83	Plutonism (e.g. 1874-1835 Ma plutonism in the La Ronge Domain); continental sedimentation, and back-arc basin development	Bickford *et al.*, (1990) Gordon *et al.* (1990) Kyser and Stauffer (1995)
1.86-1.85	Emplacement of the Wathaman-Chipewyan Batholith; onset of Reindeer-Hearne collision	Meyer *et al.* (1992) Bickford *et al.* (1990)
1.91-1.88	Generation of arc and back-arc crust within the Reindeer Zone (1882-1872 Ma in the La Ronge Domain)	Bickford *et al.* (1990) Gordon *et al.* (1990) Van Schmus *et al.* (1987)
2.10-2.00	Continental rifting and oceanic spreading	St-Onge *et al.* (1992)

Cratonization was initiated in the northwestern Reindeer Zone when La Ronge arc terrane was accreted to the Hearne continental margin (Figure 2-3B). The onset of the accretion was marked by the emplacement of the Wathaman-Chipewyan batholith

at 1865-1850 Ma, broadly coeval with widespread plutonism throughout the Reindeer Zone (1875-1830 Ma). The emplacement of the batholith was preceded by a major phase of isoclinal folding and coeval peak metamorphism on its southeastern edge (Lewry *et al.*, 1981). The location and chemistry of the Wathaman batholith indicate that the batholith is a continental arc formed in response to westward or northwestward subduction of oceanic crust beneath the Hearne continental margin (Fumerton *et al.*, 1985; Meyer *et al.*, 1992). Based on this interpretation, the suture between the Hearne craton and the juvenile arcs of the Reindeer Zone probably lies along the southeastern margin of the Wathaman Batholith.

During the later stages of the plutonism, uplift and erosion led to the development of continental molasse-like deposits, which unconformably overlie volcanic rocks and early sedimentary rocks (Stauffer, 1990; Maxeiner and Sibbald, 1995) (Figure 2-3B).

Terminal collision between the Hearne craton, Reindeer Zone and the Superior craton occurred between 1830 and 1790 Ma (Bickford *et al.*, 1990; Machado 1990), resulting in imbricated thrust faulting and the development of recumbent isoclinal folds and nappes, as well as the stacking of the Proterozoic assemblages above the Archean microcontinent (Lewry *et al.*, 1990; Bickford *et al.*, 1990) (Figure 2-3C). The terminal collision also accounts for the subsequent upright northeast-plunging folds, which oversteepened the lithostructural elements in the northwestern Reindeer Zone (Figures 2-3D).

Post-collisional deformation, uplift and cooling occurred from 1790 to 1720 Ma (Machado, 1990). The post-collisional events included continued shortening across the orogen and movement along some tectonic zones, e.g. the Needle Falls shear zone (*ca.* 1760 Ma) (Fedorowich *et al.*, 1995), the McLennan Lake Tectonic Zone (*ca.* 1750 Ma) (this study), and the Churchill-Superior Boundary Zone (1726-1720 Ma) (Machado, 1990).

Geology of Star Lake-McLennan Lake Area

Lithologic Subdivisions

The Star Lake-McLennan Lake area is underlain predominantly by the rocks of the Central Metavolcanic Belt of the La Ronge Domain (Figure 2-4). They consist of mafic to felsic metavolcanic rocks and minor pelitic rocks, intruded by the Island Lake and the Star Lake plutons. A suite of pre-tectonic mafic to felsic dykes intrudes the plutons and the metavolcanic rocks. The metavolcanic rocks are bordered to the southeast by the meta-arkoses and meta-conglomerates of the McLennan Group, and to the northwest by the pelitic rocks of the Crew Lake Belt. The following section presents brief descriptions of the major lithologies (more detailed descriptions are presented in Figure 1-1). Mineralogy of the rocks is described in detail in Chapter 4 in conjunction with the structural evolution and metamorphic history of the area.

Metavolcanic Rocks

The metavolcanic rocks consist of flows and volcaniclastic rocks of dominantly mafic to intermediate composition. Minor felsic units occur mainly in the form of lapilli and crystal tuff. In the central and southern parts of the area, metavolcanic rocks are dominated by intermediate to mafic flows with minor volcaniclastic rocks, while in the north and the northwest the rocks are mainly volcaniclastic, intercalated with mafic or intermediate flows.

Mafic metavolcanic rocks: Mafic flows are fine to medium grained and have a moderate to well developed schistosity. The flows usually have a spotted appearance due to the occurrence of amphibole porphyroblasts. Subordinate flow units, including pillow flows and flows with plagioclase phenocrysts or carbonate amygdales, are also present. Mafic volcaniclastic rocks, mainly metatuff breccia and meta-agglomerate, are less common than mafic flows, and occur intercalated with mafic and intermediate flows.

Intermediate metavolcanic rocks: Fine to medium grained flows and plagioclase porphyritic flows are the major flow-type rocks. The volcaniclastic rocks

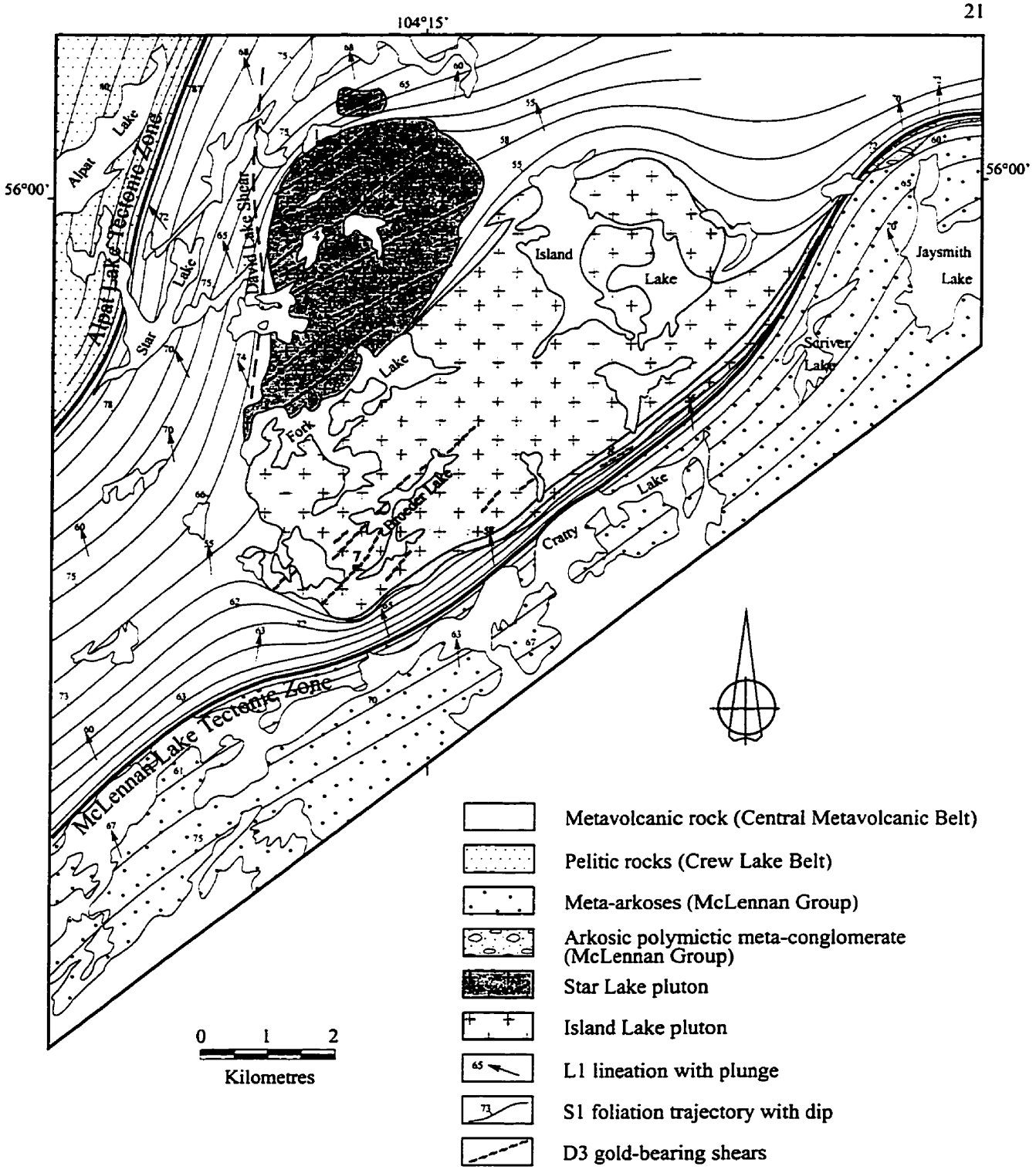

Figure 2-4. Geological map of the Star Lake-McLennan Lake area, La Ronge Domain, northern Saskatchewan. Gold deposits or occurrences: 1, Decade; 2, Jolu; 3, Rush Lake; 4, Blindman; 5, Star Lake; 6, Tamar; 7, James-Jasper-Roxy; 8, MacLeod Main.

include metatuff breccia and meta-agglomerate with unsorted, matrix-supported, heterolithic or monolithic fragments.

Felsic metavolcanic rocks: The felsic metavolcanic rocks are composed of lapilli and crystal metatuff, monolithic tuff breccia and massive flows. The felsic flows are fine-grained to aphanitic and massive to weakly foliated. They are typically interbedded with the intermediate metavolcanic rocks with abrupt lithological contacts.

Pelitic Sedimentary Rocks

Pelitic sedimentary rocks mainly occur in the Crew Lake Belt in the vicinity of the Alpat Lake. The metasediments, generally fine grained and equigranular, are often interlayered with fine grained metavolcanic rocks at the transition between the Central Metavolcanic Belt and the Crew Lake Belt. Primary sedimentary features such as bedding or lamination are largely obliterated. Compositional banding, probably representing transposed primary layering, occurs on scales from millimetres to metres.

The pelitic assemblages possess a moderately- to well-developed schistosity. The metasediments are characterized by abundant, pervasive quartz segregations one millimetre to several centimetres thick, which may make up a few percent of the rocks. The quartz segregations are concordant with the schistosity.

Meta-Arkoses and Meta-Conglomerates

The southeast part of the study area is underlain predominately by meta-arkosic rocks of the McLennan Group, which structurally underlie, and are in faulted contact with, the metavolcanic rock of the Central Metavolcanic Belt. The meta-arkosic rocks are typically medium to fine grained, and generally grey, pale pink and greyish pink, and have a strong penetrative foliation, parallel to, or slightly oblique to the compositional layering.

A unit of arkosic polymictic meta-conglomerates occurs northwest of Jaysmith Lake, in faulted contact with the metavolcanic rocks. This unit is at least 150 m thick and can be traced for approximately 500 m along the strike. The conglomerates are

predominantly arkosic-matrix supported and contain 20 to 65 percent heterolithic pebbles and cobbles of granitic and arkosic lithologies, quartz and subordinate metavolcanic rocks. The pebbles and cobbles are well rounded, and are flattened and elongated to various degrees. The matrix is comparable to the nearby meta-arkosic rocks.

Intrusive Rocks

Star Lake pluton: The Star Lake pluton is a zoned intrusion ranging from a gabbro-diorite marginal zone, through a monzonite-granodiorite transitional zone, to a quartz monzonite-granite core (Thomas, 1985; Ames *et al.*, 1987). Along the northwestern margin and localities north of the David Lake, a phase of plagioclase porphyritic diorite was mapped and included with the marginal zone (see Figure 3-23). The transitions between zones are locally precisely defined but are, more commonly, gradational.

Diorite and gabbro of the marginal zone range from medium to coarse grained. Gabbro often displays mesoscopic layering up to tens of centimetres thick, formed by cumulate augite, amphibole and plagioclase. Porphyritic diorite contains 20-35% plagioclase laths. The plagioclase laths are euhedral to subhedral, up to 8 mm long. The rocks in the marginal zone range from undeformed to moderately foliated. Granodiorite and monzonite in the transitional zone are medium to coarse grained, and are equigranular or porphyritic. The central quartz monzonite and granite are feldspar-porphyritic. The plutonic rocks in the transitional and central zones are largely undeformed.

Island Lake pluton: The Island Lake pluton is more uniform in composition than the Star Lake pluton. The bulk of the intrusion is medium to coarse grained porphyritic granite, with plagioclase phenocrysts 3 to 10 mm long. Subordinate, fine to coarse grained, equigranular to porphyritic monzodiorite and granodiorite occur as marginal phases along the southeastern and northern margins of the pluton.

Dykes: The dykes range in composition from mafic to felsic. The thickness of the dykes varies from a few centimetres to a few metres, with strike lengths up to

several hundred metres. They are subvertical with predominantly northeast strike. A small number of dykes strike approximately east-west and north-south. In the Island Lake pluton, the dykes occur mainly in the southeastern marginal phases. In the Star Lake pluton, they are more abundant and more evenly distributed. Some of the dikes show evidence of multiple emplacement episodes from early mafic to late felsic composition (Poulsen *et al.*, 1986b).

Major Structures and Metamorphism

In the northwestern part of the area, the Alpat Lake Tectonic Zone (Thomas, 1985) marks the transition from the metavolcanic rocks of the Central Metavolcanic Belt to the pelitic rocks of the Crew Lake Belt. The McLennan Lake Tectonic Zone (Lewry, 1983; Thomas, 1985) separates the metavolcanic rocks from the meta-arkoses and meta-conglomerates of the McLennan Group to the southeast. No major fold structures were identified in the metavolcanic rocks. A regional penetrative foliation with an associated lineation is developed in most of the supracrustal rocks and in the marginal phases of the plutons. The fabric is overprinted by locally developed shears and cataclastic zones, and finally by the gold-bearing shear zones in the plutons.

Peak metamorphism appears to be coeval with the development of the regional penetrative fabric (Poulsen *et al.*, 1987). Lower to middle amphibolite conditions were reached across most of the region, however, upper greenschist facies was attained in the vicinity of Jojay Lake (Thomas, 1985). Retrograde metamorphism is indicated in the high strain structures by formation of biotite and chlorite at the expense of hornblendes. However, the local preservation and growth of hornblendes within these structures, in conjunction with the post-tectonic overgrowth of hornblende porphyroblasts outside the structures, indicates that metamorphic conditions of amphibolite facies lasted through the entire deformation events. Detailed metamorphic studies are presented in Chapter 4.

Gold Mineralization

Gold mineralization occurs exclusively within northeast-striking shear zones in the Star Lake and Island Lake plutons. The location of the gold deposits and occurrences are shown in Figure 2-4. From the north to the south, the gold deposits or occurrences are Decade, Jolu, Rush Lake, Blindman, Star Lake, Tamar, and James-Jasper-Roxy. They are epigenetic, structurally controlled quartz vein type or lode gold mineralization.

The gold-bearing quartz veins are mineralogically simple, comprising ubiquitous pyrite accompanied by gold, pyrrhotite, chalcopyrite, galena and sphalerite (Table 2-2). There is no obvious wall rock alteration associated with the mineralization with the exception of the Jasper deposit, where the alteration envelope of muscovite is up to several metres wide. The previous studies of fluid inclusions in the Star Lake deposit (Ibrahim and Kyser, 1991) and the Jasper deposit (Hrdy and Kyser, 1995) indicate that the dominant fluids associated with gold-bearing quartz veins were H_2O-CO_2-NaCl in composition, with low to moderate salinity. The oxygen and hydrogen isotope compositions are compatible with formation of the fluids from devolatilization reactions during prograde metamorphism at depth (Ibrahim and Kyser, 1991; Hrdy and Kyser, 1995).

Table 2-2. Description of gold occurrences in the Star Lake-McLennan Lake area

Occurrence	Vein mineralogy[1]	Host rocks
Decade	Qtz-Pyr-Po-Cpy-Au	Star Lake pluton/ pelitic rocks
Jolu	Qtz-Po-Pyr-Cpy-Mo-Au	Star Lake pluton
Rush Lake	Qtz-Pyr-Po-Cpy-Mo-Au	Star Lake pluton
Blindman	Qtz-Pyr-Po-Cpy-Apy-Sph-Gal-Au	Star Lake pluton
Star Lake	Qtz-Pyr-Cpy-Sch-Chal-Apy-Au	Star Lake pluton
Tammar		Star Lake pluton
Jasper	Qtz-Pyr-Marc-Gal-Sph-Cpy-Au	Island Lake pluton

[1] Thomas, 1993, and references therein.

Mineralization occurred after the emplacement of the host plutons, however, the timing of gold mineralization and its relationship to regional metamorphism is uncertain. Ibrahim and Kyser (1991) and Hrdy and Kyser (1995) suggest that mineralization occurred at the waning stages of the regional metamorphism, whereas Thomas and Heaman (1994) suggest that it predated the culmination of peak thermal conditions in the immediate area but was coeval with high-grade metamorphism at deeper structural level.

CHAPTER 3

STRUCTURAL GEOLOGY

Introduction

Three phases of deformation were recognized in the McLennan Lake-Star Lake area, of which D_1 and D_2 are defined on the basis of mesoscopic structures alone. The D_3 deformation involved the development of the shears that host the gold-bearing quartz veins, and their subsequent deformation.

The McLennan Lake Tectonic Zone (MLTZ) and the Alpat Lake Tectonic Zone (ALTZ) are regional structures that pass through the map area (Figure 2-4). They predate D_2 and D_3 structures, but their relationship to D_1 is less certain and is inferred, to a large extent, from stratigraphic relationships and from a study of the internal fabric of the structures. The David Lake Shear and the Mallard Lake Shear are megascopic structures, smaller than the MLTZ and the ALTZ, and are confined to the map area. The attitude of these structures and the fact that they are post-D_1 and pre-D_3 suggest that they are large scale D_2 structures.

The following sections describe the characteristics of the structures and history of deformation. Detailed petrographic descriptions of the structures are given in Chapter 4.

D_1 Deformation

The structures developed by the D_1 deformation are a regional penetrative S_1-L_1 fabric and, in the supracrustal rocks, mesoscopic folds. The penetrative fabric is defined by the preferred alignment of amphibole, micas and feldspars, and by aggregates of these minerals, as well as by the shape of deformed pebbles, lapilli,

breccia clasts, etc. The primary lithological and compositional layering in the supracrustal rocks is transposed into the S_1 foliation.

Supracrustal Rocks

The S_1 penetrative foliation is moderately to weakly developed in most of the supracrustal rocks, and becomes more strongly developed as the MLTZ and the ALTZ are approached. The foliation has a general northeast strike, and dips 65° to 85° to the northwest. In the vicinity of the Star Lake and Island Lake plutons, it is deflected to parallel the lithological contacts, reflecting the competency contrast between the plutons and the more ductile supracrustal rocks. Figure 2-4 illustrates the continuous variation in attitude of the S_1 foliation in the supracrustal rocks and in the southern part of the Island Lake pluton.

The deformed metavolcanic rocks contain a mineral lineation, L_1, which lies in the S_1 foliation and plunges moderately to steeply NNE to NW. The relationship of the plunge of the lineation to the attitude of the foliation with which it is associated is shown in Figure 3-1A and B. The L_1 lineation in the meta-arkoses of the McLennan Group is weakly developed, but the orientation of the fabric is in good agreement with the lineation in the metavolcanic rocks (Figure 3-1C).

Because of the lack of traceable distinctive lithological units and few indicators of younging direction in the metavolcanic rocks and the meta-arkoses, the regional fold patterns in this area are not established. The largest fold defined in the area has a half-wavelength of at least 25 metres. The majority of the folds observed in the field have half-wavelengths of a few centimetres to several tens of centimetres (Figure 3-2A). They are tight to isoclinal. The fold axes plunge 40° to 70° northeast to west northwest, with the majority plunging to the north northeast (Figure 3-2B).

Plutonic Rocks

In the Star Lake and Island Lake plutons, the S_1 penetrative foliation is less

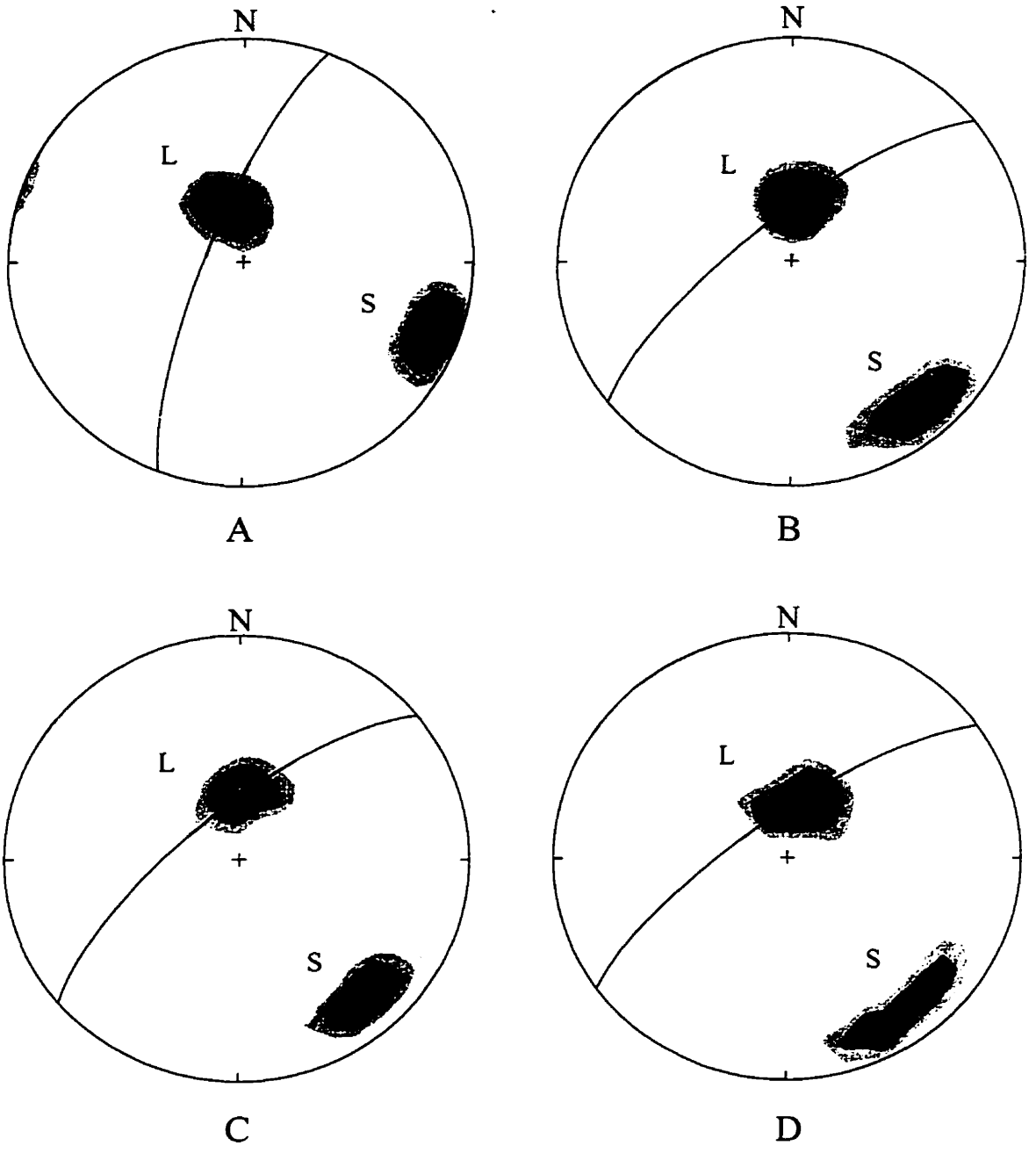

Figure 3-1. Stereographic plots of S_1-L_1 fabrics. (A) Metavolcanic rocks: S, poles to foliation with strike < 035; mean attitude 201/77 is shown as a plane. L, lineation; mean plunge 343/69 (N=85; contour interval 1.5, 9.0, 16.5, 24.0, 31.5, 39.0% per 1% area). (B) Metavolcanic rocks: S, poles to foliation with strike > 035; mean attitude 231/74 is shown as a plane. L, lineation; mean plunge 6/69 (N=74; contour interval 1.5, 8.0, 14.5, 21.0, 27.5, 34.0% per 1% area). (C) McLennan Group: S, poles to foliation; mean attitude 230/72 is shown as a plane. L, lineation; mean plunge 3/66 (N=35; contour interval 2, 10, 18, 26, 34, 42% per 1% area). (D) Island Lake pluton: S, poles to foliation; mean attitude 234/75 is shown as a plane. L, lineation; mean plunge 11/69 (N=63; contour interval 1, 8, 15, 22, 29% per 1% area).

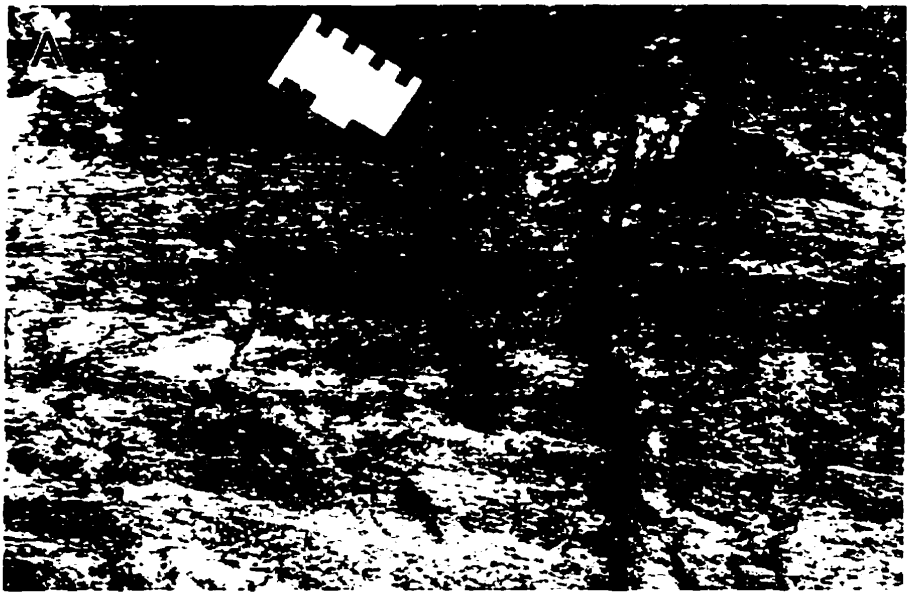

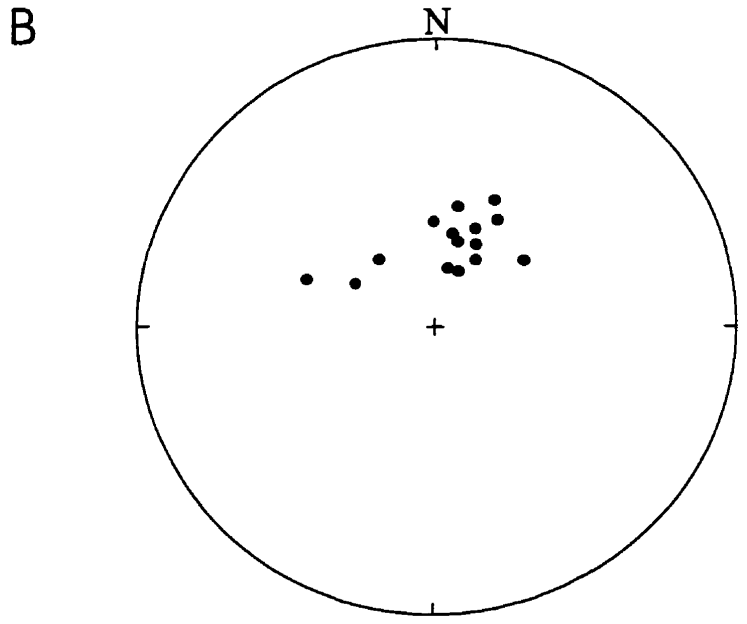

Figure 3-2. (A) Photograph of D_1 isoclinal folds in a unit of tuffaceous metavolcanic rock. (B) Stereographic plot of D_1 fold axes (N=15).

developed and less continuous, and more variable in strike than in the supracrustal rocks. Consistent S_1 in the plutons occurs only in the southern part of the Island Lake pluton, where it strikes northeast, and in the Star Lake pluton in the vicinity of David Lake, where it strikes north northeast, parallel to the penetrative foliation in the nearby metavolcanic rocks (Figure 2-4). An associated L_1 lineation plunges steeply NNE-NNW (Figure 3-1D).

Strain Pattern

The regional fabric is predominantly a S-L fabric, but locally it may be represented by S-fabric or L-fabric. It is consistent with a NW-directed flattening and a coincident subvertical extension, with local variation in the vicinity of the plutons, where the plane of flattening (X-Y plane of the strain ellipsoid) is parallel to the contact of the plutons with the supracrustal rocks.

D_2 Deformation

The structures associated with the D_2 deformation include mesoscopic shears and mesoscopic, tabular cataclastic zones.

D_2 Shears

The D_2 shears are developed in both the supracrustal and plutonic rocks. They are zones of strongly foliated rock, typically a few centimetres wide with strike lengths of several metres (Figures 3-3 and 3-4). The D_2 shears postdate the S_1 foliation, as shown by the fact that they deflect and transect the earlier fabric.

Attitude of The D_2 Shears

The D_2 shears strike between 345° and 120° and dip steeply to the north, northwest or west. Multiple sets of shears usually occur in the same outcrops (Figure

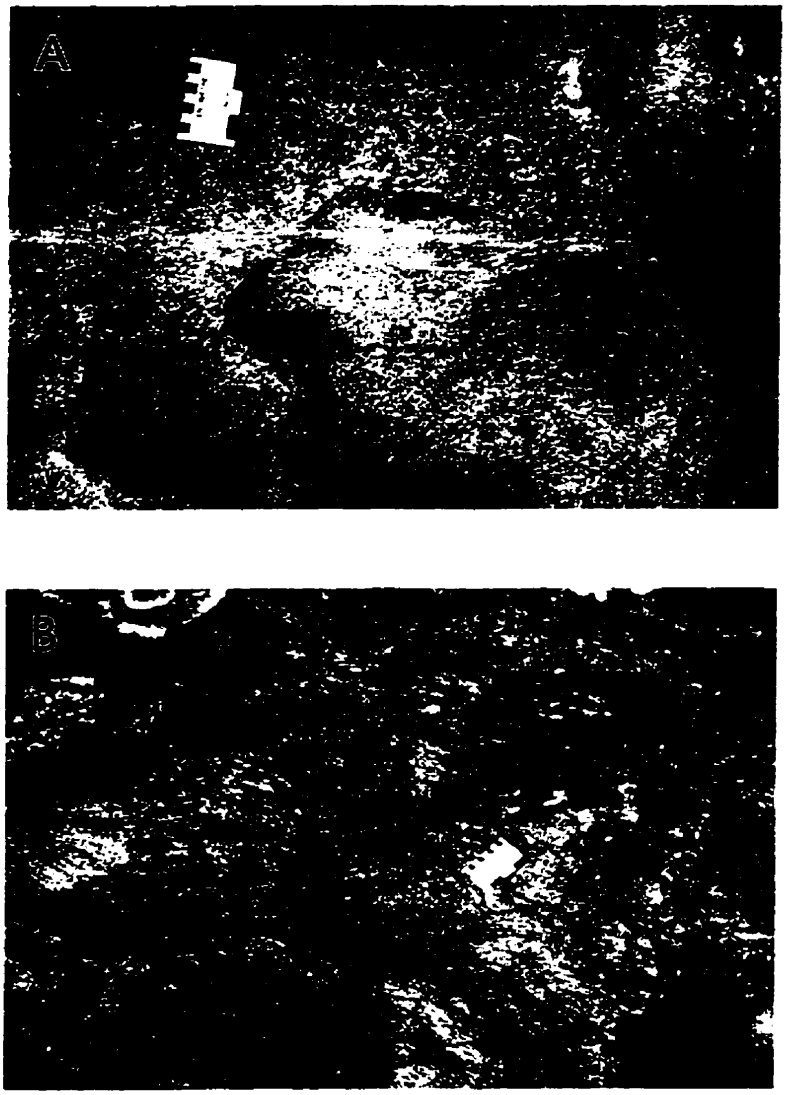

Figure 3-3. Photographs of D_2 shears. (A) An east-striking D_2 shear in granite, viewed on the horizontal surface. No S_1 was detected on the outcrop. See Figure 3-7 for details. (B) A north-striking D_2 shear in meta-arkose, viewed on the horizontal surface. S_1 is sinistrally deflected into the shear.

Figure 3-3. (C) Horizontal surface of an outcrop of mafic metavolcanic rock showing multiple sets of D_2 shears. Detailed outcrop map is shown in Figure 3-4A.

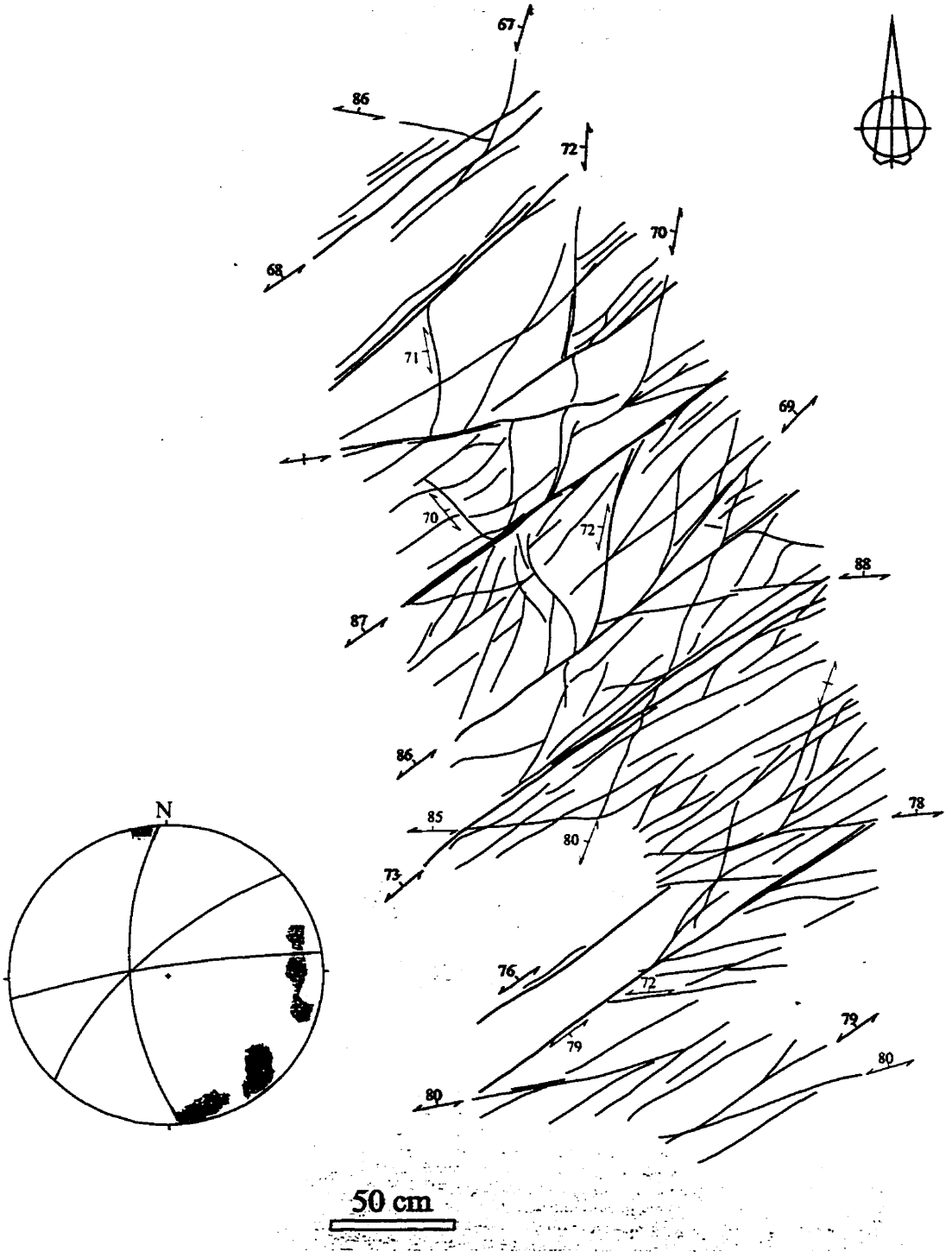

Figure 3-4. (A) Map of D_2 shears in an outcrop of mafic metavolcanic rock. Poles to the shears are plotted in the stereonet. The attitudes of the planes corresponding to the contoured maxima are 177/70, 227/75 and 262/85.

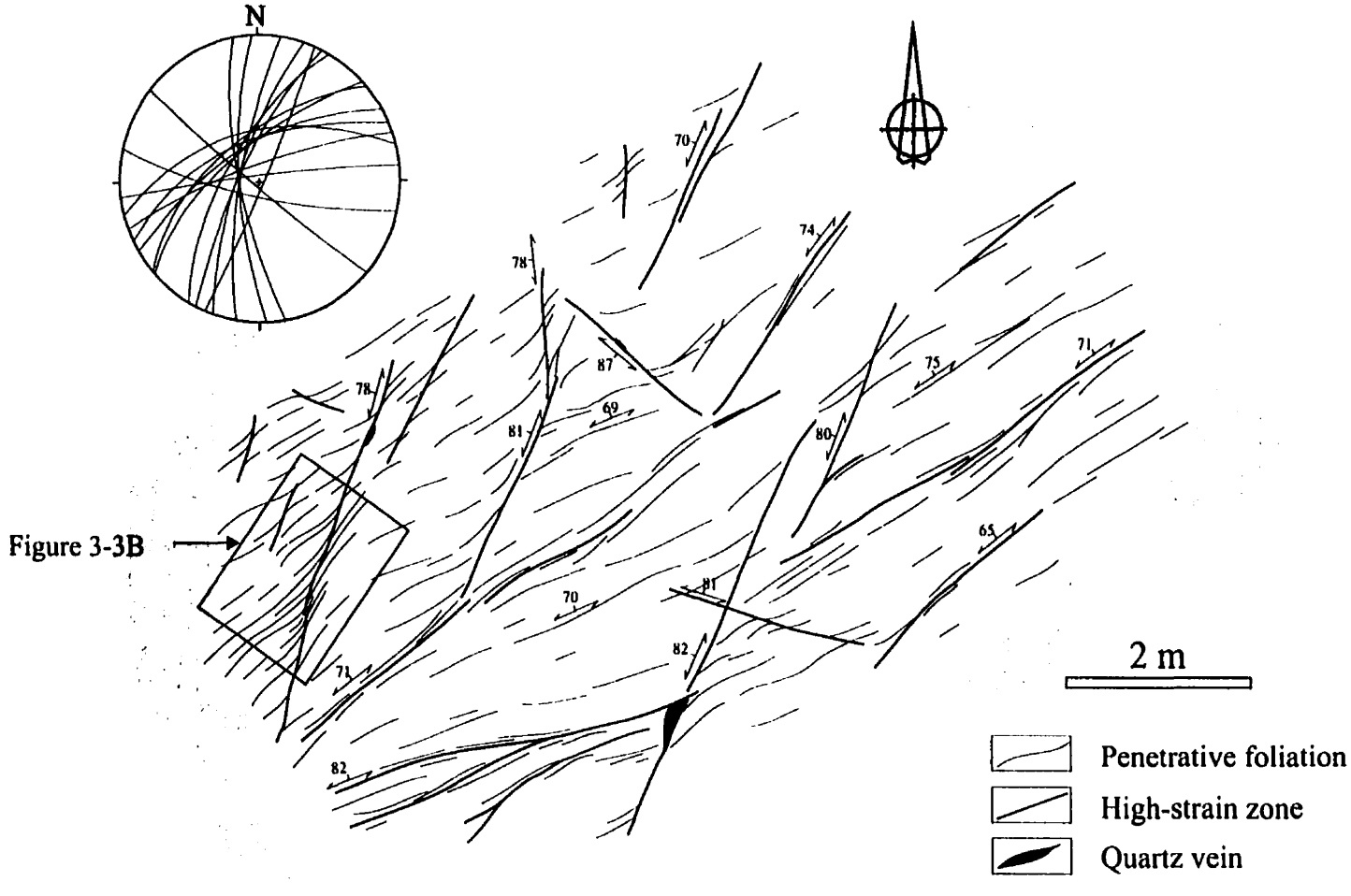

Figure 3-4. (B) Map of D_2 shears in an outcrop of meta-arkose. The shears are shown in the stereonet as planes.

3-4). Figure 3-5 summarizes the attitudes of the shears from the plutons, metavolcanic rocks and meta-arkoses. Using the subtraction method of Robin and Jowett (1986), three populations of shears were defined, the attitudes of which are given in Table 3-1.

Table 3-1. The mean attitude of each population of D_2 shears and the mean plunge of associated lineation

Lithology	Mean attitude	Mean lineation
Plutonic rocks	183/82	351/61
	232/75	022/63
	263/71	047/65
Metavolcanic rocks	178/80	344/62
	228/72	359/69
	260/82	029/78
Meta-arkoses	195/74	349/59
	235/68	020/63
	273/75	039/74

The foliation generated by the D_2 shears contains a well defined mineral lineation, which collectively plunges steeply to NE-NNW (Figure 3-5D). The mean attitudes of the lineation derived by the subtraction method are summarized in Table 3-1. Synoptic diagrams of the D_2 shears from each lithology are given in Figure 3-6. The orientation of the shears is not dependent on rock type.

The most common D_2 shears are those striking northeast and north-south, and the least common are those striking east-west.

Sense of Movement

Shear movement is indicated on horizontal outcrop surfaces by the deflection of the S_1 foliation into the shears (Figure 3-3B). On the vertical surfaces perpendicular to the shears there is no evidence for the deflection of S_1. However, the deflection of a

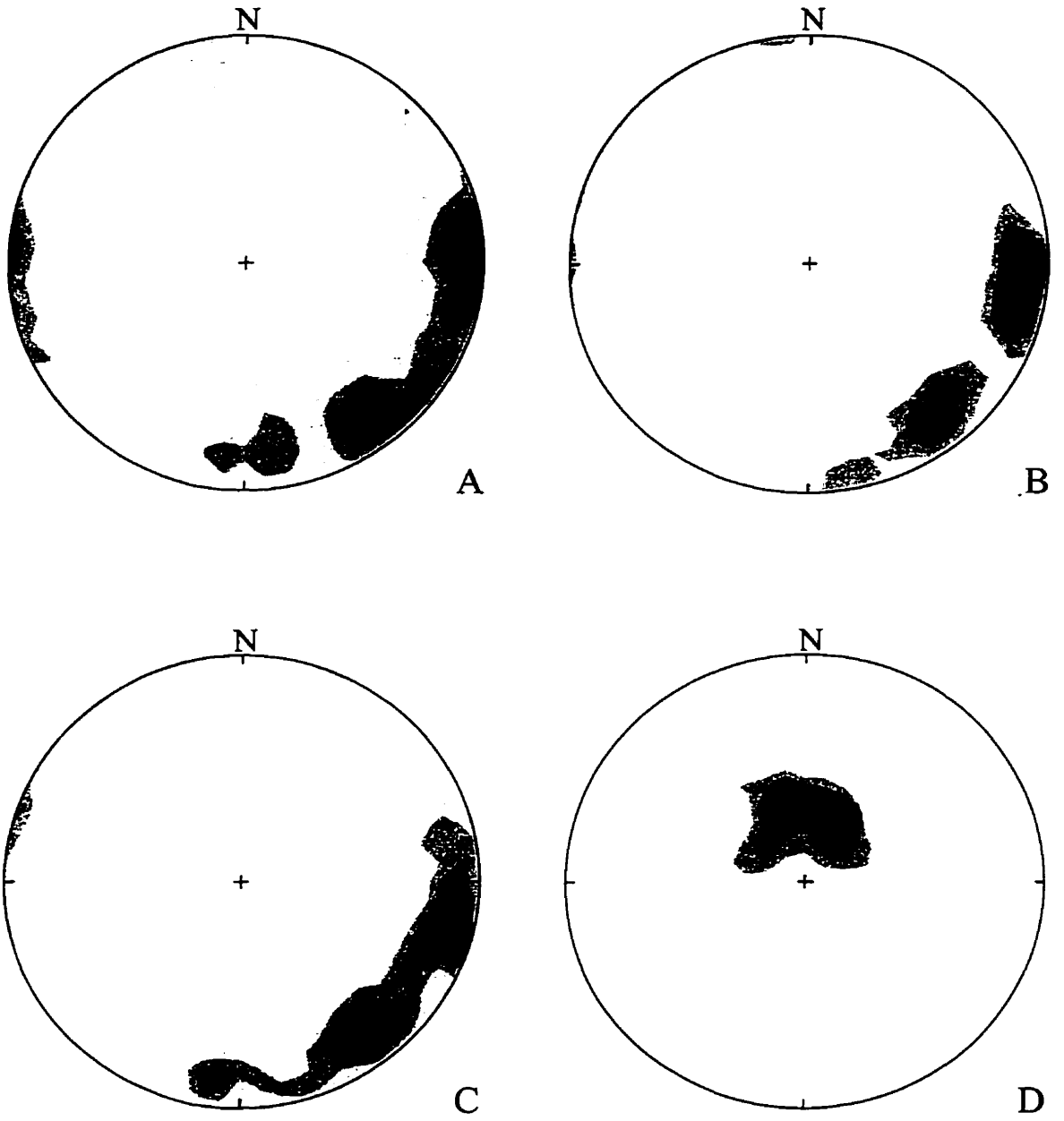

Figure 3-5. Stereographic plots of planar and linear fabrics from D_2 shears. (A) Poles to the shears in plutons (N=140; contour interval 0.7, 2.6, 4.5, 6.4, 8.3, 10.2% per 1% area). (B) Poles to the shears in metavolcanic rocks (N=114; contour interval 0.9, 3.7, 6.5, 9.3, 12.1, 14.9% per 1% area). (C) Poles to the shears in McLennan Group (N=82; contour interval 1.2, 3.5, 5.8, 8.1, 10.4, 12.7% per 1% area). (D) Mineral lineation (N=42; contour interval 2, 6, 10, 14, 18, 22% per 1% area).

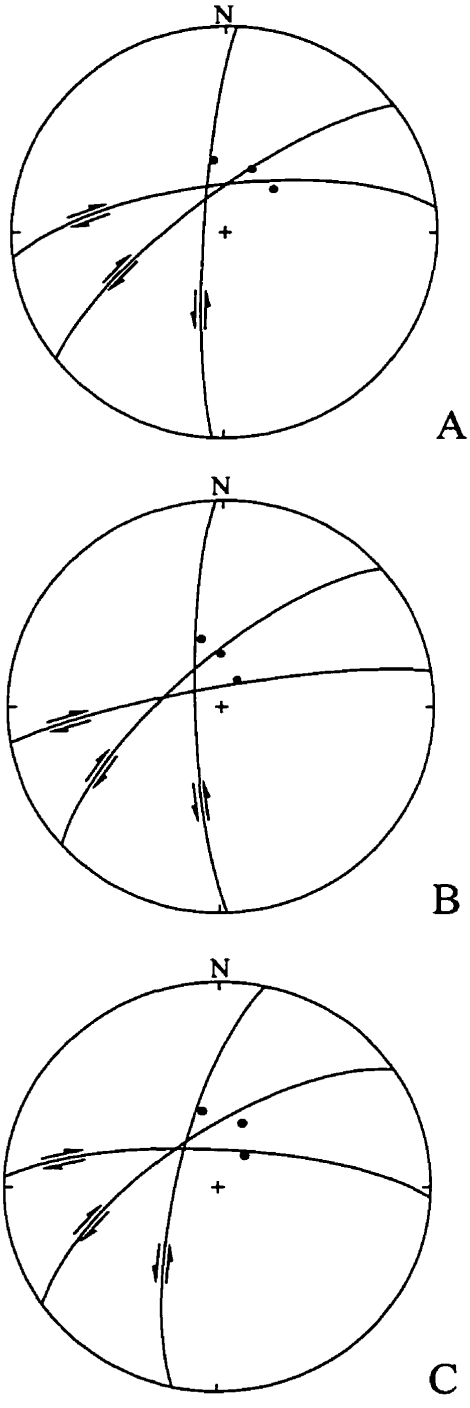

Figure 3-6. Synoptic diagrams of D_2 shears from (A) plutons; (B) metavolcanic rocks; and (C) McLennan Group.

pre-existing fabric is an imprecise indicator of shear direction. More dependable kinematic indicators were obtained from thin sections of the shears. On sections cut parallel to the lineation and perpendicular to the foliation, the fabric of the shears is invariably symmetric (Figure 3-7A); whereas on sections perpendicular to the lineation, the fabric is asymmetric (Figure 3-7B). These shear-sense indicators demonstrate sinistral movement in the north-striking shears, and dextral movement in northeast-striking and east-striking shears (Figure 3-6). Where the D_2 shears of different orientation intersect, the northeast-striking planes always deflect or dislocate the others in a dextral sense (Figure 3-4A), suggesting comparatively late or prolonged development for the northeast-striking shears.

The above observations indicate that the formation of the D_2 shears involves a shear deformation, and that the direction of shearing is at a high angle to the steeply plunging mineral lineation and accordingly at a high angle to the maximum extension axis of the strain ellipsoid.

D_2 Cataclastic Zones

The cataclastic zones, first recognized in this region by Roberts (1993), are restricted to the plutons, and are particularly abundant in the diorite of the Star Lake pluton. They are tabular structures with boundaries that mark abrupt change in grain size (Figure 3-8A). Small crushed minerals and mineral aggregates of quartz and feldspars form within the cataclastic zones whereas the wall rocks are weakly deformed or undeformed (Figure 3-8B). The structures involve the generation of new minerals, biotite and hornblende, in association with the cataclastic process. The cataclastic structures are a few centimetres wide and less than a few metres in strike length, and lack continuous foliation. Shear-sense indicators were not found in the cataclastic zones, but the S_1 foliation is locally deflected into the structures, as in the D_2 shears (Roberts, 1993).

The cataclastic zones occur in a wide range of orientations, and are classified into three sets: northeast, north-south, and southeast. The most common sets are those striking northeast and north-south. These two sets of cataclastic structures are

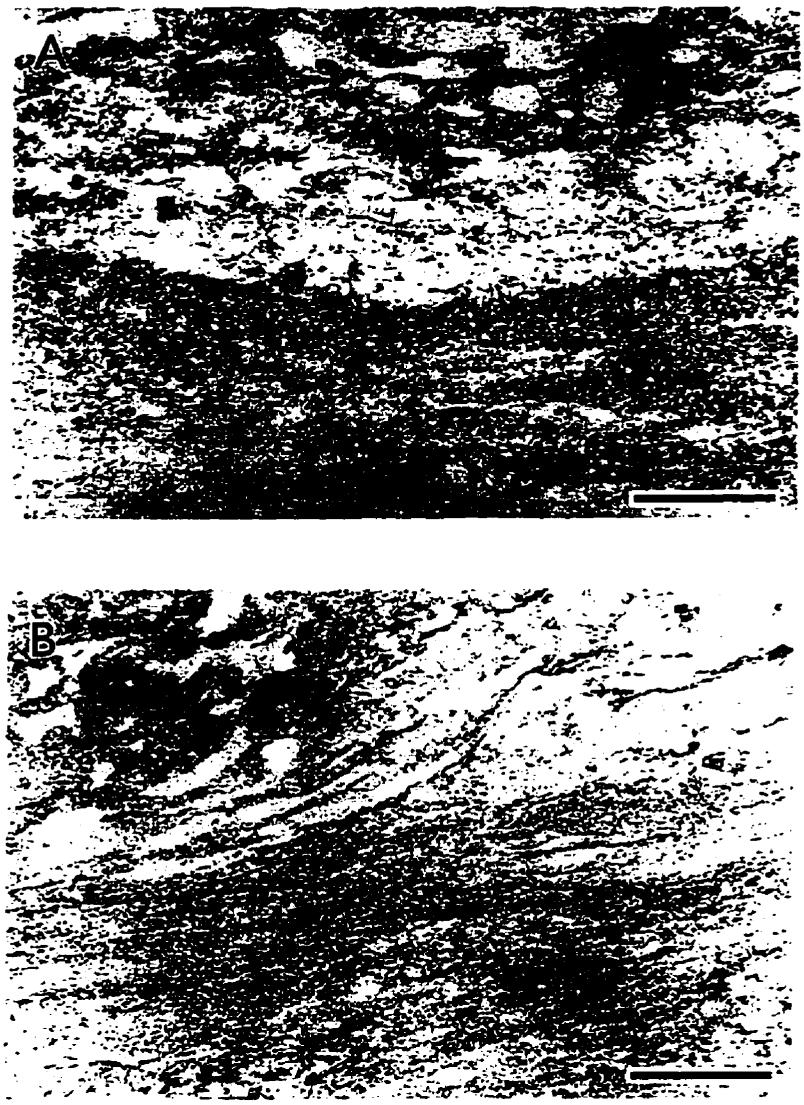

Figure 3-7. Photomicrographs of deformation features in the D_2 shear shown in Figure 3-3A (plane light, bar = 5 mm). (A) Fabric is symmetric on section parallel to the lineation and perpendicular to the foliation. (B) Asymmetric fabric indicating dextral shear on section perpendicular to the lineation.

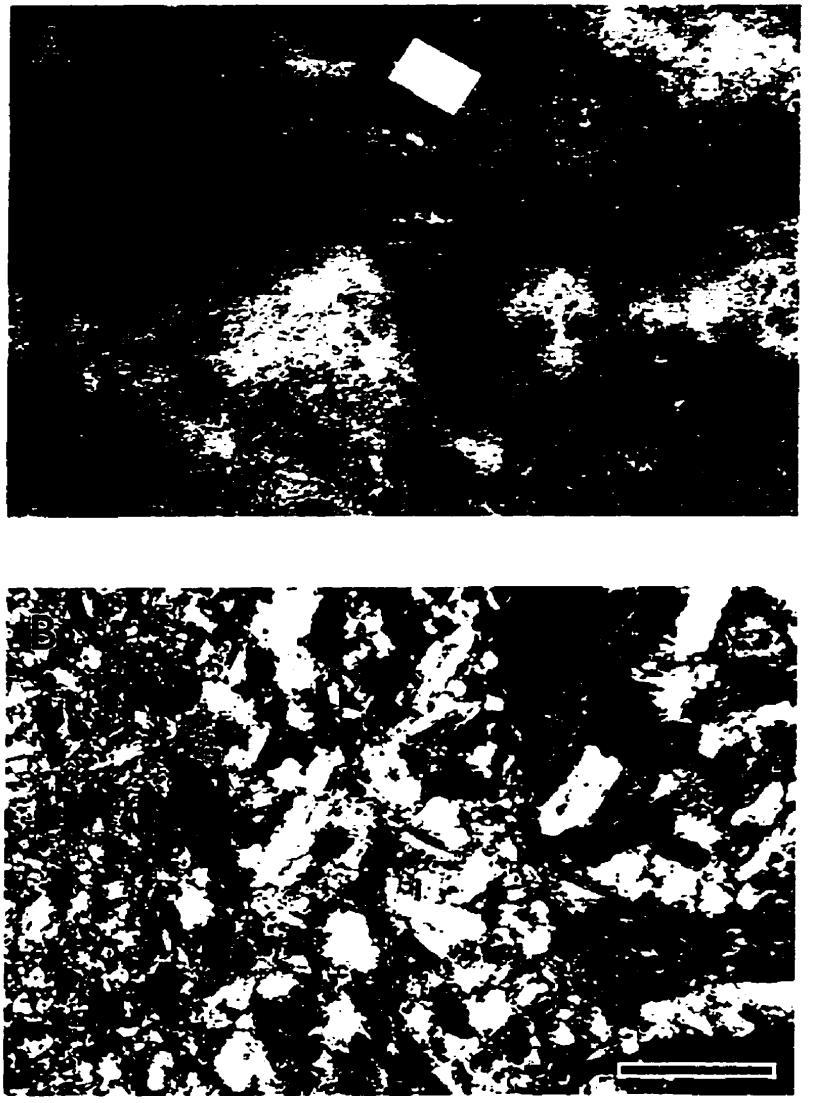

Figure 3-8. (A) A horizontal view of a tabular D_2 cataclastic zone in diorite of the Star Lake pluton. (B) Photomicrograph of the cataclastic zone in A showing successive stages of deformation. The coarse minerals in the host wall rock (right), mainly amphibole, feldspars and biotite, are replaced by rounded feldspar grains in a matrix of feldspar, quartz, biotite and trace amphibole (left) (cross nickel; bar = 4 mm).

comparable to the D_2 shears in terms of orientations. The southeast-striking set is comparatively rare. The cataclastic zones are included in the D_2 deformation because they postdate the S_1 fabric (which they deflect), and predate the D_3 shears. Furthermore, several D_2 shears contain a central, tabular zone of cataclasite identical to that in the cataclastic zones.

D_3 Deformation

Steeply-dipping shears that host the gold-bearing quartz veins were formed during the D_{3a} deformation and were subsequently deformed at a later stage of the same deformation (D_{3b}). Shallow-dipping shears with a conjugate relationship to the steeply-dipping shears were also formed during the D_{3a} deformation. The shallow-dipping shears are not as well developed nor as continuous as the steeply-dipping shears.

General Characteristics

D_3 structures are northeast-trending shears that occur in both the Star Lake and Island Lake plutons. They transect D_1 and D_2 structures and are more extensive than the earlier D_2 shears in that they are continuous virtually completely across the Star Lake pluton, and, in the Island Lake pluton, form a zone with a strike length of approximately four kilometres in the vicinity of the Broeder Lake (Figure 2-4). They are also distinguished from the earlier D_2 structures in that they contain evidence of dip-slip movement, in which the northwest side moved down relative to the southeast side.

Two episodes of deformation are recognized in the D_3 shears: the D_{3a} episode involves dip-slip movement and the formation of the shears; the D_{3b} episode involves strike slip or oblique slip on the earlier D_{3a} shear fabric. Fabrics related to the D_{3b} strike slip are found in all the shears. Oblique slip is believed to occur only in the Rod shear at the Jolu Mine. The gold-bearing quartz veins were emplaced during the D_{3a}

episode of deformation. Later quartz veins, emplaced during the D_{3b} episode, are not gold-bearing.

Two areas were examined in detail: the James-Jasper-Roxy shears in the Island Lake pluton, in which the Jasper deposit is located, and the Rod shear in the Star Lake pluton, in which the Jolu Mine is located (Figure 2-4).

James-Jasper-Roxy Shears

The James-Jasper-Roxy zone is composed of a series of narrow shears and quartz veins that strike between 030° and 040° (Figure 3-9A). The shears each typically consist of a central zone of mylonite 10 to 30 centimetres wide, bordered by protomylonite up to three metres wide. Gold-bearing quartz veins are emplaced parallel to the shear fabric in the central mylonite of the main shears. The veins are continuous, and comprise several layers of quartz that, together, constitute a single vein up to 25 centimetres thick. Geological map of shears and veins in the Roxy deposit is shown in Figure 3-10.

D_{3a} Dip-Slip Shearing

The D_{3a} dip-slip shearing in the main shears is indicated by a strongly developed mineral lineation defined by the preferred orientation of biotite and feldspars, which plunges steeply to the north (Figure 3-9A), and by a S-C fabric, which indicates movement in the direction of the lineation (Figure 3-11). Shallow-dipping shears conjugate to the main shears are exposed at the northeast end of the Jasper shear. The line of intersection of the main shears and the shallow-dipping shears is subhorizontal.

The field evidence indicates that the gold-bearing quartz veins were emplaced in the shears during the D_{3a} deformation. The principal evidence for this is that both shears and veins were subsequently deformed and folded by the strike-slip movement of the D_{3b} deformation (Figure 3-12A). Elsewhere, the veins occur in shears that show evidence of dip-slip shearing but no evidence of D_{3b} shearing, suggesting that their

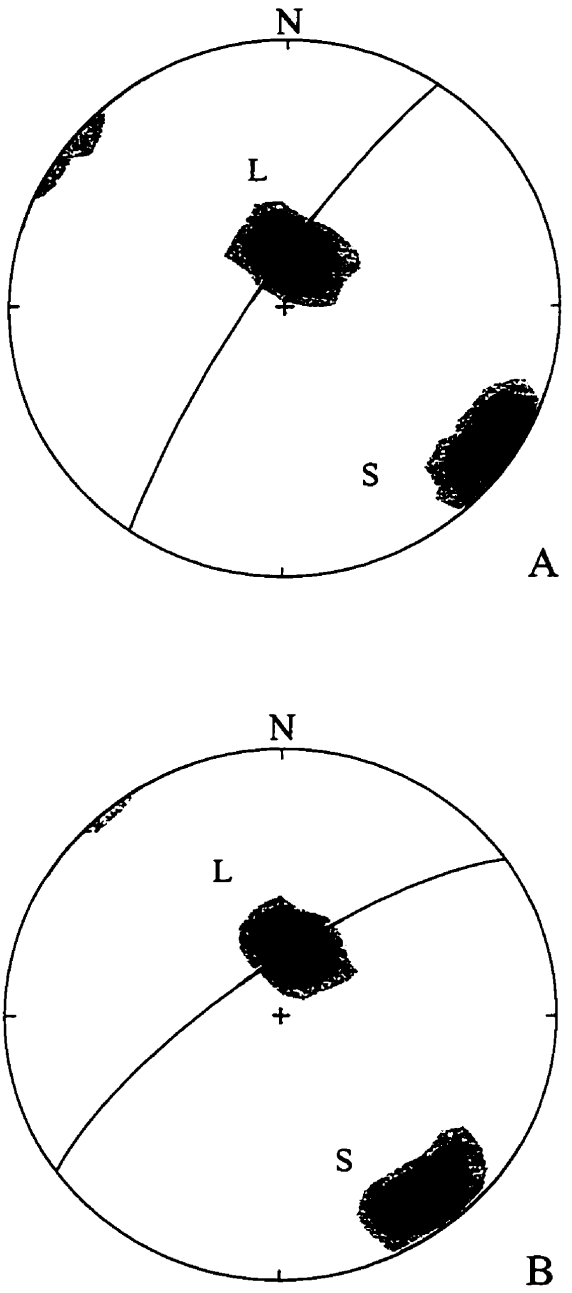

Figure 3-9. Stereographic plots of shear fabrics from D_{3a} shears. (A) James-Jasper-Roxy shears: S, poles to shear planes; mean attitude 215/82 shown as a plane. L, mineral lineation; mean plunge 9/72 (N = 58; contour interval 2, 6, 10, 14, 18, 22% per 1% area). (B) Central and northeastern segments of the Rod shear: S, poles to shear planes; mean attitude 238/78 shown as a plane. L, mineral lineation; mean plunge 9/70 (N = 69; contour interval 2, 8, 14, 20, 26, 32% per 1% area).

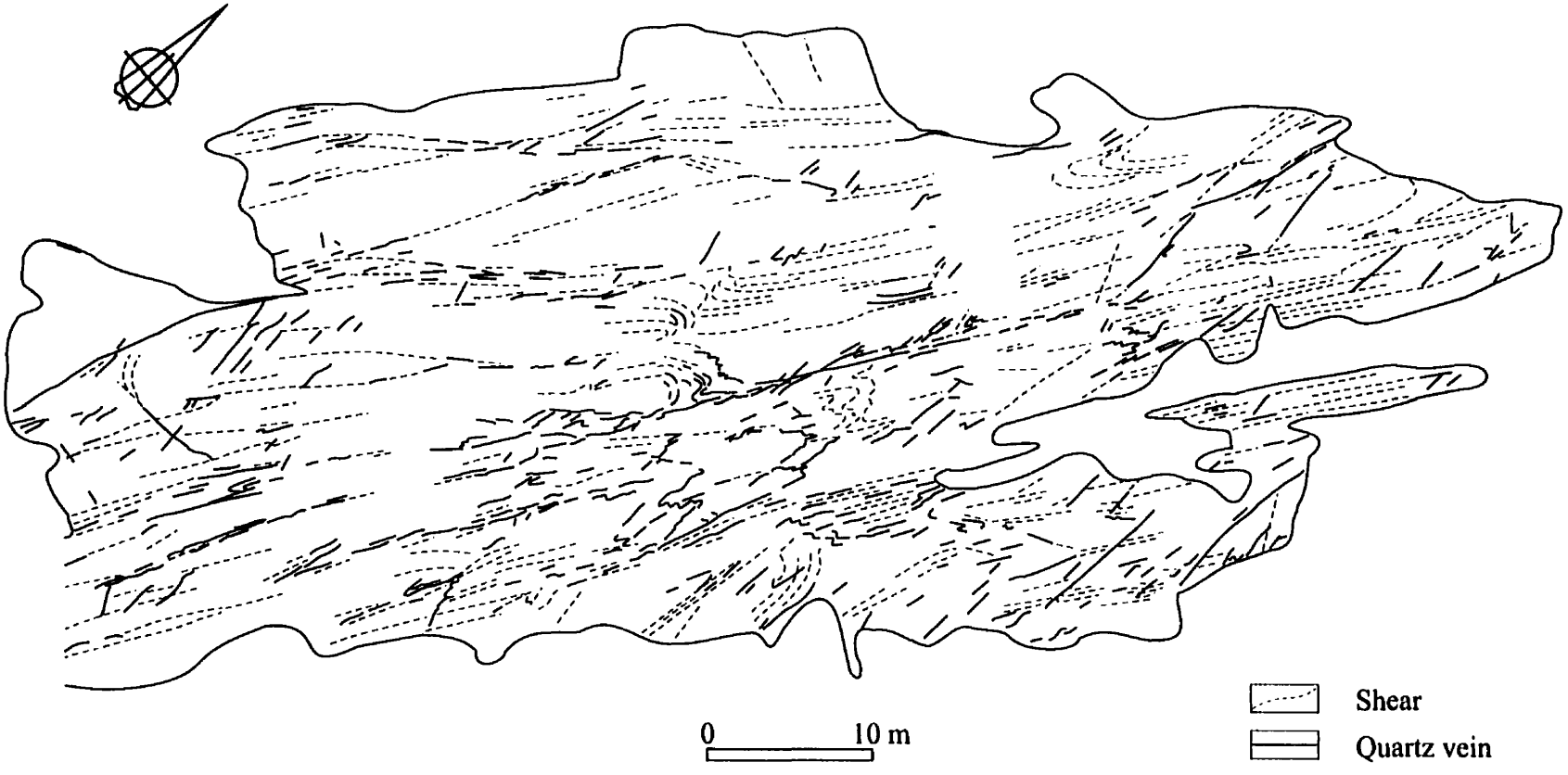

Figure 3-10. Surface geological map of the shears and veins in the Roxy deposit, modified from Roberts (1993).

Figure 3-11. S-C fabric in protomylonite in granite from the James shear indicating D_{3a} dip-slip shearing (bar = 1.25 cm).

emplacement is not associated with the D_{3b} deformation.

D_{3b} Strike-Slip Shearing

Structures related to the D_{3b} shearing are shown in Figure 3-12 and are summarized in Figure 3-13. The relationships among the structural fabrics are shown in Figure 3-14.

The D_{3b} deformation is expressed as strike-slip, dextral shearing along the shear fabric generated by the D_{3a} deformation. The mylonitized central parts of the early shears are locations of the greatest strain during the strike-slip shearing.

Striations, defined by fine-grained micaceous minerals, form on the shear planes created by the D_{3a} dip-slip shearing. The striations overprint the steep north-plunging mineral lineation. They plunge at approximately 27° to the southwest (Figure 3-13A), and are assumed to indicate the vector of the transcurrent shearing.

The most striking mesoscopic features related to the D_{3b} strike-slip shearing are a series of folds of D_{3a} fabric, and fold-related north-south shears and quartz veins. The folds have Z-shaped asymmetry, and occur in areas with relatively low strike-slip shear strain between narrow, more highly strained D_{3a} shears (Figures 3-12A and 3-14B), which typically serve as decollement structures during the D_{3b} strike-slip shearing. The axial surfaces of the folds are vertical and strike north-south (30° to 35° to the main shears), and the fold axes plunge to the north, approximately perpendicular to the striations (Figure 3-13B).

The fabric developed by the D_{3b} shearing, which overprints the D_{3a} shear fabric, is most obvious where it intersects and passes through the folded D_{3a} shear fabrics (Figure 3-12A). The development of quartz subgrains is pervasive in deformed rocks within the shears, with the shape fabric of subgrains consistently indicating dextral strike-slip shearing (Figure 3-12B).

The folds are usually accompanied by shears that develop at their axial surfaces (Figure 3-12A). The shears are two to ten centimetres wide and up to five metres

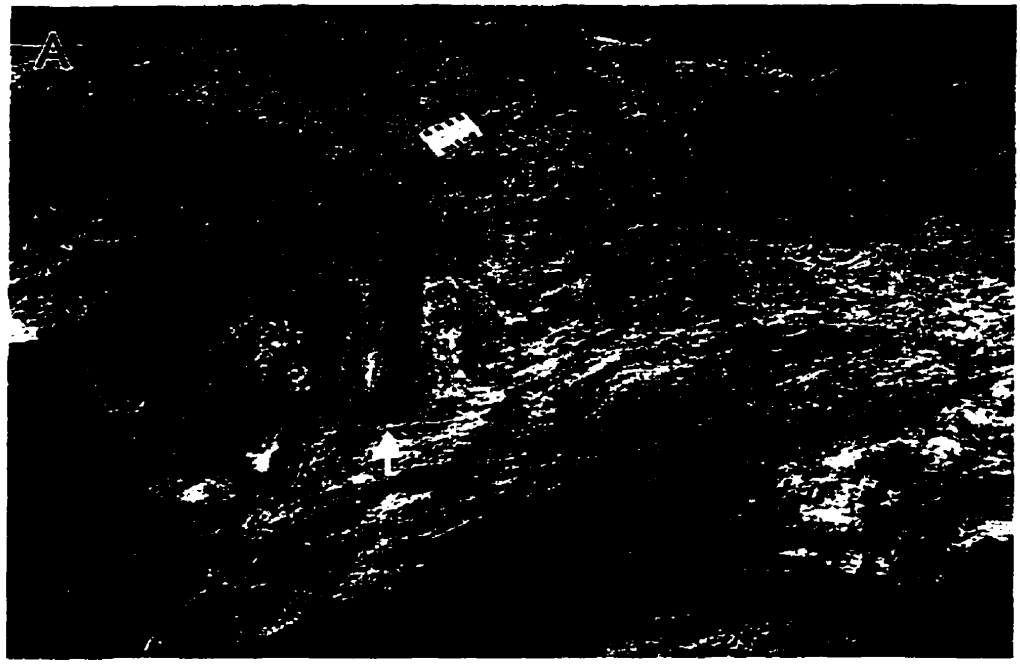

Figure 3-12. Structural features developed by D_{3b} strike-slip shearing in the James-Jasper-Roxy shears. (A) A Z-shaped, asymmetric fold of D_{3a} dip-slip shear fabric and associated veins produced by D_{3b} strike-slip shearing. A shear was formed at the axial plane of the fold. New shear planes (arrow) pass through the fold with continued strike-slip shearing.

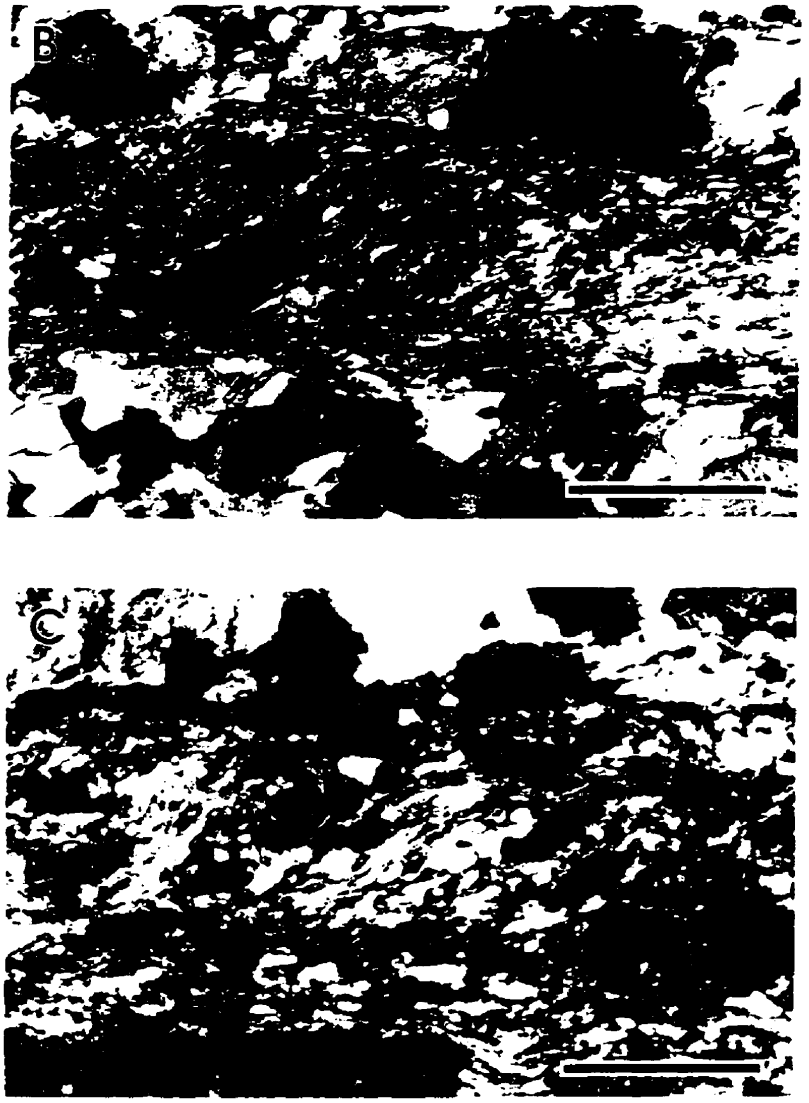

Figure 3-12. (B) Photomicrograph of quartz shape fabric in a shear striking at 035, taken from section parallel to subhorizontal striations. The sense of obliquity is indicative of dextral shearing (nicols crossed; bar = 0.05 mm). (C) Photomicrograph of sigmoidal fabric defined by micas in a north-south shear, taken from section perpendicular to the contained lineation. (nicols crossed, bar = 0.05 mm).

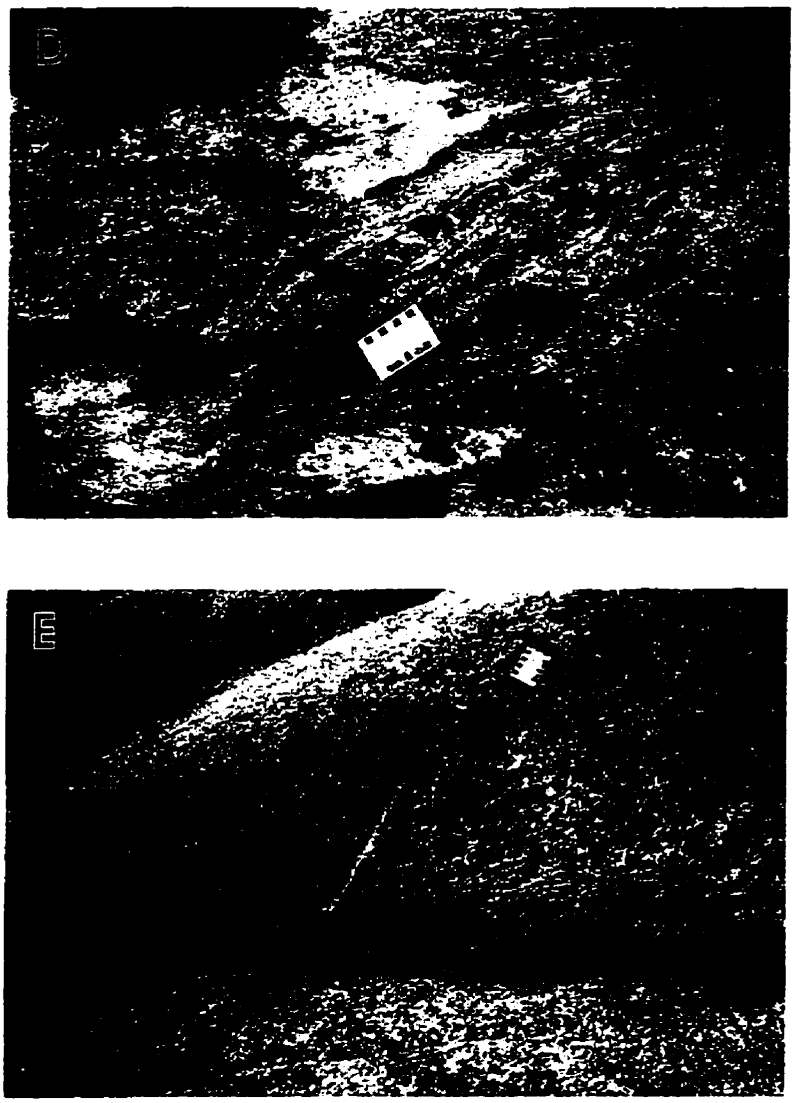

Figure 3-12. (D) A typical sigmoidal north-south quartz vein formed by deflection of the tips of vein into higher strain strike-slip shears. (E) Photograph showing the relationship of a shallow-dipping vein, lying on a subhorizontal outcropping surface, to a north-south vein (arrow). The attitudes of the shallow-dipping and north-south veins are 82/29 and 170/88, respectively.

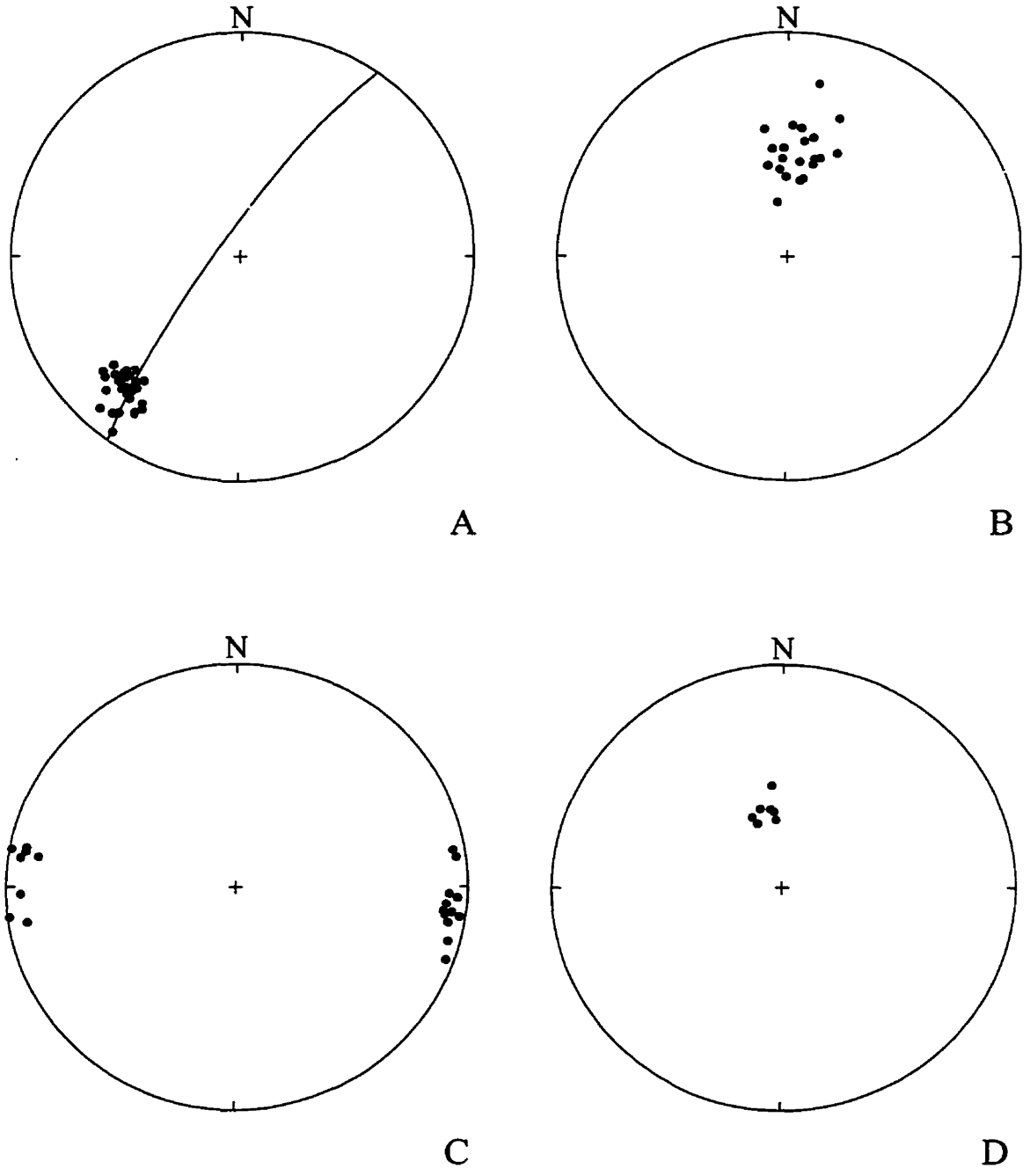

Figure 3-13. Stereographic plots of structural fabrics developed by D_{3b} strike-slip shearing in the James-Jasper-Roxy shears. (A) Striations on shear surfaces; mean plunge 221/27 (N=33). (B) Axes to folds; mean plunge 7/50 (N=21). (C) Poles to N-S shears and veins (N=20). (D) Poles to shallow-dipping veins (N=7).

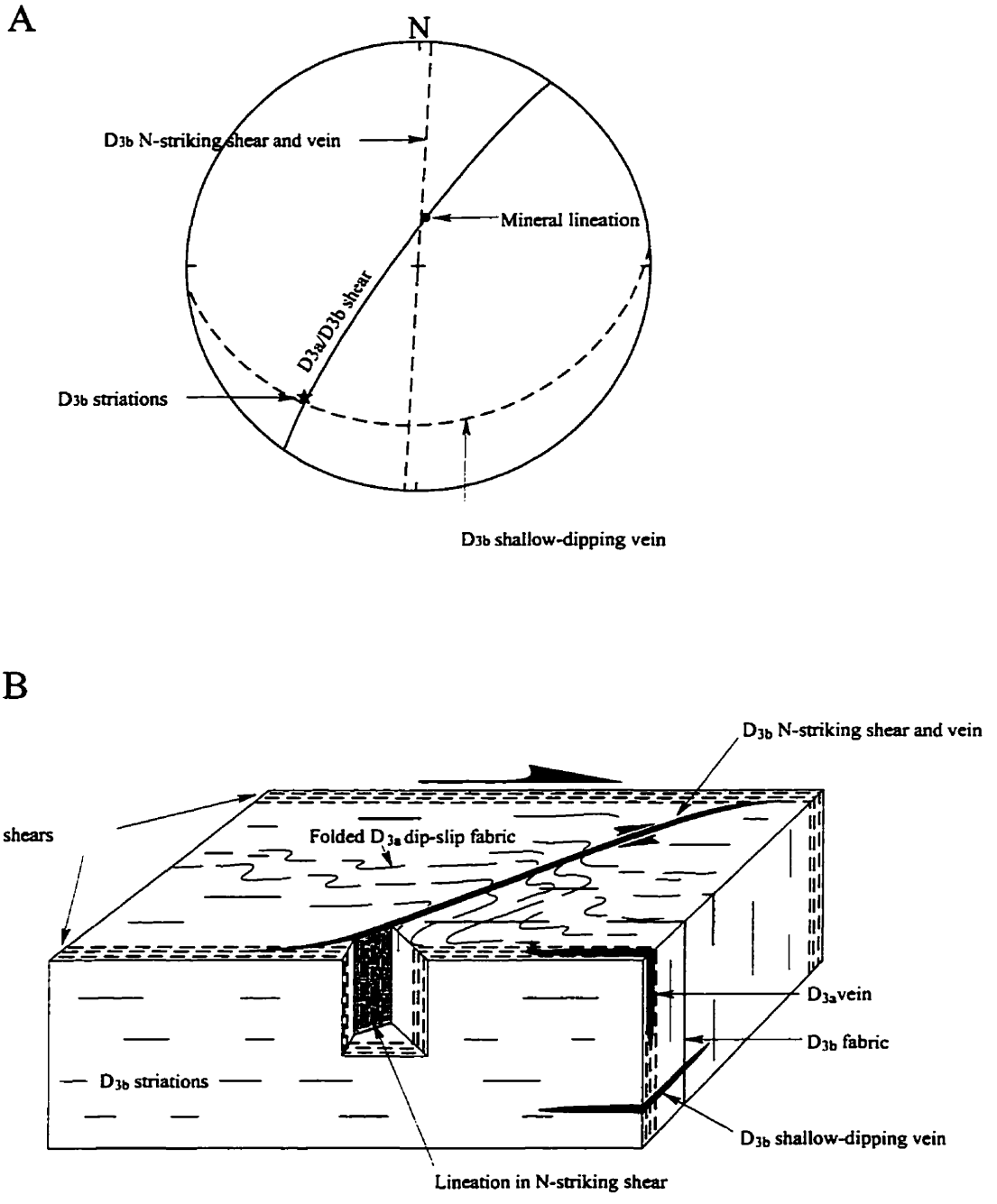

Figure 3-14. (A) Stereographic illustration of relationships among structural fabrics related to D_{3b} strike-slip shearing. (B) Schematic illustration of relationships among structural fabrics related to the D_{3b} shearing.

long. They transect and dextrally rotate the D_{3a} fabric. Within the shears, dextral sense of shearing is indicated by a mica-defined sigmoidal fabric (Figure 3-12C). A subvertical mineral lineation is developed in the shears. The north-south quartz veins are an expression of brittle deformation associated with the north-south shears and folds. The veins are typically three to five centimetres wide and up to several metres in strike length. They are not layered, and tend to be deflected dextrally into the higher strain strike-slip shears, giving them a sigmoidal shape (Figure 3-12D). No direct cross-cutting relations were observed between the north-south veins and the mineralized veins in the main shears.

Shallow-dipping veins that strike between 068° to 085° and dip at 25° to 38° to the south were also found in the area (Figure 3-12E). The veins are approximately perpendicular to the steep north-plunging mineral lineation (Figure 3-13D), and have the same oxygen isotopic compositions as the north-south veins (see Chapter 5 for details).

Rod Shear

The Rod shear occurs in the northern part of the Star Lake pluton (Figure 2-4). It trends 055° to 060° and dips steeply to the northwest in the central and northeastern segments where the shear is hosted by mafic dyke (Figure 3-9B). At the Jolu Mine, it strikes 060° and dips at 82° to 87° towards the southeast, following the contact of granodiorite with diorite or porphyritic diorite of the Star Lake pluton (Figures 3-15 and 3-16).

The highly strained central zone of the Rod shear is in diorite or porphyritic diorite, in contact with granodiorite, and consists of phyllonite. The central zone, four to six metres wide, is bordered to the northwest by a zone of interlayered protomylonite and phyllonite up to seven metres wide and to the southeast by granodioritic protomylonite up to two metres wide (Figure 3-16). The phyllonite of the central zone possesses a strong penetrative foliation defined by biotite and hornblende, and by a microlayering formed by the segregation of mafic and felsic minerals.

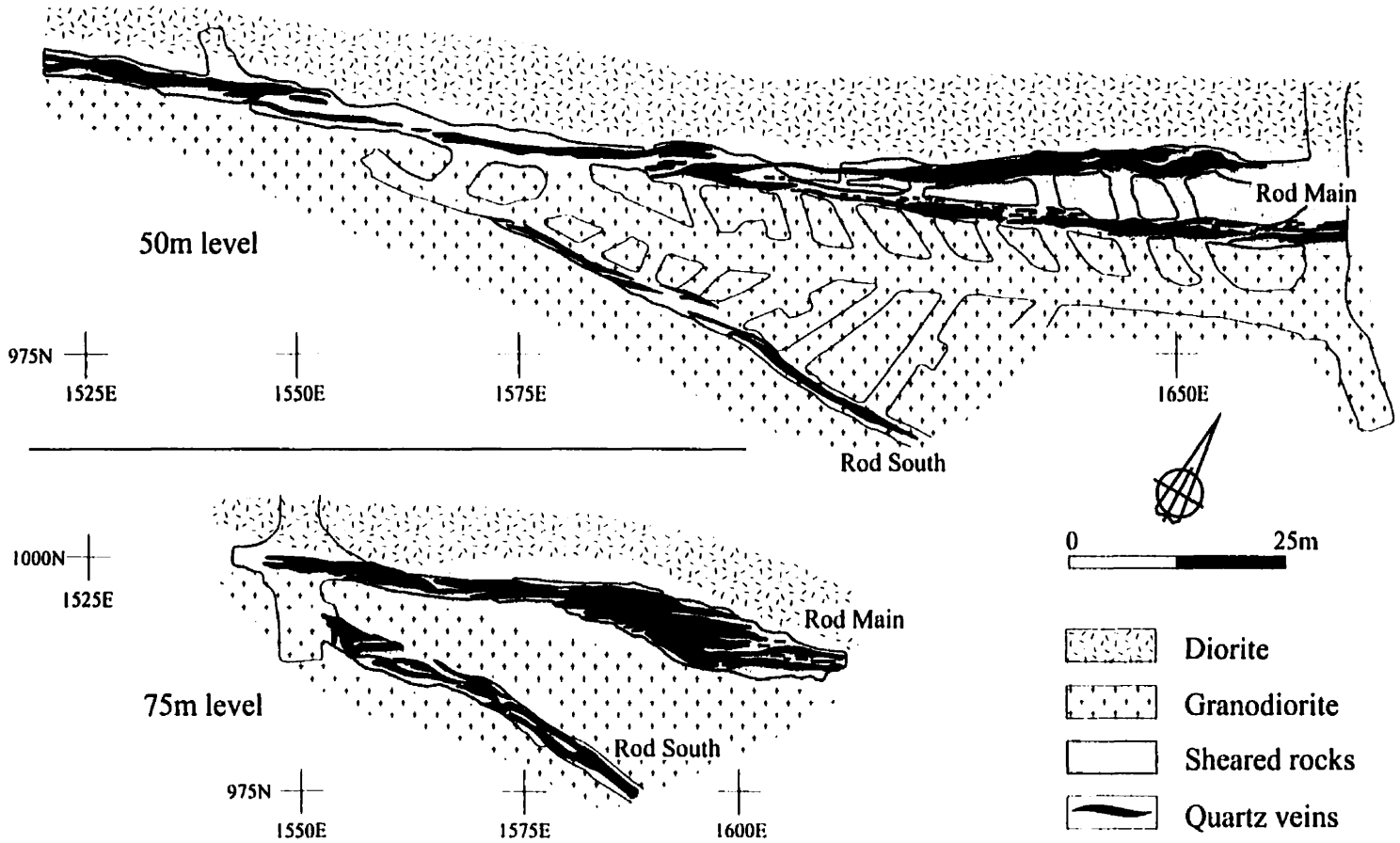

Figure 3-15. Geological maps of the Jolu Mine at the 50 m and 75 m levels (modified from Roberts, 1993). The Rod Main shear and ore zone are at the granodiorite-diorite contact and dip to the southeast. Note that the veins of the orebody lie at a low angle to the shear zone walls and step to the right.

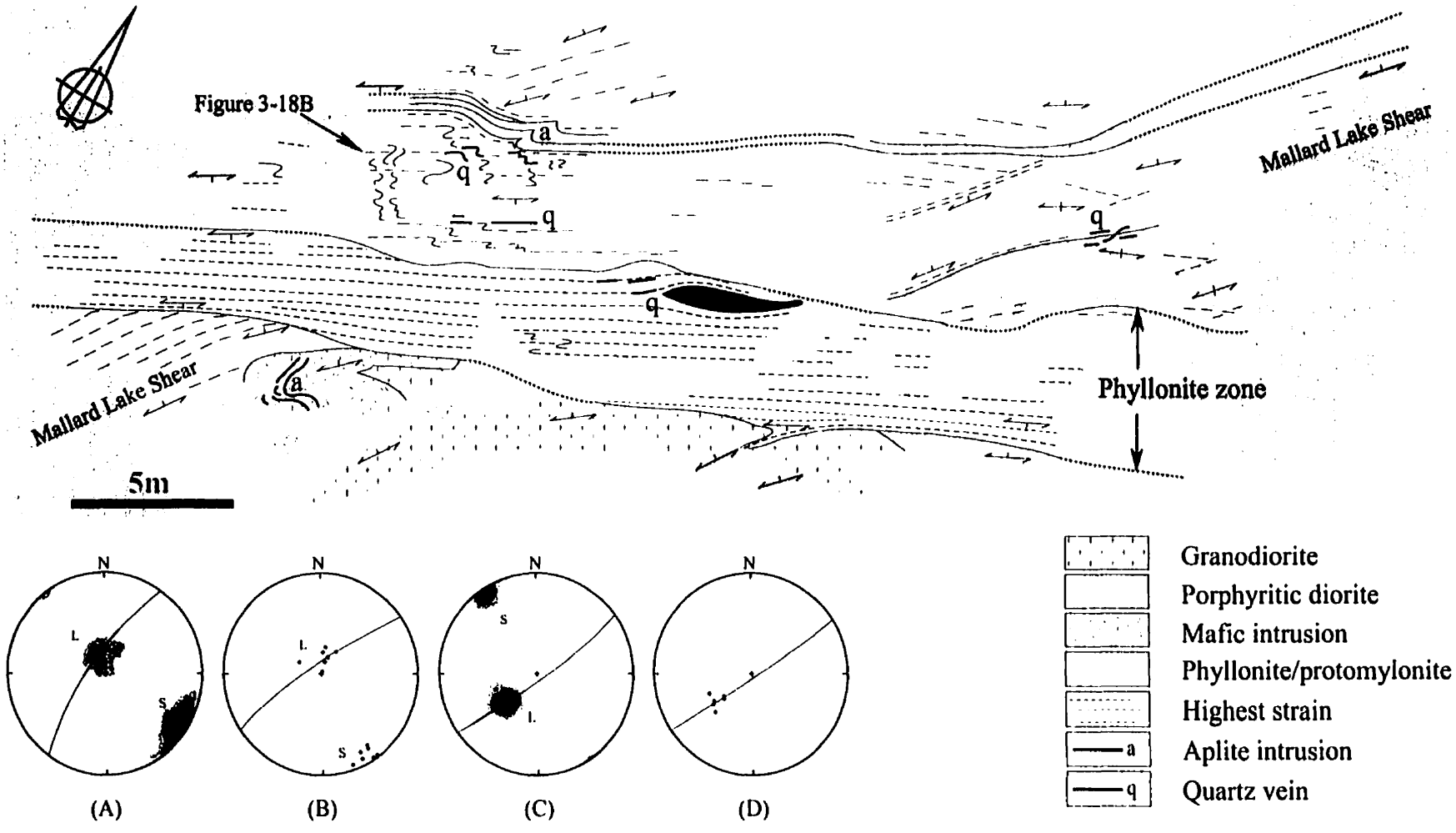

Figure 3-16. Outcrop map of the Rod shear with stereographic plots of structural data (modified from Roberts, 1993). (A) Structural data from the Mallard Lake Shear in this outcrop: poles to foliation, S, mean attitude, 210/76 (N=111, contour interval 1, 3, 5, 7, 9, 11 % per 1% area); lineation, L, mean plunge 338/73 (N=60, contour interval 2, 4, 6, 8 % per 1 % area). (B) Structural data from the protomylonite at the margin of the Rod shear: shear fabric, S, mean attitude, 240/85 (N=7); mineral lineation, L, 10/75 (N=6). (C) Structural data from the highly strained central phyllonite zone: poles to foliation, S, mean attitude, 060/85 (N=168, contour interval 2, 4, 6, 8, 10, 12 % per 1 % area); fold axes and intersection lineation, L, mean plunge 229/54 (N=42, contour interval 1, 3, 5, 7, 9, 11 % per 1% area). (D) Stereographic plot of the long axes of deformed quartz veins.

D_{3a} Dip-Slip Shearing

The dip-slip direction of shearing is most evident in the protomylonitic fabric at the outer parts of the Rod shear (Figure 3-17A). At the Jolu Mine, the shear foliation in the protomylonite dips northwestward at 80° to 85°, in contrast to the foliation in the phyllonite zone which dips steeply southeast, parallel to the shear zone and to the contact of granodiorite with diorite or porphyritic diorite (Figure 3-16). The mineral lineation in the protomylonite pitches to the northeast at 75° on the shear foliation.

Shears with conjugate relationship to the gold-bearing shears, up to ten centimetres wide and up to ten metres in strike length, were found at the Rush Lake shear and the Star Lake shear near the eastern margin of the Star Lake pluton. They are not well exposed due to their shallow dip. The strain associated with them is low relative to the main shears, and is generally represented by S-C fabric, without the development of mylonite. They strike subparallel to nearby gold-bearing shears, and dip 30° to 40° towards the northwest. The contained mineral lineation is parallel to the dip of the shear fabric, and S-C fabric indicates dip-slip reverse movement (Figure 3-17B).

D_{3b} Oblique-Slip Shearing

The oblique-slip shear movement is manifested by asymmetric folds in the D_{3a} fabric of the phyllonite zone of the shear and interlayered phyllonite and protomylonite. The folds in the phyllonite zone are isoclinal, generally with sheared out limbs (Figure 3-18A). The half-wavelength of the folds are up to three centimetres. In interlayered phyllonite and protomylonite, the half-wavelength of the folds increases to 10 to 25 centimetres as the amount of protomylonite increases, and the folds become more open (Figure 3-18B). The folds may also be defined by narrow aplite dykes in the shear and by the displacement and rotation of veins and dykes emplaced during the D_{3a} deformation. The dislocated dykes and veins form a "right stepping" pattern on horizontal surfaces (Figure 3-19). The D_{3a} phyllonitic fabric is overprinted by younger phyllonitic fabric defined by a new generation of biotite ± hornblende (Figure 3-18C).

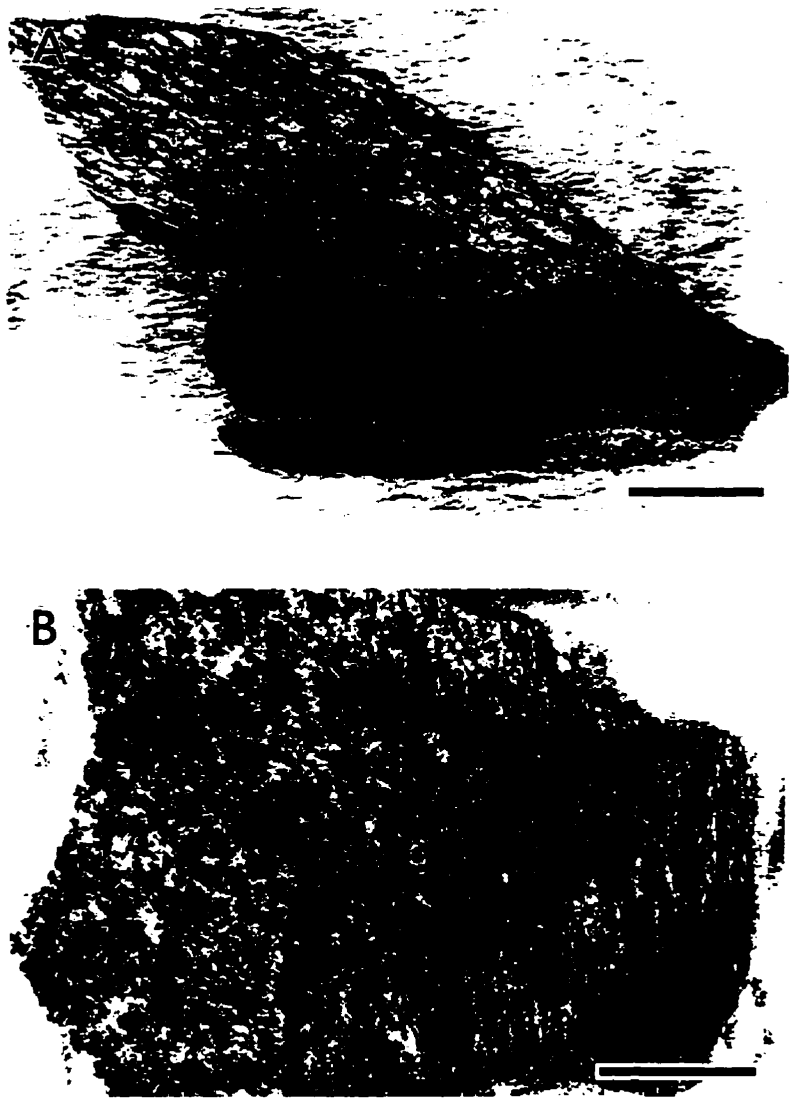

Figure 3-17. (A) S-C fabrics in protomylonite in granodiorite from the Rod shear (bar = 1.5 cm). (B) S-C fabric from a shallow-dipping shear, close to the northeastern end of the Star Lake shear (bar = 1.5 cm).

Figure 3-18. Structural features developed by D_{3b} dextral oblique-slip shearing in the Rod shear near the Jolu Mine. (A) Photomicrograph of an isoclinal fold in the central phyllonite zone (plane light; bar = 5 mm). (B) Photograph of folded phyllonite interlayered with protomylonite, looking down the fold axes (see Figure 3-16 for location). (C) Photomicrograph of the earlier folded shear fabric, overprinted by the new fabric defined by a new generation of biotite (plane light; bar = 2 mm).

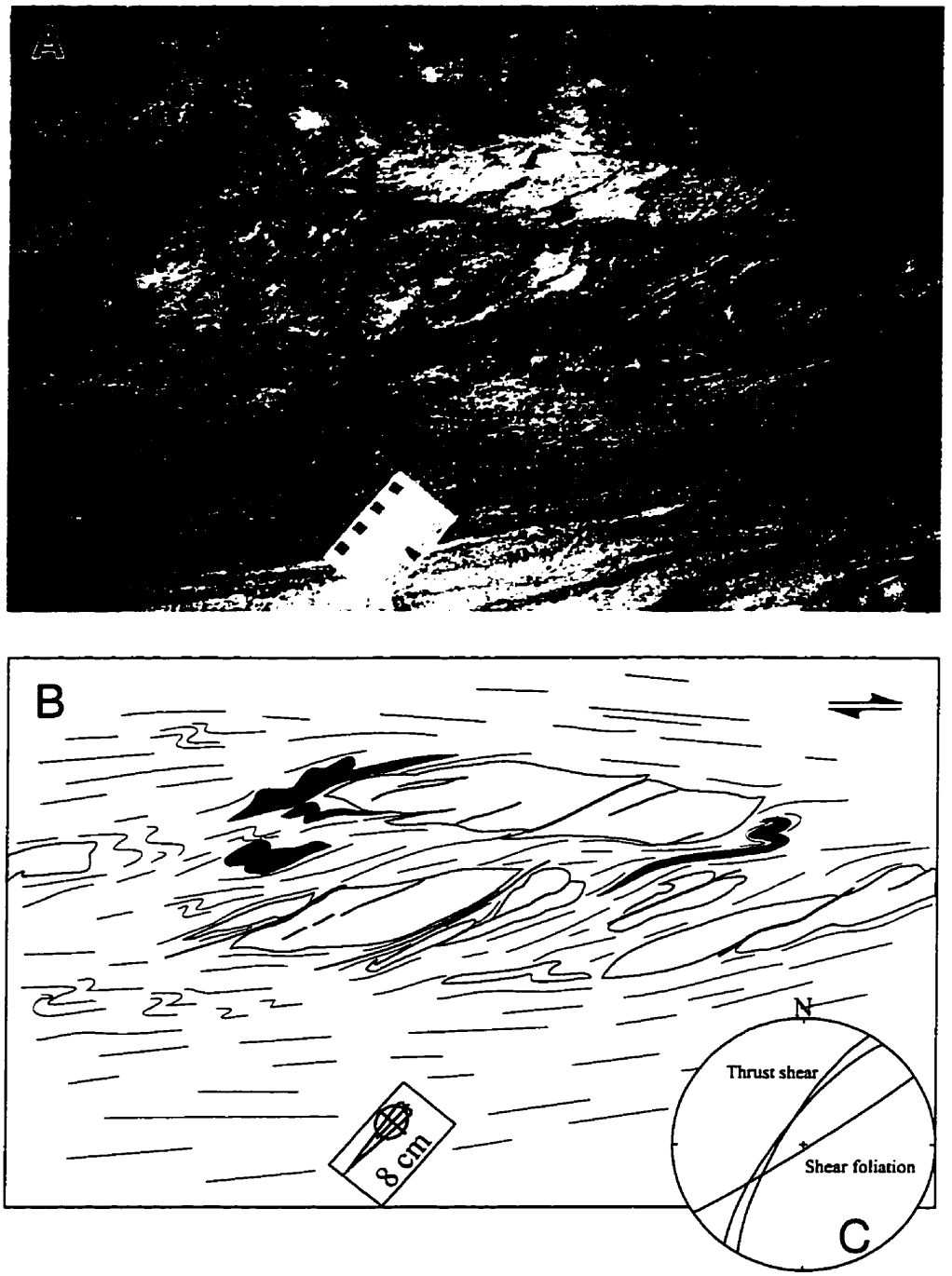

Figure 3-19. (A) Quartz vein and aplite dykes deformed during the D_{3b} oblique shearing by thrust shears oriented at low angles to the shear foliation. The segments of the dykes or veins are displaced dextrally along the thrust shears to form a right stepping pattern; horizontal surface. (B) Line drawing showing detailed structural fabrics in (A). (C) Stereographic plot of shear fabric and thrust shears from (A).

The intersection of the folded D_{3a} shear foliation with the younger D_{3b} foliation forms a lineation which plunges at 54° to the southwest, parallel to the axes of the folds (Figure 3-16). The shear vector associated with D_{3b} is assumed to be perpendicular to this direction and the sense of movement from the asymmetry of the folds and displacement of earlier veins is dextral, northwest side down.

D_{3b} Strike-Slip Shearing

Structures produced by strike-slip shear movement are illustrated in Figure 3-20. The structures occur in the protomylonite of the Rod shear at the Jolu Mine, and in the Rod shear northeast of the mine. They are comparable to those in the James-Jasper-Roxy shear system, however, the folds in the Rod shear are less abundant and tighter, with axial surfaces at lower angles (15° to 20°) to the shear zone walls (Figure 3-20B and C). In addition, quartz veins emplaced in the axial plane shears are much less common than those in the James-Jasper-Roxy system. The veins are a few millimetres to one centimetre thick and up to 0.5 metres in strike length.

Megascopic Structures

David Lake Shear

The David Lake Shear (DLS), defined by Poulsen *et al.* (1987), is a north-south trending high strain zone, in the metavolcanic rocks near the western margin of the Star Lake pluton (Figure 2-4). It is up to 30 metres wide and approximately five kilometres long. The rocks of the zone are characterized by a strong S-L fabric which strikes north-south and dips 75° to 90° to the west, and in which the strong mineral lineation plunges steeply to the north northwest (Figure 3-21A). The boundaries of the DLS are defined by the deflection of the strike of the regional S_1 foliation in the country metavolcanic rocks, from 20° ~ 30° to approximately north-south, and by an increase strain as indicated by the intensity of the foliation.

The fabric of the DLS is symmetric in sections parallel and perpendicular to the lineation. The only kinematic indicators are the sinistral deflection of the regional S_1

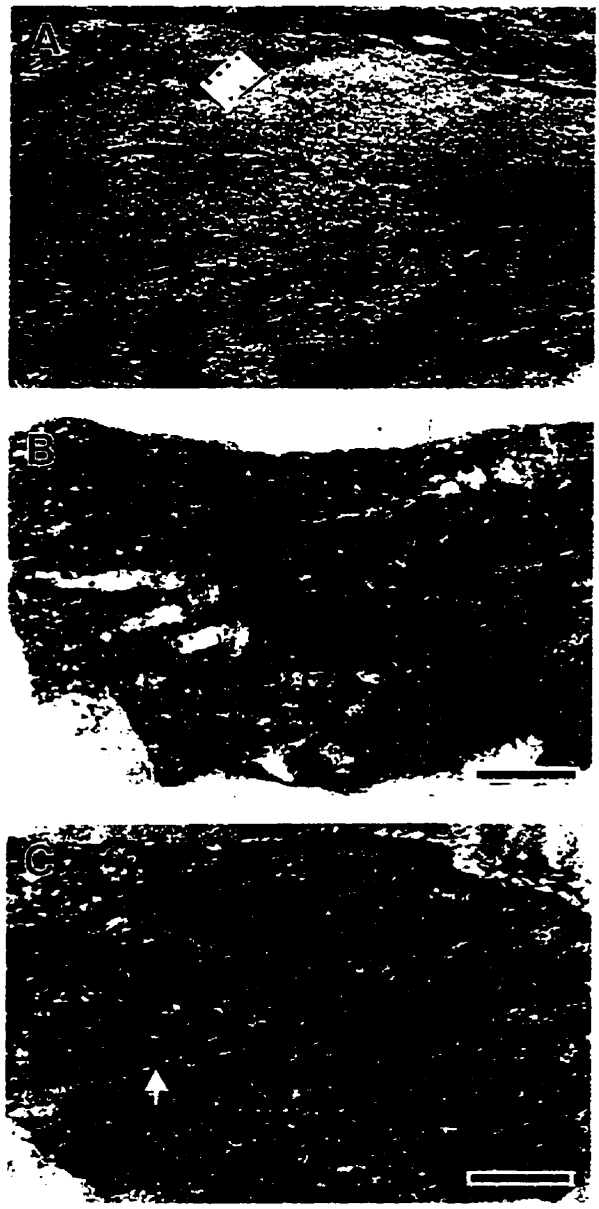

Figure 3-20. Fabrics developed by D_{3b} strike-slip shearing in the central segment of the Rod shear. (A) Shear planes related to the D_{3b} strike-slip shearing cut through the D_{3a} folded fabric, horizontal surface. (B) Steeply-plunging folds of the D_{3a} fabric and associated veins (horizontal cut surface; bar = 2.0 cm). (C) Shear and associated veinlet (arrow) formed at the axial plane to a subvertical fold. The angle between the axial surface and the shear zone wall is approximately 17 ° (horizontal cut surface; bar = 2.0 cm).

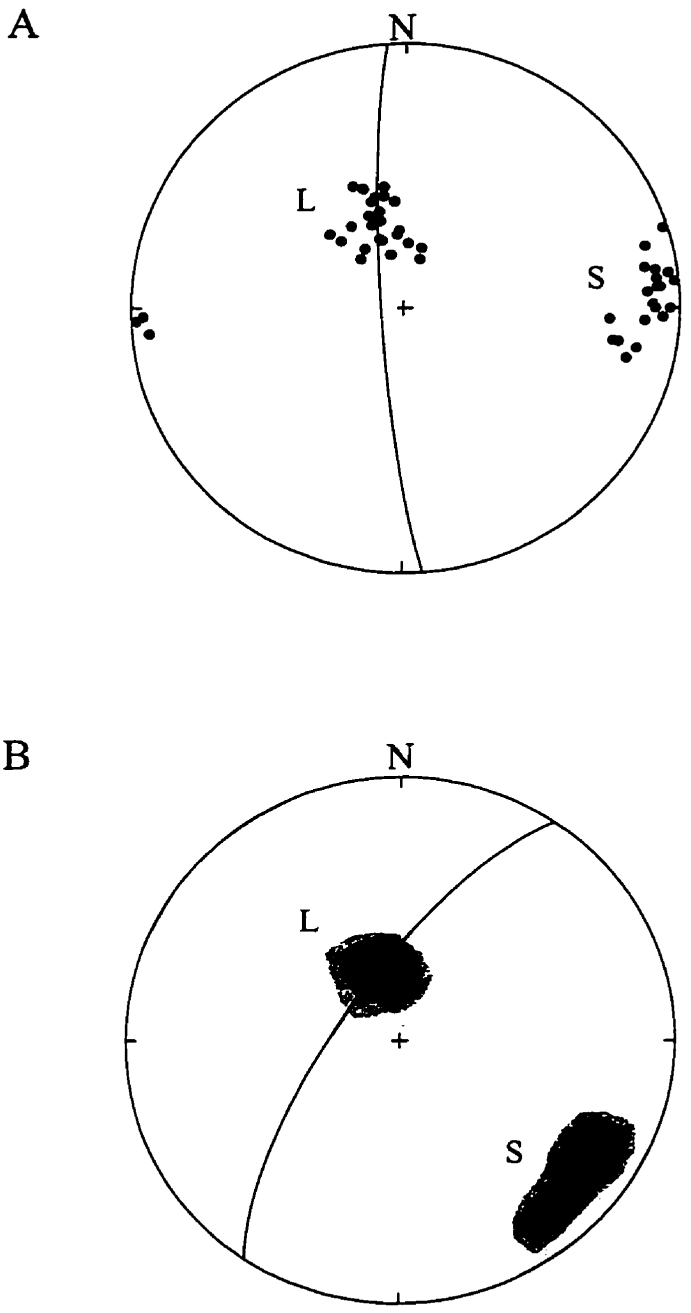

Figure 3-21. (A) Stereographic plot of foliation and lineation from the David Lake Shear: S, poles to foliation; mean attitude 178/79 shown as a plane. L, lineation; mean plunge 338/60 (N=16). (B) Stereographic plot of foliation and lineation from the Mallard Lake Shear. S, poles to foliation; mean attitude 214/72 plotted as a plane (N=78; contour interval 2, 8, 14, 20, 26, 32% per 1% area). L, lineation; mean plunge 350/68 (N=58; contour interval 2, 10, 18, 26, 34, 42% per 1% area).

fabric described above, and sinistrally rotated boudinage structures which indicate a strike-slip movement.

Mallard Lake Shear

The Mallard Lake Shear (MLS) lies at the northwestern boundary of the Star Lake pluton but cuts into the porphyritic diorite of the pluton southwest of Mallard Lake (Figure 3-22). The strike of the shear changes from NNE in the south, to NE, south and east of the Mallard Lake. It can be traced for approximately 1,500 metres from southwest of the Jolu Mine to the east of the Mallard Lake. Lineaments on air photographs indicate that it probably extends beyond the boundaries of the structure shown in Figure 3-22.

The MLS is defined by a rapid gradient in the intensity of the fabric from the D_1, S-L fabric of the country rocks to the L-S and locally L fabric of the shear. The foliation and the lineation of the shear are parallel to the fabric in the adjacent country rocks (Figures 3-21B and 3-22). There is no evidence of asymmetry in the fabrics, and hence no kinematic indicators or evidence of shearing.

The MLS is deflected by the D_3 Rod shear near the Jolu Mine (Figures 3-16 and 3-22). Southeast of Mallard Lake, the Decade shear (a D_3 gold-bearing structure) occurs within, and overprints the fabric of, the MLS (Figure 3-22). The gold-bearing structure on the surface strikes 047° and dips subvertically. The dip-slip movement on the Decade shear is indicated by deflection of the fabric of the MLS. The general attitude of the Decade shear cannot be determined on the surface due to lack of exposure of the shear. According to Thomas (1985, 1993), the main gold-bearing zone strikes 045° and occurs in the metasedimentary rocks along the northern boundary of the Star Lake pluton. Field observations indicate that the fabric of the MLS is generally conformable to this lithological contact, which dips at 75° to 80° to the northwest. Hence the overall orientation of the Decade shear is probably parallel to the fabric of the MLS.

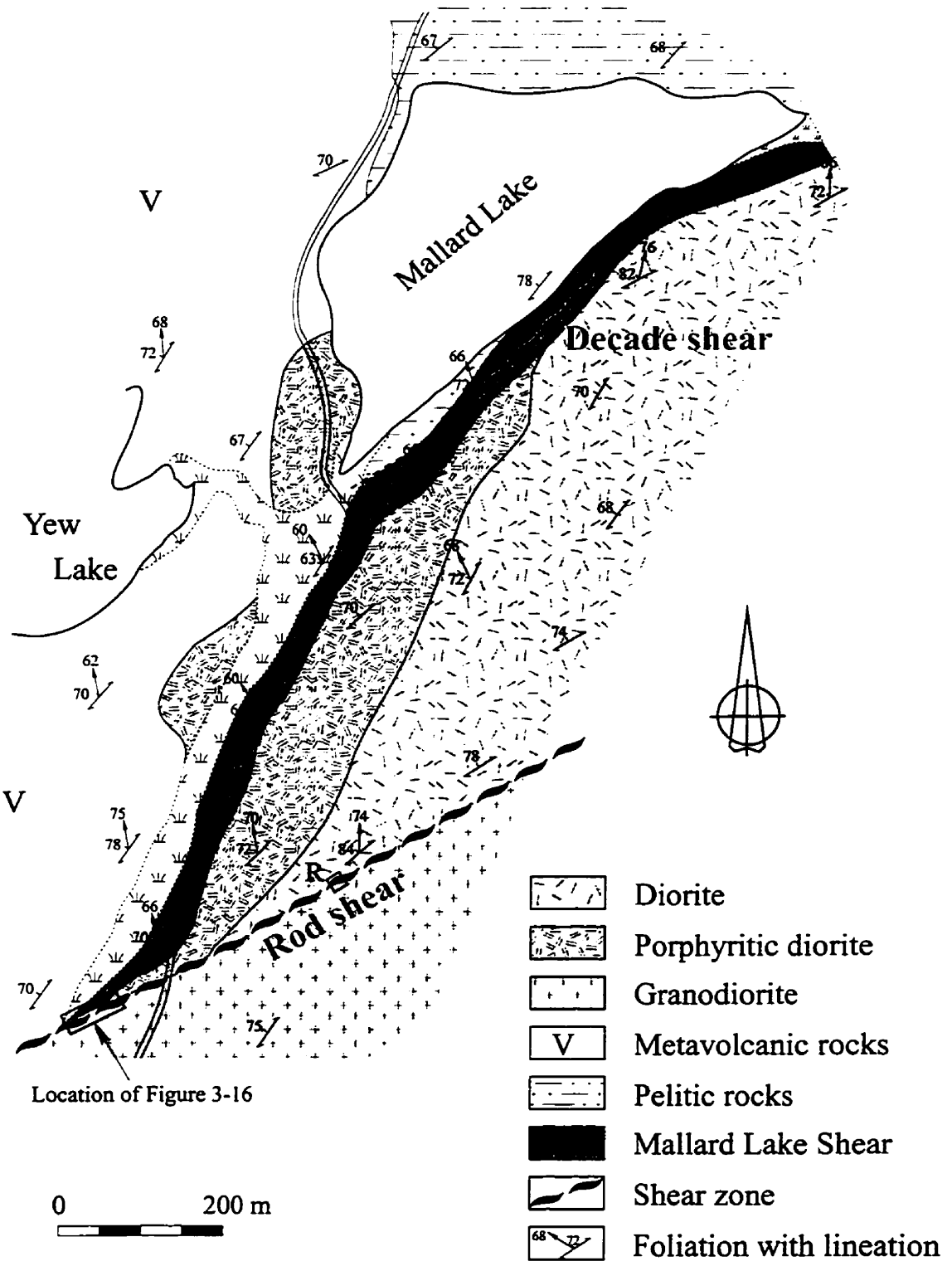

Figure 3-22. Geological map of the Mallard Lake area. R, the location of the Alimak raise at the Jolu mine.

Relationship to D_2 Structures

The MLS is deflected and overprinted by, and therefore predates, the D_3 structures (Figure 3-22). The relationship of the MLS to the D_1 deformation is ambiguous since it is parallel to S_1. It is inferred from the relationship described above that the DLS postdates the D_1 deformation. Poulsen *et al.* (1987) describe the displacement of the DLS by the Blindman shear, a D_3 structure. However, although the structure described by Poulsen *et al.* (1987) has the characteristics of the DLS, it is probably approximately 25 metres east of the DLS as determined in this study (Figure 3-23). Nevertheless, the orientation and fabric of the DLS and MLS, and the evidence of their timing, suggest that they can be classified with the D_2 structures.

Regional Structures

Definition and Stratigraphic Relationships

The regional structures in the map area are the McLennan Lake Tectonic Zone (Thomas, 1985) and the Alpat Lake Tectonic Zone (Thomas, 1985). They were defined in the field as zones of high strain expressed by distinctly more strongly foliated rocks at the contact of two lithologies.

McLennan Lake Tectonic Zone

The MLTZ is at or near the contact between the metavolcanic rocks of the Central Metavolcanic Belt to the northwest and the meta-arkoses of the McLennan Group to the southeast (Figure 3-24). It can be traced northeastward from Barker Lake, where it terminates in a series of shear splays (Thomas, 1993), to the Payne Creek pluton. In the northeast, the Redhill Lake Shear Zone, previously named Redhill Lake Tectonic Zone (Harper, 1985) and described as the northeast extension of the MLTZ (Harper, 1985; Lewry *et al.*, 1990), occurs within the McLennan Group meta-arkoses, approximately tens of metres to several hundred metres from the contact with the Central Metavolcanic Belt (Harper, 1996) (Figure 3-24).

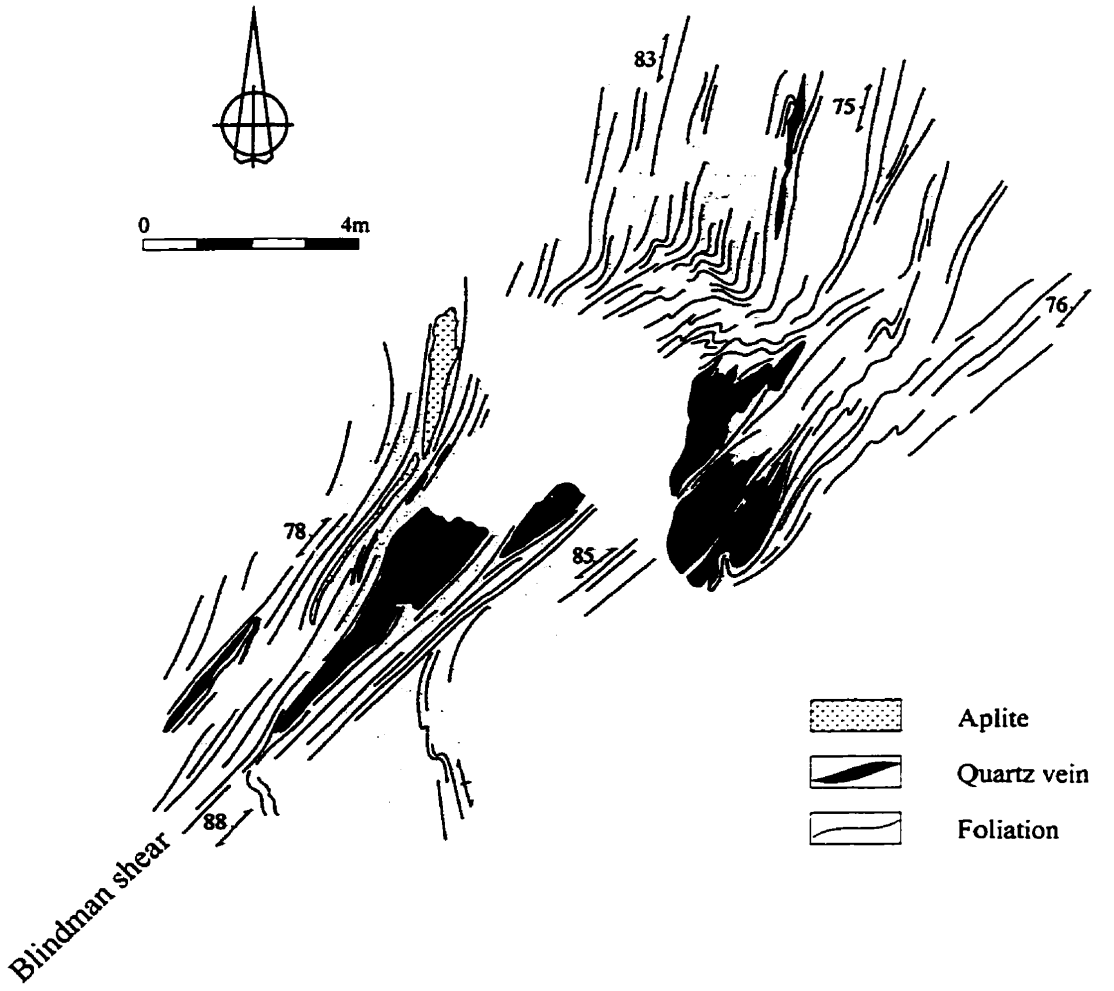

Figure 3-23. Outcrop map of the Blindman shear, approximately 25 metres east of the David Lake Shear. The foliation, which parallels the fabric of the David Lake Shear, has been dextrally deflected by the Blindman shear.

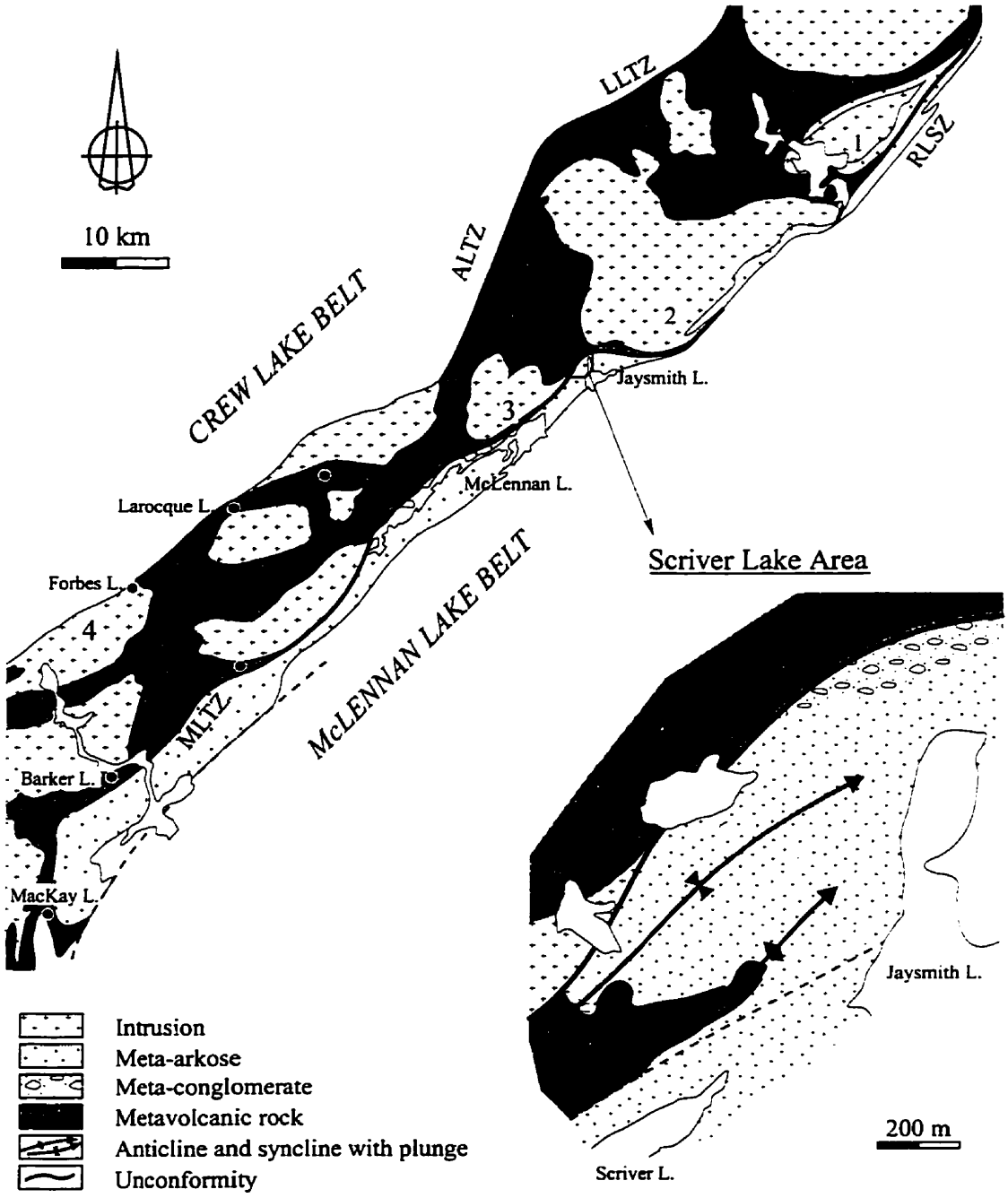

Figure 3-24. Extent of the McLennan Lake Tectonic Zone and Alpat Lake Tectonic Zone (after Thomas, 1993; Harper, 1986, 1996), and geology of the Scriver Lake area (after Yeo, 1996). ALTZ, Alpat Lake Tectonic Zone; LLTZ, Looney Lake Tectonic Zone; MLTZ, McLennan Lake Tectonic Zone; RLSZ, Redhill Lake Shear Zone. Intrusions: 1, Contact; 2, Payne Creek; 3, Island Lake; 4, Kruger Lake.

In the map area, the MLTZ is at the contact of the metavolcanic rocks and the meta-arkosic rocks, and extends laterally into both units. It also transects the southeastern boundary of the Island Lake pluton between the Cratty Lake and the Scriver Lake (Figure 2-4). The zone is wider in the metavolcanic rocks, up to several hundred metres, than in the meta-arkoses, where it is several tens of metres wide.

Largely based on the relative ages of the metavolcanic rocks and the meta-arkoses, and the presence of the down-dip mineral lineation, Lewry (1983) defined the MLTZ as the McLennan Lake Thrust, displacing the rocks of the Central Metavolcanic Belt southeasterly over the McLennan Group after the emplacement of the major regional plutons.

It is evident that the stratigraphic contact between the metavolcanic rocks of the Central Metavolcanic Belt and the meta-arkoses and meta-conglomerates of the McLennan Group is an unconformity. The unconformity was first recognized by Lewry (1986) and Thomas (1986) at the south end of the La Ronge Domain, in the MacKay Lake area, approximately 18 kilometres south of the termination of the MLTZ. During recent remapping of the MacKay-Hebden lakes area, Maxeiner and Sibbald (1995) described the contact as a volcano-sedimentary transitional suite that unconformably overlies the volcanic and intrusive rocks of the Central Metavolcanic Belt and grades to the overlying meta-arkoses and arkosic meta-conglomerates of the McLennan Group.

The unconformable relationship is exposed in the footwall of the MLTZ north of Scriver Lake (Yeo, 1996) and in the hanging wall of the Redhill Lake Shear Zone in the Sucker-Fleming lakes area (Harper, 1996) (Figure 3-24). The unconformity is overlain by polymictic meta-conglomerate, or by a transitional assemblage of mafic schists, calc-silicates and meta-arkoses similar to the sequence defined by Maxeiner and Sibbald (1995) in the MacKay-Hebden lakes area.

North of Scriver Lake, the unconformity is folded into an isoclinal anticline and syncline with a wavelength of approximately 250 metres (Yeo, 1996) (Figure 3-24). The axial planes of the folds strike northeast and dip steeply northwest. The northwestern limb of the syncline is bounded by the MLTZ, which is coincident with a

lineament that extends just north of Jaysmith Lake. A unit of polymictic meta-conglomerate occurs north and northwest of Jaysmith Lake, and is probably the continuation of the northwestern limb of the syncline. The meta-conglomerate is highly flattened at the faulted contact with the metavolcanic rocks (Figure 3-28A).

Alpat Lake Tectonic Zone

The ALTZ is part of a broad zone of high strain at the contact between the Central Metavolcanic Belt and the Crew Lake Belt (Figure 3-24). It extends southwestward through the Larocque and Forbes lakes to the Kruger Lake pluton (Thomas, 1993). The Looney Lake Tectonic Zone forms the northeast extension of the ALTZ (Harper, 1986). In the study area, the ALTZ trends north northeast and is up to 600 metres wide.

Internal Structures

Most of the internal structures of the regional-scale tectonic zones have been described from the MLTZ.

Foliation and Lineation

Both the MLTZ and the ALTZ are defined by S-L fabric, which consists of a steeply dipping foliation with an approximately down-dip mineral lineation. The fabric consists of mineral assemblages of amphibolite facies, identical to those associated with the regional S_1-L_1 fabric. The attitude of the S-L fabric of the MLTZ and the ALTZ is summarized in Figures 3-25A and 3-26A, respectively.

The S-L fabric of the MLTZ strikes approximately 050°. The mean dip of the foliation is 63° northwest (Figure 3-25A), which is 5° to 15° shallower than the S_1 foliation in both the metavolcanic rocks and meta-arkosic rocks.

The S-L fabric of the ALTZ strikes approximately 20° and dips vertically or steeply to the northwest or southeast (Figure 3-26A). The highly foliated rocks of the

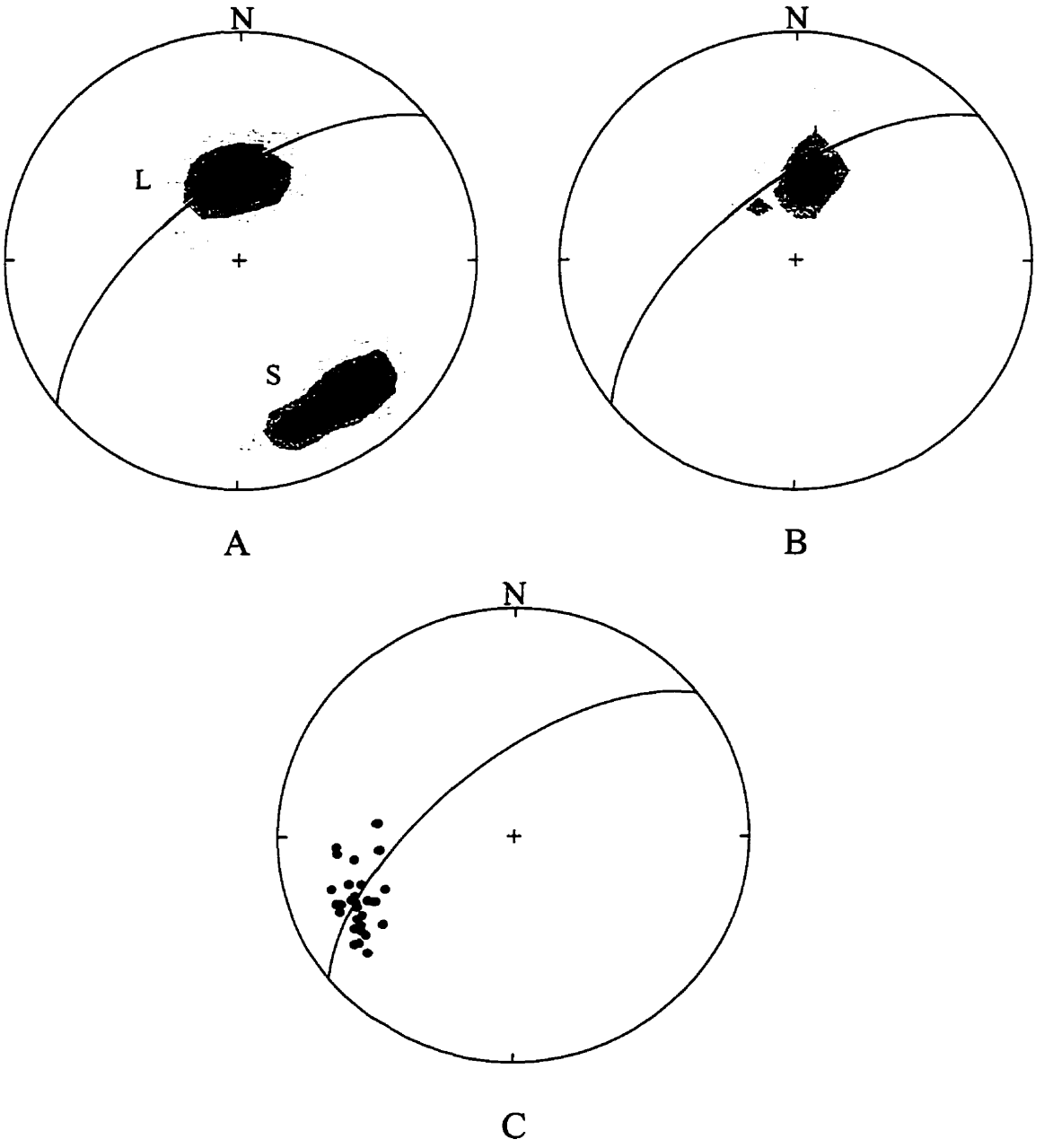

Figure 3-25. Stereographic plots of internal fabrics in the MLTZ. (A) S-L fabric: S, poles to foliation; mean foliation 231/63 shown as a plane. L, lineation; mean plunge 356/61 (N=126; contour interval 1, 8, 15, 22, 29, 36% per 1% area). (B) Asymmetric fold axes; mean plunge 11/60 (N=46; contour interval 2.2, 9.8, 17.4, 25.0, 32.6, 40.2% per 1% area). (C) Striation on foliation surfaces; mean plunge 246/26 (N=30).

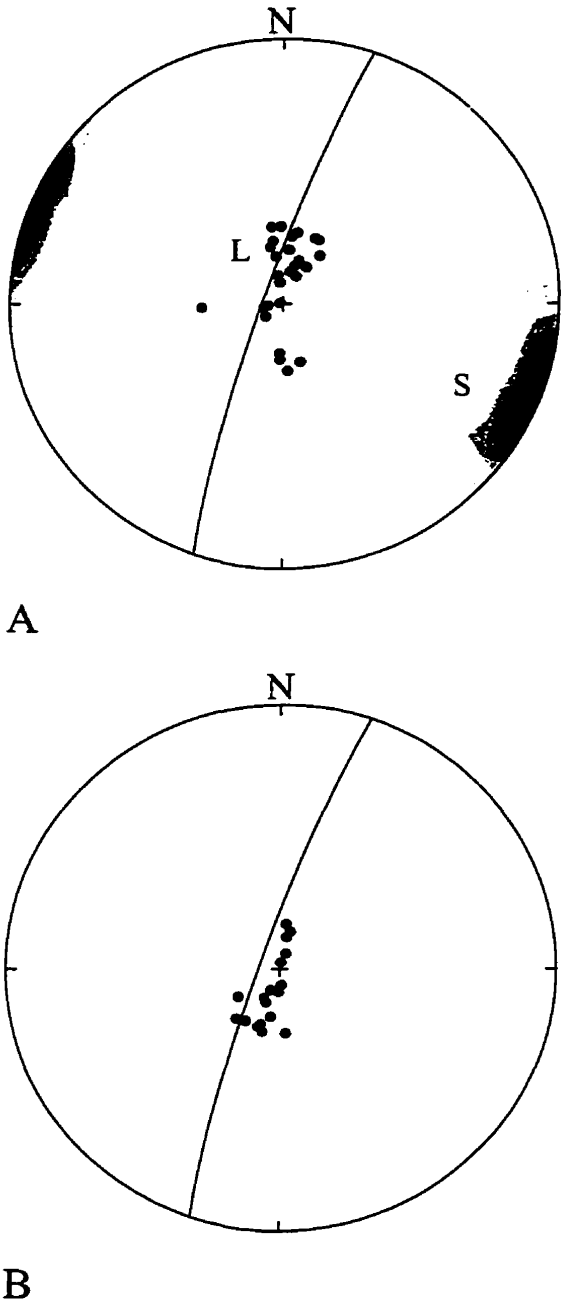

Figure 3-26. Stereographic plots of internal fabrics in the ALTZ. (A) S-L fabric: S, poles to foliation (N=75; contour interval 2, 8, 14, 20, 26, 32% per 1% area); mean attitude 199/84 shown as a plane. L, lineation (N=27); mean plunge 358/76. (B) The axes of S-shaped asymmetric folds (N=18).

ALTZ typically contain narrow quartz segregation or quartz veins one millimetres to several centimetres wide, consistently parallel to the foliation.

Finite Strains

Finite strains in the MLTZ were measured in outcrops of arkosic polymictic meta-conglomerate in contact with the metavolcanic rocks, northwest of the Jaysmith Lake (Figures 3-24 and 3-28A). Measurements were made on horizontal surfaces and vertical surfaces perpendicular to the foliation, which approximately represent the Y-Z and X-Z principal planes, respectively, of the finite strain ellipsoids. Finite strains were also measured from oriented hand specimens of lapilli tuffs taken from north of the Cratty Lake. The clasts are flattened and elongated in the foliation with their longest axes parallel to the mineral lineation (Figure 3-27C).

The results of measurements are shown in Tables 3-2 and 3-3, and are plotted on Flinn diagrams (Figure 3-27A and B). The majority of the finite strain ellipsoids are the flattening type ($0 < K \leq 1$). The type of strain is closely related to the strain intensity, in that, highest strain is associated with oblate strain ellipsoids, and lower strain with more prolate strain ellipsoids.

Evidence of Dip-Slip Shear Movement

Fabrics: The S-L fabric of the MLTZ indicates flattening in the X-Y plane and extension parallel to the X axis of the finite strain ellipsoid. There is no evidence in the fabric of shear movement.

Schaaf and Schwerdtner (1992) reported evidence for reverse shear movement in microscopic quartz shape fabric from deformed alaskite at the contact between the metavolcanic rocks and meta-arkoses in the Dickens Lake area, approximately 30 kilometres southwest of the map area. This observation is confirmed by this study (Figure 3-28B). The quartz shape fabric is composed of inequidimensional quartz subgrains of similar orientation aligned oblique to the foliation defined by micas. The fabric is interpreted as a steady state fabric formed as a consequence of shear deformation and syntectonic recrystallization. The sense of obliquity is considered to

Table 3-2. Strain data measured from meta-conglomerate

Distance to contact (m)	Axial ratio X/Y/Z	Percent extension X	Y	Z	Orientation X	XY
2	16.55/8.98/1	212	69	-81		78/69NW
10	16.35/7.69/1	226	53	-80	005/64	70/66NW
27	7.86/3.51/1	160	16	-67	002/71	75/72NW
45	9.85/3.34/1	208	4	-69	350/70	65/70NW
65	8.49/2.93/1	191	0	-66	004/69	69/70NW
98	9.69/2.95/1	217	-4	-67	000/70	74/71NW

Table 3-3. Strain data measured from metavolcanic rocks

Distance to contact (m)	Axial ratio X/Y/Z	Percent extension X	Y	Z	Orientation X	XY
10	11.58/8.45/1	210	60	-78	352/62	55/63NW
35	11.33/7.15/1	195	57	-75	357/58	58/60NW
40	9.19/5.97/1	142	57	-73	355/65	70/65NW
65	4.46/3.69/1	76	45	-61	345/62	44/65NW
120	3.64/3.29/1	59	44	-56	004/54	45/64NW
125	3.04/2.63/1	52	31	-50	035/57	70/70NW
135	6.14/3.28/1	126	21	-63	009/60	65/64NW
150	4.96/2.27/1	121	1	-55	354/59	50/63NW
180	4.79/2.61/1	106	13	-57	356/58	51/62NW
190	4.25/3.05/1	81	30	-57	018/60	70/64NW
200	4.11/3.36/1	71	40	-58	358/72	73/72NW
220	5.56/2.96/1	119	17	-61	032/61	66/73NW
260	4.94/2.87/1	104	19	-59	008/66	65/70NW
308	7.23/3.00/1	159	8	-64	037/52	62/72NW
310	5.46/2.47/1	129	4	-58	004/71	74/72NW
325	6.50/4.66/1	108	49	-68	009/53	75/55NW
340	7.64/4.90/1	128	46	-70	356/63	60/65NW
355	4.11/1.53/1	122	-17	-46	026/70	75/74NW

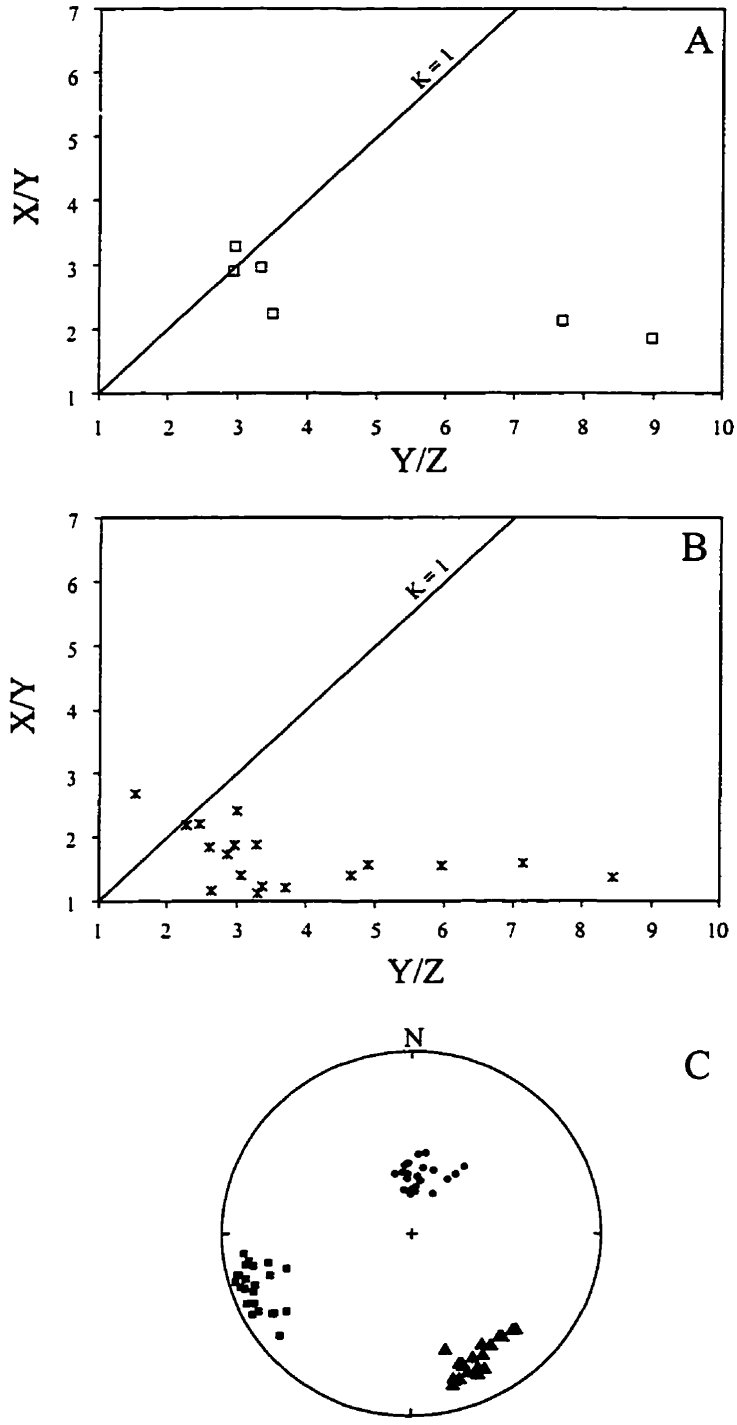

Figure 3-27. (A) Flinn diagram for deformed pebbles in meta-conglomerates from the footwall of the MLTZ, northwest of the Jaysmith Lake. (B) Flinn diagram for deformed lapilli in lapilli tuff from the hanging wall of the MLTZ, northwest of the Cratty Lake. (C) Stereographic plot of principal axes of deformed pebbles and lapilli. Circles, x-axis; squares, y-axis; triangles, z-axis (N=33).

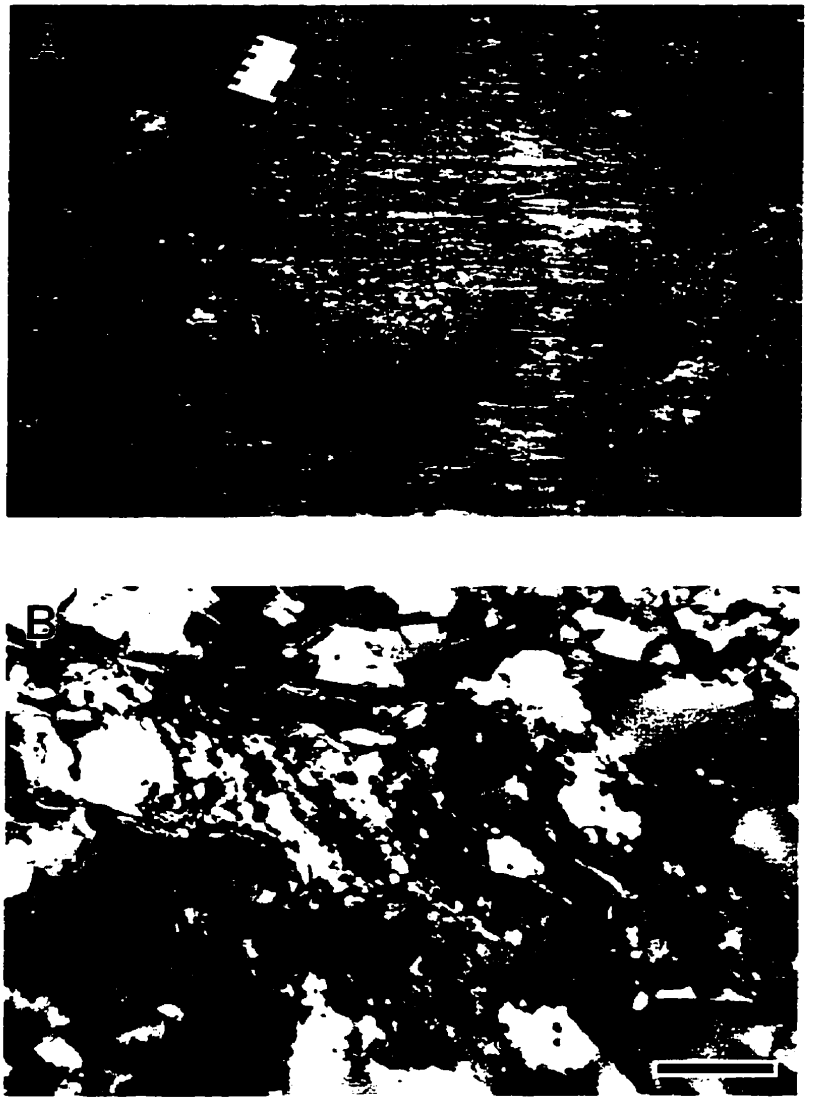

Figure 3-28. (A) Strongly flattened conglomerate pebbles at the contact with the metavolcanic rocks NW of the Jaysmith Lake, horizontal surface. (B) Photomicrograph of quartz shape fabric in highly deformed alaskite at the contact between the metavolcanic rocks and meta-arkoses, Dickens Lake area (nicols crossed; bar = 0.05 mm).

be a reliable shear sense indicator (e.g. Knipe and Wintsch, 1985; Burg, 1986).

Schaaf and Schwerdtner (1992) described a divergent pattern of stretching lineations in the map area, in which the plunge of the lineations varies from north-north northeast around Cratty Lake to approximately west close to the southwestern end of McLennan Lake. The authors suggested that the divergent pattern of the lineations is characteristic of thrust sheets, however, the present study could not reproduce the divergent pattern (Figures 2-4 and 3-25A); it was found that the lineation along the MLTZ in the map area consistently plunges to the north.

Microstructures: Quartz c-axis fabrics have been used as a tool for describing the kinematics of deformed tectonites in ductile shear zones. It is based largely on the close relationship between the symmetry of crystallographic fabrics and the flow regime. The quartz c-axis fabric was investigated in order to determine the nature of strain in the MLTZ. Five representative samples, four from the quartz-rich meta-arkoses of the McLennan Group in the study area and one from the deformed alaskite in the Dickens Lake area, were investigated. The localities of the samples are shown in Figure 3-29A.

All the specimens were subjected to recrystallization to various degrees. Specimen 92-407 contains quartz shape fabric indicative of reverse sense of shearing (Figure 3-28B). Quartz c-axis measurements were carried out on thin sections cut perpendicular to the foliation and parallel to the lineation using a universal stage. Only the grains not in contact with micaceous minerals were measured. The patterns of quartz c-axes are given in Figure 3-29B.

The c-axis figure of specimen 92-130 shows well-defined cross-girdles, characterized by an internal symmetry, and an external symmetry with respect to the foliation and the lineation. In specimen 92-57, the c-axes tend to form four maxima more or less centered around the foliation normal. Specimens 92-36 and 92-407 have similar cross-girdle patterns, with marked asymmetry with respect to the foliation. Specimen 92-35 contains a well defined maximum of c-axes close to the lineation.

Variations in the c-axis patterns of the specimens could reflect the influence of

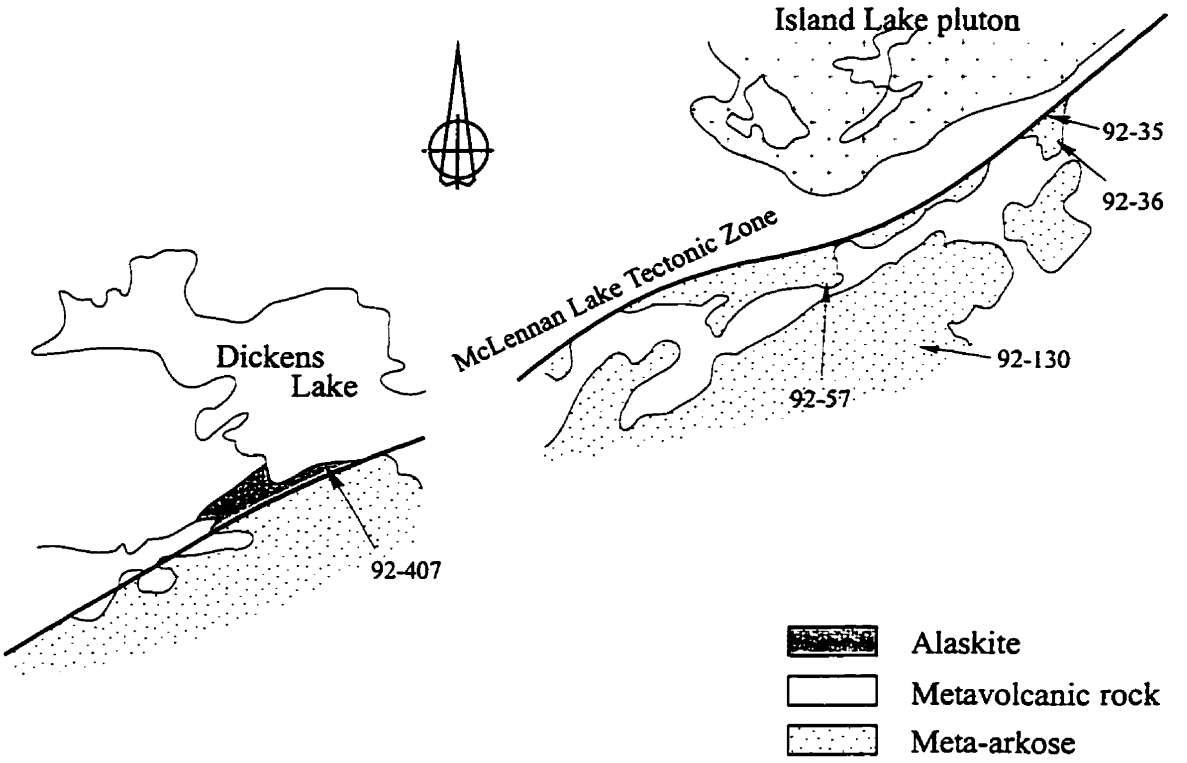

Figure 3-29. (A) Locations of specimens used to determine quartz c-axis preferred orientations in the McLennan Lake area and Dickens Lake area.

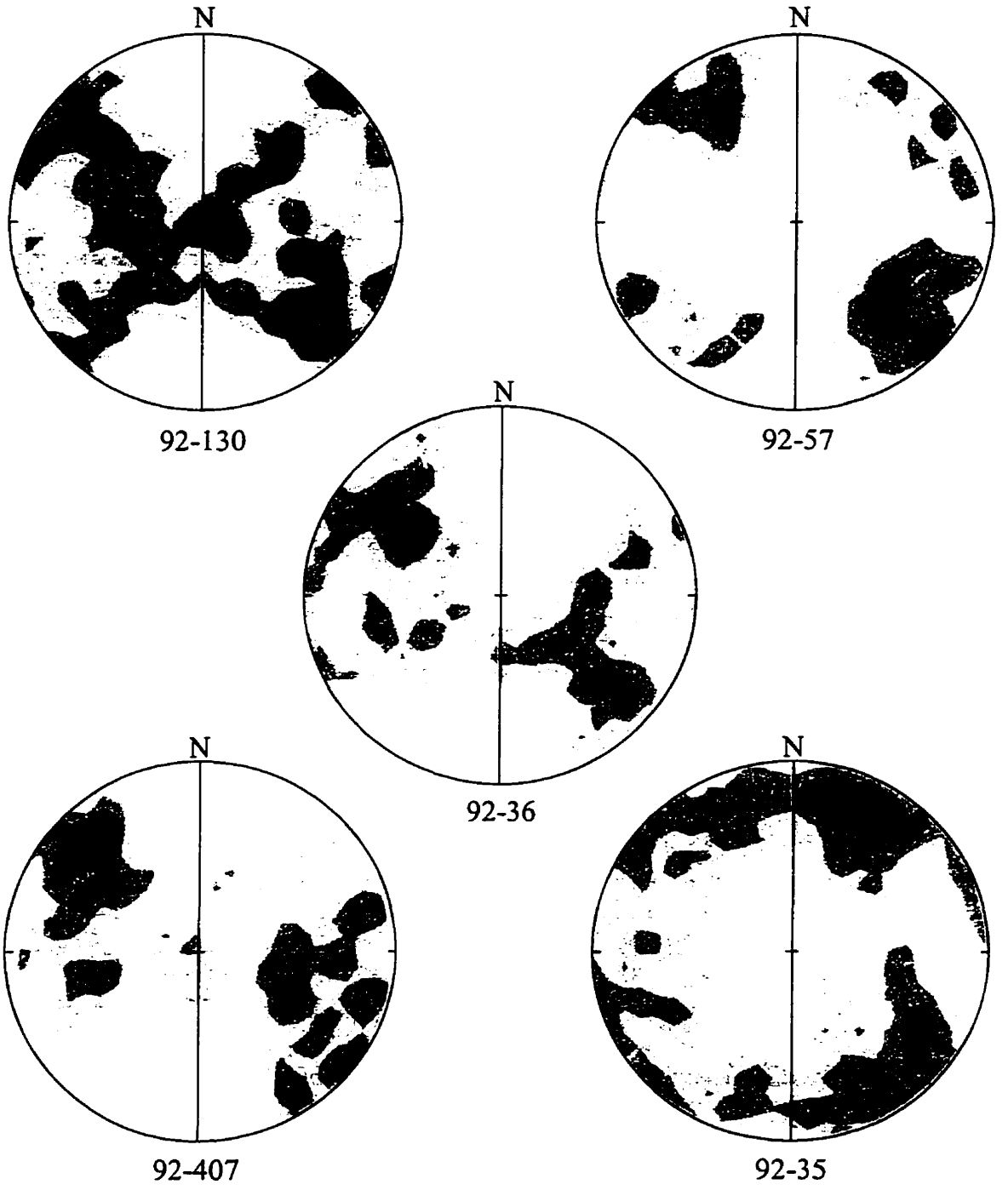

Figure 3-29. (B) Preferred-orientations diagrams of quartz c-axes. XZ sections, facing southwest, solid line is the trace of the foliation plane and of the lineation direction. 92-130: N=331, contour interval 0.6, 1.2, 1.8, 2.4, 3.0, 3.6% per 1% area. 92-57: N=461, contour interval 0.8, 1.6, 2.4, 3.0% per 1% area. 92-36: N=416, contour interval 0.8, 1.6, 2.2, 2.8, 3.4% per 1% area. 92-407: N=401, contour interval 1.0, 1.6, 2.2, 2.8, 3.4, 4.0% per 1% area. 92-35: N=328, contour interval 0.5, 1.1, 2.2, 3.3, 4.4, 5.5% per 1% area.

the type of strain history and the variations in the operative slip systems. If the strain is coaxial, then the resulting c-axis patterns will always be symmetric with respect to the foliation, whereas if the strain is non-coaxial, the resulting c-axis patterns will show asymmetry with respect to the foliation. In naturally deformed rocks, most patterns of quartz c-axis preferred orientations are involved in slip along the crystallographic <a> direction (Schmid and Casey, 1986); but under high temperature or in the presence of fluids, slip along prism <c> may be dominant (Garbutt and Teyssier, 1991).

The symmetric cross-girdles, as recorded in specimen 92-130, have been interpreted as an indicator of coaxial strain by Tullis (1977), Lister and Hobbs (1980), Schmid and Casey (1986) and Law (1986). The c-axis preferred orientation in specimen 92-57 may be also interpreted as indicative of the coaxial strain. However, the asymmetric cross-girdles of specimens 92-36 and 92-407 are indicative of a non-coaxial strain, in which the sense of shear is in the direction opposite to the inclination of the cross-girdle skeleton with respect to the foliation (Lister, 1977; Lister and Hobbs, 1980; Krohe, 1990). This sense of shear is in agreement with the reverse movement indicated by the quartz subgrain fabrics in specimen 92-407 (Figure 3-28B). The relation to the strain of the c-axis pattern in specimen 92-35 is unclear. This pattern may be suggestive of dominant prism <c> slip, promoted by fluids along the MLTZ that hydrolytically weakened quartz and allowed prism <c> slip to operate at relatively low temperature (Garbutt and Teyssier, 1991).

D_{3b} Structures

The S-L fabric of the MLTZ and ALTZ is deformed by structures identical to those recognized in the dextral strike-slip movement of the D_{3b} episode of deformation. The same structures were recognized by Poulsen *et al.* (1987).

Pull-apart structures: Boudinage and pinch-and-swell structures are developed in competent units and veins parallel to the foliation (Figure 3-30A and B). The pull-apart structures generally indicate extension both parallel and perpendicular to the lineation. Extension in the direction of the lineation causes pinch-and-swell structures; while extension perpendicular to the lineation results in both pinch-and-swell and boudinage structures. In the direction of the lineation the structures are symmetric

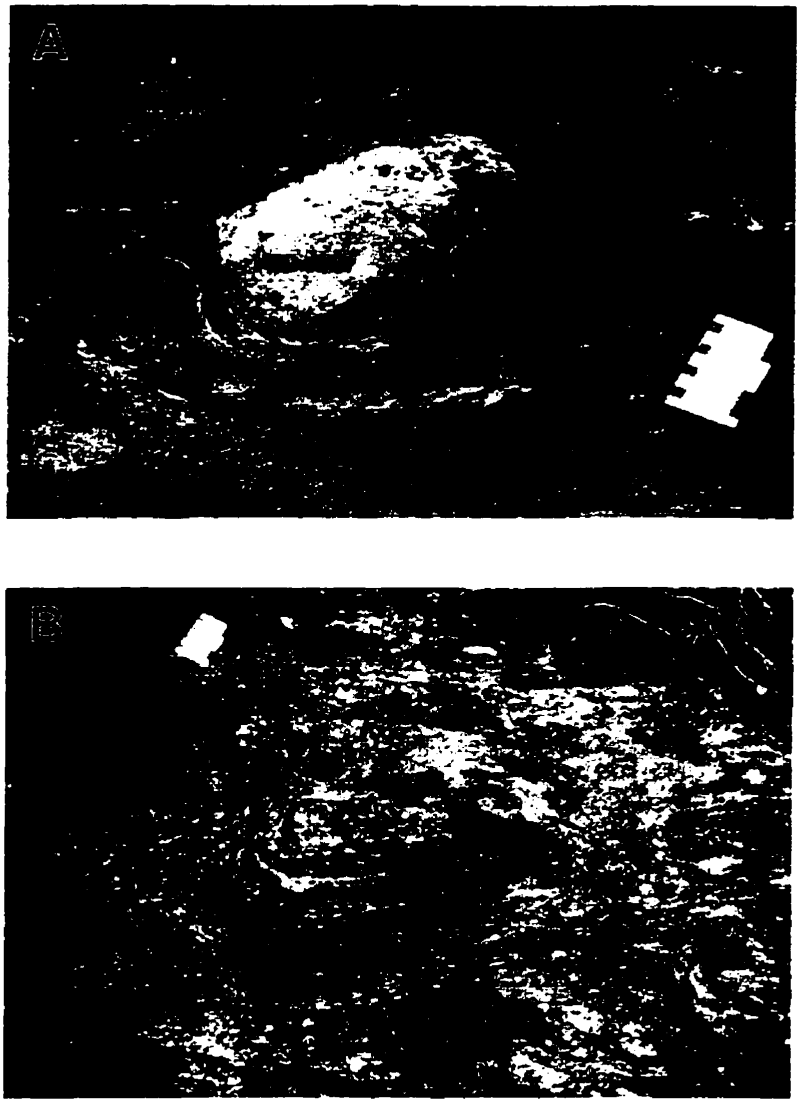

Figure 3-30. D_{3b} structures from the MLTZ and the ALTZ. (A) A horizontal view of a detached, asymmetric boudin in the MLTZ, whose asymmetry indicates a dextral sense of shearing. (B) An asymmetric pinch-and-swell structure in the MLTZ, horizontal surface. The "pinchs" are thin, approximately 0.5 cm, but still connect adjacent "swells".

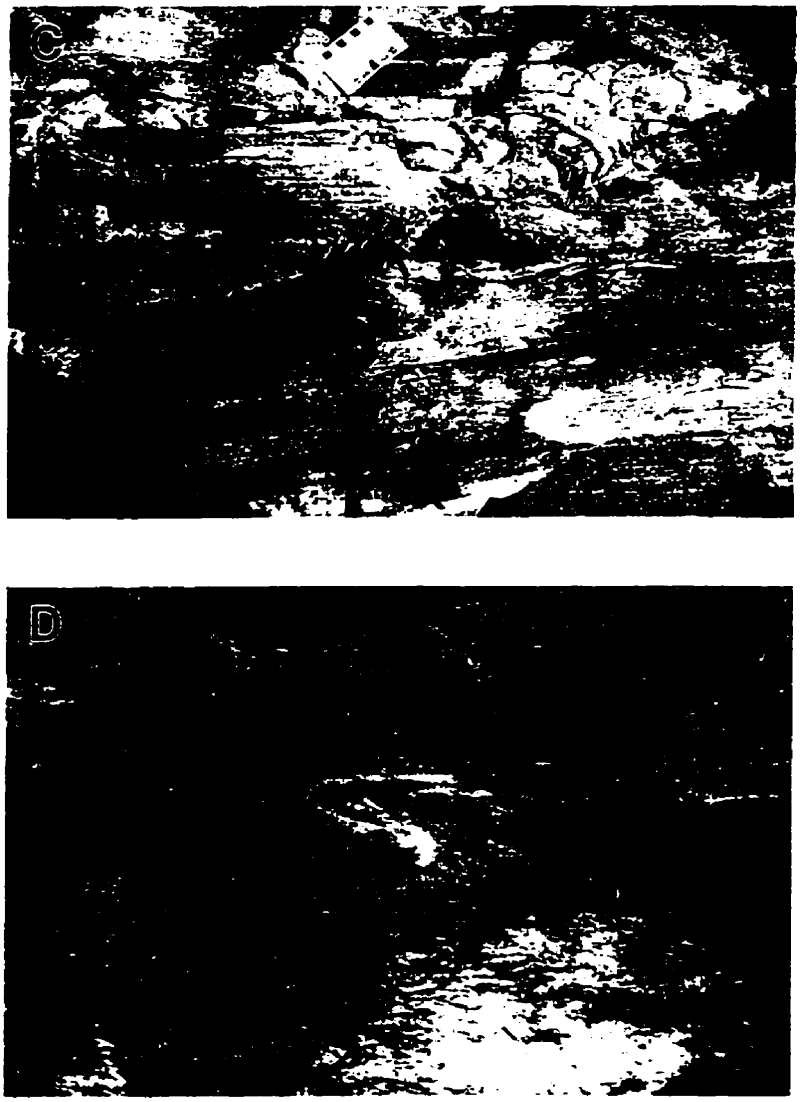

Figure 3-30. (C) A Z-shaped asymmetric fold in the MLTZ, viewed on horizontal surface. An associated vein (arrow) is formed at the axial surface of the fold. The axial surface is subvertical and strikes 18 to 20 . (D) A vertical S-shaped asymmetric fold of penetrative foliation in the ALTZ, horizontal surface.

about the foliation; however, on the horizontal surfaces, they exhibit both symmetrical and asymmetrical patterns. The asymmetry of the pull-apart structures, such as that shown in Figure 3-30A, indicates that they formed by a component of dextral progressive shear parallel to the foliation (Lister and Williams, 1983) (Figure 3-31A). The dextral shear is also indicated by back-rotation of the pinch-and-swell structures (Figure 3-30B), in which the swells and their internal foliation rotate counterclockwise approximately 15° to 20° to the overall penetrative foliation, opposite to the sense of the dextral shear (Hanmer, 1986).

Folds: In the MLTZ, folds of the foliation and transposed layering, as well as boudinage structures are characterized by their Z-shaped asymmetry on horizontal surfaces (Figure 3-30C). The asymmetrical folds occur at scales ranging from centimetres to metres, and vary from open to closed, commonly with angular fold closures. The axial surfaces strike north-south to northeast and dip steeply northwestward. The variability of the axial surface orientations can be seen in single outcrop and even in single layer. Close to the contact of the metavolcanic rocks with the meta-arkoses, the folds tend to become tighter. Crenulation cleavage is associated with the folds; it is best developed in the hinge area of the folds in mafic metavolcanic rocks. The crenulation cleavage is vertical or steeply dipping.

The Z-shaped folds generally occur as isolated folds, which die out along the strike of the axial surfaces. The axes of the folds lie in the surfaces of the foliation, and plunge to the north at 60°, approximately parallel to the earlier stretching lineation (Figure 3-25B). The consistent asymmetry of the folds indicates that dextral, foliation-parallel shearing is a viable mechanism for their formation (Figure 3-31B).

Shears and associated quartz veins, usually two or three centimetres thick, develop at the axial surfaces of some of the Z-shaped folds (Figure 3-30C). These structures are confined to the folds and terminate at the undisturbed foliation surfaces that bound the folds, and are best developed in folds located in more highly strained sections of the MLTZ. The asymmetrical folds and associated shears and veins are similar in every aspect to those in the James-Jasper-Roxy shears.

As in the MLTZ, non-coaxial strain in the ALTZ is observed on horizontal

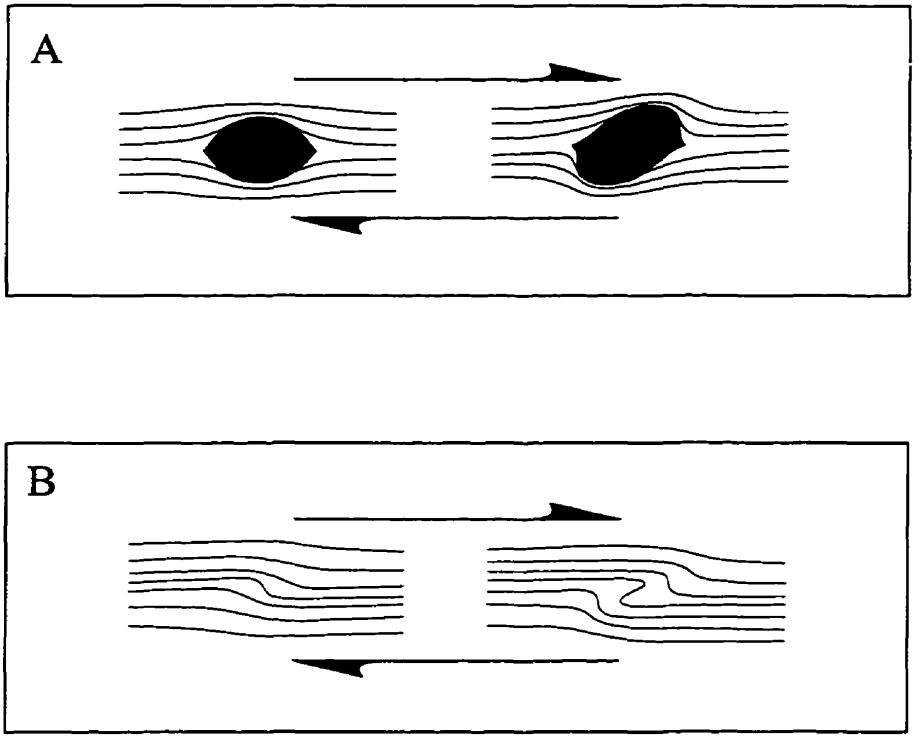

Figure 3-31. Schematic illustrations of the development of asymmetric structures as a result of progressive dextral shear deformation: (A) Boudinage structures. (B) Z-shaped folds.

erosional surfaces, and is mainly reflected in the deformation of the foliation into tight to isoclinal S-shaped asymmetrical intrafolial folds (Figure 3-30D). The folds are vertical, with subvertical fold axes lying on the penetrative foliation planes (Figure 3-26B). The folds are identical to the asymmetrical folds in the MLTZ, but with asymmetry that indicates sinistral transcurrent shear along the foliation.

Striations: In some areas, striations were observed on the surfaces of the foliation. They are defined by fine-grained micaceous minerals, overprinting the steeply to moderately plunging mineral lineation. The striations occur in both the metavolcanic rocks and meta-arkoses of the MLTZ, particularly in the more highly strained rocks. The plunge of the striations, 26° to the southwest (Figure 3-25C), is assumed to indicate the direction of a D_{3b} displacement on these foliation planes.

Discussion

The structural significance of the high strain zone that defines the MLTZ is important in terms of tectonic evolution, but it may also be significant in terms of the genesis of the gold deposits of the area. It is well established that gold deposits in the Abitibi greenstone belt of Canada and the Yilgarn Block of Australia are spatially related to regional faults or "breaks" (Colvine *et al.*, 1988; Groves and Foster, 1991). With some exceptions, the deposits are not hosted in the regional structures, but in smaller scale structures that are interpreted to be splays of the regional faults. There is good evidence that the Archean regional structures are fundamental in the sense that they penetrate deeply into the crust. The evidence includes the following: the structures may separate contrasting terranes (see Colvine *et al.*, 1988); they are associated with molasse-type (Timiskaming-type) sediments generated by movement on the faults (Corfu *et al.*, 1991); they control the distribution of alkalic plutons that are believed to have originated at the base of the crust or the mantle (McNeil and Kerrich, 1986; Corfu *et al.*, 1991). Such structures would be capable of tapping deep-seated hydrothermal fluids of metamorphic-magmatic origin.

It has been suggested by Lewry (1983) that the MLTZ is a thrust fault of regional significance, and this receives some support from the observations of Schaaf

and Schwerdtner (1992) on the divergent pattern in the stretching lineation and the microfabric (Figure 3-28B). Lewry (1983) and Lewry *et al.* (1990) pointed out that the McLennan Group forms the core of an overturned regional syncline in which the MLTZ occupies the northwest limb. This suggests that the MLTZ is a zone of high strain at the contacts of units with contrasting rheologies.

However, that the MLTZ once acted as a thrust fault with large displacement is questionable. The observed unconformable relationship between the Central Metavolcanic Belt and the McLennan Group is difficult to reconcile with large displacement on the MLTZ, since the unconformity occurs in the hanging wall of the MLTZ in the Scriver Lake area and in the footwall of the Redhill Lake Shear Zone northeast of the Payne Creek pluton (Figure 3-24). Assuming that the Redhill Lake Shear Zone serves as the northeastern extension of the MLTZ (Lewry *et al.*, 1990), the preservation of the unconformity in the hanging wall of the tectonic zone suggests that no large displacement has been taken place, otherwise, the uplift and erosion caused by the thrusting displacement would have eliminated the unconformity in the hanging wall of the tectonic zone.

The observations made in this study show that the fabric of the MLTZ is a flattening fabric, and there is no evidence for reverse-sense displacement in the S-L fabric in the deformed rocks of the MLTZ. The S-L fabric in the MLTZ is similar in style and orientation to the regional S_1-L_1 fabric. It is probable that the fabrics were formed as a consequence of the same strain, that is, northwest-directed shortening and subvertical extension. The evidence for reverse shearing, such as the asymmetry of quartz c-axis patterns and quartz shape fabric, can be explained by local rotational strain produced by heterogeneous flattening, or by shearing at a fold limb due to differential movement at the contacts of rheologically contrasting units.

In summary, the tectonic fabric of the MLTZ and its relationship to the unconformity between the Central Metavolcanic Belt and the McLennan Group are not compatible with the hypothesis that the MLTZ is a regional thrust fault. It is probably a shear zone related to limb sliding of the regional synform cored by the McLennan Group.

Transpression

Introduction

The term transpression was first introduced by Harland (1971) to describe the deformation of a zone confined within two blocks of lithosphere moving with respect to each other in combined convergent and transcurrent movements. Since then, numerous studies have been carried out to understand the structural expression of transpression (e.g. Sanderson and Marchini, 1984; Hudleston *et al.*, 1988; Fossen and Tikoff, 1993; Robin and Cruden, 1994; Tikoff and Teyssier, 1994; Krantz, 1995; Teyssier *et al.*, 1995; Greene and Schweickert, 1995; Tikoff and Greene, 1997). In these studies, the variation of the attitude of stretching lineation within a transpressional zone has received the most attention.

Transpression was first kinematically modeled by Sanderson and Marchini (1984) under conditions in which a vertical tabular zone is laterally confined between undeformed walls. In their study, the deformed material maintains constant volume and is able to escape upwards by freely slipping along the walls in response to the movement of the walls. It is assumed that the internal flow and strain are uniformly distributed across the zone. The model provides a finite strain solution which predicts that the vorticity vector, or the internal axis of rotation, is always vertical and shear-sense indicators always indicate transcurrent movement. The model also predicts that the long axis of the finite strain ellipsoid is vertical if transpression involves a large amount of pure-shear component across the deformation zone.

Robin and Cruden (1994) specifically addressed the role of stretching lineations in their model of transpression in which flow with triclinic symmetry is developed that accommodates the boundary conditions of transpression but maintains strain compatibility with the bounding walls. The model explores the instantaneous, infinitesimal strain patterns, and predicts systematic variations in lineation orientation from horizontal to vertical across a transpressional zone and the presence, at the same exposure level, of both transcurrent and dip-slip shear movements. The authors demonstrated that vertical lineation and synchronous transcurrent shear indicators are developed under transpressional conditions of high ratios of pure-shear to simple-shear

strain; and shear indicators become parallel to the vertical lineation when the ratio of pure-shear to simple-shear strain reaches maximum values.

However, the model of Robin and Cruden (1994) does not allow generalizations concerning finite strain, with which fabrics in naturally deformed rocks (e.g. foliation and lineation) are primarily associated (Tikoff and Teyssier, 1994; Tikoff and Greene, 1997). Using a strain model of homogeneous transpression, Fossen and Tikoff (1993) and Tikoff and Teyssier (1994) pointed out that the instantaneous and finite strain axes are not coincident, and there is no simple relationship between instantaneous strain and structures developed over a protracted period of deformation. In the case of pure shear-dominated transpression, the long axis of the finite strain ellipsoid is always vertical; in the case of wrench-dominated transpression, the long axis of the finite strain ellipsoid initially lies in the horizontal plane, but becomes vertical with increasing deformation (Fossen and Tikoff, 1993; Tikoff and Teyssier, 1994). This is due to the fact that the finite strain axes are parallel to the instantaneous strain axes for the pure-shear strain of transpression, and consequently, the pure-shear strain is more efficient at accumulating finite strain in the vertical direction than the simple-shear strain in the horizontal direction (Figure 3-32).

The model of homogeneous transpression assumes no discontinuity within the deforming zone. However, transpressional deformation associated with obliquely convergent plates may be accompanied by faulting or shearing. Tikoff and Teyssier (1994) suggested that in a transpressional regime, the simple-shear strain of transpression is accommodated by the development of vertical strike-slip faults, and the pure-shear strain of transpression is taken up by the formation of reverse faults.

Vertical stretching lineations within a vertical shear zone, perpendicular to the simple-shear vector of deformation, were first interpreted to be the result of transpressional deformation by Hudleston *et al.* (1988). Since then, several other transpressional shear zones containing vertical stretching lineations or both shallowly-plunging and steeply-plunging lineations have been described by Robin and Cruden (1994), Greene and Schweickert (1995), and Tikoff and Greene (1997).

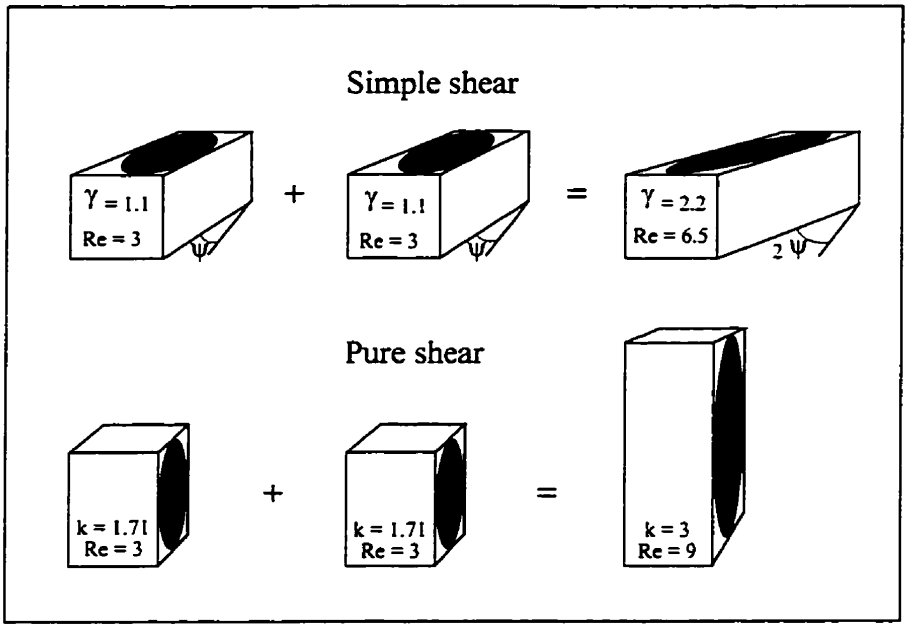

Figure 3-32. The finite strains as a consequence of two increments of decomposed pure-shear and simple-shear components of transpression (Tikoff and Teyssier, 1994). Both components are incrementally equal. Re, the ratio of the long over short axes of the strain ellipsoid; γ, the shear strain; k, the pure strain.

Tectonic Fabric Development

The tectonic fabrics of the area define three periods of deformation. Of these, the D_2 and D_{3b} fabrics have morphologies which indicate their formation by a combination of components of pure-shear strain and simple-shear strain. These fabrics, following the interpretations of Hudleston *et al.* (1988), Robin and Cruden (1993) and others, provide direct evidence of transpressional deformation. On the other hand, the fabrics of the D_1 and D_{3a} deformation, considered in isolation, do not indicate transpression; but since the fabrics of all three deformations each consist of planar structures with contained, steeply plunging lineations developed under similar metamorphic conditions (see Chapter 4), it is reasonable to assume that they were formed under the same tectonic regime. It is therefore concluded that the three deformations represent progressive strain, or the evolution of strain, in a transpressional regime.

D_1 Deformation

The S_1-L_1 fabric of the D_1 deformation is a manifestation of pure-shear strain in which the foliation lies in the XY plane of the finite strain ellipsoid for bulk deformation, and the steeply plunging mineral lineation defines the X-axis. The fabric is typically poorly developed and is absent from much of the plutons. It indicates flattening and extension as the result of northwest-directed compressional forces.

D_2 Deformation

As deformation progressed, strain increased and was partitioned into the narrow, discontinuous tabular zones which characterize the D_2 deformation. The tabular zones of high strain provide weak layers which permitted the release of the regional transcurrent stresses. The resulting kinematic indicators for subhorizontal shear on the structures, in conjunction with the subvertical lineation, provide the first manifestation of transpressional strain in the area.

The tabular zones of high strain of the D_2 deformation express the simple shear component of transpression, and their orientation is analogous to structures developed

in simple shear zones. Shear fractures developed in zones of simple shear were first described by Riedel (1929) and have since been reproduced in numerous laboratory experiments, with results that vary according to the type of material being sheared (e.g. Tchalenko, 1968, 1970; Wilcox *et al.*, 1973; Mandl *et al.*, 1977; Harris and Cobbold, 1984; Naylor, *et al.*, 1986). Typical shear fractures formed by simple shear in the experiments include: low-angle Riedel shear fractures (R), high-angle Riedel shear fractures (R′), and P shear fractures (P) (Figure 3-33A). The R and R′ shear fractures are interpreted as a conjugate set. They are the first fractures initiated in the deforming material, and are governed by the Coulomb-Mohr slip concept. The acute angle of intersection of the two fractures is dependent on the nature of the deformed material. It is given by most authors to be approximately 60° to 70°. This angle is bisected by the direction of maximum compression, which attains an instantaneous orientation at 45° to the general shear direction during simple shear (Mandl *et al.*, 1977). The P shear fractures form subsequently to the R and R′ fractures to take up increased shear displacement, since the R and R′ shear fractures are unfavourably oriented to sustain further displacement (Tchalenko, 1970; Naylor *et al.*, 1986). They are oriented approximately opposite to the R shear fractures, and frequently truncate and offset the R and R′ fractures (e.g. Tchalenko, 1968). The sense of slip along the R, and P shear fractures is the same as that of the shear zone, whereas that of the R′ shear fractures is opposite. Tchalenko (1970) demonstrated similar development and distribution patterns of shear fractures from a microscopic scale to a regional scale.

Structural features developed in simple shear zones are modified under conditions of transpression. The orientation of the horizontal section of the instantaneous strain ellipsoid depends on the ratio of pure-shear strain to simple-shear strain; at high ratios, the long axis of the horizontal ellipse approaches the shear direction (Krantz, 1995). Consequently, the conjugate R and R′ shear fractures rotate clockwise from their orientation in a simple shear zone in order to accommodate the pure-shear strain across the zone of dextral shear (Sanderson and Marchini, 1984; Krantz, 1995). The P shear fractures are expected to form close to the direction of transcurrent movement as their counterparts in a simple shear zone. Because the R and R′ shear fractures are initiated at high angles to the direction of transcurrent movement to accommodate the imposed pure-shear strain, their orientation is incapable of sustaining the increased simple-shear strain. Consequently, the P shear fractures would

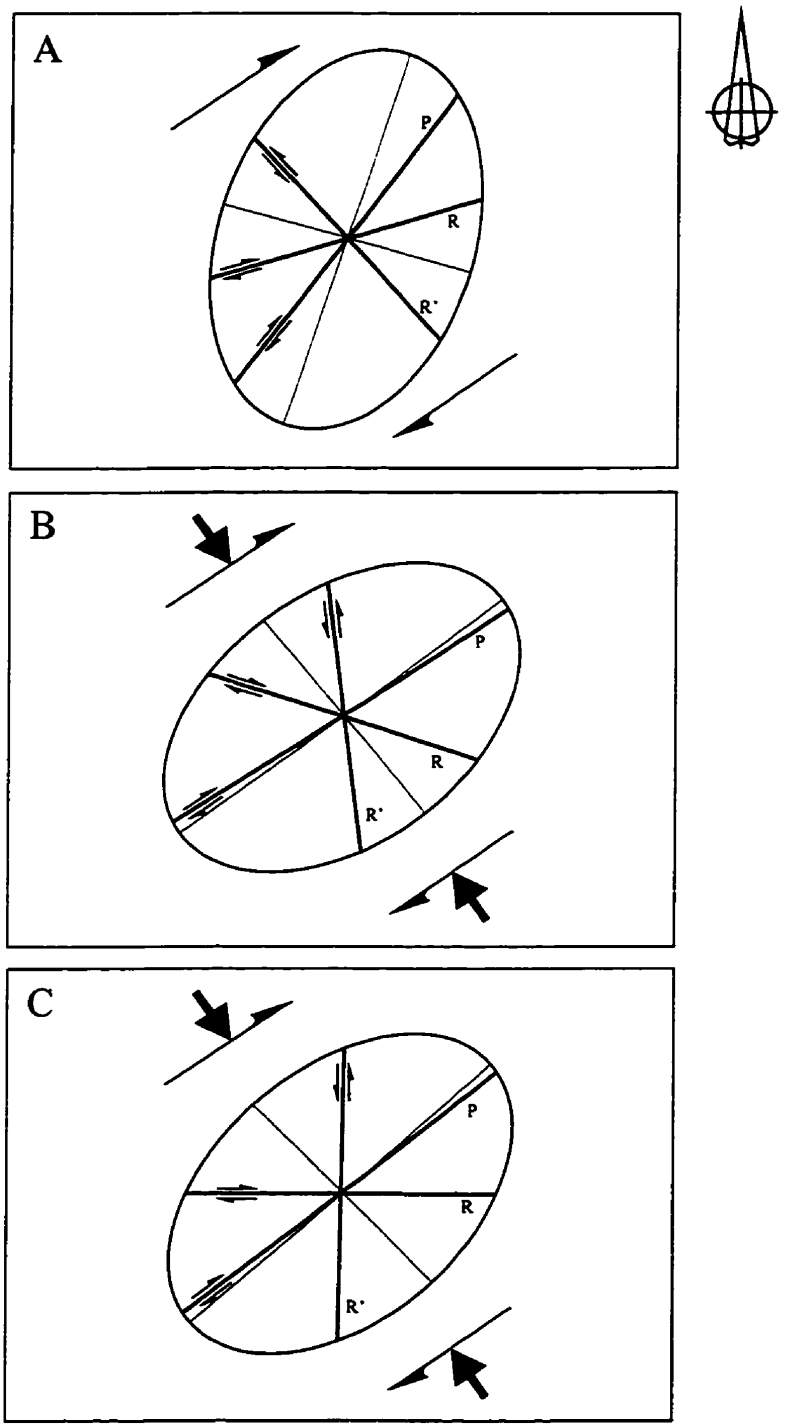

Figure 3-33. (A) Plan view of geometric relations among typical shear fractures in a simple shear zone. R, low-angle Riedel shear fracture; R', high-angle Riedel shear fracture; P, thrust shear fracture or P shear. (B) Expected modification in the orientation of the brittle shear fractures under conditions of dextral transpression, see text for detail. (C) Expected modification in the orientation of the ductile shears under conditions of dextral transpression, see text for detail.

be developed close to the simple-shear direction to efficiently accommodate the simple-shear strain. The shear fractures anticipated in a transpressional zone are given in Figure 3-33B.

The experiments that describe the generation of the R, R′ and P shear fractures model conditions of brittle deformation. The angular relationship of the conjugate shears (R and R′) under ductile conditions is such that the obtuse angle between the shears, generally 90 to 130 degrees, faces the greatest shortening direction of the deformation system, in contrast to that of brittle shear fractures where the acute angle faces the greatest shortening direction (Cobbold *et al.*, 1971; Ramsay, 1980) (Figure 3-33C).

It is suggested, therefore, that the development and orientation of the D_2 structures is controlled by the simple-shear component of transpression. The east-west, north-south, and northeast-southwest D_2 shears are equated with R, R′ and P shears developed in a ductile transpressional zone (Figure 3-33C). The cataclastic zones, which strike southeast, north-south, and northeast, are equated with the brittle conjugate shear fractures (R and R′) and P shear fractures in a transpressional zone (Figure 3-33B). The orientation of the D_2 structures is therefore defined by the horizontal ellipse of the instantaneous strain ellipsoid. Consequently, they intersect in the direction of the vertical axis of the instantaneous strain ellipsoid. In this interpretation, the D_2 structures do not form in the plane of the principal shear direction. This is assumed to be controlled by the northwest boundary of the Reindeer Zone, which, in turn, is parallel to the MLTZ. This interpretation is in agreement with the observations that the northeast structures, or the P shears in the model, always truncate and dislocate the planes of other orientations, indicating their comparatively late or prolonged development. It is suggested that the cataclastic zones developed simultaneously with the shears but in rocks with different viscosity, as suggested by their restricted location in the dioritic rocks of the plutons.

D_{3a} Deformation

The D_{3a} structures are conjugate sets of shears with stretching lineations and dip-slip shear vectors perpendicular to the subhorizontal intersection of the shears. The

steeply dipping members of the conjugate set are continuous, gold-bearing structures that extend completely across the plutons. The shallow-dipping members are characterized by low strain (S-C fabric) and are discontinuous.

As conjugate structures, the D_{3a} shears formed in response to crustal shortening across the area, and subvertical extension, with the plane of flattening approximately parallel to the MLTZ (Figure 3-34). In terms of bulk strain, they are the consequence of the pure-shear strain component of transpression.

The steeply dipping D_{3a} shears are approximately parallel to northeast-trending planes of the D_2 structures. The relationship between the D_2 and D_3 structures is illustrated southeast of the Mallard Lake, where the D_{3a} Decade shear occurs in, and is in general parallel to the fabric of, the D_2 Mallard Lake Shear (Figure 3-22). It is probable that the steeply dipping D_3 shears nucleated in the northeast set of the D_2 structures.

The dip-slip shearing along the steeply dipping D_{3a} shears was accompanied by the emplacement of layered auriferous quartz veins (see next section), indicating that the dip-slip shear movement would be enhanced and the shear system changed to brittle-ductile regime as a consequence of increased fluid pressure. This, in conjunction with the probable nucleation of the steeply dipping D_{3a} shears in the D_2 structures, may explain the better development of the D_{3a} gold-bearing shears than the shallow-dipping conjugate ones.

D_{3b} Deformation

The steeply dipping D_{3a} shears provide planar, weak structures, ideally oriented to release the stresses that generated the strike-slip or transcurrent movement of transpression: D_{3b} structures. The movement in the D_{3b} deformation is represented by two types of shearing: strike-slip shearing in all of the D_{3a} shear zones, and oblique-slip shearing in the Rod shear at the Jolu Mine. The strike-slip and oblique-slip may represent two consecutive shear movements formed according to changing strain conditions. However, there is no evidence in the James-Jasper-Roxy system of oblique-slip shearing. The differences in the slip directions and structural features are

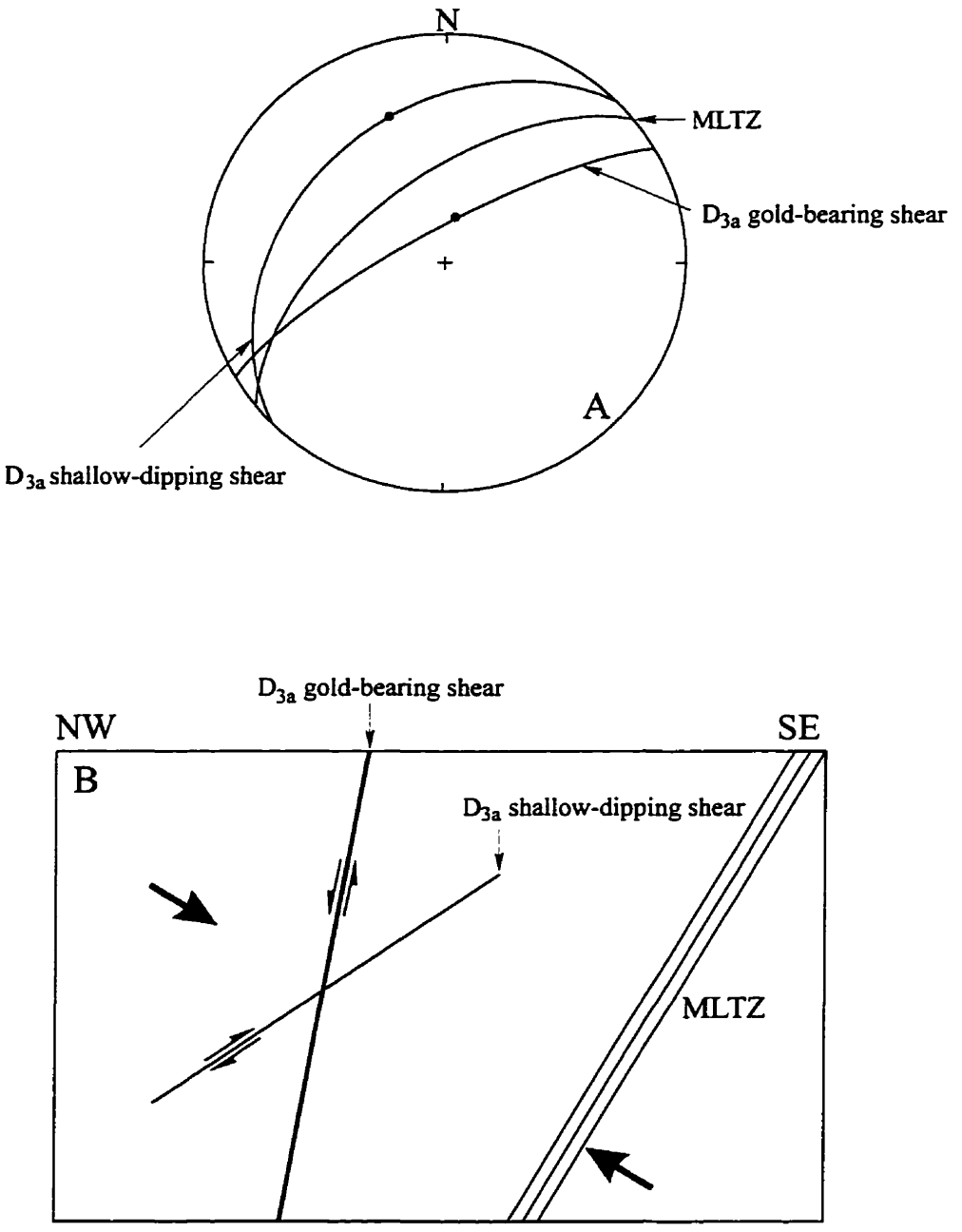

Figure 3-34. (A) Stereographic plot of mean attitudes of D_{3a} gold-bearing shears (238/78) and shallow-dipping shears (225/35), and the MLTZ (231/63). Slip on the shears are indicated by filled circles. (B) Schematic illustration of relationships among the MLTZ, D_{3a} gold-bearing shears and shallow-dipping shears. Note the flattening plane to the conjugate set of shears is approximately parallel to the MLTZ.

probably related to the mechanical properties of the shear systems rather than changing conditions of deformation.

In the James-Jasper-Roxy system, the D_{3a} deformation generated layered structures consisting of narrow, weak zones of mylonite, 10 to 30 centimetres thick, separating strong or lower strain zones or layers, which are somewhat thicker than the weak mylonite zones (Figure 3-10). The quartz veins in the central parts of the shears also provide more competent layers. The D_{3b} deformation is here represented by strike-slip shearing, largely confined to the narrow mylonite zones. The D_{3b} folds formed where the shear resistance was greatest, or where the shears locked, and movement was taken up by folding of the D_{3a}-generated shears. The north-south veins formed in sheared axial surfaces of the folds, and in some locations north-south veins and host shears formed without the formation of the folds. Such shears are indicated by the development of foliation with steeply plunging mineral lineation, and are kinematically identical to the D_2 shears. They demonstrate that a deformation took place in the wall rocks to the shears, coeval with shearing. Furthermore, this deformation involved vertical extension.

Similar D_{3b} structures, although much less abundant, occur in the protomylonite of the Rod shear. In the Rod shear at the Jolu Mine, the zone of high strain, and host to the gold-bearing quartz veins, is a phyllonite unit, up to six metres thick (Figure 3-16). The phyllonite is a homogeneous ductile unit; it does not consist of layers of alternating weak and strong units as in the Rod shear protomylonite and the James-Jasper-Roxy system.

It is assumed that the phyllonite zone formed during the dip-slip shear movement of the D_{3a} deformation when much of the stress that produced the bulk pure-shear strain was accommodated. However, during the D_{3b} deformation the phyllonite behaved as a ductile body. The oblique slip may be reconciled as the resultant of components of dextral strike-slip and dip-slip vectors of shear.

The high strain zones that define the MLTZ and the ALTZ were generated during the D_1 deformation. The high strain structures may have acted as weak planes for the release of the transcurrent stresses following their development. Therefore, the

D_{3b} structures observed within the MLTZ and the ALTZ were not necessarily exclusively produced by the D_{3b} deformation, but are more likely the expression of accumulated transcurrent strain after the D_1 deformation. Unlike the MLTZ, deformation in the ALTZ is manifested by sinistral transcurrent movement (Figure 3-30D). The sinistral movement was probably controlled by the orientation of the ALTZ, which trends north northeast in the map area. The resultant stress of transpression would be such that it pushed the northwest side south-southwestward (Figure 3-35).

Concluding Statement

The gold-bearing shears were produced during the transpressional deformation, and are in effect a "fabric" formed as deformation advanced. They were formed (as were the D_2 structures) by the concentration or partitioning of strain into tabular zones of high strain within the deforming rock units. Although it is difficult to prove conclusively, it is very probable that the footwalls and hanging walls to the shears were being deformed at the same time as deformation progressed within the shears. As such, the shears may be described as "stretching shears" according to the definition of Means (1989). This contrasts with the model of Poulsen (1989) in which the gold-bearing shear are presented as third-order structures to the second-order and first-order structures of the David Lake Shear and the MLTZ, respectively.

Relationship of Gold Mineralization to Deformation

In the following, brief descriptions are given of the Jasper and Jolu deposits, based on mapping of surface exposures and mine plans, following which arguments are presented on the relative timing of mineralization and the geometry of the deposits.

Jasper Deposit

The Jasper deposit consists of shear-hosted ore shoots on two parallel shears, the Jasper South and the Jasper North (Figure 3-36). The quartz veins are layered and

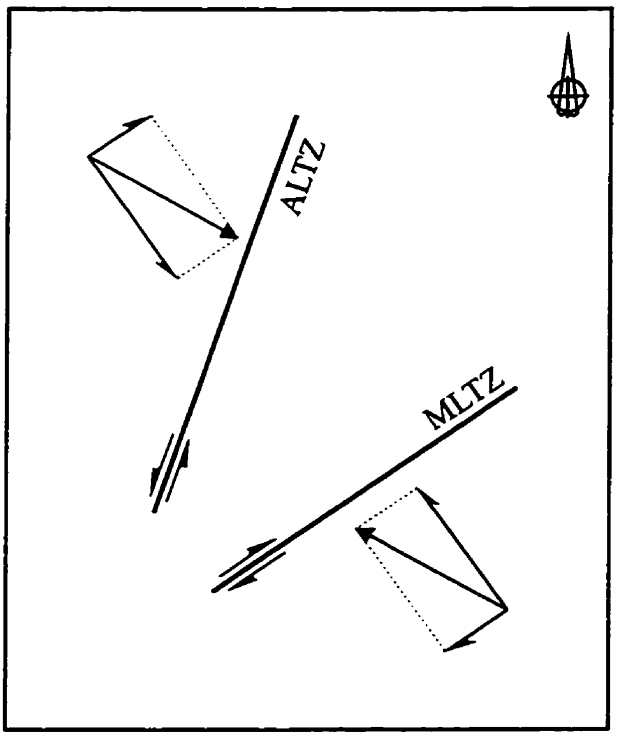

Figure 3-35. Schematic diagram illustrating sinistral transcurrent movement on the ALTZ under dextral transpression.

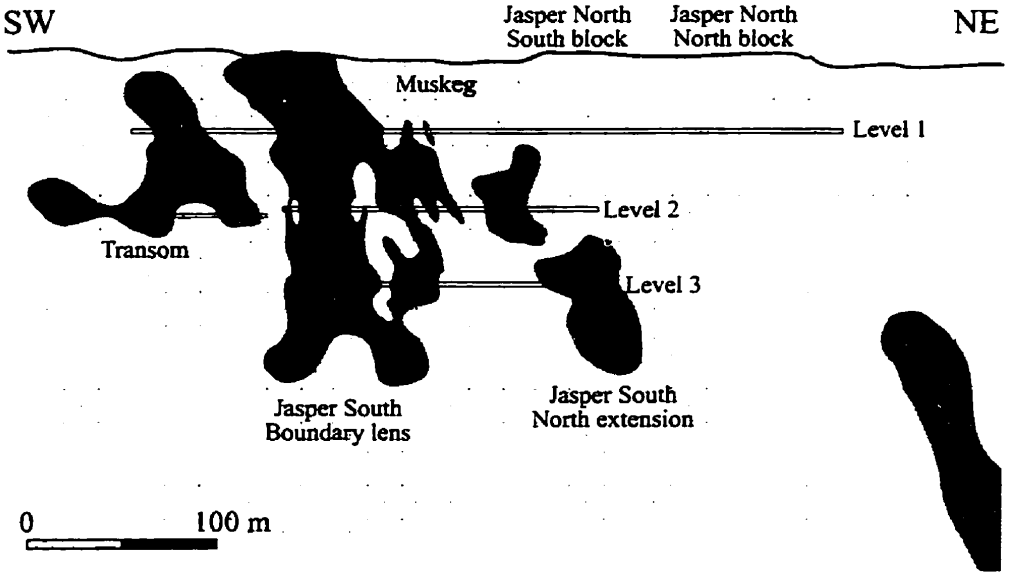

Figure 3-36. Longitudinal section of the Jasper deposit showing the steep northeast pitch of the ore shoots (modified from Roberts, 1993).

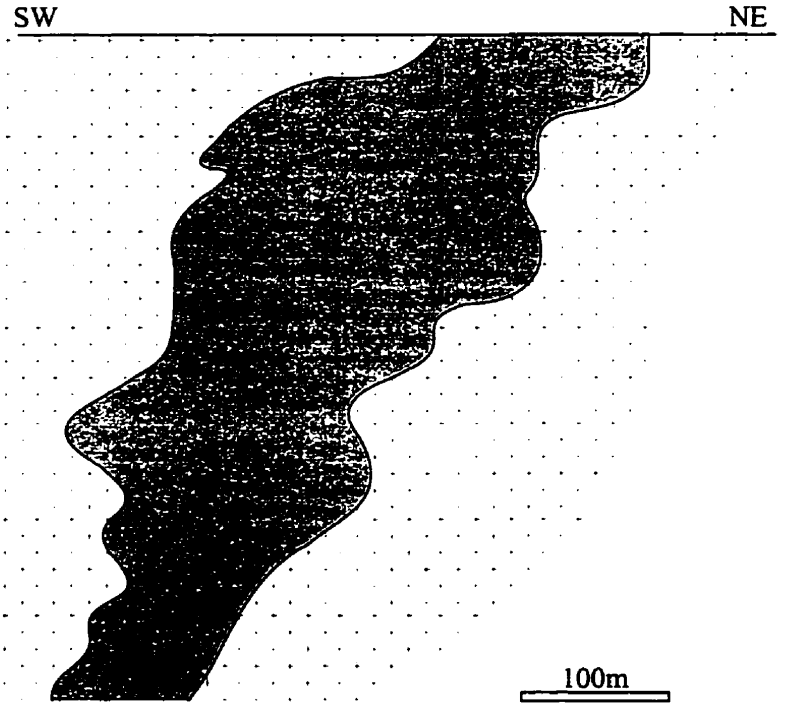

Figure 3-37. Longitudinal section of Rod Main orebody, Jolu Mine (modified from Roberts, 1993).

emplaced parallel to the shear fabric in the highly strained central parts of the shears. The ore shoots (defined by the gold content of the veins) are up to two metres thick and are elliptical, the long axes of which pitch 70° to 75° to the northeast, parallel to the steeply plunging lineation of the host shears (Figure 3-36).

Jolu Deposit

The Jolu deposit consists of Rod Main zone and Rod South zone (Figure 3-15). The Rod Main zone occurs in the central phyllonite zone of the Rod shear, which strikes 060° and dips approximately 85° southeast in the Jolu Mine area. The Rod Main is approximately 200 metres in length and up to 7 metres thick, and extends from surface to approximately 385-metre level (Thomas, 1993). The orebody dips 82° south and the long axis on longitudinal section pitches at approximately 65° to the southwest (Figure 3-37), in contrast to the Jasper deposit where the ore shoots plunge northeast, parallel to the stretching lineation of the shear. The Rod South is a smaller ore zone, occupying a subordinate shear that strikes at 080° and dips approximately 85° southeast. The Rod South orebody also pitches to southwest at approximately 65°.

Gold-bearing quartz veins of the Jolu deposit in the geological level plans are oblique to the wall of the host shears, and make up a "right stepping" pattern (Figure 3-15).

Relative Timing of Mineralization

The formation of the layered quartz veins in the central, highly strained segments of the shears indicates that the central segments of the shears are permeable zones for focusing hydrothermal fluids. The layered quartz veins, characteristic of many lode gold deposits (e.g. Robert and Brown, 1986), reflect syn-kinematic deposition of veins as a result of periodic discharge of hydrothermal fluids during progressive shearing (Robert and Brown, 1986). Sibson *et al.* (1988) proposed a "fault-valve" model, which links formation of layered quartz veins to a regime of active reverse faulting under conditions of incremental strain. According to the model,

fluid discharge and vein formation in shear zones occurred when the system was open and fluid pressure was decreasing from supralithostatic to hydrostatic values immediately following a seismic event.

The distribution pattern of gold as elliptical ore shoots in the main shears, parallel to the shear vector of the D_{3a} deformation (Figure 3-36), does not suggest the association of gold mineralization with the D_{3b} deformation. This is supported by the absence of gold in the D_{3b} north-south veins (Billard, personal communication 1991; Hrdy and Kyser, 1995, p. 1924). The pattern of the ore shoots indicates that during the D_{3a} deformation, the differential movement in the plane of shears appears to control the fluid flow. The greater focusing of flow would result in higher erosion and dissolution by hydrothermal fluids of wall rocks, which would further increase the focusing of flow. By this process, differential permeability would be generated in the direction of stretching lineation, leading to lineation-parallel ore shoots. The colinear relationship between ore shoots and shear vector is also reported in the Chimo deposit in the Val d'Or camp (see Poulsen and Robert, 1989). It is thus concluded that gold mineralization was synchronous with the dip-slip shearing during the D_{3a} deformation.

Based on a "young" muscovite $^{40}Ar/^{39}Ar$ age of 1703 Ma and the observations that gold was sited in late microfractures of quartz veins, Hrdy and Kyser (1995) speculated that quartz veining and gold emplacement in the Jasper deposit were not directly related. They suggested that barren quartz veins were emplaced into the D_3 shears (presumably during the D_{3a} dip-slip shearing) at the later stages of regional tectonic accretion (*ca.* 1820 Ma), and that gold was introduced into the late microfractures in the earlier veins approximately 100 million years later. However, this interpretation contradicts the observations that the orebodies are colinear with the D_{3a} stretching lineation, and that gold is notably absent in the D_{3b} north-south quartz veins.

The occurrence of gold in the late fractures of quartz grains does not necessarily indicate post-veining introduction of gold. Since gold is highly soluble under reduced and neutral to slightly alkaline conditions, and in the presence of pyrite (see Romberger, 1986; Roberts, 1987), remobilization during deformation and recrystallization could also produce texturally late gold that was introduced with the host veins (Romberger, 1986). The young $^{40}Ar/^{39}Ar$ age of muscovite likely reflects

the age of argon isotopic resetting or the age of closure of muscovite to argon loss, rather than the age of gold deposition (see Chapter 6). Therefore, the preferred interpretation for the siting of gold in the Jasper deposit is one in which gold was coeval with the deposition of the D_{3a} quartz veins, and was subsequently remobilized into the late microfractures in quartz grains generated by the D_{3b} deformation or any later deformation that affected the quartz in a brittle way.

The Rod Main orebody of the Jolu deposit plunges to the southwest, apparently not controlled by the D_{3a} stretching lineation. Furthermore, it cannot be shown to be controlled by the intersection of shears hosting the Rod Main and Rod South (Figures 3-15 and 3-38). The Rod Main orebody is more or less planar and is confined to the host shear zone over a length of 200 metres, and mineralization is absent from the intersection (Figure 3-15). Therefore, the intersection has no control on gold mineralization.

As was stated earlier, the Rod shear at Jolu Mine has undergone two periods of shearing (D_{3a} dip-slip shearing and D_{3b} oblique-slip shearing). Roberts (1993) suggested that the D_{3b} oblique-slip shearing of an initially steeply plunging oreshoot could explain the shape of the deposit, and the southwest plunge of the deposit. The modification of the shape and plunge of the oreshoot is illustrated in Figure 3-39. The outline of the ore in the longitudinal section is irregular; it consists of segments plunging steeply to the northeast, and segments plunging at moderate angles to the southwest (Figure 3-37). It is assumed that the orebody was originally emplaced as a single planar vein with the southwest edge of the ore pitching 75° to the northeast (Figure 3-39A). The oblique-slip shearing of the ore, operating in a shear vector plunging 36° to the northeast, disrupts the planar orebody through the development of a series of thrust shears (Figure 3-39B, C, and D), and consequently the irregular shape of the southwest boundary of the ore in the longitudinal section is developed.

Although both the Jasper and Jolu deposits have been deformed by the D_{3b} shearing, the results of deformation of the deposits are substantially different. There are two factors that probably affect the deformation processes: slip vector of the D_{3b} shearing; and response of the deformed layers to the shearing. In the Jolu deposit, the D_{3b} slip vector plunges 36° to the northeast, oblique to the inferred original plunge of

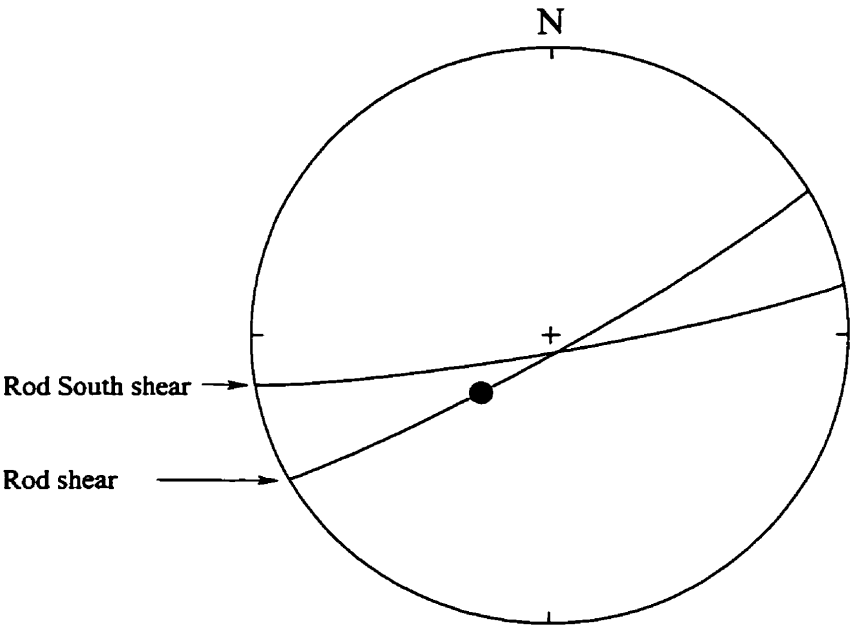

Figure 3-38. Stereographic plot illustrating the relationships between the plunge of the Rod Main orebody (solid circle) and the intersections of shears.

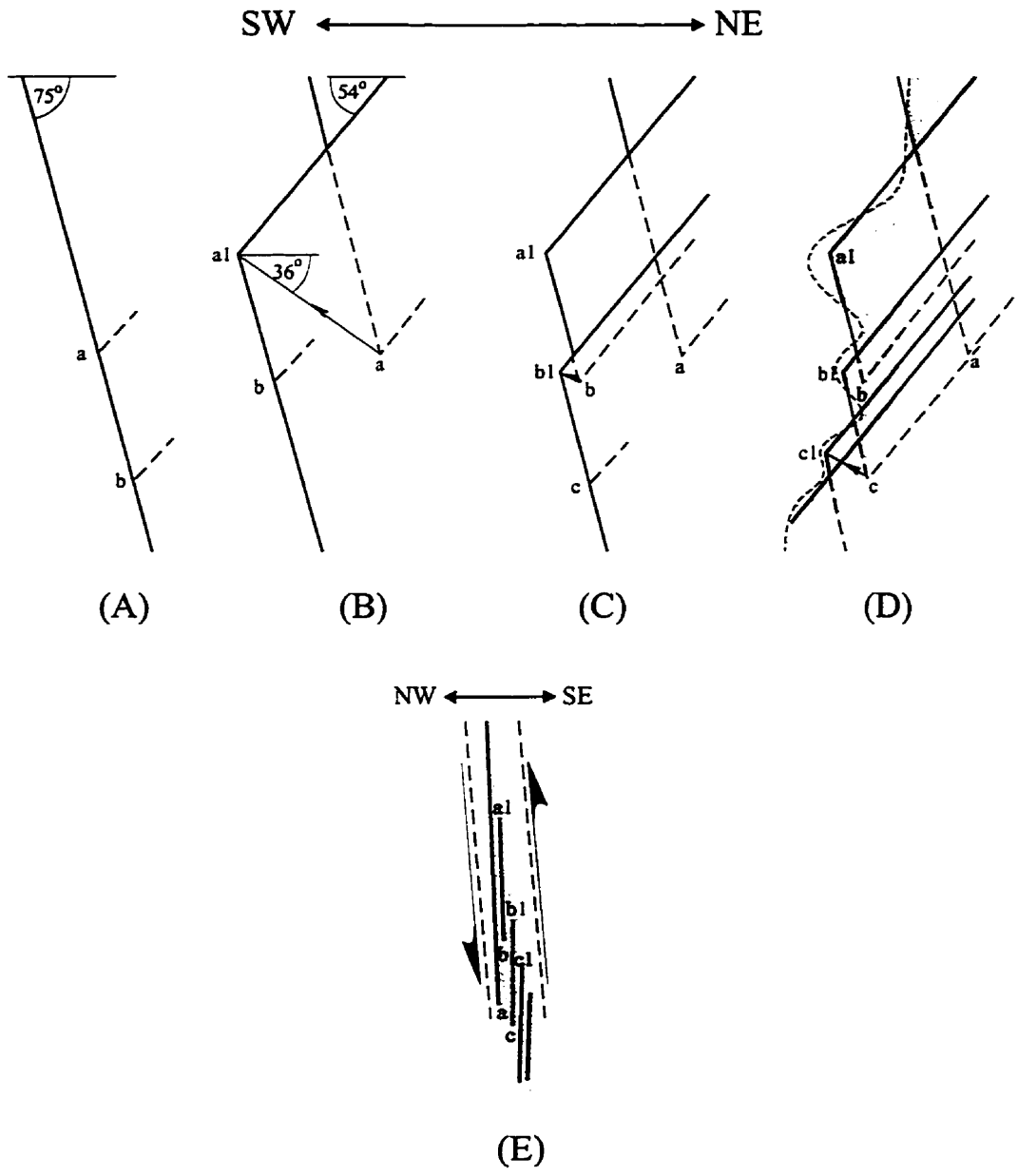

Figure 3-39. Diagrams illustrate how the shape and orientation of the Rod Main orebody in longitudinal section may be obtained by the D_{3b} oblique-slip shearing of an original orebody pitching to NE at 75° (modified from Roberts, 1993). (A) The southwest edge of the orebody pitching 75° to the northeast in the plane of the D_{3a} dip-slip shear. (B) - (D) The orebody is deformed by thrust shears acting along a shear vector that pitches at 36° to northeast. The locations at which the orebody is faulted, a, b, c, etc., and their displacements to a1, b1, c1, etc., are chosen to reproduce the present shape and orientation of the orebody. (E) The anticipated relationship of the segments of the deformed orebody, on a section perpendicular to the intersection lineation formed by the thrust shears and the shear fabric; the oblique angle of the thrust shears to the shear zone walls is based on the field data illustrated in Figure 3-19.

the oreshoot (Figure 3-39). During the D_{3b} deformation, the D_{3a} fabric and veins may initially behave as active layers, forming folds with the axes perpendicular to the shear vector (Figure 3-18A and B). However, as the deformation proceeded, and the D_{3b} shear fabric developed and overprinted the system completely, the D_{3a} fabric and veins became passive folded layers. As a result, the D_{3b} shearing changed the shape of the oreshoot, and caused it to plunge perpendicular to the D_{3b} shear vector (Figure 3-39D).

In the Jasper deposit, the slip vector of the D_{3b} transcurrent shearing plunges 27° to the southwest, approximately perpendicular to the dip-slip direction or the long axes of the ore shoots. The D_{3b} shear fabric in the Jasper shear system was less penetrative than in the Jolu shear system, and the D_{3a} fabric and associated veins behaved as active layers, forming isolated folds with the fold axes perpendicular to the D_{3b} shear vector (see Figure 3-12A). Consequently, the overall shape and orientation of the oreshoots is not substantially changed by the D_{3b} deformation.

Conclusions

The Star Lake-McLennan Lake area was deformed under conditions of transpression, which involved northwest-southeast compression with subvertical extension, coeval with dextral transcurrent movement parallel to the southeastern boundary of the Central Metavolcanic Belt, during and following the terminal continent-continent collision of the Trans-Hudson Orogen.

The transpression is manifested in the fabrics as three phases of deformation (D_1 to D_3). The gold-bearing shears were comparatively late structures in the transpressive regime, and developed during an episode of dip-slip shearing of the D_{3a} deformation. The D_{3a} shears probably nucleated in the northeast-striking D_2 structures under conditions of elevated fluid pressure.

The auriferous quartz veins were emplaced into the D_{3a} structures during the dip-slip shearing. The veins and dip-slip fabrics were subsequently deformed by transcurrent and (at the Jolu Mine) oblique-slip shearing of the D_{3b} deformation. The

D_{3b} deformation probably controlled the final shape and orientation of orebodies.

The interpretation of the McLennan Lake Tectonic Zone as a thrust fault is not supported by this study. The MLTZ is probably not a transcrustal-scale structures, but a shear zone initiated from limb sliding shear associated with a regional syncline cored by the McLennan Group meta-arkoses.

The gold-bearing shears are not subsidiary structures of the McLennan Lake Tectonic Zone nor the David Lake Shear. The shears may be stretching structures, the development of which probably involved synchronous deformation of the wall rocks.

CHAPTER 4

METAMORPHISM, METASOMATISM AND WALL-ROCK ALTERATION

Introduction

In this chapter the P-T conditions for each phase of deformation are defined using mineral assemblages and mineral chemistry. From this, constraints can be placed on the conditions under which gold mineralization took place. The geochemistry of wall-rock alteration is also described in an attempt to characterize the alteration associated with both barren and auriferous fluids.

Petrography and Mineral Geochemistry

Detailed petrography of 197 samples which cover the MLTZ and the D_1 to D_3 structures is summarized in Table 4-1. Veins associated with the structures in the plutonic rocks are also described. Microprobe analyses of major mineral phases (including amphibole, plagioclase, biotite, and garnet) were determined by wavelength-dispersive electron microscopy using a fully automated JEOL JXA-8600 X-ray microanalyser in the Department of Geological Sciences, University of Saskatchewan. Data are presented in Tables A-1 through A-4 of Appendix A. Statistical error at the 95% confidence level is ±1% for major elements and ±10% for minor elements.

D_1 Deformation

Metavolcanic Rocks

Metamorphic assemblages from mafic and intermediate metavolcanic rocks consist principally of calcic amphibole, plagioclase and biotite in varying proportions, with minor quartz, potassium feldspar, and accessory epidote, sphene, apatite, chlorite

Table 4-1. Mineral assemblages associated with D_1 to D_3 deformations

Lithology	MLTZ	D_1 Regional penetrative fabric	D_2 Shears and cataclastic zones	D_3 Gold-bearing shears	
				D_{3a} shearing	D_{3b} shearing
Pelitic rocks		Plag, Bt, Qtz, Musc, Kspar, Ep, Chl, ±Hbl, ±Gt			
Meta-arkoses	Kspar, Qtz, Musc, Plag, ±Bt, ±Sil	Kspar, Qtz, Musc, Plag, ±Bt, ±Sil	Kspar, Qtz, Musc, Plag, ±Bt		
Mafic-intermediate metavolcanics	Hbl, Plag, Bt, Kspar, Qtz, ±Ep, ±Sph, ±Ilm	Hbl, Plag, Bt, Kspar, Qtz, ±Ep, ±Sph, ±Ilm, ±Diop	Plag, Bt, Kspar, Ep, Qtz, Hbl, ±Chl, ±Cc, ±Mt		
Diorite / Porphyric diorite / Granodiorite	Plag, Hbl, Bt, Qtz, Kspar, ±Ep, ±Sph, ±Py, ±Mt, ±Cc	Plag, Hbl, Bt, Qtz, Kspar, ±Ep, ±Sph, ±Ilm, ±Mt, ±Diop	Plag, Bt, Hbl, Kspar, Qtz, Ep, ±Cc, ±Chl, ±Sph, ±Mt	Bt, Plag, Kspar, Qtz, Hbl, ±Cc, ±Sph, ±Ep, ±Mt, ±Chl	Bt, Plag, Kspar, Qtz, Hbl, Ep, Cc, ±Sph, ±Chl, ±Mt
Granite		Plag, Kspar, Qtz, Bt, Hbl, ±Musc, ±Ep, ±Mt	Plag, Kspar, Bt, Qtz, Musc, ±Cc, ±Ep	Plag, Kspar, Musc, Bt, ±Ep, ±Cc, ±Hbl	Plag, Kspar, Qtz, Musc, Ep, Cc, ±Bt

Abbreviations: Bt, biotite; Cc, calcite; Chl, chlorite; Cd, cordierite; Diop, diopside; Ep, epidote; Fspar, feldspar; Gt, garnet; Hbl, hornblende; Ilm, ilmenite; Kspar, potassium feldspar; Mt, magnetite; Musc, muscovite; Plag, plagioclase; Py, pyrite; Qtz, quartz; Sil, sillimanite; Sph, sphene.

and ilmenite.

Metamorphic amphiboles usually have a bimodal distribution of grain sizes. They occur both as coarse grained porphyroblasts and as a fine grained phase in the groundmass (Figure 4-1). The porphyroblasts, up to 4 mm long, are idioblastic or subidioblastic and occur in the form of augen aggregates 5 to 7 mm across. Some metamorphic amphiboles pseudomorph primary pyroxenes. The porphyroblasts are optically uniform, and show limited replacement by fine grained biotite and/or chlorite, forming fibrous rims around the porphyroblasts. Amphiboles in the matrix are subidioblasts to xenoblasts, less than 0.5 mm long, and show well-defined preferred orientation. The dimensional shape of amphiboles generally parallels the compositional layering and defines the S_1-L_1 fabric. Even in weakly foliated rocks, the preferred crystallographic orientation of amphiboles defines a strong subvertical linear fabric (Figure 4-2). The observations indicate that the main period of amphibole growth was coeval with the D_1 deformation. In addition to the fabric-defining grains, amphiboles also occur as large and randomly oriented idioblasts in some of mafic metavolcanic rocks, overprinting the S_1-L_1 fabric. The occurrence of the idioblasts indicates an episode of amphibole overgrowth which postdates the D_1 deformation.

Amphiboles that define S_1-L_1 fabric in the mafic metavolcanic rocks include magnesio-hornblende and ferro-hornblende (Table A-1). The hornblendic amphiboles are either uniform or zoned. The zoning pattern is core-to-rim increase of Na/(Ca + Na) and Al/(Si + Al) (Figure 4-3). The most pronounced variation is recorded in sample 457, where a magnesio-hornblende core is overgrown by a ferro-hornblende rim. This is typical of prograde (i.e. increasing temperature) amphiboles (Holland and Richardson, 1979; Laird and Albee, 1981). Zonation is difficult to ascertain in the matrix amphiboles because of the fine grain size.

Plagioclase in the metavolcanic rocks occurs as fine grained, granoblastic-polygonal crystals. It typically makes up the groundmass and occurs interstitially to fine grained amphiboles and biotite. Electron microprobe analyses of plagioclase in the mafic metavolcanic rocks yield compositions of An_{34} to An_{41} (Table A-2). Igneous phenocrysts of plagioclase are preserved in weakly foliated feldspar-phyric metavolcanic rocks and make up as much as 20% of the rocks. The phenocrysts are

Figure 4-1. Bimodal grain size of D_1 amphibole in moderately foliated mafic metavolcanic rock (plane light; bar = 4 mm).

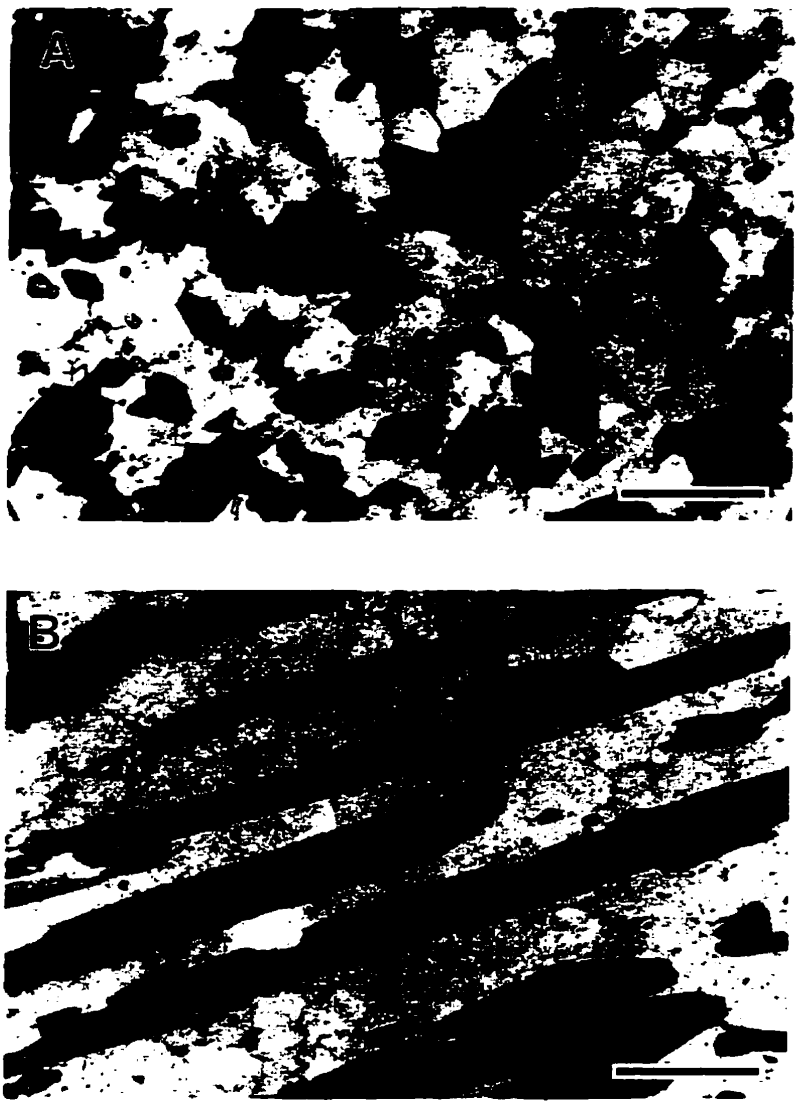

Figure 4-2. D_1 amphiboles in weakly foliated mafic metavolcanic rock (plane light; bar = 0.2 mm). (A) amphiboles in the forms of pseudohexagons or rhombs, or short prisms in the section perpendicular to the lineation; (B) long prismatic amphiboles with dimensional ratios up to 10:1 in the section parallel to the lineation and perpendicular to the foliation.

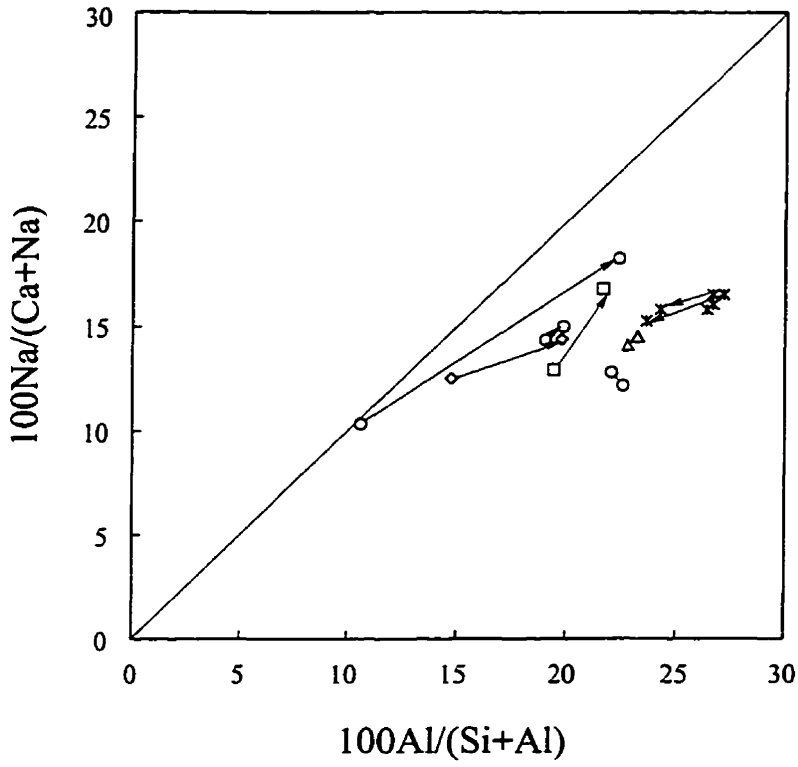

Figure 4-3. Zoning patterns of D_1 amphiboles. Amphibole core and rim compositions are joined by solid lines with arrows indicating the core-to-rim trend in composition. Circles, mafic volcanic rocks; stars, pelitic rocks; squares, granodiorite; diamonds, porphyritic diorite; triangles, diorite.

euhedral to subhedral, up to 6 mm. All the phenocrysts have been subjected to moderate to strong alteration to epidote, sericite and carbonate. The altered areas are concentrated in the cores of the phenocrysts, sometimes surrounded by virtually unaltered rims.

Biotite is absent from some mafic metavolcanic rocks, and is most abundant in intermediate to felsic metavolcanic rocks. It occurs in the groundmass as individual fine grained crystals in the form of long slender subidioblasts, intergrown with fine grained amphiboles, or as aggregates replacing amphibole porphyroblasts. The matrix biotite has a monomodal size distribution, and is unzoned and homogeneous. The Mg/(Mg + Fe) ratios in biotite range from 0.42 to 0.54 (Table A-3). The flakes of biotite typically show a marked crystallographic preferred orientation, defining the S_1-L_1 fabric. Biotite probably has a continuous, syn- to post-amphibole growth history in the metavolcanic rocks.

Pelitic Rocks

Pelitic assemblages consist mainly of plagioclase, biotite and quartz, with minor muscovite and potassium feldspar. Accessory minerals include epidote, sphene, chlorite, and carbonate. Amphibole and garnet occur as porphyroblasts in some pelitic rocks. Pelitic rocks, interlayered with metavolcanic rocks, southwest of the Jolu Mine, contain the metamorphic assemblage of garnet + amphibole + plagioclase + biotite + quartz ± muscovite ± chlorite. This assemblage was used in this study to determine the pressure-temperature conditions of metamorphism in the D_1 deformation.

Biotite and muscovite are present as fine grained, thin tabular crystals with a marked preferred alignment, defining the S_1-L_1 fabric in the pelitic rocks. The biotite flakes are unzoned, homogeneous and moderately magnesian (Table A-3).

Plagioclase and quartz occur as fine granoblastic-polygonal grains and make up most of the matrix of the rocks. In the three units of pelitic rocks analyzed, plagioclase is unzoned and has relatively narrow range of composition (An_{37} and An_{41}) (Table A-2).

Amphibole porphyroblasts range from idioblastic to xenoblastic. They are distributed sporadically in the rocks or form amphibole-rich microlayers that are conformable with the S_1 foliation, with individual grains subparallel to the foliation. Amphiboles in the pelitic rocks are tschermakite (Table A-1) and are optically homogeneous. However, the electron microprobe analyses reveal that they are weakly zoned, with the ratios of Na/(Ca + Na) and Al/(Si + Al) decreasing from core to rim (Figure 4-3).

Garnet porphyroblasts are idioblastic to subidioblastic, one to two millimetres in grain size. They contain irregular, fine grained felsic inclusion trails, some of which tend to be parallel to the S_1 foliation. Biotite flakes wrap around garnet and are incorporated into the foliation. Garnet is rich in almandine, with the mole fraction of Fe (X_{Fe}) in a narrow range of 0.61 to 0.65 (Table A-4). Minor compositional variations occur between cores and rims. Weak core-to-rim increases in Mn and Ca correspond to decreases in Fe and Mg and a decrease in Mg/Fe ratio. This type of zoning is the reverse of typical prograde garnet growth (Tracy, 1982; Spear *et al.*, 1990). Both garnet and amphibole are interpreted to grow during the D_1 deformation. The compositional zonation of garnet and amphibole may suggest retrograde growth or that diffusive exchange took place in the rims under retrograde conditions.

Meta-Arkoses

The metamorphic assemblages in the meta-arkoses are comprised predominantly of potassium feldspar, quartz and muscovite with subordinate plagioclase and sillimanite and minor biotite. The micas are moderately to well aligned whereas feldspars and quartz form polyhedral grains. Sillimanite occurs mainly as nodule aggregates. The nodules usually have an ellipsoidal shape, conformable with the S_1 foliation. The long axes of the nodules are parallel to the L_1 lineation. Inside the nodules sillimanite tends to grow parallel or subparallel to the foliation. Randomly oriented grains were also observed. The sillimanite metacrysts are partially retrogressed to muscovite, with the latter usually incorporated into the foliation. The relationships of the nodules and individual grains of sillimanite to the S_1-L_1 fabric suggest that the main period of sillimanite growth was concurrent with progressive

development of the fabric, and the randomly aligned sillimanite completed its growth under relatively static conditions at the end of or after D_1 deformation.

Plutonic Rocks

The mineral assemblages in the Star Lake and Island Lake plutons consist mainly of plagioclase, amphibole, biotite, potassium feldspar and quartz in varying concentrations according to bulk rock compositions. In the dioritic rocks plagioclase and amphibole are the major phases, whereas potassium feldspar, quartz and biotite are dominant in the granitic rocks. Other minor minerals in the plutons include epidote, magnetite, ilmenite, sphene, apatite, and rare garnet.

Plagioclase occurs as large laths up to 10 mm long and as fine grained, granoblastic, polygonal grains. The plagioclase laths are subhedral to anhedral, and are randomly distributed. In foliated rocks they show milled and rounded corners, undulose extinction and microfractures, and tend to be aligned to the foliation. The cores of the laths are moderately to extensively altered to epidote, sericite and carbonate, while the rims show little or no alteration. This alteration pattern suggests a more calcic composition of the cores relative to the rims. The plagioclase laths are interpreted to be relicts of phenocrysts based on the inferred difference in core-rim compositions and the cumulate texture that was observed in some dioritic and gabbroic rocks. The fine grained plagioclase is andesine, ranging from An_{43} in the diorite to An_{30} in the granodiorite (Table A-2). Potassium feldspar occurs as small subhedral to anhedral grains, with subordinate development of large crystals. It tends to form granoblastic mosaics along with equidimensional quartz, interstitial to larger plagioclase laths, and shows little alteration.

Amphiboles in relatively undeformed rocks occur mainly as large porphyroblasts but also form aggregates of subidioblasts. Subhedral to euhedral pyroxenes in diorite are generally pseudomorphed by aggregates of amphiboles. In the foliated rocks, amphiboles, along with biotite, define the foliation and lineation by forming aggregates with an elongation and preferred alignment. Randomly oriented amphibole porphyroblasts develop locally and overprint the foliation, suggesting a post-tectonic overgrowth. Coarse grained amphiboles are invariably retrogressed in

part to biotite or biotite and chlorite. In granodiorite and phorphyritic diorite, amphiboles are of magnesio- or ferro-hornblendic composition, and display prograde growth by having higher ratios of Al/(Si + Al) and Na/(Ca + Na) in the rims than in the cores. In diorite, amphiboles are tschermakite or ferro-tschermakite, with no substantial zoning in the grains (Figure 4-3, Table A-1).

Biotite in diorite occurs primarily as the retrogressive product of amphiboles. In granodiorite and granite, biotite is the major mafic mineral, and occurs as fine flakes which vary from random orientation to having a preferred crystallographic alignment. In some cases it is retrogressed to patches of muscovite or sericite. The ratio of Mg/(Fe + Mg) in biotite varies with the bulk rock composition, with averages of 0.41 in diorite, 0.47 in granodiorite and 0.53 in porphyritic diorite (Table A-3).

Epidote occurs as euhedral to subhedral grains in association with biotite aggregates, or as a fine grained alteration product of plagioclase. Magnetite and ilmenite are most abundant in the least deformed and altered plutonic rocks. The grains are small (< 0.2 mm) and are commonly intergrown with one another as aggregates of separate grains. Ilmenite also occurs as fine inclusions in amphibole porphyroblasts. Sphene is fine grained and euhedral, typically present with epidote as an alteration product of plagioclase.

The mineralogy of veins associated with the S_1 foliation in the plutonic rocks includes quartz + potassium feldspar + biotite ± albite, and is devoid of sulphide minerals. Quartz is the most abundant phase, and is transparent to translucent. It forms a mosaic of interlocking grains showing variable degrees of strain in the form of undulose extinction and serrated grain boundaries. Potassium feldspar makes up to 10 percent of the veins. Biotite forms a minor phase, disseminated in the veins. Some of the quartz veins have a selvage of amphibole and biotite several millimetres thick. The term selvage is used here to denote the mineral assemblages in the veins at the immediate contact between the veins and wall rocks.

McLennan Lake Tectonic Zone

The foliated metavolcanic rocks in the MLTZ are mineralogically similar to their regional equivalents (Table 4-1), however, the minerals (mainly amphibole and biotite) display a strongly preferred crystallographic orientation. No relict pyroxenes are preserved in the mafic metavolcanic rocks, suggesting a complete replacement of pyroxenes by amphiboles. Two generations of amphiboles were recognized. The earlier D_1 amphiboles are magnesio-hornblende, ferro-pargasite and pargasite (Table A-1), and are coeval with the development of the S-L fabric. Compositional zoning of amphiboles is weak or absent (Figure 4-4). The later generation of amphiboles occurs in association with the D_{3b} Z-shaped asymmetric folds, crosscutting the folded foliation (Figure 4-5). The later D_{3b} amphiboles (sample 824-1b) occur as fine grained idioblasts and have a similar composition to the earlier amphiboles (sample 824-1a) that defines the folded foliation. Plagioclase coexisting with the amphiboles has restricted compositions (An_{40} and An_{42}) (Table A-2), whereas biotite shows a range of Mg/(Mg + Fe) ratios from 0.35 to 0.55 (Table A-3).

The meta-arkoses in the MLTZ have undergone moderate to strong recrystallization. Quartz and feldspars commonly form fine grained, polyhedral grains with triple-grain junctions meeting at 100° to 120° angles. Sillimanite occurs mainly as fine crystals and less commonly as small elongated lenses of sillimanite-muscovite aggregates. In both cases sillimanite exhibits a syn-tectonic growth by being aligned parallel to the foliation.

The MLTZ transects the southeastern margin of the Island Lake pluton between Cratty Lake and Scriver Lake. The granodiorite is highly deformed, and is composed of plagioclase, amphibole, quartz, biotite, potassium feldspar, and trace epidote, magnetite and sphene. Compared with the less undeformed precursor, both plagioclase and potassium feldspar have been reduced in grain size, with concomitant occurrence of fine grained white micas. Plagioclase is of andesine composition (An_{30} to An_{34}) (Table A-2). Amphiboles (ferro-pargasite and pargasite, Table A-1) are unzoned and have a smaller grain size than the counterparts in the less undeformed rock. Biotite occurs as individual flakes or as an alteration phase of amphiboles. It is moderately magnesian, with Mg/(Mg + Fe) ratios of 0.48 to 0.50 (Table A-3).

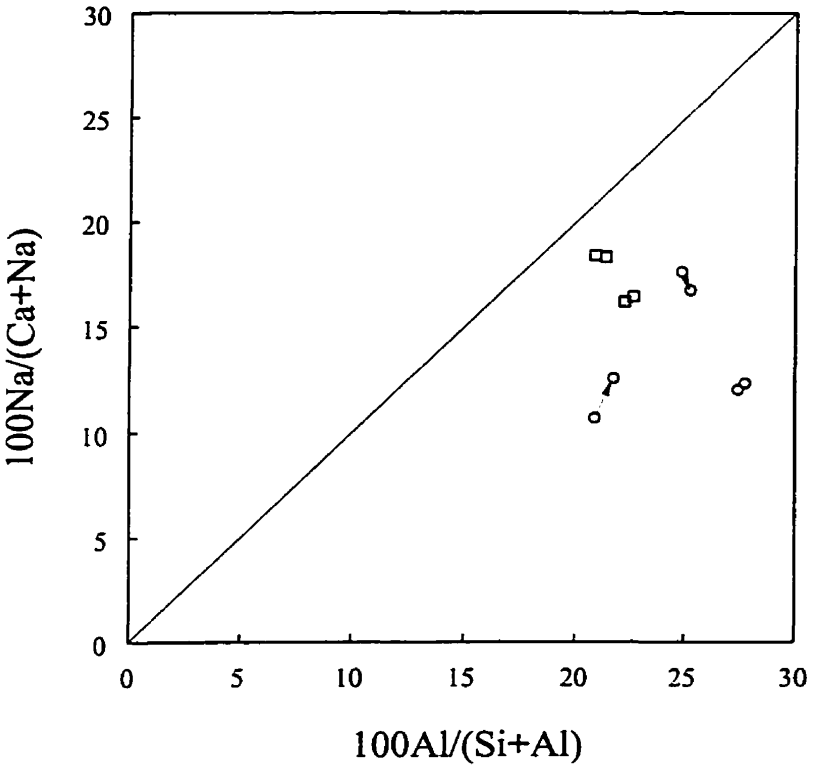

Figure 4-4. Zoning patterns of D_1 amphiboles in the MLTZ. Amphibole core and rim compositions are joined by solid lines with arrows indicating the core-to-rim trend in composition. Circles, mafic metavolcanic rocks; squares, granodiorite.

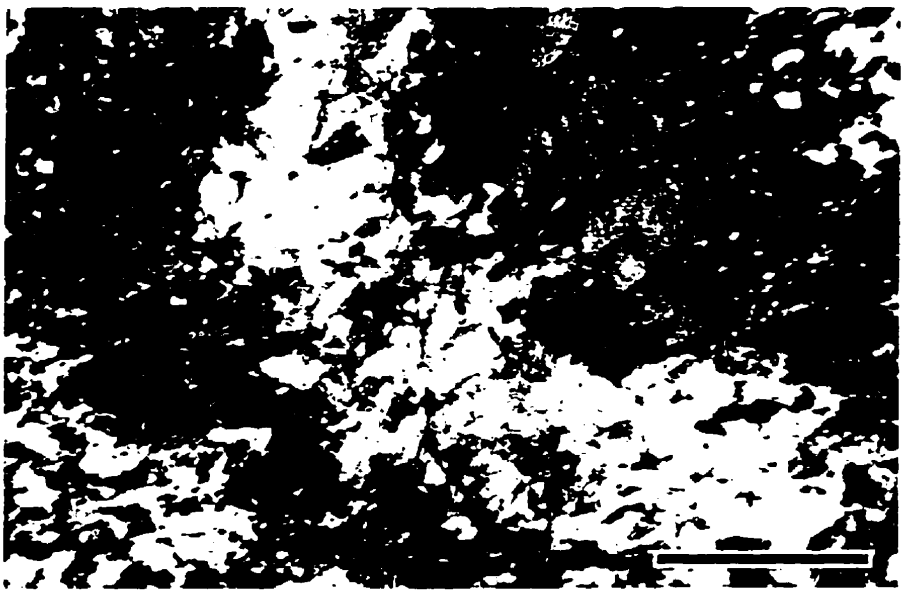

Figure 4-5. Photomicrograph of D_{3b} amphiboles growing in the hinge area of a Z-shaped asymmetric fold in the MLTZ and crosscutting the folded foliation and compositional layering defined by plagioclase- and amphibole-rich layers (plane light; bar = 0.5 mm).

Veins conformable with the S-L fabric of the MLTZ are variously deformed, either boudinaged or folded. Quartz is the principal phase of the veins, forming more than 90% of the total volume. It is translucent to transparent. Interlocking grains of quartz exhibit undulose extinction, serrated grain boundaries and subgrain development. Other phases in the veins include potassium feldspar, biotite, minor tourmaline. Potassium feldspar locally form nodule-shaped aggregates up to several centimetres long, in which potassium feldspar is brecciated with quartz, biotite and tourmaline filling the fractures.

D_2 Deformation

Minerals associated with the D_2 structures are summarized in Table 4-1. Compared with the host rocks, mineral assemblages in the D_2 structures involve a decrease of amphibole and increases of biotite and epidote. Textural evidence indicates that the formation of the assemblages was coeval with the development of the structures. This is best illustrated by a representative shear in a unit of mafic metavolcanic rock (Figure 4-6). The host rock is composed of D_1 subhedral to anhedral amphibole porphyroblasts, fine grained plagioclase and minor biotite and quartz (Figure 4-6A). Biotite occurs as the fine-grained alteration product along the margins of some of the porphyroblasts.

Towards the margin of the shear, where the mafic rock is moderately deformed, the D_1 amphiboles are strained and elongated into grains with larger aspect ratios than their equivalents in the host rock (Figure 4-6B). Recrystallization of the deformed porphyroblasts produces fine subgrains of amphiboles, which are partially altered to biotite and epidote. A later generation of amphiboles is superimposed on the amphibole subgrains and their alteration products. Within the shear, the original fabric is completely obliterated. D_2 amphiboles form as long prismatic porphyroblasts with a strong preferred orientation, defining the shear foliation (Figure 4-6C).

Similar changes in mineralogy were observed in the D_2 cataclastic zones (see Figure 3-8). The minerals in the wall rock, mainly plagioclase, amphibole, potassium feldspar, quartz and biotite, are reduced in grain size by cataclastic deformation,

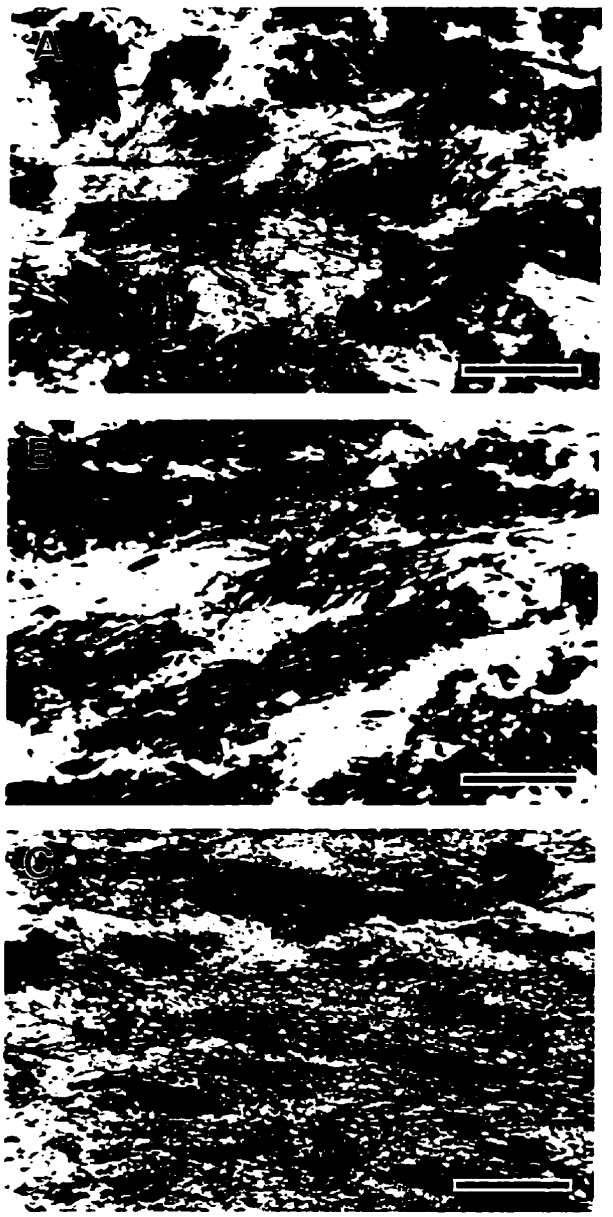

Figure 4-6. Progressive syn-kinematic metamorphism and fabric development in a D_2 shear hosted by mafic metavolcanic rock southwest of the Jolu Mine (plane light; bar = 0.5 mm). (A) weakly deformed host wall rock; (B) moderately deformed rock at the margin of the shear; (C) strongly deformed rock within the shear.

accompanied by partial to total replacement of amphiboles by biotite. Feldspars are milled and rounded. The deformed grains of feldspars show undulatory extinction and are partially recrystallized to small polygonal strain-free grains with approximate 120° triple junctions. Fine biotite flakes tend to wrap around the rounded feldspar grains, forming a short-range foliation. Amphiboles occur as a remnant of deformed porphyroblasts and make up a minor phase in the cataclastic zones.

Amphiboles formed in the D_2 structures include ferro-pargasite, ferro-tschermakite, magnesio-hornblende and ferro-hornblende (Table A-1). The bulk compositions of the host rocks appear to have an influence on the mineral chemistry of amphiboles. The amphiboles in these structures are slightly to moderately zoned, showing both core-to-rim increase and decrease in Al/(Si + Al) and Na/(Ca + Na) ratios (Figure 4-7).

Compared with D_1 amphiboles in the host rocks, D_2 amphiboles define an overall decreasing trend in the contents of Al^{IV} and $Al^{VI} + Fe^{3+} + Ti + Cr$, and in the ratios of Na/(Ca + Na) and Al/(Si + Al) (Figure 4-8). An exception was observed in the shear hosted in the mafic metavolcanic rock, where D_2 amphiboles are enriched in Al^{IV} and $Al^{VI} + Fe^{3+} + Ti + Cr$, and have higher ratios of Na/(Ca + Na) and Al/(Si + Al) than D_1 amphiboles in the host rock.

Matrix plagioclase in the D_2 structures is oligoclase-andesine (An_{28} to An_{38}) (Table A-2). Compared to plagioclase in the host rocks, plagioclase in the D_2 structures generally contains less anorthite (Figure 4-9). However, a slight increase in anorthite content is recorded in the mafic metavolcanic-hosted shear.

Biotite in the D_2 structures occurs as fine flakes. It is moderately magnesian with Mg/(Fe + Mg) ranging from 0.39 in a diorite hosted cataclastic zone to 0.56 in a porphyritic diorite hosted shear (Table A-3). Formula proportions of Al^{IV}, Al^{VI} and Ti are shown in Figure 4-10, with reference to those from the host rocks. Biotite becomes slightly to moderately enriched in Ti. Al^{IV} and Al^{VI} are either enriched or depleted, showing no systematic composition variation.

Veins in the D_2 structures occur only as lenses typically up to three centimetres

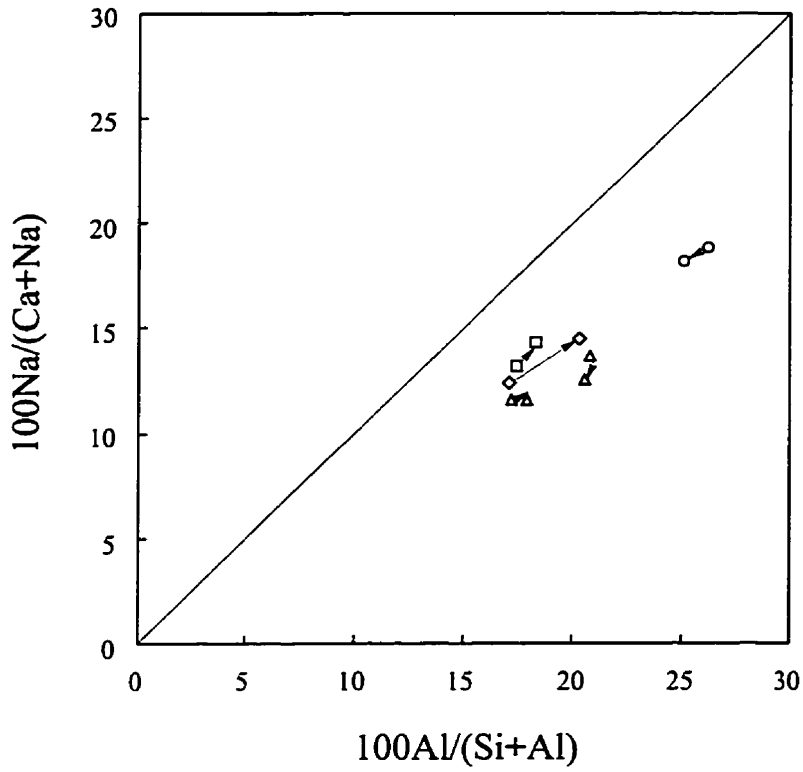

Figure 4-7. Zoning patterns of amphiboles in the D_2 structures. Amphibole core and rim compositions are joined by solid lines with arrows indicating the core-to-rim trend in composition. Circles, shear in mafic metavolcanic rock; squares, shear in granodiorite; diamonds, the Mallard Lake Shear in porphyritic diorite; triangles, cataclastic zone in diorite.

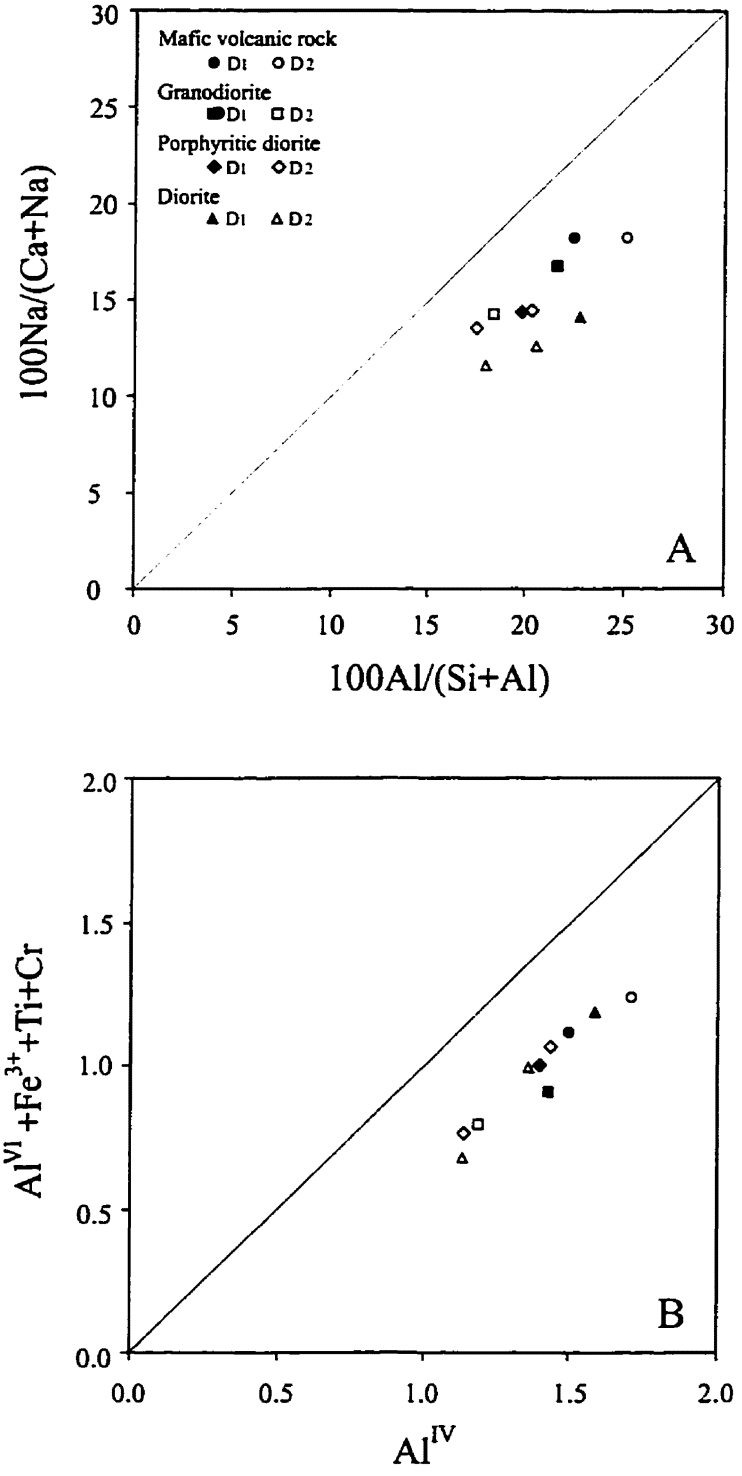

Figure 4-8. Variation in the composition of D_2 amphiboles with respect to D_1 amphiboles. (A) 100Al/(Si + Al) *vs*. 100Na/(Ca + Na); (B) Al^{IV} *vs*. $Al^{VI} + Fe^{3+} + Ti + Cr$. Only rim composition is plotted.

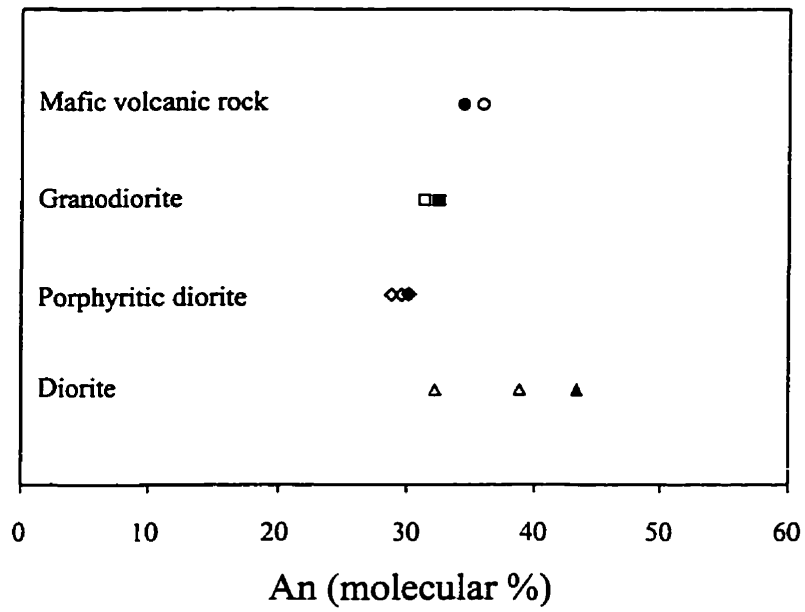

Figure 4-9. Variation in the composition of plagioclase in D_2 structures with respect to plagioclase in the host rocks.

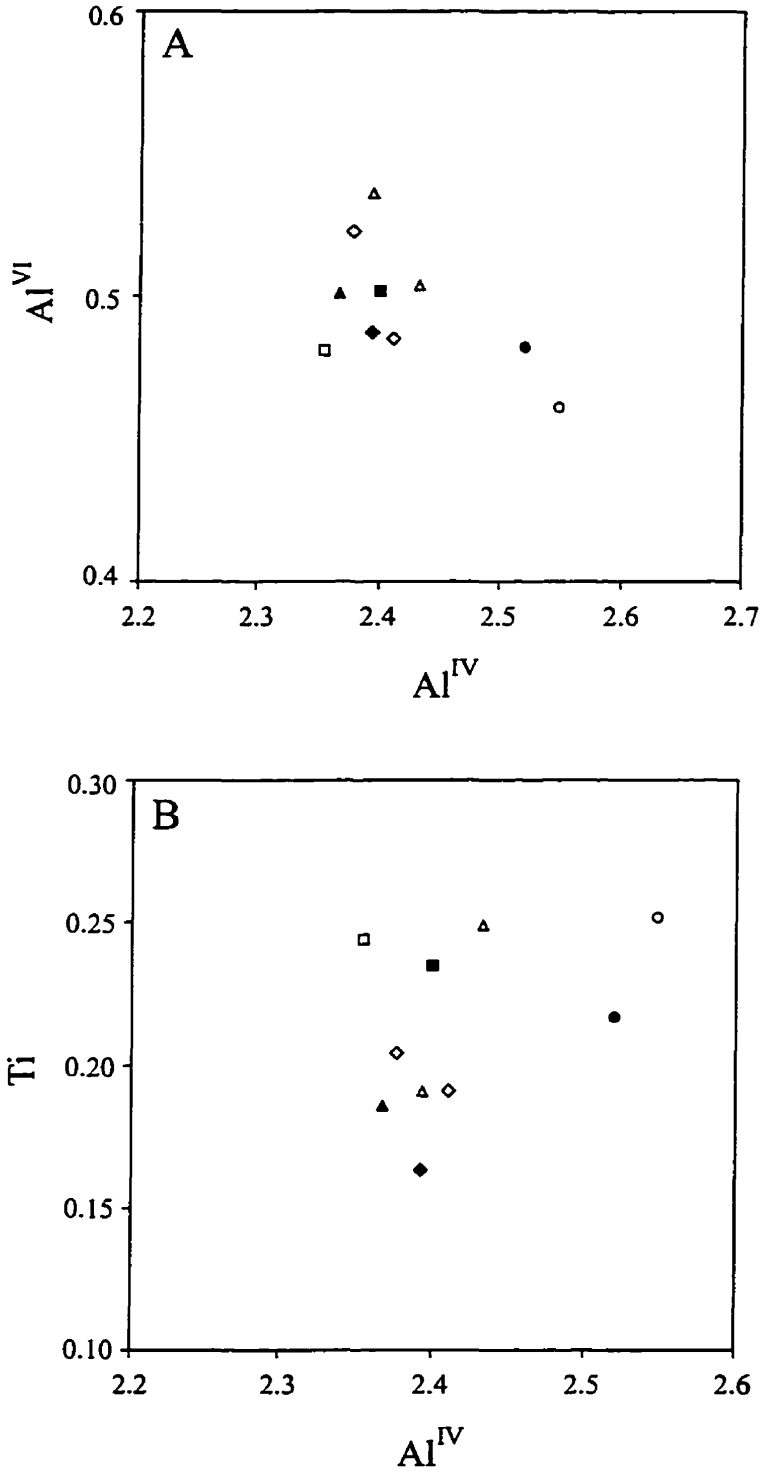

Figure 4-10. Variations in the composition of biotite in D_2 structures with respect to biotite in the host rocks. (A) Al^{IV} *vs.* Al^{VI}; (B) Al^{IV} *vs.* Ti. Symbols are as in Figure 4-8.

thick and twenty centimetres long, and consist mainly of quartz and potassium feldspar, with subordinate albite, biotite and tourmaline, and minor amphibole. Quartz comprises 75% to 100% of the vein material. It is variably deformed and shows undulose extinction, serrated grain boundaries and subgrain development. Locally, recrystallization of quartz forms polygonal grains free of strain. Potassium feldspar makes up 0% to 25% of the veins. Biotite and amphiboles occur principally in the vein selvages, and exhibit undulose extinction.

D_3 Deformation

Mineral assemblages associated with D_{3a} and D_{3b} episodes of deformation in the gold-bearing shears are shown in Table 4-1.

Rod Shear

The Rod shear which hosts the Rod Main orebody is developed at the contact of granodiorite with diorite and porphyritic diorite (see Figures 3-15 and 3-22). In the three types of host rocks to the Rod shear, the mineral assemblages are dominated by plagioclase, amphibole and biotite which make up to 80 to 90% of the rocks. Minor phases in the assemblages include potassium feldspar, epidote, quartz, calcite, magnetite, ilmenite, and sphene.

In the protomylonite where the fabric of D_{3a} dip-slip shearing is preserved, D_1 amphibole porphyroblasts are deformed into grains with larger aspect ratios. The deformed amphiboles tend to recrystallize to finer, strain-free grains, with secondary biotite along the margins or cleavages. The growth of amphiboles during D_{3a} shearing is evident in folded D_{3a} phyllonite, where vestiges of the original D_1 fabric are completely obliterated, and replaced with the D_{3a} fabric defined by subhedral to anhedral amphiboles and fine flakes of biotite (Figure 3-18C).

Amphiboles formed during D_{3b} shear deformation are anhedral, up to 2 mm. They define the axial planes of the D_{3b} folds or occur incorporated into the D_{3b} shear fabric within the phyllonite zone (Figure 4-11).

Amphiboles associated with D_{3a} and D_{3b} episodes of deformation are magnesio- and ferro-hornblende (Table A-1), and are zoned. In the deformed diorite and porphyritic diorite, the Al/(Si + Al) and Na/(Ca + Na) ratios increase from core to rim, whereas a reversal zoning pattern occurs in amphiboles from deformed granodiorite (Figure 4-12). Compared with D_1 amphiboles in the least deformed host rocks, D_{3a} and D_{3b} amphiboles contain less Al^{IV} and $Al^{VI} + Fe^{3+} + Ti + Cr$, and have lower ratios of Na/(Ca + Na) and Al/(Si + Al) (Figure 4-13).

Large plagioclase laths are milled and rounded, to attain a uniform grain size and shape. Concomitantly, they are replaced by fine-grained, euhedral epidote, and sericite. The replacement typically takes place from the cores of plagioclase. In the phyllonite, there is a complete destruction of the plagioclase laths, and plagioclase occurs only as fine-grained granoblastic-polygonal aggregates. Matrix plagioclase in the deformed rocks of the Rod shear is oligoclase (An_{23} to An_{30}) (Table A-2). It is depleted in anorthite content relative to the counterpart in its least deformed rocks (Figure 4-14). Potassium feldspar undergoes the same grain-size reduction as plagioclase, but shows only weak alteration.

Biotite occurs mainly as a replacement phase of amphiboles. It forms fine grained aggregates (0.05 ~ 0.3 mm) or large single flakes (>0.5 mm), both of which have strong crystallographic preferred orientation, defining the D_{3a} and D_{3b} fabrics. Compared with biotite in the least deformed rocks, biotite in the shear has a slight to moderate increase in Ti, but shows no systematic changes in Al^{IV} and Al^{VI} (Figure 4-15).

Chlorite occurs mainly in the dioritic segment of the Rod shear. It forms fine grained aggregates at the expense of amphiboles and biotite and is incorporated into the D_{3a} and D_{3b} shear fabrics. It shows no systematic modal variation across the Rod shear.

Calcite in the least deformed host rocks is fine grained, interstitial to biotite, amphiboles and feldspars. It increases slightly in protomylonite and phyllonite, where it also forms veinlets less than one mm thick, along the shear fabrics.

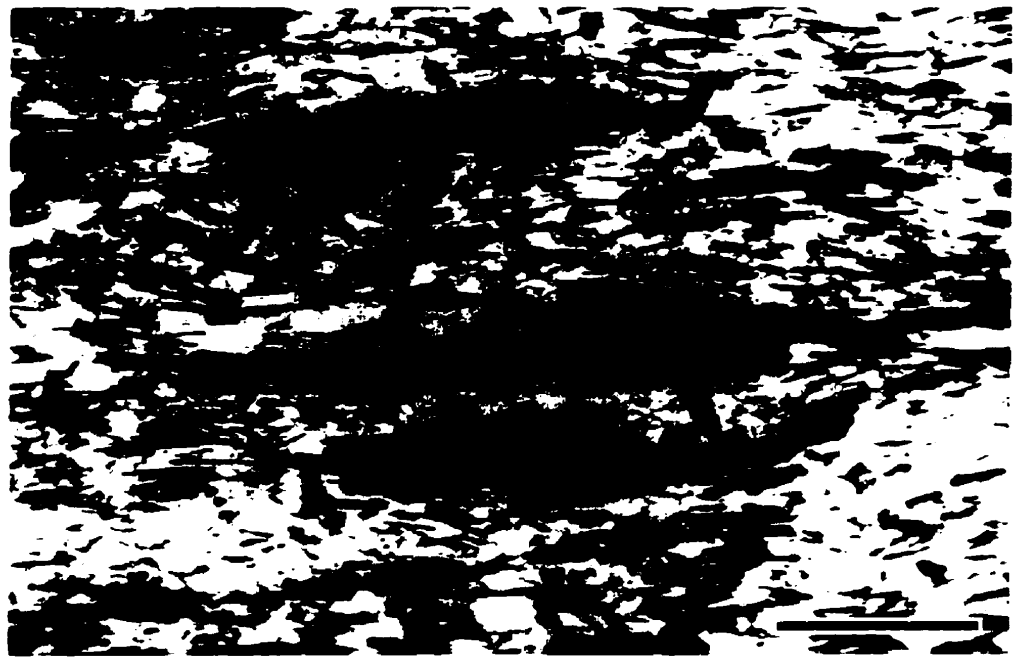

Figure 4-11. D_{3b} amphibole porphyroblasts in the central phyllonite zone of the Rod shear zone (plane light; bar = 0.5 mm).

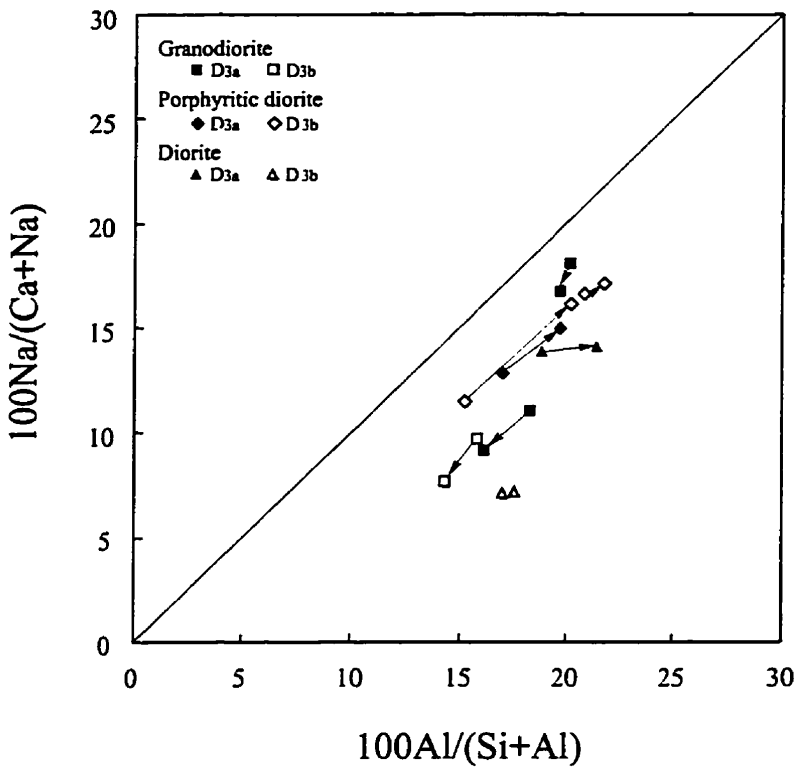

Figure 4-12. Zoning patterns of D_{3a} and D_{3b} amphiboles in the Rod shear zone. Amphibole core and rim compositions are joined by solid lines with arrows indicating the core-to-rim trend in composition.

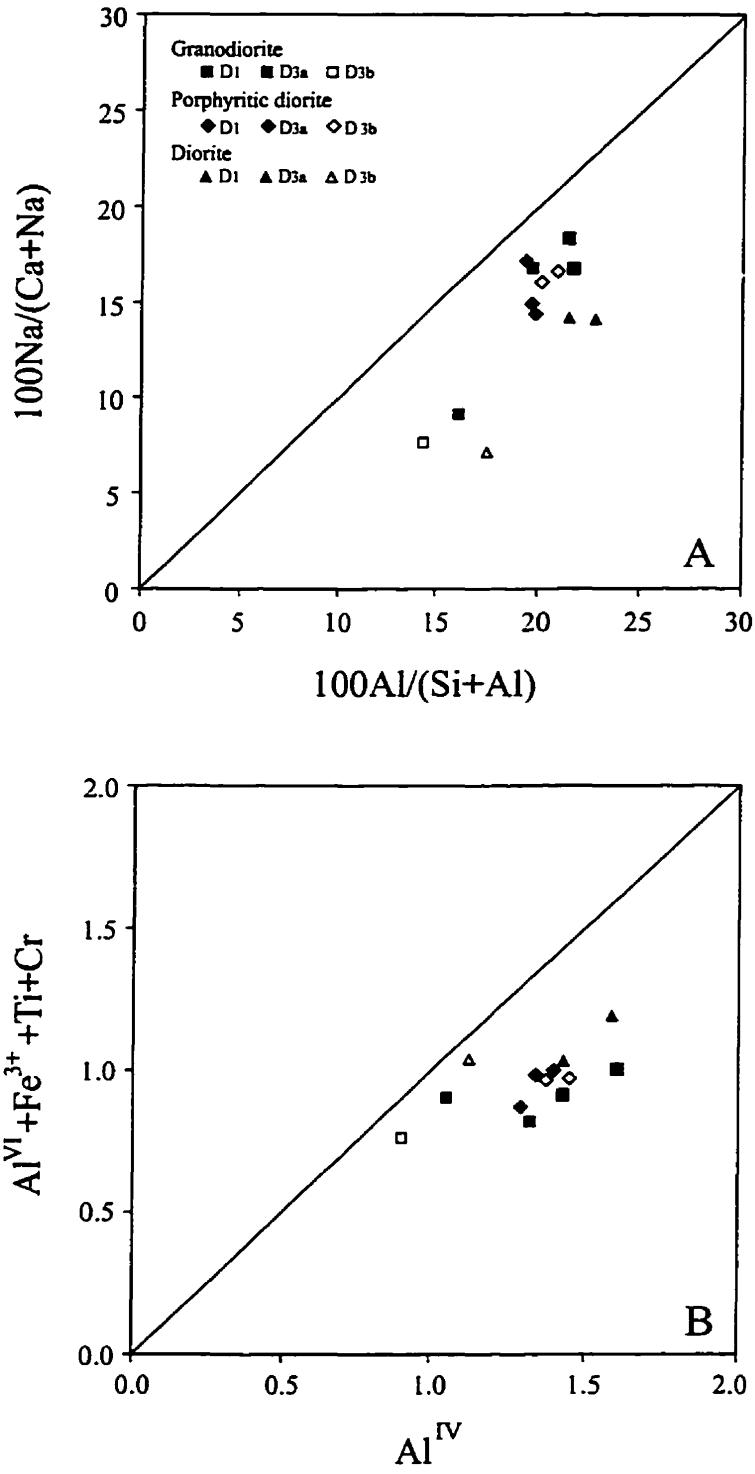

Figure 4-13. Variation in the composition of D_{3a} and D_{3b} amphiboles in the Rod shear with respect to D_1 amphiboles. (A) 100Al/(Si + Al) *vs.* 100Na/(Ca + Na); (B) Al^{IV} *vs.* $Al^{VI} + Fe^{3+} + Ti + Cr$. Only rim composition is plotted.

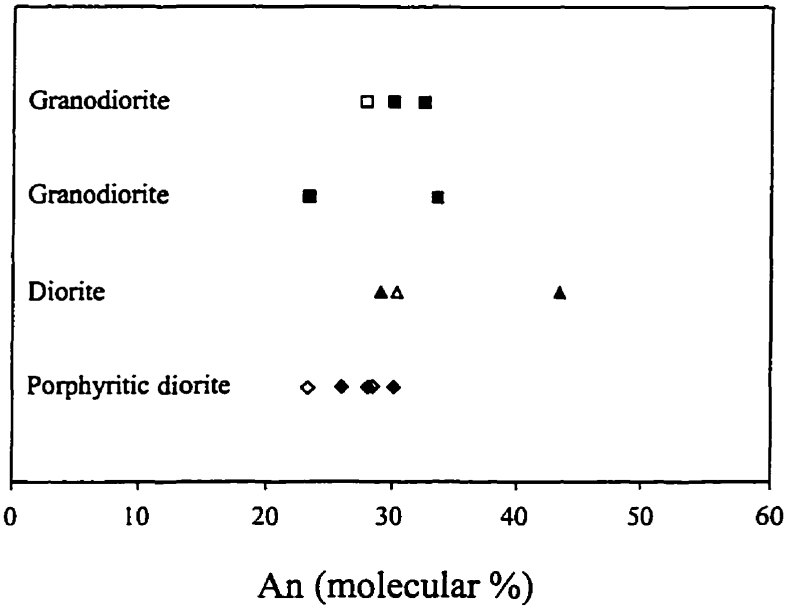

Figure 4-14. Variation in the composition of plagioclase in the D_3 Rod shear with respect to plagioclase in the host rocks.

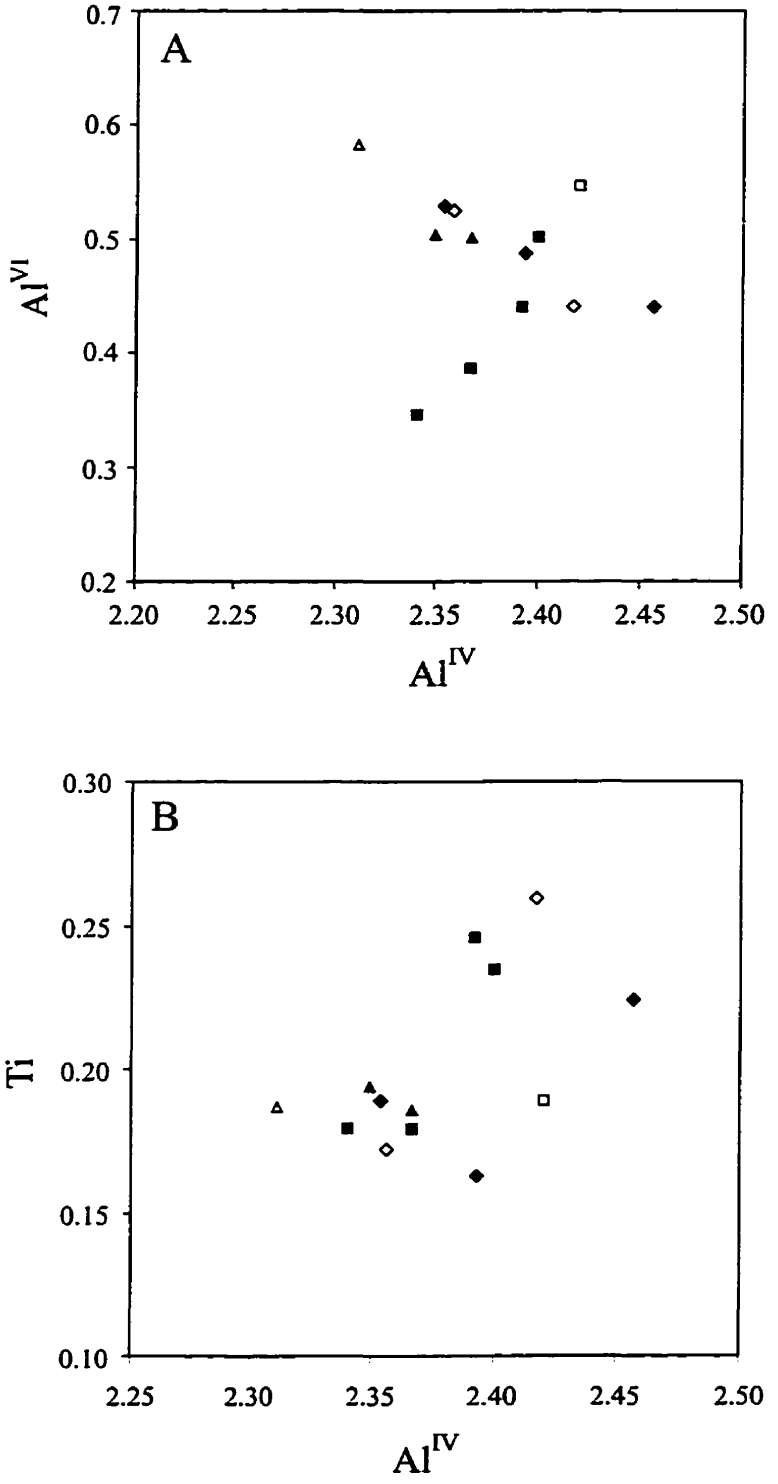

Figure 4-15. Variation in the composition of biotite in the Rod shear zone with respect to biotite in the host rocks. (A) Al^{IV} *vs.* Al^{VI}; (B) Al^{IV} *vs.* Ti. Symbols are as in Figure 4-13.

Epidote occurs as an alteration phase of plagioclase. It has no significant modal variation in the deformed diorite and granodiorite. In the deformed porphyritic diorite, epidote after plagioclase phenocrysts may account for as much as five modal percent of the rocks.

Gold-bearing veins in Rod shear consist of more than 90% quartz, intergrown with subordinate sulphide minerals, potassium feldspar, biotite, tourmaline, calcite, chlorite and albite. The sulphides are mainly pyrrhotite, pyrite, chalcopyrite, and trace molybdenite, and cobaltite (Burrill, 1987).

James-Jasper-Roxy Shears

The James-Jasper-Roxy shears are hosted in the granite of the Island Lake pluton. The least strained granite which borders the protomylonite consists of plagioclase, potassium feldspar, quartz, subordinate biotite and amphibole, and trace muscovite, epidote, magnetite, and apatite. With increasing strain towards the shears, the mineral assemblage exhibits systematic variations which involve modal increases in muscovite, potassium feldspar, quartz and calcite, and modal decreases of plagioclase and biotite, as well as complete destruction of amphiboles.

Both plagioclase and potassium feldspar are deformed and reduced in grain size. The breakdown of plagioclase is typically accompanied by appearance of muscovite. The relict plagioclase is recrystallized to form relatively-low strain, polygonal grains. The deformed grains of potassium feldspar generally show no sign of alteration but are instead replaced by aggregates of dynamically recrystallized polygonal grains.

Amphibole porphyroblasts are replaced by flakes of biotite. Most of the replacement is completed in the protomylonite and there are no amphiboles preserved in the mylonite. Both D_1 biotite and secondary biotite after amphiboles are altered to muscovite. The alteration is most pervasive in the mylonitized central parts of the shears, where the greatest strain of the D_{3b} strike-slip shearing is located. The flakes of muscovite always show evidence of strain in the form of undulose extinction.

Quartz in the deformed rocks shows abundant evidence of deformation in the form of undulose extinction, subgrain formation and dynamic recrystallization. The recovery process, in the form of quartz subgrains, is most prevalent in the mylonite.

The auriferous quartz veins contain approximately 70-80% chert-like quartz and 5-20% pyrite, with minor muscovite, tourmaline, biotite, chlorite, carbonate and albite. Other minerals include hematite, chalcopyrite, sphalerite, bornite, galena, gold, and trace Ag-Au tellurides, magnetite, pyrrhotite, molybdenite, scheelite, monazite, uraninite, and rutile (Hrdy and Kyser, 1995).

The deformed rocks of the north-south D_{3b} shears consist of muscovite, quartz, feldspars, epidote and trace biotite. The north-south veins are composed of irregular and ribbony quartz grains which show variable strain in the form of undulose extinction and serrated grain boundaries, and have less pervasive subgrain development than the auriferous quartz. The veins also contain minor muscovite, biotite and potassium feldspar.

Relative Timing of Deformation and Metamorphism

As described previously, the growth of minerals, notably amphiboles, was coincident with the structural development associated with the D_1 to D_3 deformations. Based on episodes of growth of amphiboles and their relationships with the deformations, three metamorphic events (M_1 to M_3) were defined in this region.

Early metamorphism M_1 was synchronous with the D_1 regional penetrative deformation and gave rise to syntectonic assemblages of hornblende + plagioclase ± biotite ± epidote in the metavolcanic and plutonic rocks, plagioclase + hornblende + garnet + biotite + quartz in the pelitic rocks as well as sillimanite + muscovite in the meta-arkoses. The deformed rocks in the MLTZ are mineralogically similar to their regional equivalents, suggesting that they underwent the same metamorphism as the regional rocks. The mineral assemblages indicate that the peak metamorphism of amphibolite facies was attained during the D_1 deformation.

M_2 metamorphism followed M_1 metamorphism and was concurrent with the development of the D_2 structures. M_{3a} episode of metamorphism was defined in association with the D_{3a} dip-slip shear deformation in the gold-bearing shears, and M_{3b} was coeval with D_{3b} dextral shear deformation in the gold-bearing shears and the MLTZ.

Post-M_1 amphiboles are not restricted to the D_2 and D_3 structures, they also occur as randomly oriented idioblasts in the metavolcanic and plutonic rocks, outside the D_2 and D_3 structures, overprinting the D_1 fabric.

Temperature and Pressure of M_1 Metamorphism

As described in Chapter 2, metamorphic grade changes from amphibolite facies across most of the study area to upper greenschist facies in the vicinity of Jojay Lake. In order to minimize the effect of spatial variation in metamorphic grade, P-T conditions for the deformations were determined from the D_1, D_2 and D_3 structures around the Jolu Mine.

Geothermobarometry

Pressure and temperature conditions of M_1 metamorphism were constrained on the basis of the mineral assemblage garnet + amphibole + biotite + quartz + plagioclase ± muscovite ± chlorite in the pelitic rocks southwest of the Jolu Mine. The applied geothermobarometry for this mineral assemblage includes garnet-biotite geothermometry (Ferry and Spear, 1978; Hodges and Spear, 1982), garnet-hornblende geothermometry (Graham and Powell, 1984), and garnet-hornblende-plagioclase-quartz geobarometry (Kohn and Spear, 1989). In addition, quartz-hornblende isotopic geothermometry of Bottinga and Javoy (1973, 1975) was used to estimate temperature of formation of metamorphic assemblages in the plutonic rocks (see Chapter 5).

Garnet-Biotite Geothermometer

The garnet-biotite geothermometer of Ferry and Spear (1978) is the most widely used geothermometer for greenschist and amphibolite grade rocks. As stated previously, biotite is unzoned and homogeneous, whereas garnet experienced retrograde growth or retrogressive diffusion exchange in the rims as indicated by the slight increases of Mn and Ca in rims relative to cores. To avoid any potential compositional disequilibrium between garnet and biotite due to re-equilibration, only rim composition of garnet was used in calculation. Garnet and biotite are in contact in all cases analyzed. Compositional variation from grain to grain is insignificant and consequently, average compositions were used in the temperature calculations.

Garnet-biotite geothermometry is based on the distribution of Mg and Fe between coexisting garnet and biotite according to the exchange reaction:

$$\underset{\text{almandine}}{Fe_3Al_2Si_3O_{12}} + \underset{\text{phlogopite}}{KMg_3AlSi_3O_{10}(OH)_2} = \underset{\text{pyrope}}{Mg_3Al_2Si_3O_{12}} + \underset{\text{annite}}{KFe_3AlSi_3O_{10}(OH)_2}.$$

Several activity models for garnet have been proposed for use with the garnet-biotite thermometer. The two models used in this study are the ideal activity model used in the original calibration by Ferry and Spear (1978) and the non-ideal activity model of Hodges and Spear (1982). An estimate of pressure is required in these calibrations of the garnet-biotite geothermometer. But since the geothermometer is relatively insensitive to pressure (for example, a change of 1 kbar yields only a 4°C temperature change using these calibrations), any reasonable pressure would have little effect on the calculated temperatures. Therefore, a pressure of 4 kbars was used for the calculations and the results are presented in Table 4-2.

The calibration of Ferry and Spear (1978) yields temperatures between 545° and 575°C. Hodges and Spear's (1982) model gives temperatures more than 50°C higher (599° to 631°C). Ferry and Spear (1978) reported an experimental error of ±50°C for their calibration. The temperatures from Ferry and Spear's (1978) model are favored since they are in agreement with the temperature calculated from garnet-hornblende thermometry of Graham and Powell (1984) (see below).

Application of the garnet-biotite geothermometer may be hindered by the effect of Mn and Ca in garnet and Al and Ti in biotite. High Mn and Ca in garnet leads to preferential Fe^{2+} substitution in garnet relative to biotite and a corresponding increase in calculated temperature. Conversely, an increase in Ti and Al^{VI} in biotite results in preferential Fe^{2+} substitution in biotite and corresponding decrease in calculated temperature (Dallmeyer, 1974). With these considerations, Ferry and Spear (1978) cautioned that this calibration can only be applied without correction when X_{Ca+Mn} in garnet, or (Ca + Mn)/(Ca + Mn + Fe + Mg), is ≤ 0.20 and $X_{Ti+Alvi}$ in biotite, or (Ti + Al^{VI})/(Ti + Al^{VI} + Fe + Mg), is ≤ 0.15. Biotite in the pelitic rocks has $X_{Ti+Alvi}$ of 0.11 to 0.12, while X_{Ca+Mn} in garnet ranges from 0.23 to 0.29, higher than the recommended limit of application of this thermometer. Therefore, the calculated temperatures may overestimate rim temperature.

Table 4-2. Temperature and pressure associated with M_1 metamorphism in pelitic rocks southwest of the Jolu Mine. The temperatures are rounded to the nearest 5°C, and the pressures to the nearest 0.5 kb.

GT321 Core	GT321 Rim	GT325 Core	GT325 Rim	GT327 Core	GT327 Rim	References
			Temperature (°C)			
	560		545		575	(1)
	620		560		630	(2)
585	580	580	550	560	550	(3)
			Pressure (Kbars)			
	5.0		4.5		4.5	(4)

1.Garnet-biotite geothermometry (Ferry and Spear, 1978).
2.Garnet-biotite geothermometry (Hodges and Spear, 1982).
3.Garnet-hornblende geothermometry (Graham and Powell, 1984). Fe in hornblende is present as Fe^{2+} in calculation.
4.Garnet-hornblende-plagioclase-quartz geobarometry (Kohn and Spear, 1989). Fe in hornblende is present as Fe^{2+} in calculation.

Garnet-Hornblende Geothermometer

The garnet-hornblende geothermometer of Graham and Powell (1984) is a function of the exchange reaction:

$$\underset{\text{Fe pargasite}}{3NaCa_2Fe_4Al_3Si_6O_{22}(OH)_2} + \underset{\text{pyrope}}{4Mg_3Al_2Si_3O_{12}} = \underset{\text{Mg pargasite}}{3NaCa_2Mg_4Al_3Si_6O_{22}(OH)_2} + \underset{\text{almandine}}{4Fe_3Al_2Si_3O_{12}}.$$

The thermometer is applicable at temperatures below 850°C to rocks containing Mn-poor garnet ($X_{Mn} < 0.1$) and common hornblende with restricted range of chemistry. The slightly higher Mn concentration in garnet ($X_{Mn} = 0.12$ to 0.15, Table A-4) may cause this geothermometer to lose some precision.

The porphyroblasts of hornblende and garnet in the pelitic rocks are compositionally zoned, and the zoning patterns suggest retrograde growth or re-equilibration in the rims during cooling from metamorphic peak. Both the core and rim compositions of the two minerals were used in calculation with assumption that thermal peak may be reflected in the cores of the minerals. Using Graham and Powell's (1984) empirical calibration, the calculated temperatures from mineral rims are from 550° to 580°C, in satisfactory agreement with the garnet-biotite temperature estimates of Ferry and Spear (1978) (Table 4-2). The mineral cores yield temperatures of 560° to 585°C, 5° to 30°C higher than the rim temperatures. Uncertainties for the garnet-hornblende geothermometer were not quoted by Graham and Powell (1984). An average error of ±45°C was reported by Boyle and Westhead (1992) for this geothermometer in their study of metamorphism in Sulitjelma, Scandinavian Caledonides.

Quartz-Hornblende Isotopic Geothermometry

Using the quartz-hornblende isotopic geothermometer of Bottinga and Javoy (1973, 1975), the $\delta^{18}O$ values of coexisting quartz and hornblende from the D_1

metamorphic assemblages in the plutonic rocks yield isotopic equilibration temperatures of 500° to 590°C, with an average of 550°C (see Chapter 5).

Garnet-Hornblende-Plagioclase-Quartz Geobarometers

The samples used for temperature calculation also satisfy the compositional criteria of minerals that were used for the calibrations of the garnet-hornblende-plagioclase-quartz geobarometers (Kohn and Spear, 1989). The geobarometers of Kohn and Spear (1989) are based on the reactions:

$$\underset{\text{anorthite}}{6CaAl_2Si_2O_8} + \underset{\text{albite}}{3NaAlSi_3O_8} + \underset{\text{tremolite}}{3Ca_2Mg_5Si_8O_{22}(OH)_2} =$$

$$\underset{\text{grossular}}{2Ca_3Al_2Si_3O_{12}} + \underset{\text{pyrope}}{Mg_3Al_2Si_3O_{12}} + \underset{\text{pargasite}}{3NaCa_2Mg_4Al_3Si_6O_{22}(OH)_2} + \underset{\text{quartz}}{18SiO_2}$$

and

$$\underset{\text{anorthite}}{6CaAl_2Si_2O_8} + \underset{\text{albite}}{3NaAlSi_3O_8} + \underset{\text{Fe-actinolite}}{3Ca_2Fe_5Si_8O_{22}(OH)_2} =$$

$$\underset{\text{grossular}}{2Ca_3Al_2Si_3O_{12}} + \underset{\text{almandine}}{Fe_3Al_2Si_3O_{12}} + \underset{\text{Fe-pargasite}}{3NaCa_2Fe_4Al_3Si_6O_{22}(OH)_2} + \underset{\text{quartz}}{18SiO_2}.$$

Since plagioclase in these samples is fine-grained and unzoned, and probably re-equilibrated after peak metamorphic conditions, only the rim compositions of garnet and hornblende were used in pressure calculations. Temperatures obtained from Ferry and Spear's (1978) calibration were adopted because of the consistency between this calibration and the garnet-hornblende thermometer of Graham and Powell (1982). The geobarometers yield pressures of 4.5 to 5.0 kbars (Table 4-2). The reported imprecisions for the geobarometers are ±1 to ±2 kbars (Kohn and Spear, 1989).

Summary

Temperature and pressure of M_1 metamorphism in the Jolu Mine area were calculated to be approximately 545° to 575°C and 4.5 to 5.0 kbars, respectively, from the rim compositions of coexisting minerals in the pelitic rocks interlayered with metavolcanic rocks. Higher temperatures of 560° to 585°C were derived from the

cores of garnet and hornblende. The core-to-rim decrease in the calculated temperature is consistent with the zoning patterns in garnet and hornblende. Therefore, the actual temperatures of peak metamorphism were probably higher, and the temperatures of 545° to 575°C and the pressures of 4.5 to 5.0 kbars are considered as minimal for M_1 metamorphism. The calculated P-T conditions, in addition to the petrographic observations, are consistent with peak metamorphism in low to middle amphibolite facies (Spear, 1993).

Figure 4-16 shows the range of the calculated temperatures and pressures for M_1 metamorphism and the petrogenetic grid for pelitic rocks in the system SiO_2-Al_2O_3-FeO-MgO-K_2O-H_2O (KFMASH) of Spear and Cheney (1989). As indicated by Spear and Cheney (1989), the addition of MnO and CaO to garnet increases the stability field for the assemblage garnet + chlorite + biotite. The thin lines in Figure 4-16 outline the expansion of the garnet + chlorite + biotite stability field as a result of the addition of MnO to garnet. Garnet porphyroblasts in the pelitic rocks of this study contain approximately 0.15 to 0.20 of Mn/Mn+Fe+Mg and coexist with biotite and chlorite. The range of the calculated temperatures and pressures for the pelitic rocks is largely within the expanded stability field, and are consequently consistent with the mineral paragenesis in the rocks.

Temperature and Pressure of M_2 and M_3 Metamorphism

Geothermobarometry

In addition to quartz-hornblende isotopic geothermometry, Spear's (1980) plagioclase-amphibole thermometer and Plyusnina's (1982) plagioclase-hornblende thermobarometer were applied to constrain temperature and pressure of M_2 and M_3 metamorphism associated with the D_2 structures and D_3 gold-bearing shears. Plagioclase and amphibole associated with S-L fabric of the MLTZ and S_1-L_1 fabric in metavolcanic rocks and plutonic rocks were used as comparison. The samples of the pelitic rocks are excluded since the occurrence of garnet has a considerable effect on the composition of amphibole (Laird and Albee, 1981). All the samples chosen contain

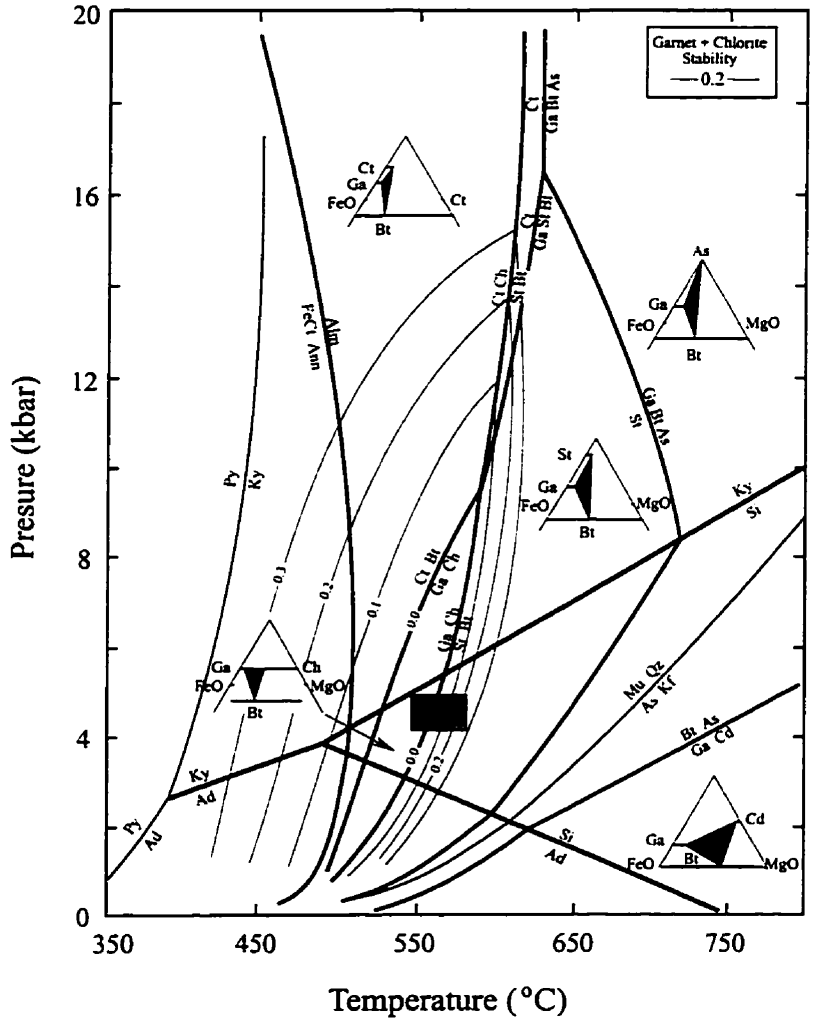

Figure 4-16. Petrogenetic grid for the KFMASH system (Spear and Cheney, 1989). Thin lines depict the effect of X_{spes} (Mn/Mn+Fe+Mg) in garnet on the stability of garnet + chlorite. Abbreviations: Ad, andalusite; Alm, almandine; Ann, annite; Bt, biotite; Cd, cordierite; Ch, chlorite; Ct, chloritoid; Ga, garnet; Kf, K-feldspar; Ky, kyanite; Mu, muscovite; Py, pyrophyllite; Qz, quartz; Si, sillimanite; St, staurolite.

amphibole + plagioclase + chlorite + epidote + Ti phase + Fe oxide + quartz ± carbonate ± mica, the "common assemblage" of Laird and Albee (1981).

Plagioclase-Amphibole Geothermometry

The plagioclase-amphibole geothermometry of Spear (1980) is based on an empirical calibration of the exchange equilibrium between plagioclase and amphibole:

$$\underset{\text{albite}}{2NaAlSi_3O_8} + \underset{\text{tschermakite}}{Ca_2Mg_3Al_4Si_6O_{22}(OH)_2} = \underset{\text{anorthite}}{2CaAl_2Si_2O_8} + \underset{\text{glaucophane}}{Na_2Mg_3Al_2Si_8O_{22}(OH)_2}.$$

The geothermometry is considered suitable for use in the region of approximately 450° to 750°C, with an accuracy of approximately ±50°C (Spear, 1980). The uncertainties in the calculation of the amphibole formula from a microprobe analysis may hinder the application of the thermometer.

The plagioclase-amphibole geothermometer is given in Figure 4-17. The S_1-L_1 regional fabric falls in the range of 510° to 540°C. Temperatures from the S-L fabric of the MLTZ, from 510° to 550°C, is approximately in the same range as the S_1-L_1 fabric. Samples from D_2 structures yield temperatures of 500° to 510°C, whereas the D_{3a} and D_{3b} fabrics of the gold-bearing shears are approximately 480° to 500°C.

Plagioclase-Hornblende Geothermobarometry

The plagioclase-hornblende geothermobarometer of Plyusnina (1982) is applicable in mafic rocks containing the "common assemblage" of Laird and Albee (1981), of which calc amphibole + plagioclase + epidote or zoisite is considered as the major limiting assemblage (Plyusnina, 1982). The geothermobarometer was experimentally calibrated based on the reaction:

$$\text{hornblende} + \text{zoisite (epidote)} + H_2O + CO_2 = \text{plagioclase} + \text{chlorite} + \text{carbonate} + \text{quartz}$$

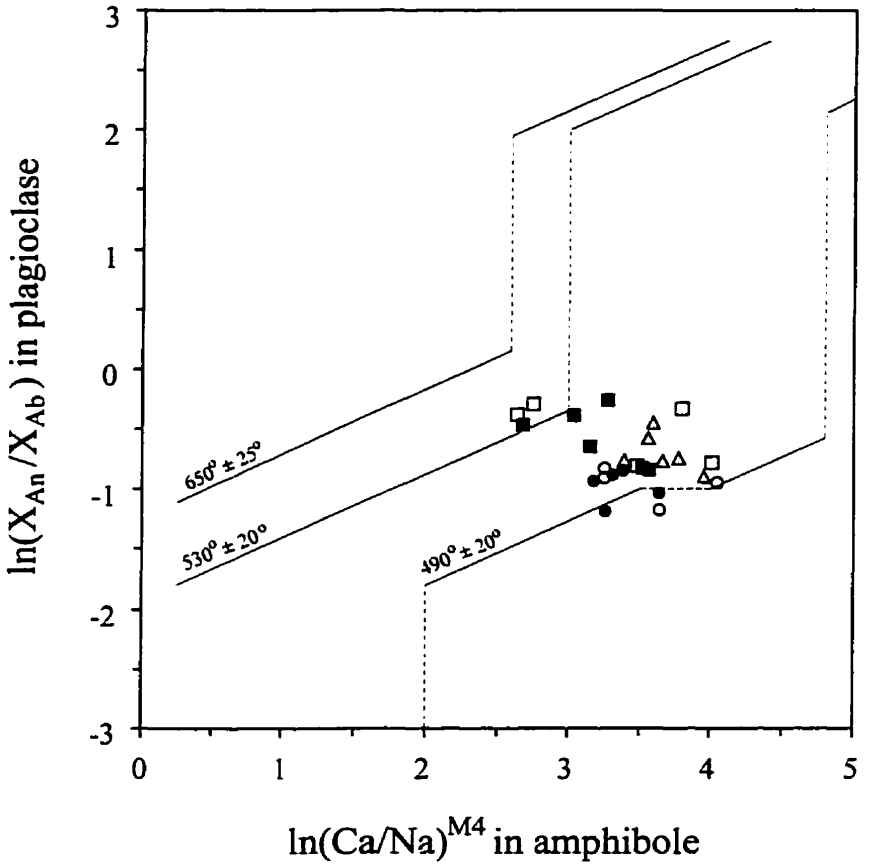

Figure 4-17. Empirical geothermometer for plagioclase-amphibole exchange equilibrium (Spear, 1980). Filled squares, D_1 fabric; open squares, S-L fabric of the MLTZ; triangles, D_2 structures; shaded circles, D_{3a} structures; open circles, D_{3b} structures.

under hydrothermal conditions of P_{total} = 2, 4, 6 and 8 kbar and X_{co2} = 0.1. The resolution of this thermobarometer is ±1 kbars and ±15°C on an analytical uncertainty of ±1.0 mole % Al and Ca in amphibole and plagioclase (Plyusnina, 1982). The geothermobarometer and the compositions of coexisting amphibole and plagioclase are given in Figure 4-18.

Temperatures estimated from the thermometer are approximately 540° to 590°C for the S_1-L_1 regional fabric and the S-L fabric of the MLTZ, 535° to 570°C for D_2 structures, and 525° to 540°C for D_{3a} and D_{3b} fabrics of the gold-bearing shears. This thermometer yields higher temperatures than Spear's (1980) calibration by 30° to 40°C, but both of the thermometers outline similar relative temperature variations for the structures.

The geobarometer gives pressures of 2.5 to 4.5 kbars for the S_1-L_1 regional fabric and 3.0 to 5.0 kbars for the MLTZ, with the majority plotting between 3.0 and 4.5 kbars. The pressures for the D_2 structures range from 3.0 to 5.0 kbars, with five of the six samples within a more restricted range of 3.0 to 4.0 kbars. The D_{3a} and D_{3b} fabrics of the gold-bearing shears have the most scattered pressure estimates, from less than 2.0 kbars to 5.0 kbars, with most falling between 3.0 and 4.0 kbars.

Quartz-Hornblende Isotopic Geothermometry

The quartz-hornblende isotopic geothermometer of Bottinga and Javoy (1973, 1975) yields isotopic equilibration temperatures of 500° to 520° for the MLTZ, 550° for the D_2 structures and 480° to 510° for the D_3 gold-bearing shears (see Chapter 5).

Discussion

The estimated temperatures and pressures derived from the above geothermobarometers are summarized in Table 4-3. The S-L fabric of the MLTZ indicates similar P-T conditions to the S_1-L_1 regional fabric, whereas the D_2 and D_3 structures probably developed subsequent to the attainment of the peak of M_1 metamorphism. This can be evaluated from the variations in the compositions of

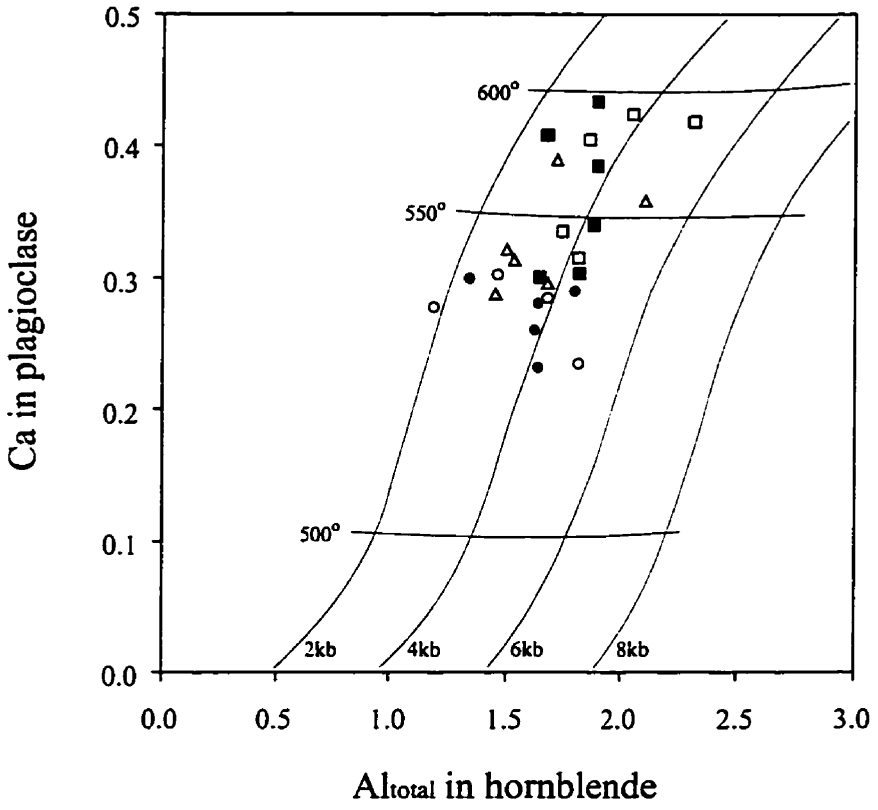

Figure 4-18. Experimental plagioclase-hornblende geothermobarometer (Plyusnina, 1982). Symbols are as in Figure 4-17.

minerals associated with D_1 to D_3 deformations.

Table 4-3. Temperature and pressure of deformation and metamorphism derived from plagioclase-amphibole geothermometry (Spear, 1980), plagioclase-hornblende geothermobarometry (Plyusnina, 1982), and quartz-hornblende isotopic geothermometry (Bottinga and Javoy, 1973; 1975)

M_1 (S_1-L_1 fabric)	MLTZ (S-L fabric)	M_2 (D_2 structures)	M_{3a}/M_{3b} (D_3 shears)	References
		Temperature (°C)		
510 - 550	510 - 550	500 - 510	480 - 510	(1)
540 - 590	540 - 590	535 - 570	525 - 540	(2)
500 - 590	500 - 520	550	480 - 510	(3)
		Pressure (Kbars)		
3.0 - 4.5	3.0 - 4.5	3.0 - 4.0	3.0 - 4.0	(2)

1.Plagioclase-amphibole geothermometry (Spear, 1980).
2.Plagioclase-hornblende geothermobarometry (Plyusnina, 1982).
3.Quartz-hornblende isotopic geothermometry (Bottinga and Javoy, 1973; 1975).

The important chemical changes of amphibole and plagioclase in mafic rocks that occur in response to changing P-T conditions during metamorphism were summarized by numerous studies (e.g. Laird, 1980; Laird and Albee, 1981; Jacobson, 1995), and were confirmed by experimental work on rocks of basaltic composition (e.g. Spear, 1981). Unlike pelitic rocks, which may undergo various divariant exchange reactions separated by discontinuous univariant reactions, mafic assemblages have a relatively constant assemblage over a substantial range in metamorphic grade. Reactions during the metamorphism of mafic rocks are typically continuous and result in compositional changes of mineral solid solutions. Laird and Albee (1981) outlined the metamorphism of the "common assemblage" and identified systematic mineral compositional variations which occur in response to changing metamorphic conditions. With increasing temperature and pressure, amphiboles become enriched in Al, Ti, Na and ($Al^{VI} + Fe^{3+} + Ti + Cr$) and depleted in Si, Ca and Mg. Plagioclase becomes more anorthitic with increasing grade and shows discrete compositional jumps at the peristerite gap (albite to oligoclase) in medium- to low-pressure facies series (Laird

and Albee, 1981). In addition to amphibole and plagioclase, biotite may show increases in Ti and Al^{IV}, and probably Al^{VI} with increasing metamorphic grade (Laird and Albee, 1981). A decrease in Al^{VI} with metamorphic grade was reported by Guidotti (1984).

However, because the parameters showing chemical variations are dependent on the normalization method used to convert analytical data to formula proportions, some of the apparent variations could be artifacts of data normalization. Na^{M4} in amphiboles is particularly sensitive to Fe^{2+}/Fe^{3+} recalculation. The ratios of Na/(Ca + Na) and Al/(Si + Al), however, are independent of the method of Fe^{2+}/Fe^{3+} recalculation and assignment of cations to sites within the structures, and are most suitable for illustrating the chemical variations of amphiboles with varying P-T conditions (Laird and Albee, 1981).

The chemical variations in amphiboles from the D_2 and D_3 structures, with respect to amphiboles from D_1 structure, are summarized in Figures 4-8 and 4-13. The metamorphic changes in D_2 and D_3 structures are predominantly the reverse of the regional prograde variations. The exceptions are amphiboles in the D_2 shear hosted in the mafic metavolcanic rock, which show prograde variation (Figure 4-8), and amphiboles in deformed porphyritic diorite of the Rod shear, which exhibit either minor prograde (Figure 4-13A) or retrograde variations (Figure 4-13B).

There are two situations that could lead to the observed chemical changes in amphiboles: the growth of M_2 and M_3 amphiboles under lower P-T conditions than M_1 metamorphism; or M_2 and M_3 amphiboles undergoing more extensive retrograde diffusion exchange with infiltrating fluids than M_1 amphiboles. If the chemical changes were caused by retrograde diffusion exchange following the formation of M_2 and M_3 amphiboles, it would be expected that the amphiboles would have a unique retrograde zoning pattern. However, the majority of the M_2 and M_3 amphiboles show a prograde zoning pattern (Figures 4-7 and 4-12), indicating that no retrograde exchange was substantially involved following their formation. Therefore, the changes in amphibole chemistry likely reflect declining P-T conditions as deformation proceeded.

The development of the D_2 and D_3 structures under lower-than-peak metamorphic conditions is also suggested by plagioclase, which becomes less anorthitic in the D_2 and D_3 structures than in the least deformed host rocks, with the exception of the D_2 shear in the mafic metavolcanic rock (Figures 4-9 and 4-14).

Biotite shows no systematic variation in Al^{IV} and Al^{VI}, but becomes enriched in Ti in the D_2 and D_3 structures (Figures 4-10 and 4-15). The latter suggests increasing P-T conditions (Laird and Albee, 1981; Ghent and Stout, 1984). The reasons for this are uncertain. It may be such that biotite probed in the relatively undeformed rocks is not a phase of the peak metamorphic assemblage. Petrographic observations indicate that biotite is a minor phase in mafic rocks and mainly occurs as a retrograde product after amphiboles. Although an effort was made to use biotite least likely to be a replacement phase, it cannot ruled out that the alteration phase was probed. Therefore, biotite is not as good an indicator of relative metamorphism as amphibole and plagioclase.

The major problems in utilizing the chemistry of amphibole to indicate P-T variations are the influences that bulk rock composition, composition of the fluid phase, and f_{O2}, have on the mineral chemistry and mineral stability fields (Brodie and Rutter, 1985). Although comparisons of amphibole compositions were only made between relatively undeformed rocks and their deformation products in order to limit the effect of variation in bulk rock composition on the mineral chemistry, metasomatism which took place coeval with the development of the D_2 and D_3 structures resulted in changes in bulk, trace and isotopic chemistry of the deformed rocks (see below and Chapter 5). Whether or not metasomatism played a critical role in the systematic variation in chemistry of amphiboles, or the degree of the variation is difficult to evaluate. Figure 4-19 gives amphibole compositions with reference to the host-rock chemistry. It shows that the changes in amphibole and the host-rock chemistry are not necessarily coincident. In addition, the relative P-T conditions suggested by chemical variation of amphibole and plagioclase are in good accord with the quartz-hornblende oxygen-isotopic geothermometry, which is independent of the bulk rock composition. Therefore, the variation in amphibole composition is more likely controlled by changing P-T conditions than by the variation in the bulk rock chemistry.

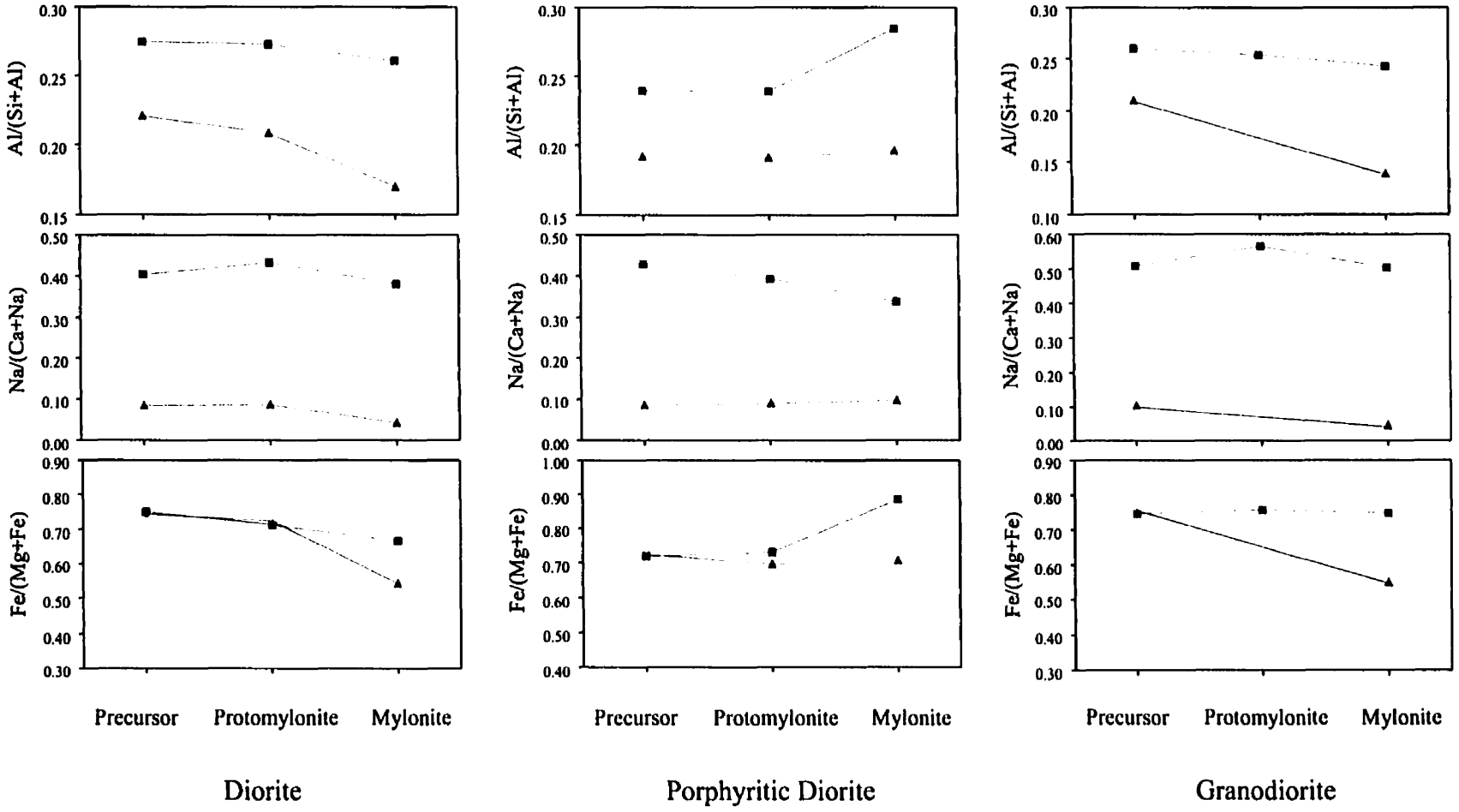

Figure 4-19. Variation in amphibole composition (triangles) with reference to variation in the host-rock chemistry (squares).

Chemistry of Wall-Rock Alteration

Wall-rock alteration associated with the D_3 gold-bearing structures, including the James-Jasper-Roxy shears, the 21 zone of the Star Lake mine, and the Rush Lake shear, has previously been studied by Appleyard (1991). The present study of alteration was carried out on: the MLTZ; the D_2 Mallard Lake Shear; the D_3 Rod shear; and the D_3 MacLeod Main shear, in addition to the D_3 James-Jasper-Roxy shears. Deformed rocks and reference precursors which show no evidence of alteration and minimal effects of shearing were sampled and analyzed for major and minor elements. The analytical results are presented in Table B-1.

Chemical Mass Balance

Chemical data were corrected for mass and volume changes using the general metasomatic equation of Gresens (1967) and the procedures outlined in Appleyard (1990). In order to identify a meaningful reference frame for alteration, immobile components must be known. Mass balance calculations presume that immobile elements can be identified by a clustering of FV^0 (volume change factor for zero element change) values (Taylor and Appleyard, 1983; Appleyard, 1990). Elements found to be immobile are given in Table B-2. The most immobile element, in terms of frequency in mass balance calculations, is Ti (14), followed by Al (8), Tb (7), Sm (5), Yb (5), Nb (4), Hf (4) and Sc (4). In the absence of clustering of FV^0 values, Ti is assumed to have acted as an immobile element. Once immobile elements are determined, the volume change and the mass flux of elements are computed relative to the reference precursor. The calculations were carried out only for elements analyzed with the same analytical technique to ensure that variations in composition are not the result of variations in the analytical techniques. Table B-2 lists the computed results in terms of net compositions, i.e. the amount of each element remaining after cubic units of the host rock have been altered. Major elements are presented as grams per one hundred cubic centimetres of the protolith (g/100cc) and trace elements as grams per cubic metre of the protolith (g/m^3).

The calculated volume changes for all structures are between -9.9% and

+11.0% (Table B-2), indicating rock volume was slightly changed during deformation and wall-rock alteration. The positive volume changes suggest net precipitation of material during alteration; the negative volume changes suggest leaching of material during alteration.

Alteration Chemistry

Selected elements from the results of mass balance calculations are plotted in Figures 4-20 to 4-22. The data from the MLTZ and the D_2 Mallard Lake Shear are illustrated in terms of percentage gains and losses relative to reference precursors (Figures 4-20 and 4-21). The data from the D_3 gold-bearing shears, including the James shear, Roxy shear, Rod shear and MacLeod Main shear, are summarized as variation diagrams (net composition versus distance) (Figure 4-22).

Because the D_3 gold-bearing shears involved two episodes of deformation (D_{3a} and D_{3b}), the alteration chemistry of the shears probably reflects the net alteration effects associated with the D_{3a} and D_{3b} deformations. This may also hold true for the MLTZ, where the alteration associated with the D_{3b} deformation may overprint the earlier alteration associated with the development of the S-L fabric.

McLennan Lake Tectonic Zone

The host granodiorite to the MLTZ in the southern edge of the Island Lake pluton has consistent major and trace element chemistry (see samples 93-4 and 93-118 in Table B-1), suggesting that the calculated elemental flux represents alteration effects and is not a result of variations in the primary geochemistry of the host rock. The mass flux is characterized by a gain of Ca and a loss of K (Figure 4-20). Si, Fe and Na display minor fluctuations. Mg and P are added to or stripped from the deformed rocks. Ba and Rb are lost from the deformed rocks along with K, whereas Sr shows no correlation with Ca. Au is either enriched or depleted, and is positively correlated with Cu. The K/Rb and K/Ba ratios from the deformed granodiorite are 160 to 244 and 13 to 25, respectively (Table 4-4).

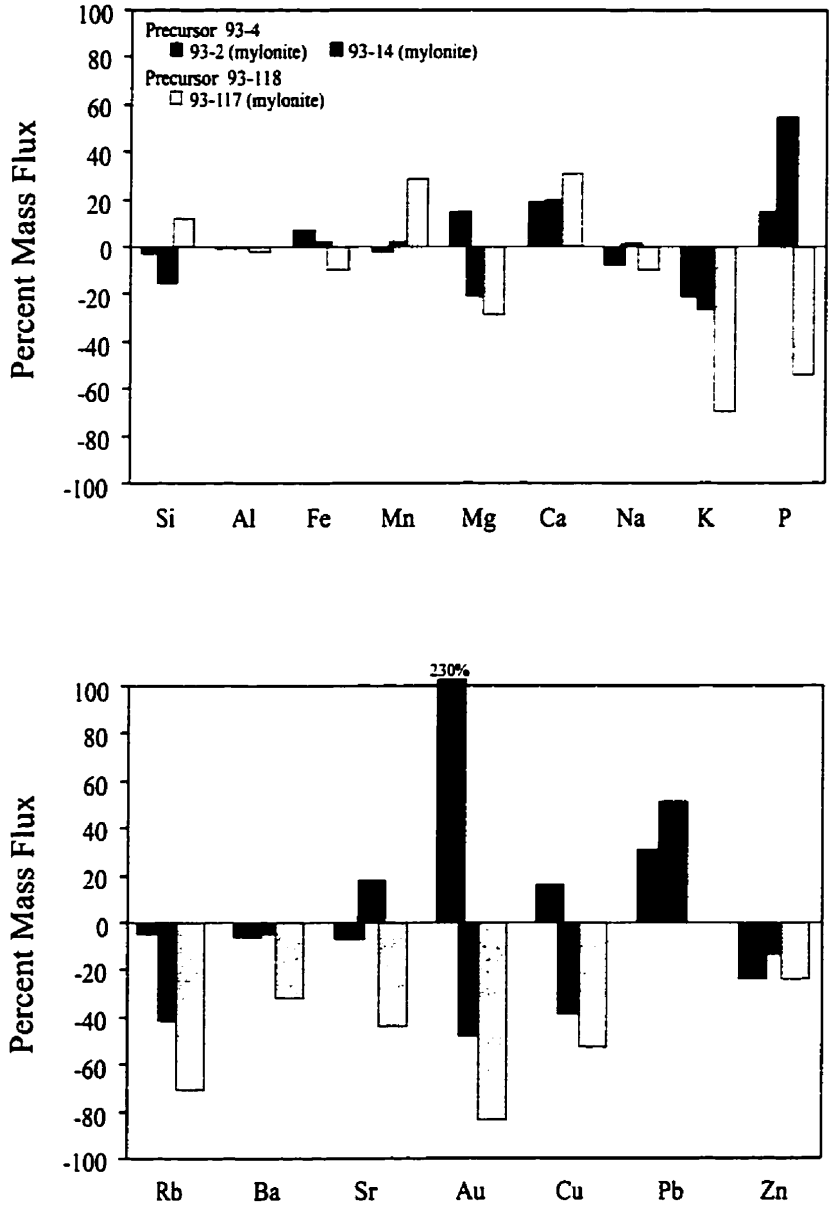

Figure 4-20. Percent mass flux of selected major and trace elements in the deformed granodiorite of the McLennan Lake Tectonic Zone.

Table 4-4. K/Rb and K/Ba ratios from the MLTZ, D_2 shears and D_3 gold-bearing shears and from the host Star Lake pluton (SLP) and Island Lake pluton (ILP). Ratios from potassic alteration zones of Archean lode gold deposits and average crust are given for comparison

Ratio	SLP and ILP	MLTZ	D_2 shears	D_3 shears	Archean lode Au deposits[1]	Average crust[2]
K/Rb	192-365	160-244	247-410	132-366	220-400	~ 260
K/Ba	14-30	13-25	6-45	14-38	30-85	20-60

1. Kerrich and Fryer (1988) and Kerrich (1989).
2. See Kerrich (1989).

D_2 Mallard Lake Shear

The mass flux in the D_2 Mallard Lake Shear in the porphyritic diorite-hosted portion involves the addition of K by 147% to 156% and loss of Na by up to 86%, with the former being accompanied by strong gains in Ba and Rb (Figure 4-21). Al, Fe, Mn, Ca and P display overall gains, Mg is either added or removed, and Si is relatively unchanged. Sr behaves antipathetically to Ca, being stripped by hydrothermal solutions. Au, Cu and Zn are introduced into the shear during alteration. The deformed rocks of the Mallard Lake Shear and other D_2 shears have K/Rb ratios of 247 to 410 and K/Ba ratios of 19 to 45 (Table 4-4).

D_3 Gold-Bearing Shears

The alteration associated with the D_3 shears is characterized by a strong introduction of Au, coupled with a moderate gain of K and a loss of Na (Figure 4-22). An exception is observed in the dioritic segment of the Rod shear, where the introduction of Au is coincident with a minor loss of K and a minor gain of Na.

Si shows a systematic gain throughout most of the shears with the exception that slight depletions occur in the mylonites of the Roxy shear and the Rod shear hosted in the porphyritic diorite.

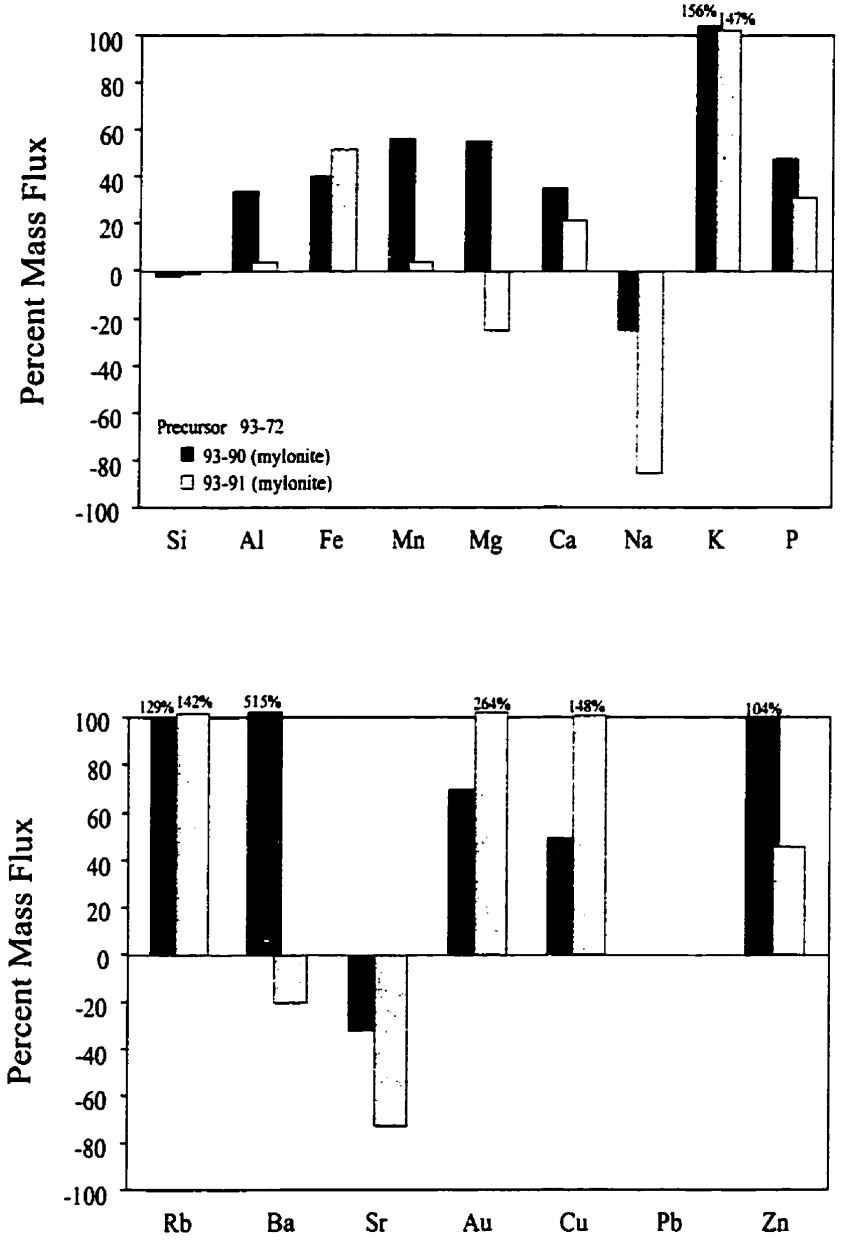

Figure 4-21. Percent mass flux of selected major and trace elements in the deformed porphyritic diorite of the D2 Mallard Lake shear.

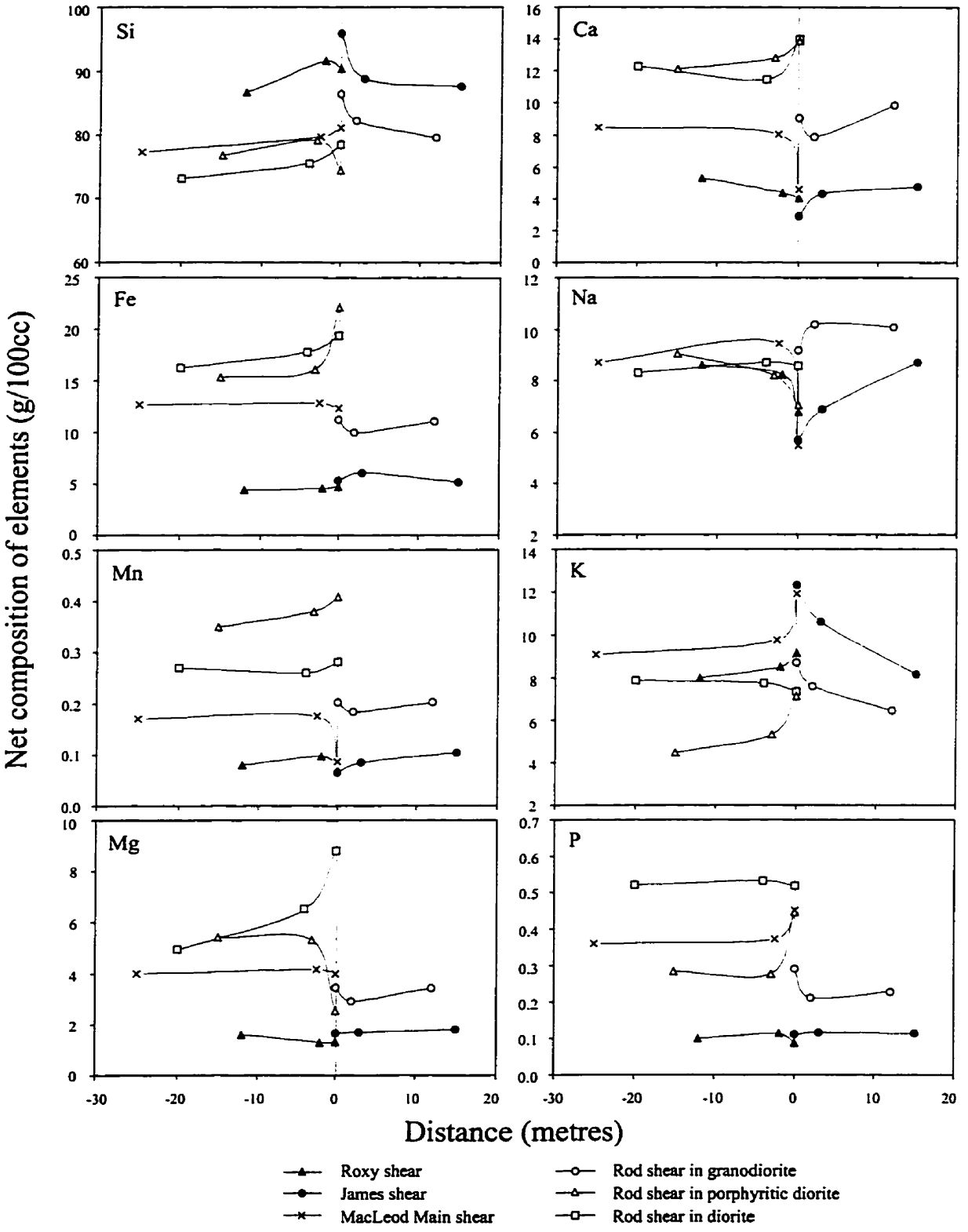

Figure 4-22. Geochemical variation diagrams for selected elements from the D3 gold-bearing shears.

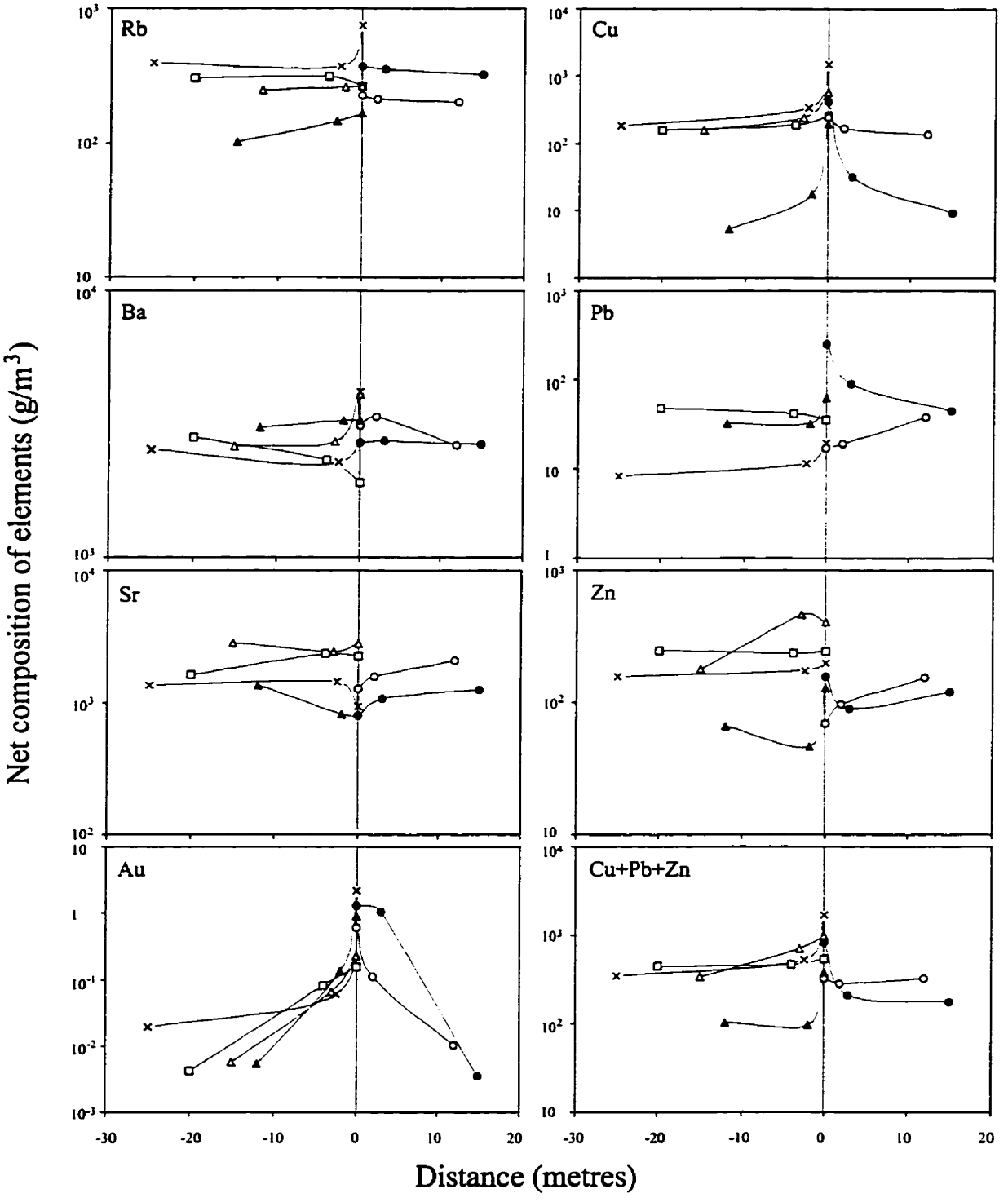

Figure 4-22. (continued) Composition scales are linear for major elements and logarithmic for trace elements. Distance scales are fixed with point zero at the central mylonite zone of the shears; minus values extending towards the northwestern wall and plus values towards the southeastern wall.

Fe, Mn, Mg, and Ca are either added to or removed from the shear systems, showing no consistent variations. P is largely enriched, except for minor downturns in the mylonites of the James and Roxy shears and in the dioritic segment of the Rod shear.

Among the trace elements, the moderate to strong, systematic introduction of Cu is notable throughout the sequences. Rb and Ba exhibit strong co-variations with K, with K/Rb = 132 ~ 366 and K/Ba = 14 ~ 38 (Table 4-4), whereas Sr behaves sympathetically with Ca. Although Zn and Pb are either introduced or lost, the sum of the base metals (Cu + Pb + Zn) is systematically increased towards the central mylonites of the shears, showing consistent co-variations with the introduction of Au.

Discussion

As pointed out by Appleyard (1992), a study of alteration does not specifically describe the nature of the hydrothermal fluids. However, through the nature of the elemental fluxes that occurred during alteration, it is possible to determine the relative abundances of elements between the fluid and the rock it infiltrated.

The effects of hydrothermal alteration are controlled by temperature, pressure, the availability of elements in the host rock, permeability, fluid composition, and duration of fluid activity (Appleyard, 1990). Of these, temperature, pressure and fluid composition are the most important factors in controlling elemental fluxes occurred during alteration (Appleyard, 1990).

The porphyritic diorite-hosted D_2 Mallard Lake Shear and D_3 Rod shear exhibit remarkable similarity in gain-loss profiles (Figure 4-23). Because the D_2 and D_3 structures developed under similar P-T conditions (Table 4-3), the similarity would be critically controlled by the composition of the infiltrating fluids. In this regard, elemental fluxes in these structures would have resulted from interaction with fluids of similar composition. The fluids were enriched in Au, Al, Fe, Mn, Ca, K, P, Ba and Rb, and depleted in Na, Sr and possibly Mg with reference to the porphyritic diorite. An implication of this is that gold-bearing hydrothermal fluids may already have been

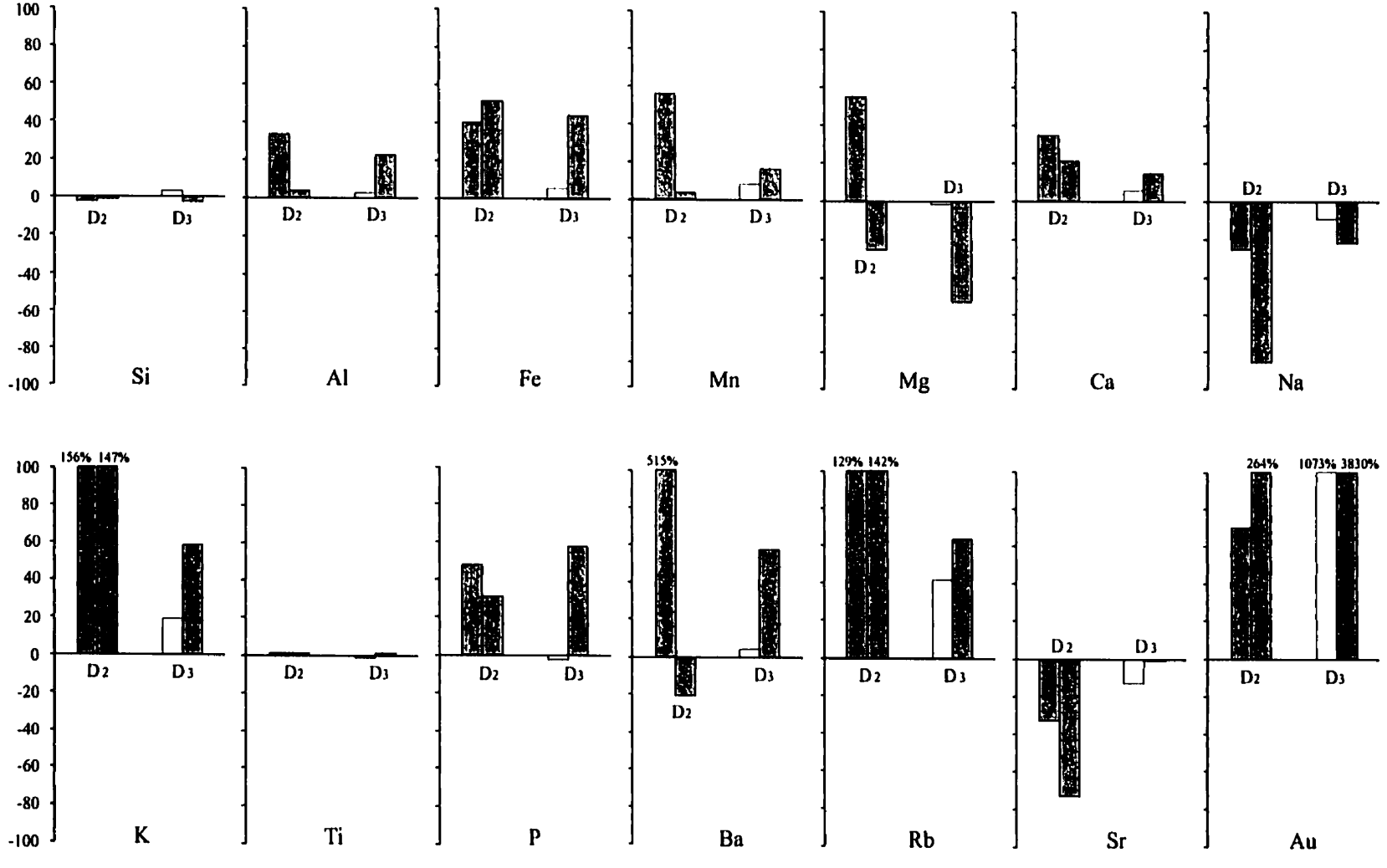

Figure 4-23. Comparison of percent mass fluxes of selected elements between porphyritic diorite-hosted D2 Mallard Lake Shear and D3 Rod shear. Shaded bars, mylonite; unshaded bars, protomylonite.

generated prior to the development of the D_3 structures. In the course of D_{3a} deformation, the northeast-striking D_2 structures were developed into D_3 shears with dip-slip shearing (see Chapter 3), likely along with increased permeability. The enhanced permeability would allow a larger volume of fluid to pass through the D_3 shears than the D_2 structures, as indicated by the fluid/rock oxygen ratios (see Figure 5-8, Chapter 5), and consequently, it may play an important role in controlling gold mineralization in the D_3 shears.

The alteration geochemistry of the D_3 gold-bearing structures is similar to that of typical Archean lode gold deposits, which are characterized by major introduction of SiO_2 and CO_2, along with additions of K, Rb, Li and Cs and depletion of Na (Kerrich, 1983; McCuaig and Kerrich, 1994). The structures also show co-enrichment in K, Rb and Ba, with K/Rb and K/Ba ratios comparable to the ratios of the potassic alteration zones of the Archean lode gold deposits and the average crust (Kerrich and Fryer, 1988; Kerrich, 1989) (Table 4-4).

Kerrich and Fryer (1988) and Kerrich (1989) suggested that the co-enrichment of K, Rb and Ba in the gold deposits, in conjunction with the compliance of K/Rb and K/Ba with the ratios of average crust, would not be expected from late-stage magmatic processes involving crystal fractionation of biotite, plagioclase and K-feldspar. Such processes systematically reduce K/Rb and enhance K/Ba in residual magma and magmatic volatiles. The authors suggested that the compliant K/Rb and K/Ba ratios would be generated by dehydration reactions in the source rocks or by equilibration with the source rocks under conditions of low water/rock ratio, resulting in partitioning of K, Rb, and Ba into the hydrothermal fluids in approximately the same ratios as in the source rocks.

The elemental flux of the MLTZ involves addition of Ca to the deformed granodiorite and release of K, Rb, and Ba from the deformed rocks (Figure 4-20). The irregular gain and loss of Au suggest a local migration of Au within the MLTZ. This elemental flux may result from fluid infiltration during peak metamorphism. As previously described, the ductile deformation in the MLTZ was coeval with M_1 amphibolite facies metamorphism. The development of S-L fabric in deformed rocks increased the permeability with respect to the relatively undeformed rocks, allowing

infiltration of hydrothermal fluid. When the fluid was transported through the deformed rocks along the closely spaced S-L fabric, it interacted with, and leached K, Rb and Ba from, the deformed rocks of the MLTZ.

Conclusions

The Star Lake-McLennan Lake area was subjected to three metamorphic events (M_1 to M_3). The peak metamorphism of amphibolite facies, M_1, was attained during the D_1 deformation. Temperature and pressure of M_1 metamorphism were approximately 545° to 575°C and 4.5 to 5.0 kbars, respectively. The MLTZ was probably deformed and metamorphosed under the same conditions as the D_1 regional fabric.

The subsequent metamorphic events, M_2 and M_3, were coincident with the D_2 and D_3 deformations, respectively, following the attainment of the peak metamorphism. M_2 metamorphism involved temperatures of approximately 500° to 550°C and pressures of 3.0 to 4.0 kbars. The M_3 metamorphism, including M_{3a} and M_{3b}, took place under conditions of 480° to 500°C and 3.0 to 4.0 kbars.

Amphibole and plagioclase associated with M_2 and M_3 metamorphism show systematic variations in chemistry relative to their M_1 equivalents. The changes in mineral chemistry were likely caused by changing P-T conditions.

The deformed rocks of the MLTZ, D_2 and D_3 structures underwent compositional changes through interaction with hydrothermal fluids. The fluids that infiltrated the D_2 and D_3 structures were possibly of similar composition, and were possibly generated by dehydration reactions in the source rocks or by equilibration with the source rocks under conditions of low water-rock ratio.

Mineralization is strongly associated with the introduction of K, Rb, Ba, and Cu (+ Pb + Zn), and depletion of Na. The variations in concentration of these elements in the rocks could be used as criteria to identify potential gold-bearing structures.

CHAPTER 5

OXYGEN AND HYDROGEN ISOTOPIC SYSTEMATICS

Introduction

The purpose of this study is to use oxygen and hydrogen isotopic analyses of well defined structures to address aspects of the nature of hydrothermal fluids and thermal conditions associated with structural development and gold mineralization. Previous studies of isotopic systematics were carried out on the Star Lake deposit and the Jasper deposit by Ibrahim and Kyser (1991) and Hrdy and Kyser (1995), respectively. These studies mainly focused on quartz veins on deposit scale, with little effort to relate hydrothermal auriferous activities to regional deformational events.

Since deformation was typically accompanied by the emplacement of quartz veins, many structures are composed of two or three structurally and compositionally distinct lithologies: veins of quartz plus other minor phases, mylonitic or phyllonitic rocks immediately adjacent to the veins, and/or protomylonitic rocks bordering the mylonite or phyllonite. Stable isotopic data in this study were collected from these individual lithologies in order to relate isotopic data to the processes of fluid-rock interaction in the structural-controlled systems and to present reliable evidence to elucidate their formation and tectonic significance.

Sampling and Analytical Techniques

Samples for isotopic analyses were chosen after petrographic examinations. Mineral concentrates from granodiorite and granite and their deformed rocks were prepared from the crushed and sieved samples using conventional magnetic and heavy-liquids techniques, and quartz was separated from alkali feldspar by brief washing in dilute hydrofluoric acid. Mineral separates were finally hand-picked from the

concentrates to remove altered, ragged, and composite grains. Mineral separates from quartz veins were obtained by hand-picking from the crushed and sieved samples.

Stable isotopic analyses were performed in the Department of Geological Sciences, the University of Saskatchewan. Oxygen was extracted from silicates using the BrF_5 technique developed by Clayton and Mayeda (1963). Hydrogen and the water content of hydrous minerals were obtained using the uranium technique of Bigeleisen *et al.* (1952) as modified by Kyser and O'Neil (1984). An internal laboratory standard was included in each run of the analyses. Isotopic data are reported as δ-values in units of per mil relative to Vienna Standard Mean Ocean Water (VSMOW). Isotopic ratio measurements were made with conventional isotopic ratio mass spectrometers. Replicate analyses show that reproducibility at the 2σ confidence level is ±0.2 per mil for oxygen and ±3 per mil for hydrogen.

Oxygen and Hydrogen Isotopic Data

Over 110 oxygen and hydrogen isotopic analyses of mineral separates from quartz veins and the bordering deformed rocks were performed in this study. Minerals selected from veins include quartz, feldspars, tourmaline, biotite, muscovite and calcite. Minerals obtained from the host rocks include quartz, hornblende, biotite, and muscovite. The analytical results are given in Tables 5-1 and 5-2 and are summarized in Figures 5-1 to 5-3. The isotopic data from previous studies of the Star Lake deposit (Ibrahim and Kyser, 1991) and the Jasper deposit (Hrdy and Kyser, 1995) are also compiled in these tables and figures.

Oxygen and Hydrogen Isotopic Compositions of Quartz Veins

Oxygen Isotopes

Quartz veins associated with the MLTZ, the D_1 regional penetrative fabric and the D_2 structures are barren. Quartz $\delta^{18}O$ values fall to the narrow ranges of 10.6 ~ 11.0 per mil, 10.2 ~ 11.9 per mil, and 9.9 ~ 10.8 per mil, respectively (Figure 5-1A).

Table 5-1. Oxygen and hydrogen isotopic compositions of vein minerals; calculated temperatures; and oxygen and hydrogen isotopic compositions of hydrothermal fluids.

Structural event	Sample	Mineral[1]	Mineral $\delta^{18}O$	Mineral δD	Equilibration Temperature (°C)[2]	Water[3] $\delta^{18}O$	Water[3] δD
	The MLTZ						
	93-5	Qtz	10.6			7.8	
	93-11	Qtz	10.8			8.0	
	93-12	Qtz	11.0			8.2	
		Kspar	9.6		560 (Qtz-Kspar)		
		Tour	8.6	-104 (1.9)		7.8	-89
D_1	Regional Penetrative Fabric						
	163	Qtz	10.2			7.8	
	377	Qtz	10.5			8.1	
	378	Qtz	11.9			9.5	
D_2	Shears and Cataclastic Zones						
	165	Qtz	10.2			7.8	
	449	Qtz	9.9			7.5	
		Kspar	10.8				
		Tour	7.2	-60 (2.8)		6.7	-48
	453-2	Qtz	10.5			8.1	
		Ab	8.9		510 (Qtz-Ab)		
		Biot	5.2	-86 (3.4)	520 (Qtz-Biot)	7.7	-52
	453-5	Qtz	10.6			8.2	
	454	Qtz	10.7			8.3	
		Ab	9.0		480 (Qtz-Ab)		
D_3	Rod Shear						
	(Jolu Deposit)						
	93-8	Qtz	10.1			6.8	
		Biot	5.0	-85 (3.3)	530 (Qtz-Biot)	7.4	-46
		Calc	7.9		450 (Qtz-Calc)		
	185	Qtz	11.2			7.9	
	230	Qtz	12.3			9.0	
	419	Qtz	11.2			7.9	
	93-53	Qtz	11.1			7.8	
		Tour		-45 (3.2)			-26
	455-4	Qtz	11.5			8.2	
		Kspar	9.9		510 (Qtz-Kspar)		
		Biot	5.1		450 (Qtz-Biot)		
	93-59	Qtz	10.9			7.6	
		Tour	8.2	-58 (3.1)		7.0	-39

Table 5-1. (continued)

Structural event	Sample	Mineral	Mineral $\delta^{18}O$	Mineral δD	Equilibration Temperature (°C)	Water $\delta^{18}O$	Water δD
	(Pam South)						
	188	Qtz	11.4			8.1	
		Tour		-47 (3.1)			-28
	(Pam North - NE Portion)						
	225	Qtz	10.5			7.2	
	227	Qtz	14.1				
	416	Qtz	10.7			7.4	
	Rush Lake Shear[4]						
	Rush-Au	Qtz	10.7			7.4	
		Tour	8.9	-50 (2.9)		7.7	-31
	Rush-con.	Qtz	10.8			7.5	
		Tour	8.5	-52		7.3	-33
	0066	Qtz	10.5			7.2	
	0068	Qtz	10.8			7.5	
	0071	Qtz	11.1			7.8	
	HT-1	Qtz	11.3			8.0	
		Biot	5.9	-93 (3.0)	510 (Qtz-Biot)	8.3	-54
	HT-2	Qtz	11.3			8.0	
		Tour	8.4	-108 (2.6)		7.2	-89
		Biot	5.7	-111 (2.7)	500 (Qtz-Biot)	8.1	-72
	Star Lake Shear						
	(Star Lake Deposit)[4]						
	60 ft-2	Qtz	10.2			6.9	
		Biot	4.0	-98	460 (Qtz-Biot)	6.4	-59
	60-4b	Qtz	10.3			7.0	
	60-5	Qtz	11.1			7.8	
	60-6	Qtz	10.6			7.3	
	21009A	Qtz	11.5			8.2	
		Calc	9.5		480 (Qtz-Calc)	8.0	
		Hbl	6.8	-113 (1.4)	520 (Qtz-Hbl)	8.6	-80
	260 ft-1	Qtz	10.4			7.1	
		Biot	4.7	-86 (4.1)	490 (Qtz-Biot)	7.1	-47
	260 ft-6	Qtz	10.5			7.2	
		Biot	4.4	-108 (3.2)	470 (Qtz-Biot)	6.8	-69
	360-1	Qtz	11.2			7.9	
	360-3	Qtz	10.1			6.8	
	HG-14	Qtz	10.1			6.8	
		Mt	0.8		500 (Qtz-Mt)	6.9	

Table 5-1. (continued)

Structural event	Sample	Mineral	Mineral $\delta^{18}O$	Mineral δD	Equilibration Temperature (°C)	Water $\delta^{18}O$	Water δD
	K18-1	Qtz	10.8			7.5	
		Kspar	9.4		560 (Qtz-Kspar)		
	K18-2	Qtz	10.7			7.4	
		Kspar	8.6		410 (Qtz-Kspar)		
	16-912	Qtz	10.9			7.6	
		Epid	8.2	-78 (2.0)	490 (Qtz-Epid)	8.0	-43
	DN-2	Qtz	11.2			7.9	
		Biot	4.1	-88	420 (Qtz-Biot)	6.5	-49
	DN-3	Qtz	11.2			7.9	
		Biot	5.3	-99 (4.3)	480 (Qtz-Biot)	7.7	-60
	(Central and NE portions)						
	120	Qtz	10.5			7.2	
		Kspar	9.9				
	122	Qtz	10.2			6.9	
	162	Qtz	10.3			7.0	
	169	Qtz	10.4			7.1	
	183	Qtz	10.7			7.4	
	Broeder Lake Shear						
	(James)						
	478	Qtz	12.6			9.3	
	(Jasper)[5]						
	12	Qtz	12.2			8.9	
	15	Qtz	12.7			9.4	
	17	Qtz	12.9			9.6	
	18	Qtz	11.9			8.6	
	28	Qtz	13.0			9.7	
		Biot	7.5	-67	500 (Qtz-Biot)	9.9	-28
		Biot	6.7		460 (Qtz-Biot)	9.1	
		Tour	10.6	-67		9.4	-48
	104	Qtz	13.8			10.5	
		Musc	10.2		460 (Qtz-Musc)	10.0	
	301	Qtz	13.4			10.1	
		Biot	5.5		390 (Qtz-Biot)	7.9	
	Highgr.#1	Qtz	13.3			10.0	
	Highgr.#2	Qtz	13.7			10.4	
		Musc	10.3	-63	480 (Qtz-Musc)	10.1	-44

Table 5-1. (continued)

Structural event	Sample	Mineral	Mineral $\delta^{18}O$	Mineral δD	Equilibration Temperature (°C)	Water $\delta^{18}O$	Water δD
	(Roxy)						
	182	Qtz	12.3			9.0	
		Kspar	9.9		360 (Qtz-Kspar)		
		Musc	8.2	-51 (4.5)	420 (Qtz-Musc)	8.0	-32
	(NE portion)						
	205	Qtz	10.6			7.3	
	208	Qtz	10.4			7.1	
	212	Qtz	10.1			6.8	
	213	Qtz	9.8			6.5	
D_{3b}	North-South Veins and Flat Veins in James-Jasper-Roxy						
	468	Qtz	11.1			7.8	
	472	Qtz	12.6			9.3	
	473	Qtz	12.5			9.2	
	474A	Qtz	10.0			6.7	
	474B	Qtz	9.7			6.4	
	93-72	Qtz	9.8			6.5	

Notes:

1. Mineral abbreviation: Ab, albite; Biot, biotite; Calc, calcite; Epid, epidote; Hbl, hornblende; Kspar, potassium feldspar; Mt, magnetite; Musc, muscovite; Qtz, quartz; Tour, tourmaline.
2. Calculation of equilibration temperatures was based on the fractionation factors of Bottinga and Javoy (1973, 1975), and O'Neil *et al.* (1969).
3. Calculation of fluid isotopic composition was based on the fractionation factors of Bottinga and Javoy (1973, 1975), and Suzuoki and Epstein (1976), and the average temperatures as estimated from quartz-hornblende fractionations.
4. Compiled and calculated from Ibrahim and Kyser (1991).
5. Compiled and calculated from Hrdy and Kyser (1995).

Table 5-2. Oxygen isotopic composition of minerals and calculated equilibration temperatures from deformed rocks of the MLTZ and D_1 to D_3 structures; and oxygen isotopic composition of hydrothermal fluids in equilibrium with the quartz

Structural Event	Sample	Rock Type & Fabric	Mineral[1]	$\delta^{18}O$ (Mineral)	Equilibration Temperature (°C)[2]	$\delta^{18}O$ (H_2O)[3]
	The MLTZ					
	93-4	Granodiorite	Qtz	10.0	520 (Qtz-Hbl)	7.6
			Hbl	5.3	480 (Qtz-Biot)	
			Biot	4.1	330 (Hbl-Biot)	
	93-3	Protomylonite	Qtz	10.7	500 (Qtz-Hbl)	7.9
			Hbl	5.8	450 (Qtz-Biot)	
			Biot	4.3	280 (Hbl-Biot)	
	93-2	Mylonite	Qtz	11.5	520 (Qtz-Hbl)	8.7
			Hbl	6.8	440 (Qtz-Biot)	
			Biot	4.9	220 (Hbl-Biot)	
D_1	Regional Penetrative Fabric[4]					
	7071	Mafic volcanic rock	Hbl	6.8		
D_2	Structures					
	93-102	Dioritic cataclasite	Qtz	10.8	550 (Qtz-Hbl)	8.4
			Hbl	6.5		
	NS-2	Granodiorite mylonite	Qtz	10.7		
D_3	Rod Shear					
	(Jolu Deposit)					
	93-42	Granodiorite	Qtz	10.3	500 (Qtz-Hbl)	7.9
			Hbl	5.2	440 (Qtz-Biot)	
			Biot	3.6	260 (Hbl-Biot)	
	93-44	Protomylonite	Qtz	10.8	450 (Qtz-Biot)	7.8
			Biot	4.4		
	93-46	Mylonite	Qtz	11.1	490 (Qtz-Hbl)	7.8
			Hbl	6.0	440 (Qtz-Biot)	
			Biot	4.4	260 (Hbl-Biot)	
	228	Mylonite	Hbl	8.7	200 (Hbl-Biot)	
			Biot	6.6		
	(Pam South)					
	93-62	Granodiorite	Qtz	10.1	570 (Qtz-Hbl)	7.7
			Hbl	6.0	500 (Qtz-Biot)	
			Biot	4.5	280 (Hbl-Biot)	
	93-63	Protomylonite	Qtz	11.2	470 (Qtz-Biot)	8.2
			Biot	5.1		

Table 5-2. (continued)

Structural Event	Sample	Rock Type & Fabric	Mineral	$\delta^{18}O$ (Mineral)	Equilibration Temperature (°C)	$\delta^{18}O$ (H_2O)
	93-64	Mylonite	Qtz	11.3	480 (Qtz-Hbl)	8.0
			Hbl	6.1	450 (Qtz-Biot)	
			Biot	4.8	310 (Hbl-Biot)	
	Star Lake Shear					
	93-18	Protomylonite	Qtz	10.9	510 (Qtz-Hbl)	7.9
			Hbl	6.0	460 (Qtz-Biot)	
			Biot	4.6	290 (Hbl-Biot)	
	93-17	Mylonite	Qtz	11.2	480 (Qtz-Hbl)	7.9
			Hbl	6.0	440 (Qtz-Biot)	
			Biot	4.5	280 (Hbl-Biot)	
	Broeder Lake Shear					
	(James)					
	93-29	Granite	Qtz	9.4	590 (Qtz-Hbl)	7.0
			Hbl	5.5	480 (Qtz-Biot)	
			Biot	3.4	200 (Hbl-Biot)	
	93-28	Protomylonite	Qtz	13.0		10.0
			Biot	6.2	430 (Qtz-Biot)	
	93-26	Mylonite	Qtz	13.9		10.6
			Biot	8.1	490 (Qtz-Biot)	
	(Jasper)[5]					
	62-50	Granite	Qtz	9.5		7.1
			Biot	4.0	500 (Qtz-Biot)	
	62-70		Qtz	9.2		
			Biot	4.2	540 (Qtz-Biot)	
	62-90.3		Qtz	11.0		
			Biot	4.2	430 (Qtz-Biot)	
	62-95.1		Qtz	10.0		
			Biot	4.3	490 (Qtz-Biot)	
	62-102.3		Qtz	11.1		
			Biot	4.6	450 (Qtz-Biot)	
	62-107		Qtz	9.3		
			Biot	4.7	570 (Qtz-Biot)	
	62-113.1	Mylonite	Qtz	12.4		9.1
		(Centre of the shear)	Biot	5.6	430 (Qtz-Biot)	
	62-117.3		Qtz	10.5		
			Biot	3.3	410 (Qtz-Biot)	

Table 5-2. (continued)

Structural Event	Sample	Rock Type & Fabric	Mineral	$\delta^{18}O$ (Mineral)	Equilibration Temperature (°C)	$\delta^{18}O$ (H_2O)
	62-140	Granite	Qtz	9.4		7.0
			Biot	2.9	450 (Qtz-Biot)	
	(Roxy) 904-1	Mylonite	Qtz	11.5		8.2
			Musc	8.1	480 (Qtz-Musc)	
			Biot	5.0	450 (Qtz-Biot)	

Notes:

1. Mineral abbreviation: see Table 5-1.
2. Calculation of equilibration temperatures was based on the fractionation factors of Bottinga and Javoy (1973, 1975).
3. Calculation of fluid oxygen isotopic composition was based on the fractionation factors of Bottinga and Javoy (1973, 1975), and the average temperatures as estimated from quartz-hornblende fractionation.
4. Samples of granodiorite and granite are presented with their deformed rocks associated with the MLTZ and D_3 shears.
5. Temperatures calculated from Hrdy and Kyser (1995). Rock fabric is not described in the literature.

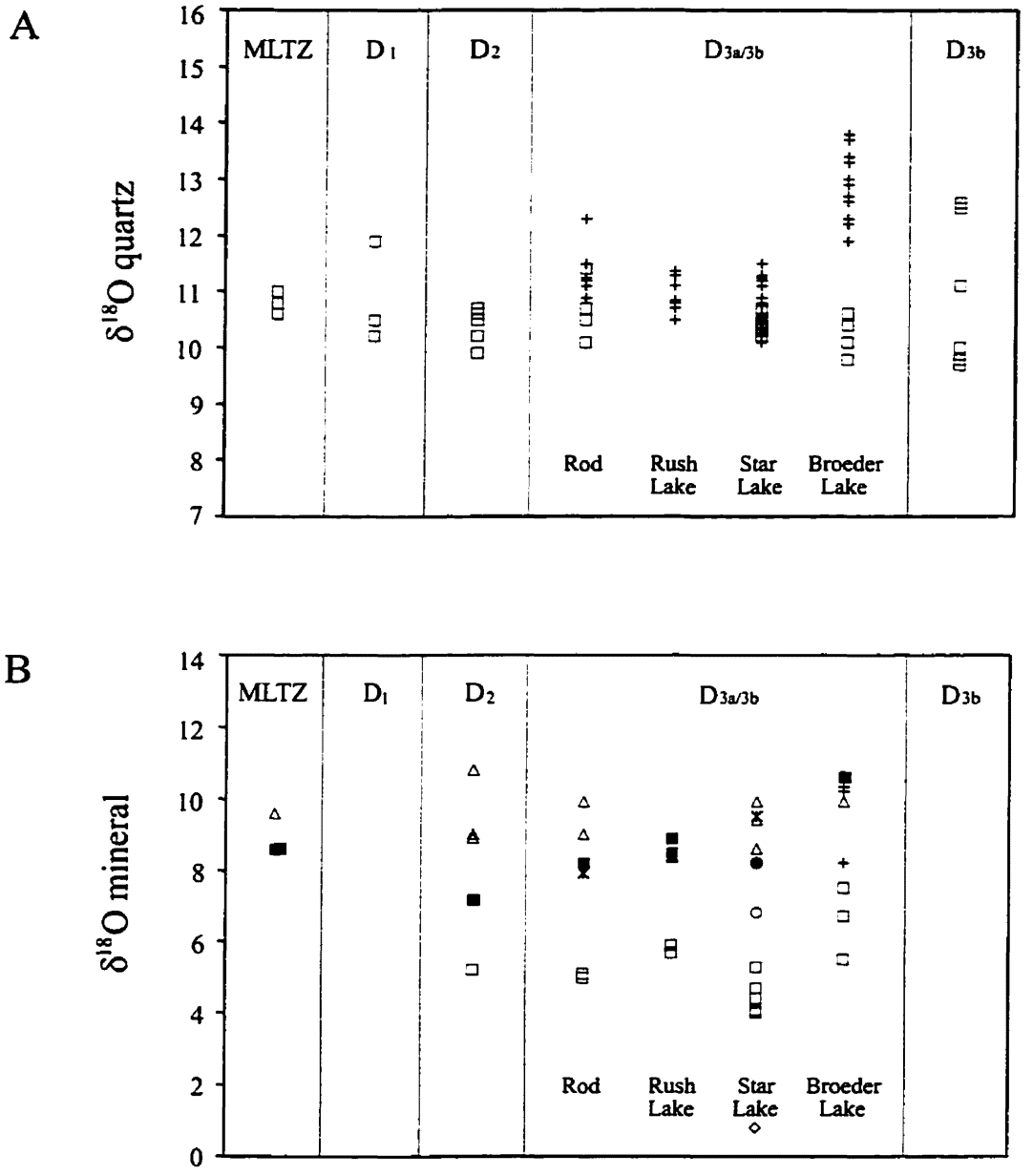

Figure 5-1. Plots of oxygen isotopic compositions of minerals from veins with respect to host structures. (A) Quartz; crosses represent quartz samples from ore bodies. (B) Tourmaline (filled squares); K-feldspar (triangles); biotite (open squares); muscovite (pluses); calcite (stars); epidote (filled circles); hornblende (open circles); magnetite (diamonds).

Quartz from veins in the D_3 shears displays wider variations of oxygen isotopic composition, from 10.0 to 13.8 per mil. The range of $\delta^{18}O$ values, however, is more restricted in individual D_3 shears (e.g. the Rod shear, 10.1 ~ 12.3 per mil; the Rush Lake shear, 10.5 ~ 11.3 per mil; the Star Lake shear, 10.1 ~ 11.5 per mil). Quartz from the orebodies generally shows minor ^{18}O enrichment relative to quartz from the other parts of the shears (Figure 5-1A). Barren quartz veins enriched in ^{18}O were also found sporadically in the shears, such as sample 227 from the northeast of the Pam North of the Rod shear (14.1 per mil) (Table 5-1). They are massive, lenticular quartz veins, undeformed or weakly deformed, and were considered to have been emplaced into the D_3 shears after major periods of shear development. This type of veins is excluded from further discussion in this study.

The auriferous veins in the D_3 James-Jasper-Roxy system are characterized by the enriched $\delta^{18}O$ values of 12.0 ~ 13.8 per mil (Figure 5-1A). The $\delta^{18}O$ values differ substantially from the other deposits in the study area by approximately 2 to 3 per mil. The variation in the oxygen isotopic composition of quartz also occurs along the trend of the Broeder Lake shear zone. The $\delta^{18}O$ values decrease from 12.0 ~ 13.8 per mil in the James-Jasper-Roxy system to 9.8 ~ 10.6 per mil in the northeastern segment of the Broeder Lake shear zone (Table 5-1).

Quartz veins associated with the D_{3b} north-striking shears in the James-Jasper-Roxy system are unmineralized (David Billard, personal communication 1991; Hrdy and Kyser, 1995). The $\delta^{18}O$ values of quartz range from 9.7 to 12.6 per mil, with the majority falling between 9.7 and 11.1 per mil (Figure 5-1A).

Minerals associated with the quartz veins have similar patterns of oxygen isotopic compositions to the quartz (Figure 5-1B). Biotite, tourmaline and potassium feldspar are isotopically uniform in structures other than the James-Jasper-Roxy shears, with the $\delta^{18}O$ values of 4.0 ~ 5.9 per mil, 7.2 ~ 8.9 per mil, 8.6 ~ 10.8 per mil, respectively. In the James-Jasper-Roxy shears, enrichment in ^{18}O was observed in biotite (5.5 ~ 7.5 per mil) and tourmaline (10.6 per mil).

Hydrogen Isotopes

All hydrous silicates analyzed for hydrogen isotopic composition were from vein materials. Hydrous silicates in sufficient abundance to allow analysis could not be found in veins associated with the D_1 fabric and the D_{3b} north-south veins. The hydrous vein minerals, mainly biotite and tourmaline, have a wide range of δD values from -45 to -113 per mil (Table 5-1; Figure 5-2). The variation in δD values is more restricted for individual minerals. Biotite has δD values of -67 to -111 per mil, with biotite from the Jasper deposit lying at the deuterium rich end of the range (Hrdy and Kyser, 1995) (Figure 5-2). The δD values of vein biotite are either identical to or lower than the values of biotite from plutonic rocks, which range from -70 to -80 per mil (Kyser *et al.*, 1986). Tourmaline from the D_2 shears and the D_3 gold-bearing shears is substantially more deuterium enriched (-45 to -67 per mil), with the exception of sample HT-2 from the D_3 Rush Lake shear, which has a δD value of -108 per mil (Ibrahim and Kyser, 1991). Tourmaline from the MLTZ is low in δD value (-104 per mil).

Oxygen Isotopic Composition of Deformed Rocks

To permit meaningful comparison and interpretation of oxygen isotopic composition of the deformed rocks, minerals from the least deformed granodiorite and granite of the Star Lake and Island Lake plutons close to the MLTZ, the D_2 shears and the D_3 gold-bearing shears were chosen to constrain the initial oxygen isotopic composition of the deformed materials (Table 5-2). The $\delta^{18}O$ values of minerals from granodiorite of the Star Lake and Island Lake plutons indicate uniform oxygen isotopic compositions of quartz (10.0 ~ 10.3 per mil), hornblende (5.2 ~ 6.0 per mil) and biotite (3.6 ~ 4.1 per mil). The granite of the Island Lake pluton also has uniform $\delta^{18}O$ values of 9.4 ~ 9.5 per mil and 2.9 ~ 4.0 per mil for quartz and biotite, respectively. The $\delta^{18}O$ value of hornblende from the granite is 5.5 per mil. The isotopic data from the plutonic rocks presumably reflect the thermal conditions of the M_1 metamorphism.

Minerals, including quartz, hornblende and biotite, in deformed rocks

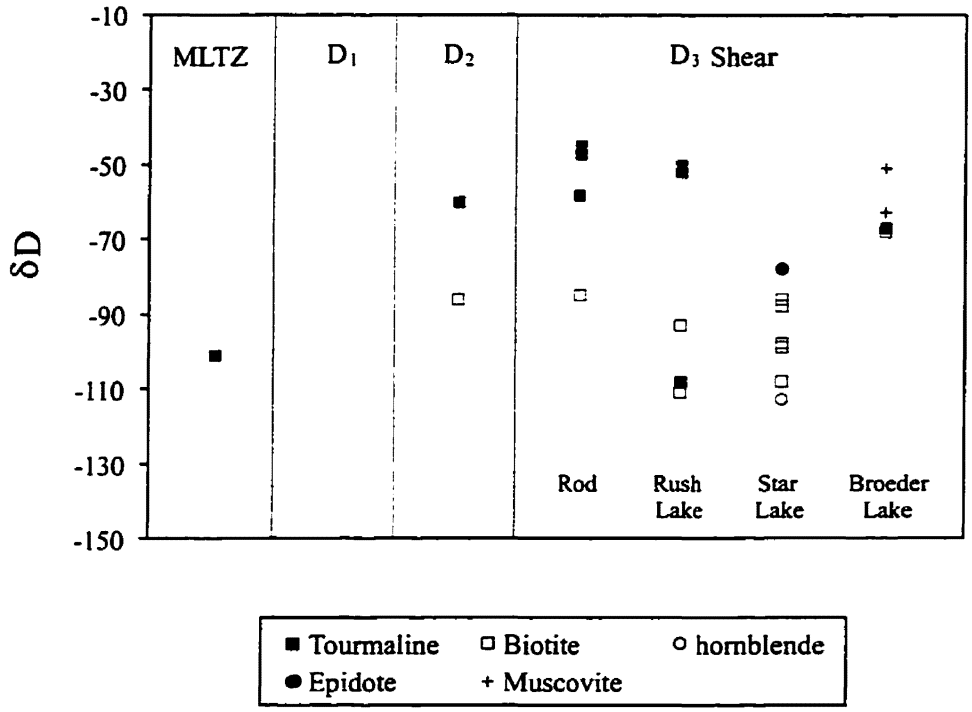

Figure 5-2. Plot of hydrogen isotopic composition of hydrous vein minerals with respect to host structures.

associated with the MLTZ, the D_2 shears and the D_3 gold-bearing shears show positive shifts in oxygen isotopic composition from the least deformed precursors to the mylonite of the structures (Figure 5-3). A similar trend of $\delta^{18}O$ variation was reported in quartz and biotite from the host rock of the Jasper deposit (Hrdy and Kyser, 1995). The $\delta^{18}O$ values of the minerals in the mylonite of the bounding wall rocks are comparable to the values of their vein counterparts (Tables 5-1 and 5-2), indicating that the fluids infiltrating the structures acquired isotopic equilibrium with the immediate mylonitic wall rocks.

Isotopic Geothermometry

Oxygen isotopes provide a useful pressure-independent equilibrium temperature by virtue of the fractionation of ^{18}O and ^{16}O with temperature between different phases (Clayton and Epstein, 1961; O'Neil, 1986). The variation in the differences between the $\delta^{18}O$ values of quartz and any other phase with temperature is described by an equation of the form:

$$\Delta_{quartz\text{-}mineral} = 1000\ ln\alpha_{quartz\text{-}mineral} = A + B/T^2$$

where α is the fractionation factor for quartz and a coexisting mineral, A and B are experimentally or empirically derived constants, and T is temperature. For relatively small fractionation, $\Delta_{quartz\text{-}mineral}$ can be approximated by $\delta_{quartz} - \delta_{mineral}$ (Kyser, 1987).

Equilibrium temperatures for quartz veins and bounding deformed rocks associated with various structures were calculated from oxygen-isotopic fractionation between quartz and coexisting minerals, employing appropriate fractionation equations. The use of three phases permits an evaluation of the extent of isotopic equilibrium preserved in a sample. The empirical isotope geothermometers of Bottinga and Javoy (1973, 1975) were chosen for this study because they include an internally consistent set of fractionation factors for most of the concerned minerals. This avoids the problems inherited from experimentally determined calibrations such as inaccuracies in their determination, uncertainty in the CO_2-H_2O isotopic fractionation factor, differences in the composition of solutions used in the laboratory for synthesis

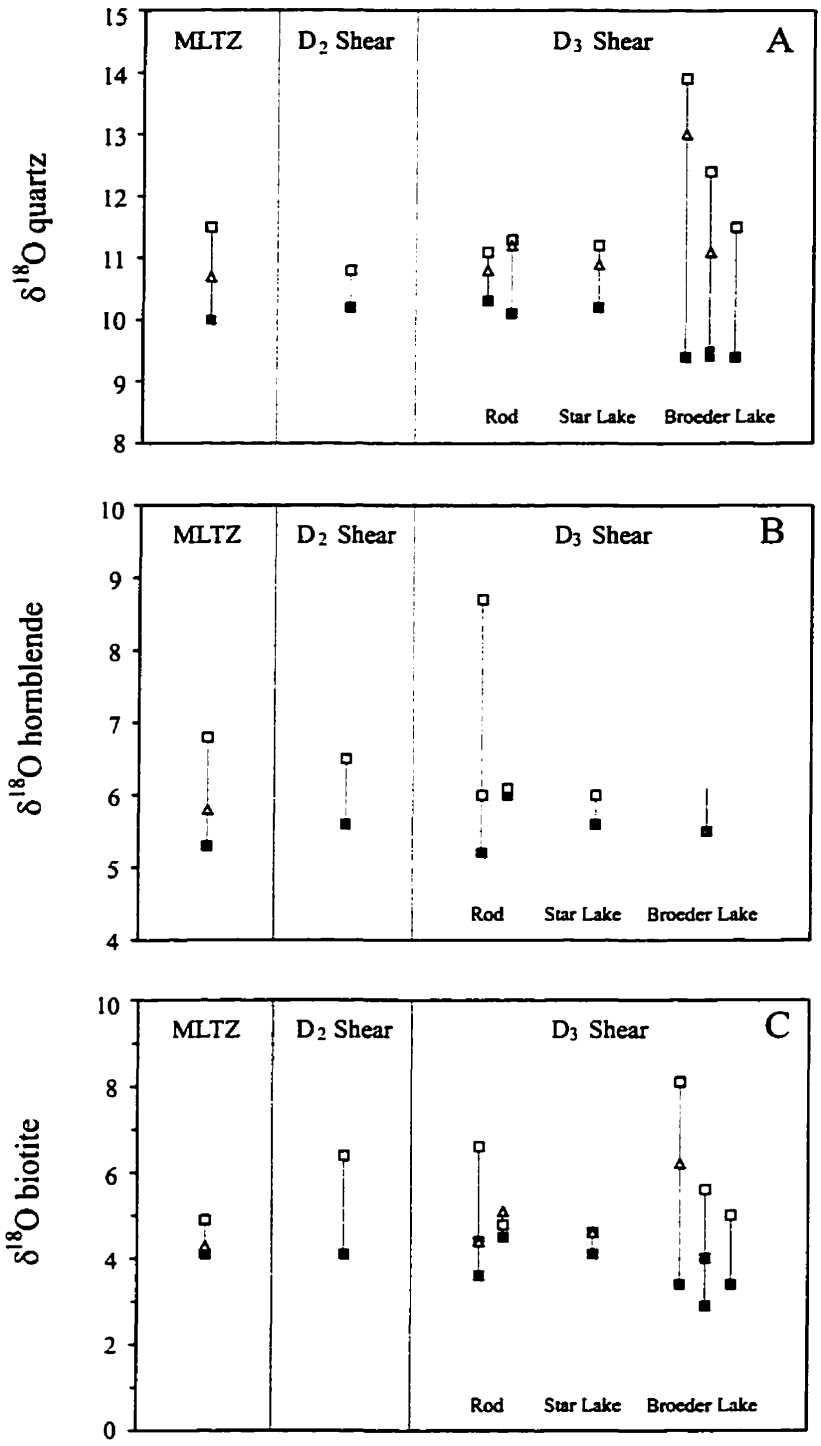

Figure 5-3. Positive shifts in oxygen isotopic composition of minerals in deformed rocks associated with the MLTZ, D_2 shear and D_3 gold-bearing shears. (A) Quartz. (B) Hornblende. (C) Biotite. Average $\delta^{18}O$ mineral values of the granodiorite of the Star Lake pluton are used as the precursors for D_2 shear and D_3 Star Lake shear. Filled squares = Precursors; triangles = protomylonites; open squares = mylonites.

of different minerals, as well as differences in chemistry between the solutions used in laboratory experiments and the natural fluids from which the minerals grew (Deines, 1977). Although internally consistent, experimentally based, fractionation factors for many of the common silicate minerals are available (Chiba *et al.*, 1989), hornblende and biotite, which are the major concern in this study, are not as yet included. Isotopic temperatures from quartz-calcite pairs were obtained using the empirical isotope geothermometers of O'Neil *et al.* (1969) and Bottinga and Javoy (1973).

The calculated temperatures are rounded to the nearest 10°C. The results are presented in Tables 5-1 and 5-2. For respective fractionation factors, the analytical reproducibility of ±0.2 per mil for oxygen isotopic composition translates into errors of calculated temperatures of up to ±50°C (Table 5-3). The isotopic data are also plotted on isotherm plots (Javoy *et al.*, 1970) in Figure 5-4 to assess the degree of relative isotopic equilibrium among the minerals. The solid lines in Figure 5-4 represent the theoretical equilibrium fractionation between quartz and other minerals at the temperatures of 300°, 400°, 500°, and 600°C using the empirical thermometers of Bottinga and Javoy (1973, 1975).

Table 5-3. Temperature uncertainties resulting from a ±0.2‰ precision of the $\Delta^{18}O_{quartz\text{-}mineral}$ and $\Delta^{18}O_{hornblende\text{-}biotite}$ measurements.

Temperature °C	350°	400°	450°	500°	550°	600°
Quartz-Hornblende			±12	±14	±17	±20
Quartz-Biotite		± 8	±10	±12	±15	±17
Quartz-Muscovite		±13	±16	±20		
Quartz-Magnetite				± 8		
Quartz-Epidote			±23	±28		
Quartz-Calcite			±27	±33		
Quartz-K-feldspar	±24	±29	±36	±44	±52	
Hornblende-Biotite		±50	±61	±74	±87	±102

Temperatures Calculated from Quartz Veins

Veins associated with the MLTZ, the D_2 structures, and the D_3 gold-bearing shears typically have one or more phases of silicates that are in textural equilibrium with quartz. This provides an opportunity to assess the temperatures at which minerals acquired their isotopic equilibrium. The lack of sufficient quantity of silicates other than quartz in veins related to the D_1 penetrative fabric and the D_{3b} north-south veins prevents the calculation of isotopic equilibrium temperatures for these structures.

The isotopic fractionation between quartz and potassium feldspar yields a temperature of 560°C for the MLTZ (Table 5-1). In the D_2 structures, the quartz-biotite and quartz-albite pairs give concordant temperatures of 480° to 520°C (Table 5-1).

Isotopic equilibrium temperatures derived from quartz-potassium feldspar pairs from the D_3 gold-bearing shears scatter between 360° and 560°, whereas the other quartz-mineral pairs exhibit closely concordant temperatures (Table 5-1; Figure 5-4A). Quartz-biotite pairs constrain a range of temperatures from 420° to 530°, with only one falling out of this range. Quartz-muscovite and quartz-calcite fractionations correspond to the temperatures of 420° to 480° and 450° to 480°, respectively. The pairs, quartz-magnetite, quartz-hornblende and quartz-epidote, from the Star Lake deposit give concordant temperatures between 490° and 520°. Using the calibration of Eslinger *et al.* (1979), Hrdy and Kyser (1995) gave considerably lower temperatures of 300° to 310° from the quartz-muscovite fractionation for the Jasper deposit.

Temperatures Calculated from Deformed Rocks

Temperatures for the MLTZ, the D_2 shears, and the D_3 gold-bearing shears were obtained from deformed rocks associated with these structures. For the D_1 regional penetrative fabric, temperatures were calculated from the least deformed plutonic rocks close to the MLTZ and the shears. The results are presented in Table 5-2 and Figure 5-4B.

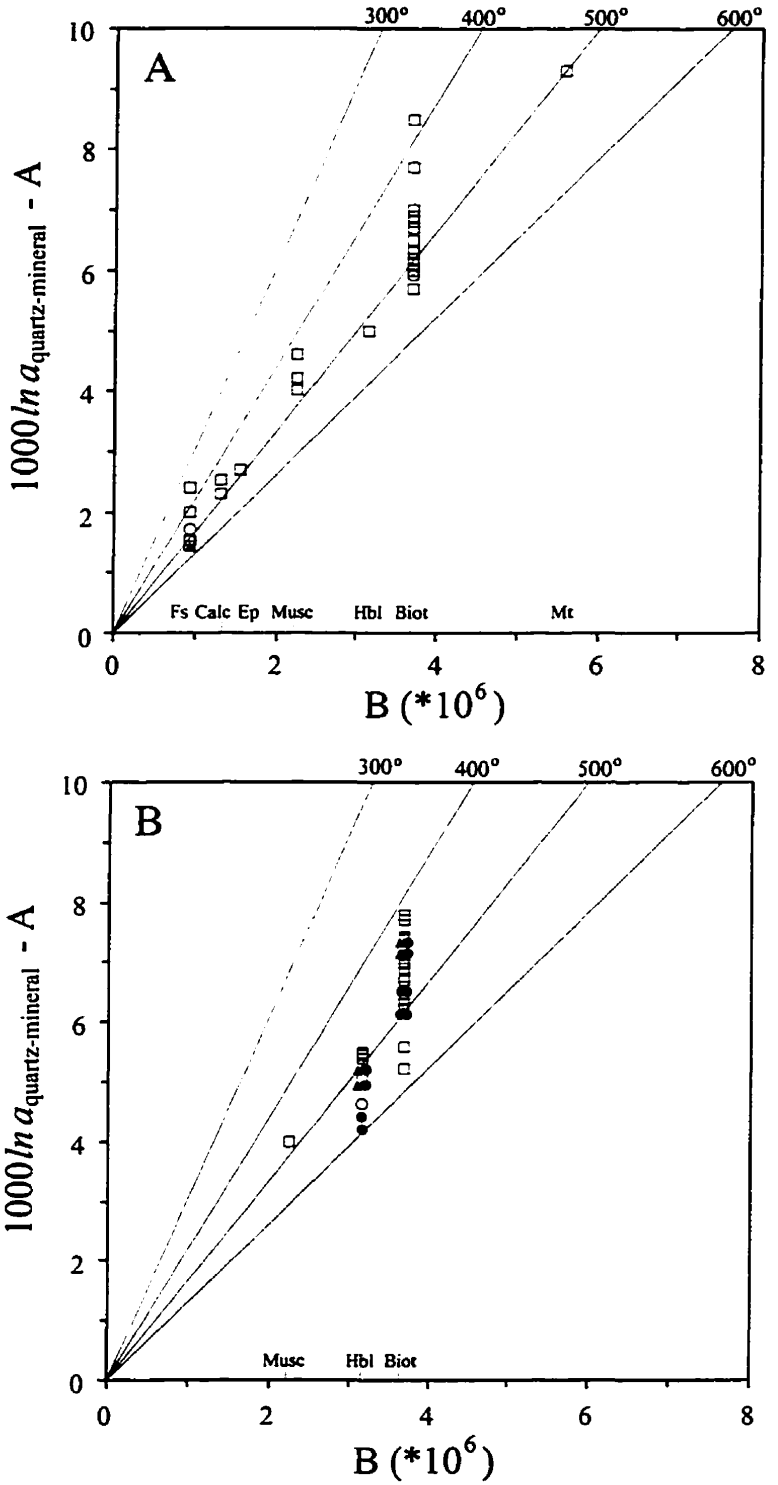

Figure 5-4. Isotherm plots of oxygen isotopic equilibration temperatures for quartz and coexisting minerals. (A) Quartz veins. (B) Host rocks. Filled triangles, the MLTZ; filled circles, D_1 fabric; open circles, D_2 structures; open squares, D_3 gold-bearing shears. A and B are constants for each quartz-mineral pair in the equation 1000 *lna* (quartz-mineral) = A + B/T^2 (Bottinga and Javoy, 1975).

The deformed granodiorite of the MLTZ yields quartz-hornblende temperatures of 500° to 520°C. Quartz-hornblende fractionations associated with the D_1 regional deformation correspond to equilibration temperatures of 500° to 590°C, with an average of 550°C. A single temperature of 550°C was obtained for the D_2 shears. Quartz and hornblende in the deformed rocks of the D_3 gold-bearing shears, including protomylonite and mylonite, define a narrow range of temperatures from 480° to 510°C. The temperatures calculated from the quartz-hornblende pairs are in good agreement with temperatures derived from the cation exchange geothermometers as presented in Chapter 4.

Quartz-biotite equilibration temperatures range from 410° to 570°C for all the structures (Figure 5-4B). The majority of the temperatures cluster at 430° to 500°C. Sample 904-1 yields quartz-muscovite equilibration temperature of 480°C, very close to the quartz-biotite temperature of 450°C. The quartz-biotite pairs yield consistently lower temperatures than quartz-hornblende pairs by 30° to 110°. The discrepancies in apparent temperatures calculated from different pairs of minerals are common in metamorphic rocks and igneous rocks (e.g. Deines, 1977; Bowman and Ghent, 1986).

Discussion

Diffusion Effect on Oxygen Isotopic Exchange

Vein minerals contemporaneously precipitated from hydrothermal fluids are generally considered capable of recording isotopic equilibrium. For oxygen isotopes of deformed rocks to record fluid interactions and fluid temperature accurately, isotopic exchange equilibrium must occur between the rocks and infiltrating fluids. The isotopic data presented above indicate that the $\delta^{18}O$ values of the minerals in the host rocks associated with the structures of high strain, i.e. the MLTZ, D_2 structures and D_3 gold-bearing shears, were shifted positively from the granodiorite or granite to the deformed rocks, and approximated the values of vein minerals, presumably as a result of interaction with a fluid phase (Figure 5-3). Quartz is the most notable mineral that records the shift. This indicates that fluids and rocks appeared to be approaching oxygen isotopic equilibrium with one another, and that oxygen isotopic compositions

of the minerals in the deformed rocks adjacent to the quartz veins can be used to reflect fluid-rock interaction.

The general assumption in measuring the oxygen isotopic compositions of minerals, in order to derive the equilibration temperatures, is that minerals equilibrate at temperatures close to temperatures of formation, and then remain closed systems to oxygen thereafter (e.g. Bottinga and Javoy, 1973). Isotopic equilibrium may be verified if the isotopic compositions of three associated minerals yield two temperature estimates that agree within experimental error (Clayton and Epstein, 1958). The calculated isotopic equilibrium temperatures in this study, particularly the temperatures from the granodiorite and granite, and their deformed rocks, show inconsistencies between different quartz-mineral pairs. Such temperature discrepancies derived from isotopic geothermometers have been recognized in previous studies (e.g. Huebner *et al.*, 1986). They may be ascribed to low temperature fluid exchange and/or continued diffusion of oxygen between mineral phases after crystallization at peak conditions.

The low temperature fluid exchange and continued diffusion of oxygen during cooling may be responsible for the temperature discrepancies if the rates of oxygen diffusion in the minerals are substantially different (Huebner *et al.*, 1986). To evaluate oxygen diffusion in minerals, it is useful to consider the concept of closure temperature. The closure temperature is defined as the temperature at which measurable isotopic exchange of oxygen by diffusion would cease in a given phase during cooling. The closure temperature depends on the shape and size of the mineral, the diffusion rate, and the rate of cooling (Giletti, 1986). Parameters related to oxygen-isotopic exchange for various minerals are summarized in Table 5-4 and Figure 5-5 along with computed closure temperatures and diffusion rates at 550°C and 600°C. There are no published data for oxygen diffusion in epidote and calcite. The closure temperatures for the phases in question were calculated using an equation of Dodson (1973), assuming a crystal 0.05 cm in diameter and using cooling rate of 10°C/m.y. This cooling rate approximates the estimated cooling rate from the $^{40}Ar/^{39}Ar$ systematics of hornblende and biotite (see Chapter 6).

The diffusion data and calculated closure temperatures indicate that the order of oxygen-isotope closures among minerals from the earliest to the latest is

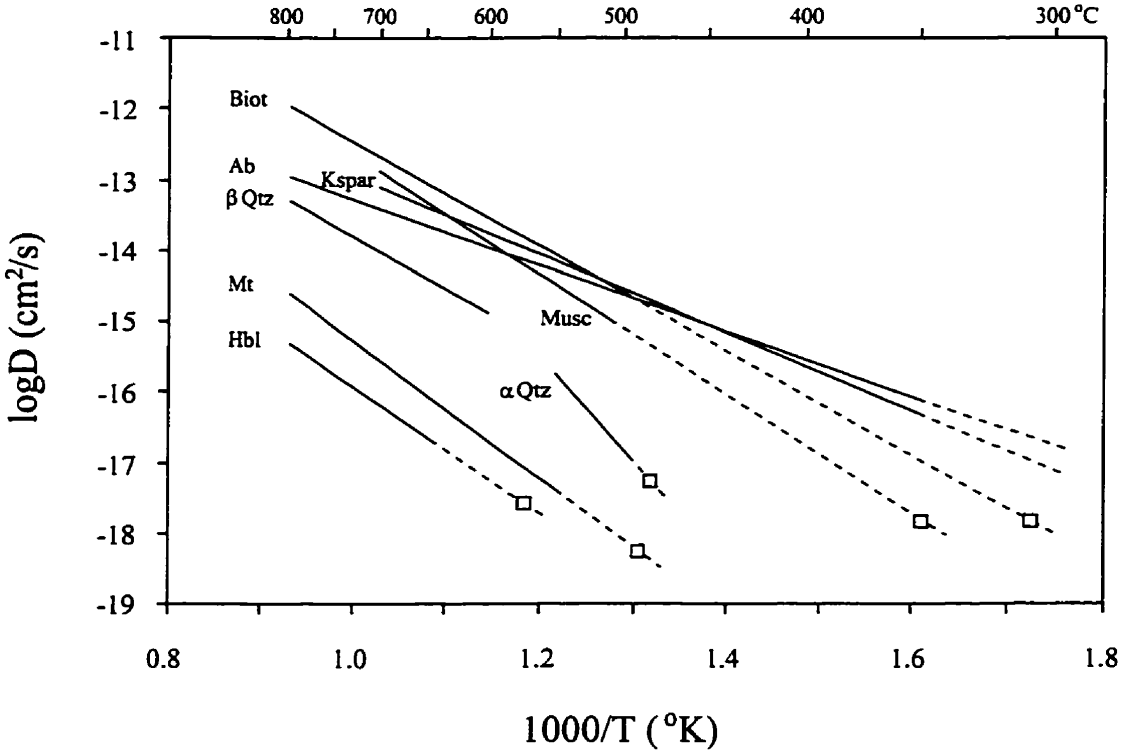

Figure 5-5. Diffusion rate of ^{18}O in minerals plotted as a function of temperature. Also included on this diagram are closure temperatures (open squares) calculated for oxygen exchange in 0.05 cm diameter crystals of the minerals except feldspars using cooling rate of 10 °C/m.y. See Table 5-3 for the origins of the mineral diffusion data.

Table 5-4. Closure temperatures (T_c) and diffusion rates (D) of ^{18}O in various minerals

Mineral	D_0 (cm^2/sec)	Q (kJ/mole)	D (550°)	D (600°)	T_c (°C)[1]	References[2]
α Quartz	1.90×10^{2}	284	1.79×10^{-16}	1.93×10^{-15}	486	1
β Quartz	4.00×10^{-7}	142	3.88×10^{-16}	1.28×10^{-15}		1
Hornblende	1.00×10^{-7}	171	1.40×10^{-18}	5.86×10^{-18}	571	2
Magnetite	3.50×10^{-6}	188	4.09×10^{-18}	1.97×10^{-17}	494	3
Muscovite	7.70×10^{-5}	163	3.47×10^{-15}	1.36×10^{-14}	348	4
Biotite	9.10×10^{-6}	142	8.83×10^{-15}	2.90×10^{-14}	307	4
K-feldspar	4.51×10^{-8}	107	7.29×10^{-15}	1.79×10^{-14}	282	5
Albite	2.31×10^{-9}	89	5.18×10^{-15}	1.09×10^{-14}	254	5

1.Closure temperatures for these minerals were calculated using equation of Dodson (1973), assuming a crystal 0.05 cm in diameter or length and using the cooling rate of 10°C/m.y.
2.References: (1) Giletti and Yund (1984), (2) Farver and Giletti (1985), (3) Giletti and Hess (1988), (4) Fortier and Giletti (1991), (5) Giletti *et al.* (1978).

hornblende, magnetite, quartz, muscovite, biotite and feldspars. The diffusivities of feldspars are comparable to those of micas, but in most cases micas become closed systems for oxygen isotopic exchange before feldspars. The implications of the diffusion rates and closure temperatures for natural systems are such that hornblende is resistant to oxygen isotopic exchange at comparatively high temperature, followed by magnetite and quartz at temperature of approximately 480° to 490°. Muscovite and biotite, especially biotite, can continue to exchange oxygen isotopes by diffusion as temperature drops to as low as 300° while feldspars readily exchange isotopes down to approximately 250° or less. The differences in diffusion rates and closure temperatures are crucial to evaluate the calculated isotopic equilibration temperatures since the calculated temperatures are based on the partitioning of oxygen between two minerals.

In view of these considerations, the temperature disequilibrium seen in the minerals may be collectively interpreted in terms of differential oxygen exchange rates of the minerals with fluids during cooling. It is probable that hornblende, magnetite

and quartz became closed systems to oxygen diffusion exchange at relatively high temperatures, but that biotite and muscovite continued to exchange to lower temperatures. Consequently, quartz-hornblende and quartz-magnetite pairs can provide the best estimates of temperatures, and the quartz-mica or hornblende-mica pairs would not give the same estimates. It is concluded that the differences in oxygen diffusion exchange result in the discordant equilibration temperatures observed between quartz-hornblende and quartz-biotite or quartz-muscovite pairs. This is only one possible explanation, however, since other factors such as susceptibility to mineral reactions and/or the poorly constrained nature of the oxygen isotopic fractionation factor for biotite (Bottinga and Javoy, 1975) might also be responsible for the observed behaviour.

Isotopic Equilibration Temperatures of Deformation and Alteration

As noted above, oxygen isotopic equilibration temperatures require isotopic concordance among coexisting minerals. The application of this criterion must take into consideration the isotopic diffusion of mineral phases. The diffusion discussed in the previous section suggests that even though isotopic equilibrium is found among minerals, the concordant temperatures do not necessarily reflect the peak thermal condition at which the minerals attain their first isotopic equilibrium, because the minerals may remain close to isotopic equilibrium with one another at lower temperatures during retrograde exchange if they have similar diffusion rates (Deines, 1977). In addition, the absolute temperature at which isotopic exchange equilibrium was attained cannot be estimated from the isotopic data alone because calibrations of isotopic exchange geothermometers by different workers are not in good agreement. The calculated equilibration temperatures, either derived from the empirical set of thermometers or deduced from experimentally determined fractionation factors, may not represent real temperatures. But they do indicate the relative equilibration temperatures for various mineral pairs despite differences in their absolute temperatures. Therefore, it is critical that other independent geothermometers are employed to evaluate the isotopic equilibration temperatures.

In this study, hornblende has the slowest diffusion rate and therefore, the

highest closure temperature. Although quartz differs slightly from hornblende in closure temperature, the similarity between the quartz-hornblende equilibration temperatures and the temperatures calculated independently from mineral chemistry indicates that the isotopic composition of quartz did not change substantially as temperature fell below the closure temperature of hornblende. It is likely that both the quartz and hornblende have retained their isotopic compositions and the fractionation between these two minerals can yield good temperature estimates. This may be applied to the mineral pairs of quartz-magnetite as well.

Variations in oxygen isotopic fractionations between the mineral pairs of quartz-hornblende, quartz-biotite and hornblende-biotite during the development of the D_3 gold-bearing shears are shown in $\delta^{18}O$-$\delta^{18}O$ plots of Figure 5-6. The isotopic data from the granodiorite and granite, and the deformed equivalents (protomylonite and mylonite) define good linear relationships, which are subparallel to theoretical equilibrium fractionations at specific temperatures. While all of the minerals shift in oxygen isotopic composition to progressive enrichment of $\delta^{18}O$ towards the central mylonite of the structures (Figure 5-3), the fractionations between the mineral phases increased slightly. Although retrograde exchange may have occurred to one or both phases of the mineral pairs, the linear relationships in the $\delta^{18}O$ - $\delta^{18}O$ diagrams, and thus the relative temperatures among the least deformed plutonic rocks and their deformed rocks, have not been modified considerably. It is therefore concluded that the thermal conditions did not change substantially during the development of the D_3 shears.

The isotopic equilibration temperatures for the structural development and alteration from the isotopic fractionation between quartz and hornblende are summarized in Table 5-5. Also listed for comparison are quartz-biotite and hornblende-biotite temperatures. The hornblende-biotite pair yields unrealistically low equilibration temperatures of 200° to 330°C. This raises the question about the possibility that hornblende and biotite might never have reached isotopic equilibrium. However, because the oxygen isotopic fractionation between hornblende and biotite is small, a ±0.2‰ analytical precision would result in an uncertainty as high as 75°C at 500°C (Table 5-3). Furthermore, a small isotopic shift by diffusion exchange in biotite would cause a large temperature difference since biotite has a rapid rate of exchange

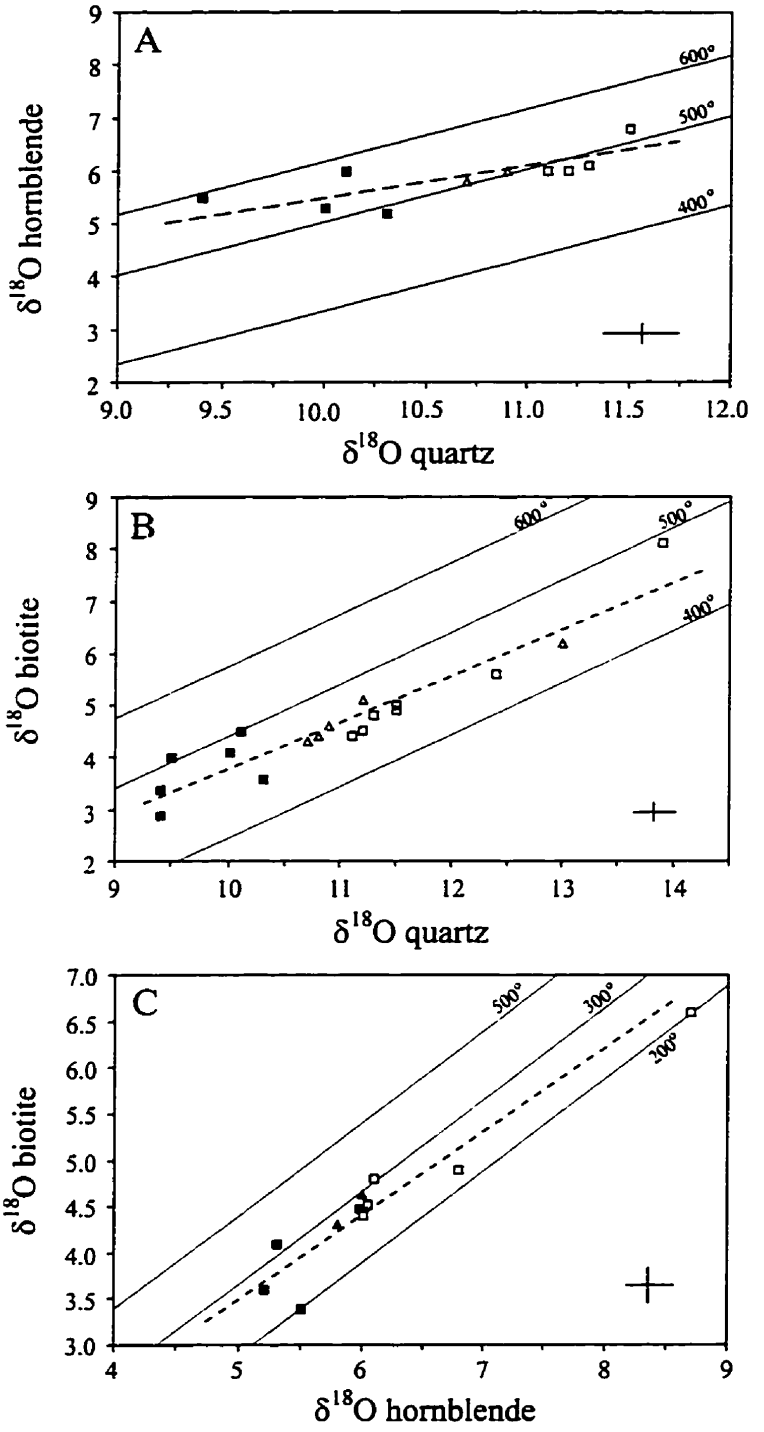

Figure 5-6. $\delta^{18}O$ - $\delta^{18}O$ plots of coexisting mineral pairs from granodiorite and granite (filled squares), and the D_3 shear-related protomylonite (open triangles) and mylonite (open squares). (A) Quartz *vs.* hornblende. (B) Quartz *vs.* biotite. (C) Hornblende *vs.* biotite. The family of solid lines are temperatures corresponding to equilibrium fractionation between the mineral pairs (Bottinga and Javoy, 1973; 1975). The dashed line is regression of the plotted isotopic data, representing the trend of oxygen isotopic variation. Bars represent +/- 0.2 per mil uncertainties.

and, therefore, substantially lower closure temperature than hornblende. It is therefore concluded that temperatures based on fractionation between hornblende and biotite are not meaningful.

Table 5-5. Quartz-hornblende oxygen isotopic equilibration temperatures (°C). Average temperatures are in parentheses

Structure	$T_{quartz\text{-}hornblende}$	$T_{quartz\text{-}biotite}$	$T_{hornblende\text{-}biotite}$
The MLTZ	500 - 520 (510)	440 - 450 (445)	280 - 220 (250)
D_1 Penetrative Fabric	500 - 590 (550)	440 - 500 (475)	200 - 330 (270)
D_2 Structures	550		
D_3 Gold-Bearing Shears	480 - 510 (490)	430 - 490 (450)	200 - 310 (265)

The mineral pairs from quartz veins, mainly quartz-biotite, generally give comparable apparent temperatures to their counterparts from the wall rocks (Tables 5-1 and 5-2; Figure 5-4). The quartz-feldspar pairs yield a wide range of apparent temperatures from 360° to 580°C, some of which are even higher than the quartz-hornblende temperatures. The high temperatures recorded by the quartz-feldspar pairs do not necessarily mean a lack of retrograde exchange. Quantitative modeling of oxygen exchange by diffusion indicates that quartz-feldspar fractionations may become less than those at peak conditions, and in some cases may even be slightly negative (Massey *et al.*, 1994).

The equilibration temperatures of the quartz-hornblende pair from the deformed rocks of the D_3 deformation are consistent with temperatures of 490° to 520° from quartz-hornblende, quartz-magnetite and quartz-epidote fractionations from the auriferous veins of the Star Lake deposit (Ibrahim and Kyser, 1991). The temperatures are substantially higher than the quartz-muscovite equilibration temperatures of 300° to 310° from the Jasper deposit (Hrdy and Kyser, 1995). The difference in the calculated temperature is primarily due to the different calibrations used for the calculations. The calibration of Eslinger *et al.* (1979) on the quartz-muscovite pair was used in Hrdy and Kyser's (1995) calculation, which generally gives

lower temperatures than Bottinga and Javoy's (1973, 1975). In addition, isotopic diffusion of muscovite during cooling would also contribute to the big difference between the quartz-hornblende and quartz-muscovite pairs.

In summary, integration of isotopic and mineralogical data indicates that oxygen isotopic exchange equilibrium was likely obtained at approximately 500° to 590°C during the D_1 regional deformation. The temperature was 550° for the D_2 structures, and 480° to 510°C for the D_3 gold-bearing shears. Isotopic exchange equilibrium and mineral-fluid equilibrium were likely attained in the gold-bearing shears under conditions close to the peak metamorphism.

Isotopic Compositions of Hydrothermal Fluids

The oxygen isotopic composition of the hydrothermal fluids was calculated on the basis of the measured quartz $\delta^{18}O$ values and temperatures estimated above, in conjunction with the quartz-water fractionation equation of Bottinga and Javoy (1973). The hydrogen isotopic composition of the fluids were obtained by the same means as for $\delta^{18}O_{H2O}$, employing the measured δD values of minerals, mainly biotite and tourmaline, and the estimated temperatures, coupled with the appropriate mineral-water fractionation equations (Suzuoki and Epstein, 1976). Because the exchange of hydrogen between water and hydrous minerals is more rapid than the exchange of oxygen (O'Neil and Kharaka, 1976), hydrogen may continue to exchange well below the closure temperature of oxygen. Thus the δD values of the fluids, which were calculated to be in equilibrium with the hydrous minerals on the basis of the apparent temperatures recorded by $^{18}O/^{16}O$ partitioning between quartz and hornblende, represent only the minimum values.

Given the high estimated temperatures for the structural development and vein emplacement, the magnitude of corrections to the calculated isotopic composition of hydrothermal fluids is probably small. Evidence from the study of fluid inclusions indicates that most hydrothermal fluids involved were dilute solutions (Ibrahim and Kyser, 1991; Hrdy and Kyser, 1995). Accordingly, it is assumed that any such corrections to take account of salinity are small.

The calculated oxygen and hydrogen isotopic compositions of waters from vein minerals are given in Table 5-1 and plotted in Figure 5-7. The $\delta^{18}O$ values of hydrothermal fluids in equilibrium with the deformed wall rocks were also calculated and are presented in Table 5-2. The majority of calculated oxygen isotopic composition values of hydrothermal fluids, based on the isotopic composition of the dominant vein quartz, are in the restricted interval between 6.8 and 8.3 per mil for almost all structures with the exception of the James-Jasper-Roxy shears, where the fluids are enriched in oxygen isotopic composition by up to 2 per mil. The hydrogen isotopic composition of hydrothermal fluids varies from -89 to -26 per mil, in contrast to the uniform fluid $\delta^{18}O$ composition. The compositional range of the hydrothermal fluids in equilibrium with the vein minerals overlaps the fields of fluids that have derived from or interacted with metamorphic or magmatic rocks at high temperatures (Figure 5-7). The fluids are comparable to those from the lode gold deposits in the Flin Flon domain of the Trans-Hudson orogen (e.g. Ansdell and Kyser, 1992; Fedorowich *et al.*, 1991) and the Archean counterparts (see Kerrich, 1987).

Estimate of Water-Rock Ratios

The amount of hydrothermal fluids that exchanged with the deformed rocks of the quartz-bearing structures may be estimated by calculating ratios of water oxygen to rock oxygen according to the mass-balance formula for a "single pass" open system:

$$W/R\ (oxygen) = \ln\{(\delta^{18}O^{f}_{rock} - \delta^{18}O^{i}_{rock})/[\ \delta^{18}O^{i}_{water} - (\delta^{18}O^{f}_{rock} - \Delta)] + 1\}$$

(Taylor, 1977). $\delta^{18}O^{i}_{rock}$ and $\delta^{18}O^{f}_{rock}$ are the oxygen isotopic composition of the rock prior to and following fluid-rock interaction, respectively; $\delta^{18}O^{i}_{water}$ refers to the initial composition of infiltrating fluid prior to interaction with the rock mass; and $\Delta = \delta^{18}O^{f}_{rock} - \delta^{18}O^{f}_{water}$. The Δ value is conveniently approximated by assuming that rock $\delta^{18}O$ at equilibrium is equal to the $\delta^{18}O$ value of plagioclase (An_{30}) (Taylor, 1977).

In this study, the calculation of the water-rock ratio was based on quartz $\delta^{18}O$ due to the lack of whole rock $\delta^{18}O$ values. The calculation, however, is reasonable because quartz, hornblende and biotite from the deformed wall rocks are all enriched

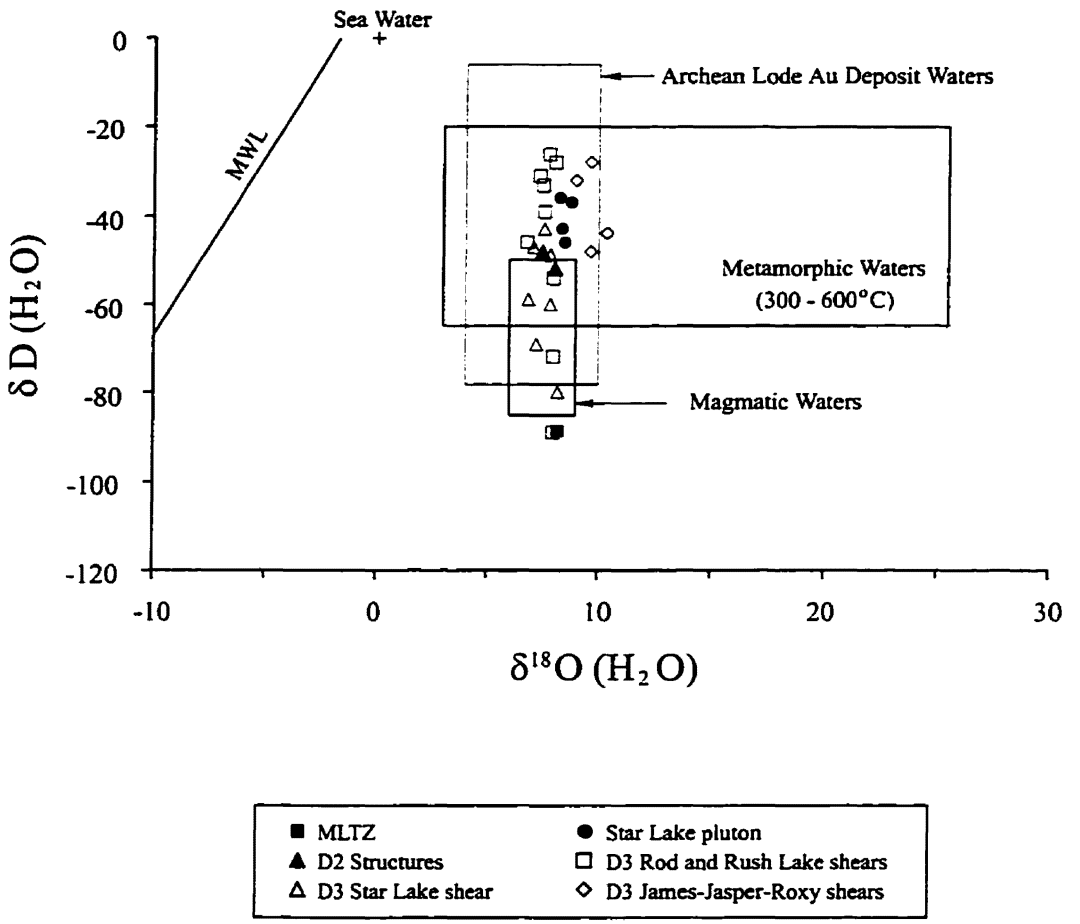

Figure 5-7. Calculated oxygen and hydrogen isotopic compositions of waters involved in the formation of quartz veins. Metamorphic fluid in equilibrium with the Star Lake pluton, presumably during the D_1 regional penetrative deformation, was obtained from Kyser *et al.* (1986). The isotopic compositions of meteoric waters, sea water, and values typical of metamorphic and magmatic waters are shown for reference (Taylor, 1974; Kyser, 1987). The typical range of values exhibited by Archean lode gold deposits is taken from Kerrich (1987).

in $\delta^{18}O$ with respect to the counterparts in the contiguous parent rocks (Figure 5-3), and have comparable $\delta^{18}O$ values to their vein equivalents. The observations suggest that the deformed wall rocks, like the constituent minerals, would exchange with and approach oxygen isotopic equilibrium with the fluid phase that deposited the veins.

The results of the calculations are presented in Figure 5-8. For comparison, the water-rock ratio based on the whole-rock $\delta^{18}O$ values in the Jasper deposit was also calculated from the isotopic data of Hrdy and Kyser (1995). Although the quartz-based calculation does not allow strict constraints on water-rock ratios for the structures as a whole, it places the upper limits on the water-rock ratios and allows comparisons between the structures. Assuming that the deformed rocks of the structures of high strain interacted with a single uniform fluid with an initial $\delta^{18}O$ value of 11.0 per mil, the oxygen water/rock ratios for the MLTZ, the D_2 shear, the D_3 Rod shear and Jasper shear are 0.40, 0.23, 0.53, and 1.95, respectively. The mass water/rock ratios are slightly greater than half the oxygen water/rock ratios since the granodiorite and water contain approximately 50% and 89% oxygen, respectively. The water/rock ratios of the structures are in the order of D_3 Jasper shear > D_3 Rod shear > MLTZ > D_2 shear. It is evident that for fluids with reasonably enriched ^{18}O composition, the water-rock ratios of the structures are fairly large, sufficiently so that an externally-derived hydrothermal fluid is indicated.

Controls on The Oxygen Isotopic Composition of Quartz Veins

The oxygen isotopic composition of quartz veins is primarily controlled by ambient temperature of deposition, the oxygen isotopic composition of fluids and fluid/rock ratios (Kerrich, 1989; Ansdell and Kyser, 1992).

Except for auriferous quartz in the D_3 James-Jasper-Roxy system, the oxygen isotopic composition of vein quartz from the other structures is rather uniform, with the auriferous quartz from the Jolu, Rush Lake and Star Lake deposits showing only limited enrichment in $\delta^{18}O$ (Figure 5-1). The uniformity in oxygen isotopic composition of quartz implies a corresponding uniformity in the $\delta^{18}O$ values of the hydrothermal fluids. The minor enrichment of $\delta^{18}O$ in the auriferous quartz relative to

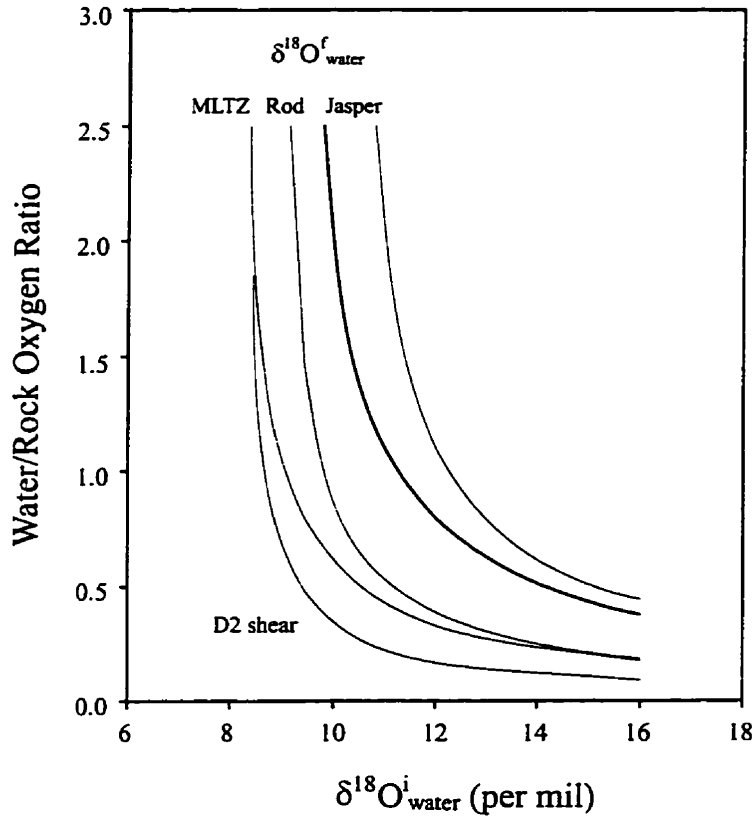

Figure 5-8. Fluid/rock oxygen ratio versus $\delta^{18}O$ of infiltrating fluids in the MLTZ, D_2 shear, D_3 Rod and Jasper shears on the basis of quartz $\delta^{18}O$ values (thin lines). The thick line is based on the whole rock $\delta^{18}O$ values in the Jasper deposit (Hrdy and Kyser, 1995). As granodiorite and water are approximately 50% and 89% oxygen, respectively, the mass water-rock ratio is slightly over half the oxygen water-rock ratio (Taylor, 1977).

barren quartz could be the result of difference in ambient temperature of vein deposition. It could also be the result of interaction with wall rocks at conditions of different fluid/rock ratios. It has been shown that the hydrothermal fluids passing through the host structures were not in isotopic equilibrium with the wall rocks, and the wall rocks became enriched in $\delta^{18}O$ through interaction with the fluids (Figure 5-3). By implication, the isotopic composition of the fluids would shift towards that of the rocks as a result of interaction. The extent of modification of the fluid composition is critically controlled by fluid/rock ratios. At a low fluid/rock ratio the isotopic composition of the fluids would be buffered by the isotopic composition of the wall rocks contiguous to the fluid conduit, whereas at a high fluid/rock ratio the control of the $\delta^{18}O$ of the fluids by the wall rocks is minimal and the fluids more likely retain their composition. Since the barren structures have low fluid/rock ratios with respect to the D_3 gold-bearing structures (Figure 5-8), the fluids infiltrating the barren structures would have become relatively depleted in $\delta^{18}O$ compared with the fluids infiltrating the D_3 structures.

With respect to the other deposits, the auriferous quartz from the James-Jasper-Roxy system is enriched in $\delta^{18}O$ by up to three per mil (Figure 5-1). If the variation in the isotopic composition is solely the result of difference in depositional temperature, a range of temperature of up to approximately 200° would be required. Although the temperature in the James-Jasper-Roxy system is not as well defined as in the other deposits due to the absence of minerals with high closure temperatures to oxygen exchange, such low temperature of deposition would not be expected because it cannot be reconciled with the history of deformation and metamorphism in this area. Thus, the temperature variation alone is an unlikely explanation for the observed variation in the isotopic composition between the James-Jasper-Roxy system and the other deposits. The hydrothermal fluid that deposited the auriferous quartz veins in this system must have acquired the distinct isotopic composition, possibly through interaction with ^{18}O-enriched conduit rocks or mixing with a local reservoir of ^{18}O-enriched fluids before it reached the site of deposition.

Conclusions

The oxygen isotopic composition of quartz from all types of structures is mostly in the restricted range of 10.0 to 11.5 per mil. Auriferous quartz of the Jolu, Rush Lake, and Star Lake deposits has minor $\delta^{18}O$ enrichment relative to the barren quartz. The difference in isotopic composition between the auriferous and barren quartz could be the result of interaction of the fluids with the wall rocks at different fluid/rock ratios, and/or the result of changing temperature of vein deposition.

The auriferous quartz in the James-Jasper-Roxy shears is enriched in $\delta^{18}O$ by up to 3 per mil relative to the other deposits. The enrichment in $\delta^{18}O$ is possibly the result of interaction with ^{18}O-enriched rocks or mixing with a local reservoir of ^{18}O-enriched fluid.

The enrichment of quartz $\delta^{18}O$ from the auriferous veins relative to the barren veins indicates that the oxygen isotopic composition of quartz is a potential tool for exploration.

Minerals in the deformed rocks associated with the McLennan Lake Tectonic Zone, the D_2 structures and the D_3 gold-bearing shears are enriched in oxygen isotopic composition with respect to their equivalents in the precursors. The minerals are isotopically comparable to their vein counterparts. Isotopic equilibrium has been attained between hydrothermal fluids and the bounding deformed wall rocks.

Stable-isotopic systematics yield different isotopic equilibration temperatures among different mineral pairs, of which the pair quartz-hornblende yields temperatures that are closest to temperatures given by independent cation exchange geothermometers. The lower temperatures of the other mineral pairs probably indicate retrograde diffusion exchange.

The fractionation of oxygen isotopes between coexisting quartz and hornblende indicates that oxygen isotopic exchange equilibrium was probably achieved at 500° to 590°C during the D_1 deformation. In the course of the development of the

D_2 structures and D_3 gold-bearing shears, isotopic exchange equilibrium and mineral-fluid equilibrium were attained at approximately 550° and 480° to 510°, respectively.

The oxygen and hydrogen isotopic compositions of hydrothermal fluids that deposited quartz veins are 6.8 to 10.3 per mil and -89 to -26 per mil, respectively. The fluids may have been derived from or interacted with metamorphic or magmatic rocks at high temperatures.

The D_3 gold-bearing shears have larger water/rock ratios than the McLennan Lake Tectonic Zone and the D_2 structures. The deformed rocks associated with the structures may have interacted with externally-derived hydrothermal fluids.

CHAPTER 6

GEOCHRONOLOGY

Introduction

Recent attempts to date the age of gold mineralization in shear-hosted, lode-gold deposits in the Star Lake-McLennan Lake district, based on the age of formation of associated hydrothermal minerals, have produced results that span over 80 Ma (Ibrahim and Kyser, 1991; Hrdy and Kyser, 1995; Thomas and Heaman, 1994). The wide span of the ages may be due to gold emplacement (or remobilization) at successive deformation episodes, or they may reflect the specific mineral isotopic systems used for age determination.

A detailed $^{40}Ar/^{39}Ar$ study was undertaken on metamorphic hornblendes from structures of different ages as demonstrated by their crosscutting relationships, including hornblende from a gold-bearing shear, in an attempt to bracket the timing of gold mineralization and to test whether the dates given by $^{40}Ar/^{39}Ar$ technique represent the ages of mineralization or only reflect argon resetting subsequent to the peak of regional metamorphism.

Previous Results

Previous geochronological data from the La Ronge Domain are summarized in Tables 6-1 and 6-2, and are outlined in Figure 6-1. The ages for volcanism in the Central Metavolcanic Belt were determined by Bickford *et al.* (1986) from U-Pb ages of zircons to be 1882 to 1879 Ma. The U-Pb and Pb-Pb ages of zircons of magmatic origin from the Star Lake and Island Lake plutons, from three sources, Bickford *et al.*, (1986), Thomas and Heaman (1994) and Hrdy and Kyser (1995), are 1855 to 1846 Ma. U-Pb and Pb-Pb ages of metamorphic zircons from seven plutons in the southern part of the La Ronge Domain, and one from metamorphic zircons in metavolcanic

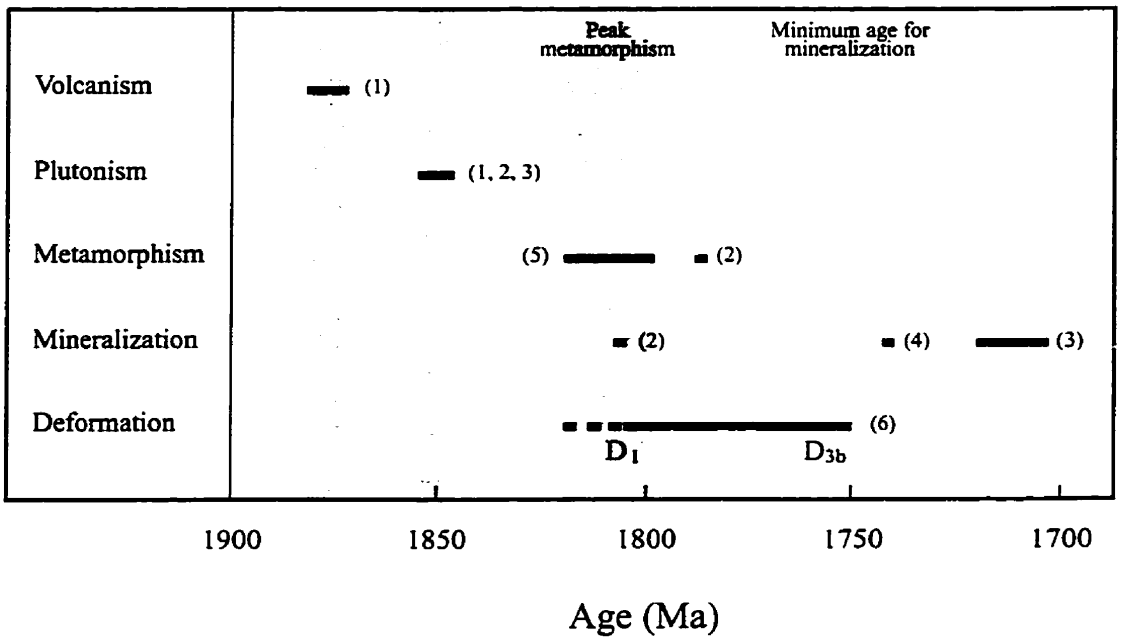

Figure 6-1. Schematic diagram outlining the major geological events through time that affected the Star Lake-McLennan Lake area. References: 1, Bickford *et al.* (1986); 2, Thomas and Heaman (1994); 3, Hrdy and Kyser (1995); 4, Ibrahim and Kyser (1991); 5, Kyser and Stauffer (1995); 6, this study.

Table 6-1. Summary of geochronological data for volcanism, plutonism, metamorphism and gold mineralization from the Star Lake-McLennan Lake area

Mineral Host	Mineral Origin	Dating Method	Age (Ma)	References*
		Volcanism and Plutonism		
Felsic metavolcanic	Magmatic	U-Pb zircon	1879 ± 66	1
Felsic metavolcanic	Magmatic	U-Pb zircon	1882 ± 9	1
Star Lake pluton	Magmatic	U-Pb zircon	1848 ± 14	1
		U-Pb zircon	1846 ± 2	2
Island Lake pluton	Magmatic	U-Pb zircon	1855 ± 22	1
		Pb-Pb zircon	1855 ± 8	3
		Metamorphism		
Star Lake pluton	Metamorphic	U-Pb titanite	1784	2
		Mineralization		
Mineralized mafic dyke, Jolu deposit	Hydrothermal /metamorphic	U-Pb titanite	$1807\ ^{+28}_{-5}$	2
Gold-bearing quartz vein, Star Lake deposit	Hydrothermal	Rb-Sr tourmaline-feldspar	1742 ± 87	4
Gold-bearing quartz vein, Jasper deposit	Hydrothermal	Rb-Sr tourmaline-muscovite	1720 ± 8	3
		Ar-Ar muscovite	1703 ± 3	3

* References: 1, Bickford *et al.* (1986); 2, Thomas and Heaman (1994); 3, Hrdy and Kyser (1995); 4, Ibrahim and Kyser (1991)

rocks, constrain ages of regional metamorphism to 1798 to 1820 Ma (Kyser and Stauffer, 1995). The metamorphic ages are consistent with what have been observed elsewhere in the Trans-Hudson Orogen, such as the Glennie Domain (1830-1800 Ma, Chiarenzelli, 1989; 1815 Ma, Durocher, 1997), the Hanson Lake Block (1808-1804 Ma, Heaman *et al.*, 1994), the Kisseynew Domain (1815-1810 Ma, Gordon *et al.*, 1990; 1808-1804 Ma, Ashton *et al.*, 1992), and northwestern Flin Flon Domain (1807-1806 Ma, Ashton *et al.*, 1992). Thomas and Heaman (1994) reported a

significantly younger age of 1784 Ma for metamorphism of the Star Lake pluton on the basis of the U-Pb systematics of titanite.

Table 6-2. Metamorphic zircon ages from the southern portion of the La Ronge Domain (Kyser and Stauffer, 1995)

Mineral Host	Dating Method	Age (Ma)
Jepson Lake pluton	U-Pb	1798 ± 3
Sulphide Lake volcanic complex	Pb-Pb	1805 ± 5
Bridgeman Lake pluton	Pb-Pb, U-Pb	1820 ± 10
Bing Lake pluton	Pb-Pb	1805 ± 5
Kruger Lake pluton	Pb-Pb	1820 ± 5
Moir Lake pluton	Pb-Pb	1800 ± 5
Wilson Lake stock	Pb-Pb	1805 ± 5
Roundish Lake stock	Pb-Pb	1805 ± 5

Ibrahim and Kyser (1991) presented a Rb-Sr age of 1742 ± 87 Ma from hydrothermal tourmaline and feldspar in the Star Lake deposit. Hrdy and Kyser (1995) constrained the age of gold mineralization in the Jasper deposit at 1703 Ma from a disturbed $^{40}Ar/^{39}Ar$ age of gold-related muscovite, and 1720 Ma from Rb-Sr isotope systematics of muscovite and tourmaline. From this, the authors concluded that mineralization postdated peak metamorphism by as much as 100 million years. Thomas and Heaman (1994) dated mineralization at 1807 Ma, based on a U-Pb titanite age from a deformed and mineralized mafic dyke in the Jolu Mine. This predated peak metamorphism, 1784 Ma, by as much as 20 m.y.

$^{40}Ar/^{39}Ar$ Hornblende Systematic

Sampling and Analytical Method

Three hornblende samples, representing three episodes of hornblende growth

in the D_1, D_2 and D_3 structures, were selected from the Jolu Mine area. HBL7071 defines the S_1-L_1 penetrative fabric in a unit of mafic metavolcanic rock (Figure 4-1). HBL072 comes from a D_2 shear hosted in the mafic metavolcanic rock (Figure 4-6C). HBL228 is from the central phyllonite zone of the Rod shear that hosts the Rod Main orebody and represents the D_{3b} episode of hornblende growth (Figure 4-11).

Samples for age determination were selected after detailed petrographic examination and electron microprobe analyses, which are presented in Table A-1. Mineral concentrates were prepared by standard crushing, sieving, magnetic separation and heavy-liquid flotation. Final sample separates were hand-picked to ensure purity. Ar-Ar isotope analyses were performed at the Department of Geological Sciences, Queen's University using irradiation, extraction, mass spectroscopic, and correction procedures as described by Baksi *et al.* (1996).

Results

The isotopic data for the three hornblende samples and one duplicate from the step-heating analyses are presented in Table 6-3 and, in the form of step-heating age spectra, in Figure 6-2. An age plateau is one where at least two successive heating steps which represent more than 50% of the total gas released have apparent ages that are identical within experimental uncertainty at the 2σ level (Fleck *et al.*, 1977). Accordingly, the spectra of hornblende HBL7071, HBL072 and HBL228 have plateau ages of 1753 ± 6 Ma (seven steps representing 92.4% of the total ^{39}Ar released), 1754 ± 10 Ma (two steps, 84.5% of the total gas) and 1748 ± 9 Ma (six steps, 76.4%), respectively. The spectrum of HBL072 duplicate has a 1752 ± 13 Ma plateau (six steps, 92.7% of the total gas). The age spectra of hornblendes have young ages in the first or second low-temperature increments, but acquire well-defined plateaus quickly and systematically in their higher-temperature increments. Such datum profiles may reflect $^{40}Ar^*$ loss resulting from late-stage heating or volume diffusion which likely causes more $^{40}Ar^*$ loss in the rims than in the cores of the mineral.

Table 6-3. Analytical data for $^{40}Ar/^{39}Ar$ step-heating experiments

Power	$^{40}Ar/^{39}Ar$	$^{37}Ar/^{39}Ar$	$^{36}Ar/^{39}Ar$	Ca/K	$\%^{40}Ar^*$	$\%^{39}Ar$	$^{40}Ar^*/^{39}Ar_K$	Age (Ma ± 2σ)
HBL7071(104°17'47", 56°00'05"; J=0.028576)								
1000	70.143	1.000	0.143	7.35	42.57	0.66	28.718	1081 ± 187
1500	57.910	1.448	0.015	11.54	97.64	5.89	57.440	1752 ± 28
1750	56.958	1.458	0.007	11.63	99.21	12.52	57.247	1749 ± 8
2000	57.137	1.509	0.004	12.03	99.63	19.94	57.642	1756 ± 10
2250	57.229	1.469	0.003	11.74	99.30	30.09	57.519	1754 ± 7
2500	57.315	1.516	0.008	12.10	98.46	10.95	57.119	1746 ± 11
2750	57.204	1.459	0.010	11.81	99.29	8.65	57.565	1755 ± 25
3000	57.167	1.500	0.000	12.53	100.81	1.04	60.395	1809 ± 372
4000	56.400	1.520	0.000	12.42	99.87	4.36	57.886	1761 ± 75
6000	54.716	1.481	0.012	12.13	99.20	7.10	55.406	1712 ± 24
HBL072 (104°17'20", 55°59'54"; J=0.028579)								
1500	72.409	2.409	0.091	19.60	64.45	7.18	48.285	1564 ± 55
2000	57.507	3.412	0.007	27.33	98.22	48.92	57.626	1756 ± 12
2500	56.963	3.546	0.009	28.54	98.50	35.61	57.409	1752 ± 19
2750	55.200	3.200	0.000	25.27	91.43	1.69	50.560	1613 ± 623
3250	55.375	3.125	0.125	27.24	85.31	2.53	50.622	1614 ± 268
3750	60.400	3.600	0.000	28.00	97.55	1.74	57.396	1752 ± 481
4200	60.667	3.333	0.000	27.15	82.65	1.08	47.398	1545 ± 1332
6000	59.556	3.556	0.000	28.89	95.84	3.04	57.137	1747 ± 256
HBL072 Duplicate								
750	98.222	0.444	0.222	3.02	41.34	2.04	42.401	1432 ± 147
1250	56.176	1.588	0.059	12.56	85.88	3.95	48.452	1568 ± 250
1500	57.167	2.833	0.000	22.98	93.82	2.84	53.314	1670 ± 155
1750	57.472	3.151	0.019	25.65	97.41	12.18	56.795	1740 ± 29
2000	56.279	3.213	0.007	26.34	98.99	30.96	56.968	1743 ± 13
2250	57.289	3.114	0.009	25.38	99.88	26.11	58.152	1766 ± 16
2750	57.659	3.171	0.000	25.79	100.05	9.44	58.479	1773 ± 76
3750	55.174	3.000	0.000	24.95	98.94	5.18	56.677	1738 ± 108
6000	56.231	3.103	0.026	25.62	98.98	8.86	57.151	1747 ± 38
HBL228 (104°16'52", 56°00'06"; J=0.028559)								
1000	52.792	0.333	0.083	2.57	65.79	2.61	34.485	1237 ± 55
1500	56.056	1.167	0.011	9.45	97.79	9.58	55.581	1715 ± 24
1750	57.348	1.489	0.004	12.10	99.59	24.23	57.778	1758 ± 12
2000	56.787	1.429	0.003	11.64	99.40	36.97	57.181	1747 ± 7
2250	57.377	1.651	0.009	13.46	99.17	11.27	57.851	1760 ± 26
2500	55.200	1.400	0.000	10.97	99.02	0.56	52.750	1658 ± 480
3000	54.083	1.333	0.000	10.83	99.06	1.30	53.498	1673 ± 231
3500	54.105	1.263	0.000	10.04	97.27	2.02	53.479	1673 ± 160
4000	49.412	1.000	0.000	8.06	98.32	1.79	49.933	1599 ± 161
6000	53.853	1.196	0.010	9.76	99.07	10.82	54.278	1689 ± 26

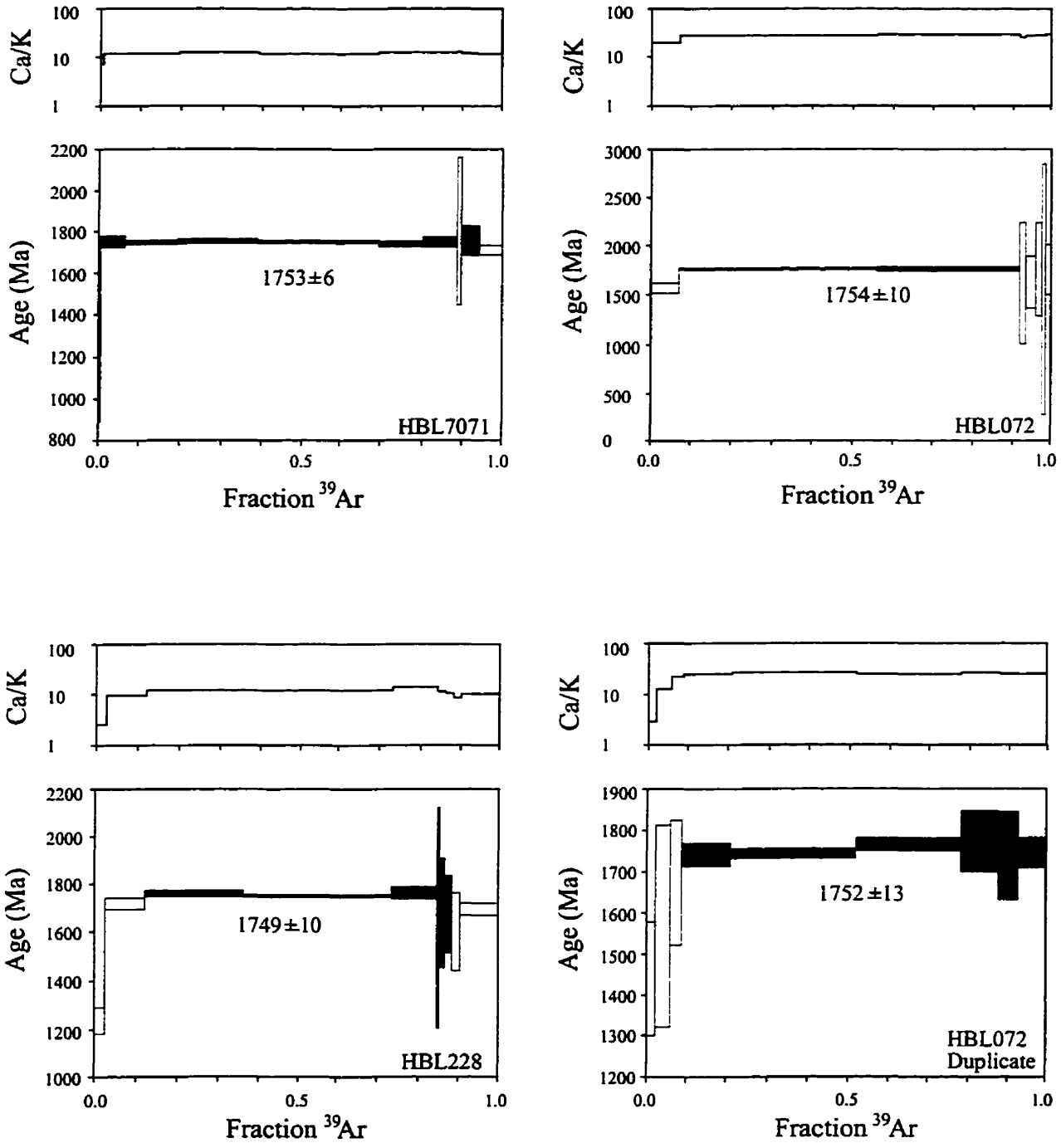

Figure 6-2. $^{40}Ar/^{39}Ar$ incremental-release age spectra and apparent Ca/K spectra of hornblende separates. Uncertainty in ages (2σ) is represented by vertical heights of the bars. Plateau ages are indicated by shaded bars.

Implications of The Age Data

The $^{40}Ar/^{39}Ar$ hornblende dates presented in this study are the same within error and show no dependence on paragenesis. The consistency of the dates strongly indicates a close link of $^{40}Ar/^{39}Ar$ systematics to closure of hornblende to argon loss with decreasing regional temperature. The loss of argon is very probable, because the generally accepted closure temperature to argon diffusion in hornblende isapproximately 500°C (Harrison, 1981), which is below the estimated temperature of hornblende formation associated with M_1 and M_2 metamorphic events. The $^{40}Ar/^{39}Ar$ plateau ages of hornblendes, therefore, would record the time of cooling through approximately 500°C, rather than the time of hornblende crystallization.

The last thermal event M_{3b}, which was coeval with the D_{3b} dextral shear deformation, attained estimated temperatures of approximately 480° to 510°C. The temperatures are roughly equal to the blocking temperature of hornblende for argon retention. Consequently, the $^{40}Ar/^{39}Ar$ plateau age of *ca.* 1750 Ma may be able to provide a close estimate for the time of the D_{3b} deformation and the coeval metamorphism, and a minimum estimate of age for gold mineralization.

The relationship of $^{40}Ar/^{39}Ar$ systematics to closure of minerals to argon diffusion indicates that a dated mineral that has a lower closure temperature would yield a younger age. Based on this consideration, the disturbed $^{40}Ar/^{39}Ar$ muscovite age of 1703 Ma from the Jasper deposit (Hrdy and Kyser, 1995) would approximate the time of cooling through 350°C, the closure temperature of muscovite to argon loss (Hanes, 1991). Comparatively, young ages of 1719 Ma are also reported for biotite from the Rush Lake shear zone and adjacent wall rock (Kyser *et al.*, 1992), reflecting the 300°C closure temperature for biotite (Harrison *et al.*, 1985). The $^{40}Ar/^{39}Ar$ ages of hornblende and biotite, in conjunction with the closure temperatures for these minerals, reveal a slow linear cooling rate of approximately 6.5°C/m.y. after the regional temperature dropped through 500°C.

The structural and metamorphic evidence from this study does not support a pre-peak metamorphic model for gold mineralization as proposed by Thomas and Heaman (1994), but does agree with the suggestion that gold-bearing quartz veins

were emplaced into the shear zones subsequent to the attainment of regional peak metamorphism (Kerrich, 1989). Thomas and Heaman's (1994) model does not take into consideration metamorphic paragenesis. Because this region underwent several episodes of deformation and metamorphism, several generations of titanite may be anticipated. Therefore, the interpretation of 1784 Ma age from a single fraction of titanite as the age of peak metamorphism is questionable. The reported metamorphic zircon ages in the southern part of the La Ronge Domain span a period of *ca.* 20 m.y. from 1798 to 1820 Ma (Kyser and Stauffer, 1995). Six of the eight samples, including two from the Wilson Lake pluton and Roundish Lake stock, approximately 15 to 20 km to the southwest of the study area, have a more restricted range of 1798 to 1805 Ma, as much as 20 m.y. earlier than the 1784 Ma titanite age. It is probable that these dates represent different metamorphic events. If the metamorphic zircon ages of 1798 to 1805 Ma are taken to constrain the timing of peak metamorphism, then the 1784 Ma titanite age may represent one of the post-peak thermal events.

The geochronologic studies to date have yet to provide a convincing timing of gold mineralization in this region. The U-Pb titanite age of 1807 Ma, which was proposed as the best estimate for gold mineralization by Thomas and Heaman (1994), is approximately identical to the metamorphic zircon ages of 1798 to 1805 Ma. The titanite fractions were sampled from an amphibolitized mafic dyke in the mineralized zone. As stated by the authors, the origin for the titanites is likely hydrothermal or metamorphic. The titanite dates are somewhat discordant (2.6 to 5.1%). One titanite fraction is distinctly low in uranium content (38 ppm) relative to the other two fractions (207 and 276 ppm, respectively), which suggests a mixed origin or paragenesis of titanites in this sample. If the titanites are of hydrothermal origin, the gold mineralization was thus broadly syn-metamorphic. If they are a metamorphic phase, the age provides a maximum estimate for mineralization. In conjunction with the $^{40}Ar/^{39}Ar$ hornblende ages of this study, the timing of gold mineralization in the region can be bracketed in a broad period between 1807 and 1750 Ma.

Conclusions

The hornblende ages derived from the $^{40}Ar/^{39}Ar$ technique are the same, within error, and there is no relationship between the ages and paragenesis. The hornblende ages of *ca.* 1750 Ma probably reflect the time of cooling through the closure of hornblende to argon diffusion at 500°.

The age of *ca.* 1750 Ma may approximate the time of the D_{3b} deformation and the simultaneous metamorphism, and provides a minimum age for gold mineralization.

The emplacement of the gold-bearing quartz veins into the shear zones probably took place subsequent to the peak of regional metamorphism, at the time of 1807 to 1750 Ma.

The Star Lake-McLennan Lake area underwent a slow cooling of approximately 6.5°C/m.y. after the temperature passed below 500°C.

CHAPTER 7
SUMMARY AND DISCUSSION

Summary and Contributions to Knowledge

1. The shear-hosted lode gold deposits are located in the calc-alkaline Star Lake and Island Lake plutons (Janser, 1993), emplaced in the calc-alkaline and low-potassium tholeiitic volcanic rocks of the Central Metavolcanic Belt (Harper *et al.*, 1986; Watters and Pearce, 1987). The Central Metavolcanic Belt represents the remnant of one of the juvenile island arcs formed during the Trans-Hudson Orogen, which involved convergence and collision between the Archean Superior and Hearne cratons during the Paleoproterozoic Era (Hoffman 1988, 1990).

2. During and following the terminal continent-continent collision of the Trans-Hudson Orogen, the area underwent a period of transpression, which involved northwest-southeast compression and associated subvertical extension, and simultaneous dextral transcurrent shearing parallel to the southeastern boundary of the Central Metavolcanic Belt. The transpression is expressed in the fabrics as three episodes of deformation: D_1 regional penetrative deformation; D_2 deformation which resulted in the formation of mesoscopic shears and cataclastic zones; and D_3 deformation which involved the development of the gold-bearing shears, and their subsequent deformation.

3. The gold deposits were emplaced into the D_3 shears during the relatively late stage of transpression, synchronously with the dip-slip shearing. The deposits were subsequently deformed by the strike-slip and (at the Jolu Mine) oblique-slip shearing of the D_{3b} deformation.

4. The McLennan Lake Tectonic Zone is probably not a transcrustal-scale feature, but a shear zone related to limb sliding of the regional synform cored by the McLennan Group, developed at the contacts of lithological units with

contrasting rheologies. The rocks of the McLennan Lake Tectonic Zone were deformed and metamorphosed under the same conditions of the D_1 regional penetrative fabric.

5. There are no intrinsic relationships between gold mineralization and the tectonic history of the McLennan Lake Tectonic Zone. The interpretation of the D_3 gold-bearing shears as subsidiary structures of the McLennan Lake Tectonic Zone is not justified.

6. Three episodes of metamorphism are defined in the area from the fabrics of the D_1 to D_3 deformation. The peak metamorphism of low to middle amphibolite grade (M_1) was coeval with the D_1 deformation. Temperature and pressure of the M_1 metamorphism were approximately 545° to 575°C and 4.5 to 5.0 kbars (Table 4-2). The P-T conditions of the M_2 metamorphism, which was synchronous with the D_2 deformation, were approximately 500° to 550°C and 3.0 to 4.0 kbars (Table 4-3). The M_3 metamorphism, with which the gold mineralization was associated, was under conditions of 480° to 500°C and 3.0 to 4.0 kbars (Table 4-3).

7. Amphibole and plagioclase associated with the D_1, D_2 and D_3 structures show systematic changes in chemistry (Figures 4-8, 4-9, 4-13 and 4-14), which reflect the changing P-T conditions of the D_1 to D_3 deformations.

8. The $^{40}Ar/^{39}Ar$ ages of hornblendes from the D_1, D_2 and D_3 structures are the same, within error. Consequently, there is no relationship between the ages and paragenesis. The hornblende $^{40}Ar/^{39}Ar$ ages of *ca.* 1750 Ma probably reflect the time of cooling through the closure of hornblende to argon loss at 500°C, and approximate the time of D_{3b} deformation and synchronous metamorphism.

9. Hydrothermal activity linked to the formation of the gold deposits is bracketed between 1807 Ma (Thomas and Heaman, 1994) and *ca.* 1750 Ma. The mineralization postdates volcanism at 1882 to 1879 Ma (Bickford *et al.*, 1986), the emplacement of the Star Lake and Island Lake plutons at 1855 to 1846 Ma (Bickford *et al.*, 1986; Thomas and Heaman, 1994; Hrdy and Kyser, 1995),

and the early episode of transpressional deformation (D_1), and synchronous peak metamorphism (M_1) at 1820 to 1798 Ma (Kyser and Stauffer, 1995).

10. As a result of the geochronological study, it is concluded that the muscovite $^{40}Ar/^{39}Ar$ age of 1703 Ma from the Jasper deposit (Hrdy and Kyser, 1995) reflects the time of closure of muscovite to argon diffusion at approximately 350°C, and not the time of gold mineralization as suggested by Hrdy and Kyser (1995). The siting of gold in late microfractures in quartz grains (Hrdy and Kyser, 1995) would be caused by remobilization processes related to the D_{3b} deformation or any later deformations that affected the quartz veins in a brittle way.

11. The alteration associated with the MLTZ, the D_2 structures and the D_3 gold-bearing shears involved enrichment of $\delta^{18}O$ of silicate minerals (quartz, amphibole and biotite) in the deformed rocks relative to the least deformed precursors (Figure 5-3), reflecting the interaction with relatively ^{18}O-enriched hydrothermal fluids. The water/rock ratio associated with alteration in the structures was greater in the D_3 shears than in the MLTZ and the D_2 structures (Figure 5-8).

12. The hydrothermal fluids that infiltrated the D_2 and D_3 structures were possibly of similar composition, and the occurrence of gold mineralization in the D_3 structures was related to a larger fluid flow. The alteration associated with the D_2 Mallard Lake Shear and the D_3 gold-bearing shears involved introduction of Au, Cu, and Cu + Pb + Zn, and co-enrichment of K, Rb, and Ba (Figures 4-21 and 4-22). The K/Rb and K/Ba ratios are comparable to the ratios in the potassic alteration zones of Archean lode gold deposits (Table 4-4).

13. Quartz from all types of structures, with the exception of the Jasper deposit, has a restricted range of oxygen isotopic composition of 10.0 to 11.5 per mil, with auriferous quartz showing minor ^{18}O enrichment relative to the barren quartz (Figure 5-1A). The restricted range of oxygen isotopic composition of quartz suggests a uniformity in the $\delta^{18}O$ values of hydrothermal fluids.

Relative to the Jolu, Rush Lake and Star Lake deposits, the auriferous quartz in the Jasper deposit is enriched in the oxygen isotope composition by up to 3 per mil (Figure 5-1A). This enrichment is possibly the result of interaction with ^{18}O-enriched rocks or mixing with a local reservoir of ^{18}O-enriched fluids.

14. The application of oxygen isotopic geothermometers requires the consideration of the isotopic diffusion of mineral phases. Quartz and hornblende have similar diffusion rate and high closure temperatures to oxygen exchange; the mineral pair of quartz-hornblende provides the better estimates of temperature than quartz-mica or quartz-feldspar pairs.

15. The calculated oxygen and hydrogen isotopic compositions of hydrothermal fluids that deposited the quartz veins in all types of structures are 6.8 to 10.3‰ and -89 to -26‰, respectively (Figure 5-7). Such oxygen and hydrogen isotopic values are comparable with fluids derived from a metamorphic or magmatic source, or with fluids that acquired isotopic equilibrium with metamorphic or magmatic rocks at high temperatures.

16. The hydrothermal fluids associated with the gold-bearing quartz veins from the Star Lake and Jasper deposits are CO_2-bearing and of low salinity (Ibrahim and Kyser, 1991; Hrdy and Kyser, 1995).

Discussion

The gold deposits in the Star Lake-McLennan Lake area are epigenetic, structurally controlled quartz vein type or lode gold deposits. They are similar to Archean mesothermal lode gold deposits in that they are associated with greenstone belts, and are located at convergent plate margins (Hodgson, 1993). They are also similar to their Archean counterparts in terms of alteration, isotopic geochemistry and fluid composition (Kerrich, 1989; McCuaig and Kerrich, 1994). The Proterozoic deposits of the Star Lake-McLennan Lake area are associated with a calc-alkaline and low potassium tholeiitic assemblage, in contrast to the Archean deposits that are most

typically associated with a komatiitic and high-magnesian assemblage (Hodgson, 1993).

Sources of Hydrothermal Fluids

The similarities in the characteristics of Proterozoic and Archean lode gold deposits possibly reflect similar ore-forming processes (Kerrich and Wyman, 1990). In a convergent plate tectonic setting, there is the potential for large volumes of hydrothermal fluids to be generated from magmatism, or from metamorphic devolatilization (Hodgson, 1993). Accordingly, the proposed primary sources for hydrothermal fluids which formed the lode gold deposits revolve around magmatic or metamorphic origin.

Magmatic Hydrothermal Fluids

The models for a magmatic origin for hydrothermal fluids argue for the ubiquitous association of gold mineralization with episodes of magmatism. Gold-bearing hydrothermal fluids are considered to be generated by exsolution of volatile phases from the felsic intrusions, and magmatic or magmatic-hydrothermal processes provided the ingredients and driving mechanism for ore concentration and deposition. The magmatic-hydrothermal fluids are suggested by the following:

1. Many Archean lode gold deposits are spatially associated with post-volcanic felsic plutons (Hodgson and Troop, 1988; Colvine *et al.*, 1988). In the Abitibi greenstone belt, the felsic plutons constitute less than 4% of the belt, but make up more than 25% of the host rocks to mineralization (Colvine *et al.*, 1988).

2. Some Archean lode gold deposits have close connection to episodes of magmatism. In the Kiena mine, the Val d'Or camp, Morasse *et al.* (1995), based on precise U-Pb zircon dating of a granodiorite dyke that crosscuts the gold-bearing vein system, constrained a minimum age of 2686 Ma for mineralization. In conjunction with other U-Pb dating of intrusive events in the area, the authors concluded that gold mineralization occurred at *ca.* 2694 to

2686 Ma, coeval with the emplacement of intrusions (*ca.* 2694 to 2680 Ma), but before regional synmetamorphic deformation (*ca.* 2677 to 2645 Ma). The conclusion is strengthened by Robert's (1997) observations of some syenite-associated gold deposits in the Abitibi greenstone belt. The deposits were broadly coeval with Timiskaming sedimentation and syenitic magmatism, and were overprinted by subsequent folding and penetrative deformation. This suggests that gold mineralization was linked to large magmatic-hydrothermal systems generated by the emplacement of the syenite stocks (Robert, 1997).

Although the emplacement of some gold deposits have been demonstrated to be temporally associated with episodes of magmatism (Morasse *et al.*, 1995; Robert, 1997), in most cases, gold mineralization postdates the host intrusions by several tens of million years (see Colvine *et al.*, 1988). The time intervals strongly implicate no genetic connection between mineralization and magmatism (Colvine *et al.*, 1988; Hodgson, 1993). This is reinforced by the lack of spatial association of mineralization with any known plutons in the Archean goldfield, Kalgoorlie, Australia (Groves and Phillips, 1987).

Metamorphic Fluids

The association of gold mineralization with the metamorphic fluids is suggested by the following:

1. The ubiquitous occurrence of the lode gold deposits in a range of metamorphic settings world wide from subgreenschist to lower granulite facies, with the majority in metamorphic terranes of greenschist facies. The gold-bearing structures were developed during crustal shortening and metamorphism.

2. The timing of gold mineralization is variable with respect to peak metamorphism. Mineralization in lower grade metamorphic terranes largely postdates peak metamorphism (e.g. Clark *et al.*, 1989), whereas mineralization in higher grade metamorphic terranes is broadly synchronous with peak metamorphism (e.g. Barnicoat *et al.*, 1991; McCuaig *et al.*, 1993; Knight *et al.*, 1993). This is consistent with suggestions that peak metamorphic

conditions would be attained later at deeper crustal levels due to crustal thickening as a consequence of transpressional collision (England and Thompson, 1984, Kerrich and Wyman, 1990).

3. Most lode gold deposits show common timing of mineralization throughout the Yilgarn Block of Australia (see Groves, 1993) and the Abitibi greenstone belt of Canada (see Colvine *et al.*, 1988). The mineralization postdates the host plutons by several tens of million years (Colvine *et al.*, 1988).

Groves and Phillips (1987) proposed a metamorphic model which suggests that the metamorphic fluids were an integral part of greenstone belt development. The model favours generation of hydrothermal fluids by devolatilization of stratigraphically lower parts of greenstone successions at greenschist-amphibolite transition during prograde metamorphism and synchronous regional deformation. Gold is considered to be leached from the underlying supracrustal rocks by the metamorphic fluids, which were driven by seismic pumping and channeled upward via transcrustal-scale fault zones. Gold mineralization occurred in the subsidiary structures of the regional fault zones, largely at greenschist facies conditions as a result of a decrease in temperature and fluid-rock interaction.

Recently, the model of metamorphic fluids has been replaced by the crustal continuum model (Groves *et al.*, 1992; Groves, 1993). The model describes the occurrence of the lode gold deposits in a range of metamorphic settings extending from subgreenschist to lower granulite facies. The model involves deeply sourced hydrothermal fluids for the lode gold deposits, including metamorphic fluids and magmatic fluids in the lower crustal levels undergoing granulite facies metamorphism, rather than the ubiquitous origin of fluids by devolatilization of the greenstone succession at the greenschist-amphibolite transition as described above.

A major problem arising with both the metamorphic fluid model and the crustal continuum model is that they cannot account for the pre-metamorphic gold deposits such as those described by Morasse *et al.* (1995) and Robert (1997).

Genesis of Mineralization in The Star Lake-McLennan Lake Area

The gold deposits in the Star Lake-McLennan Lake area are hosted in shears developed during an episode of transpressional deformation. The mineralization postdates the emplacement of the Star Lake and Island Lake plutons by more than 50 million years, and postdates the culmination of regional metamorphism. The temporal relationships of gold mineralization suggest a closer connection of mineralization to metamorphism than to plutonism.

Since the deposits were sited in the amphibolite grade terrane, and the emplacement of the deposits postdates the attainment of peak metamorphic conditions, the fluids must be sourced in deeper levels of the crust which underwent higher grade metamorphism and possibly partial melting as predicted by the crustal continuum model (Groves et al., 1992; Groves, 1993). Hodgson (1993) proposed a mechanism for gold mineralization, assuming that barren fluids were originally generated by metamorphic devolatilization at lower levels of the crust. The fluids were likely driven into the crust of higher levels by buoyancy forces and high fluid pressure due to continued devolatilization reactions (Etheridge *et al.*, 1984). Such a fluid flow may occur by microfracturing along the foliation formed as a result of regional penetrative deformation (Walther and Orville, 1982; McCuaig, 1984). By this process, local fluid reservoirs would form in the rock profile above the zone of fluid generation. While the fluids were stored in these reservoirs they would be expected to react with, and leach gold from, the wall rocks of the reservoir.

Although the gold deposits were exclusively emplaced into the D_3 shears in the plutons during the dip-slip shearing of the D_{3a} deformation, it is possible that the hydrothermal fluids were generated prior to the development of the D_3 structures. This is suggested by (a) the uniform oxygen isotopic composition of vein quartz related to the D_1 to D_3 structures (Figure 5-1), which indicates the corresponding uniform isotopic composition of the hydrothermal fluids; and (b) by the similar alteration geochemistry of the D_2 structures to the D_3 structures (Figure 4-23), which reflects interaction of the host structures with auriferous fluids of similar composition.

The above observations, in conjunction with the observations that the D_3

shears have larger fluid flow than the D_2 structures (Figure 5-8), indicate that mineralization was critically controlled by the effectiveness of the host structures to focus large volume of auriferous fluids from depth. Sibson *et al.* (1988) and Cox *et al.* (1991) suggested that the structures most favourable for fluid focusing are steeply dipping, reverse shears and faults, developed in a compressional or transpressional regime, which have the potential to function effectively as fault-valve systems for a rapid, high volume discharge. The D_2 structures, with the exception of the Mallard Lake Shear and the David Lake Shear, have a limited strike length of a few metres, and the structures are discontinuous. Presumably the limited strike dimension, coupled with strike-slip shear movement, is indicative of a limited dip dimension. It is probable that during the D_2 deformation, the strike-slip D_2 structures did not act as effective fault-valve systems in tapping the fluids from depth; consequently, insufficient volume of fluids was introduced into the D_2 structures to form mineralization. By contrast, since the steeply dipping D_{3a} shears are continuous structures that extend completely across the plutons, and involve dip-slip shear movement, they probably have correspondingly large dip dimension. The D_{3a} structures were thus capable of establishing contact with a hydrothermal fluid reservoir at depth, forming effective pumping systems which focused the ascent of larger volumes of fluids along the permeable zones provided by the D_{3a} shears.

However, the involvement of a magmatic source for the mineralizing fluids cannot be discounted on the basis of the time interval between plutonism and the emplacement of gold in the host structures. Studies carried out in the Chibougamau area, Quebec suggest that Cu-Au vein-type mineralization associated with pre-tectonic intrusions could be sited into syn-tectonic shear zones tens of millions of years later. The Cu-Au vein-type mineralization is hosted in shear zones close to the margins of the Chibougamau pluton, a high-level cauldron subsidence complex (Pilote and Guha, 1995). The Cu-Au deposits are surrounded by extensive mineralized zones of disseminated or fracture-controlled sulphide minerals, tens to hundreds of metres wide (Sinclair *et al.*, 1994). Robert (1994) and Sinclair *et al.* (1994) demonstrated that the Cu-Au deposits are closely associated with porphyry copper mineralization. Both types of mineralization are believed to be related to the same pre-tectonic magmatic-hydrothermal activity produced by the emplacement of the late intrusive phases (*ca.* 2715 to 2718 Ma) of the Chibougamau pluton (see Pilote and Guha, 1995). The shear

zones hosting the Cu-Au orebodies are interpreted to be subsidiary structures of regional, east-west trending fault zones, which were developed during the final stage of the Kenoran event (Chown *et al.*, 1995), a period of regional penetrative deformation that occurred at *ca.* 2695 to 2700 Ma (Corfu *et al.*, 1989). The shear zones are commonly localized in the sericite alteration zones related to fractures that focus an early stage of hydrothermal activity (Robert, 1997). The orebodies show signs of overprinting by the shear zones (Sinclair *et al.*, 1994). Although there is no consensus on the timing of the emplacement of the Cu-Au deposits in the shear zones, it is possible that the mineralization predates the development of shear zones, and was subsequently remobilized into the shear zones during the regional deformation (Pilote and Guha, 1995), or that the magmatic hydrothermal fluids were active during the shear zone development (Guha *et al.*, 1983). Nevertheless, the final siting of the mineralization was syn-tectonic, postdating the genetic-related intrusive event by *ca.* 15 to 20 million years.

The alteration associated with the gold deposits in the study area is generally weak, and there is no evidence of pre-shear zone, fracture-hosted porphyry-type mineralization that represents an early stage of hydrothermal activity, as was observed in the Chibougamau area (e.g. Robert, 1994). This rules out the possibility that gold was associated with an episode of porphyry-type mineralization or that gold was remobilized from porphyry-type deposits to the shears as suggested by Tessier and Hodgson (1994) in the study of the Portage mine, Chibougamau.

If the gold deposits were formed directly from fluids generated by the emplacement of the host plutons, the fluids must have been stored in reservoirs in the plutons or surrounding supracrustal rocks for more than 50 million years before they were tapped by the D_3 structures. There is no evidence to support or refute the possibility of occurrence of pre-D_1 fluid reservoirs. However, the reservoirs formed in the rock profiles, if any, were possibly limited in size due to the limited availability of space in the rocks. Consequently, supply of hydrothermal fluids by the reservoirs would be limited. This cannot be reconciled with the suggestions that a large volume of hydrothermal fluids was required for gold mineralization (Sherlock, 1993). It is concluded, therefore, that direct involvement in the gold mineralization of magmatic-hydrothermal fluids generated by the host plutons is unlikely.

The formation of the gold deposits in the D_3 shears within the Star Lake and Island Lake plutons is possibly attributed to the higher competency of the plutons relative to the surrounding supracrustal rocks. Such a competency contrast is well demonstrated in the S_1 foliation trajectory in Figure 2-4. The higher competency of the plutons would permit a relatively brittle response to deformation even at deep levels of the crust, and consequently retain relatively high permeability that focused the ascent of hydrothermal fluids (Colvine, 1989). In addition, the pathways of pluton ascent that connect the lower crust and the site of emplacement may also be the preferential pathways for fluid focusing, leading to the occurrence of mineralization in the plutons.

The lack of evidence for direct derivation of ore fluids from the host plutons does not necessarily preclude a magmatic source for the hydrothermal fluids. As described above, the gold deposits were sited in the amphibolite grade terrane, the hydrothermal solutions would be sourced in the lower crust levels that involved higher grade metamorphism, i.e. upper amphibolite to granulite facies. Partial melting would occur in the source areas under the high metamorphic conditions, resulting in magmatism that outlasted the peak metamorphism in the upper levels of the crust. The post-tectonic magmatic activities, exhibited in the form of small intrusions in higher levels of the crust, may last as late as 1773 to 1780 Ma in the Reindeer Zone (Bickford *et al.*, 1990), broadly coeval with gold mineralization in the study area. The generation of auriferous fluids may be related to the post-tectonic magmatic processes. This makes magmatic or metamorphic origin for hydrothermal fluids indistinguishable.

Although the gold deposits of the region are broadly similar to the Archean mesothermal gold deposits, a major difference is that the amount of gold discovered is small in comparison to their Archean counterparts. This possibly reflects the difference in the structural setting of the deposits. The Archean mesothermal gold deposits are spatially associated with regional-scale fault zones that were active during the later stages of arc-continent or continent-continent collision (Hodgson and Hamilton, 1989). The fault zones commonly separate contrasting terranes (see Colvine *et al.*, 1988), and are characterized by carbonate alteration dominated by mantle-derived carbon (Groves *et al.*, 1988). They control Timiskaming-type sedimentation and alkaline igneous intrusions that have probably been derived at the base of the crust or the mantle (McNeil and Kerrich, 1986; Corfu *et al.*, 1991). The transcrustal-scale

structures would be capable of tapping deeply sourced hydrothermal fluids of metamorphic-magmatic origin. Consequently, the Archean gold-forming processes may have involved large, deep-sourced reservoirs of hydrothermal fluids.

The gold-bearing D_3 shears in the study area occur in the hanging wall of the McLennan Lake Tectonic Zone, and are viewed as subsidiary structures to the latter (Poulsen, 1989). However, the structural analyses carried out in this study indicate that there is no genetic association of the D_3 structures with the MLTZ. The MLTZ lacks the features that characterize the regional fault zones in Archean greenstone belts as transcrustal-scale structures (see above). The interpretation of the MLTZ as a regional thrust fault is rejected. Thus, it is unlikely that the MLTZ acted as a primary fluid conduit connecting the deep crust and the sites of deposition. Although it is possible that fluids were driven upwards via the pathways of the pluton ascent as suggested above, the access was possibly very limited. This is because the plutons were emplaced *ca.* 50 million years earlier than the mineralization, the regional penetrative deformation, resulted from the closure of the Trans-Hudson Orogen, may have obliterated the pathways and reduced their effectiveness for later fluid transport. Therefore, it is concluded that the lack of continuous, penetrative structures limited the access to large fluid reservoirs, and constrained the gold mineralization in the Star Lake-McLennan Lake area, and by implication, in the Central Metavolcanic Belt.

In summary, the gold mineralization in the Star Lake-McLennan Lake area was likely the result of lower crustal tectonothermal activities related to crustal thickening caused by transpressional collision during the final stages of the Paleoproterozoic Trans-Hudson Orogen. The hydrothermal fluids were possibly derived by devolatilization of the lower levels of the crust during prograde metamorphism. The small size of gold deposits with respect to Archean counterparts may stem from the lack of deep plumbing systems that connect the deep crust and the deposition sites.

REFERENCES

Abbas-Hasanie, S., Lewry, J.F., and Perkins, D., 1991, Metamorphic P-T studies in the Jan Lake area, Hanson Lake Block: *in* Summary of Investigations 1991, Saskatchewan Geological Survey, Saskatchewan Energy and Mines, Miscellaneous Report 91-4, p. 69-71.

Ames, D.E., Poulsen, K.H., and Galley, A.G., 1987, Geology and gold deposits, Star Lake pluton, La Ronge Domain, Saskatchewan: Geological Survey of Canada, Open File Report 1469, 1:10,000 scale map with marginal notes.

Ansdell, K.M., and Kyser, T.K., 1992, Mesothermal gold mineralization in a Proterozoic greenstone belt: western Flin Flon domain, Saskatchewan, Canada: Economic Geology, v. 87, p. 1496-1524.

Ansdell, K.M., and Yang, H., 1995, Detrital zircons in the McLennan Group meta-arkoses and MacLean Lake Belt, western Trans-Hudson Orogen: *in* Hajnal, Z., and Lewry, J., eds., Lithoprobe, THOT Report, No. 48, p. 190-197.

Appleyard, E.C., 1990, Mass balance corrections applied to lithogeochemical data in mineral exploration: *in* Beck, L.S. and Harper, C.T. eds., Modern exploration techniques, Sask. Geol. Soc., Spec. Publ., v. 10, p. 27-40.

Appleyard, E.C., 1991, Alteration halos associated with gold-bearing shear zones in the Star Lake and Island Lake plutons: *in* Summary of Investigations 1991, Saskatchewan Geological Survey, Saskatchewan Energy and Mines, Miscellaneous Report 91-4, p. 85-92.

Appleyard, E.C., 1992, Alteration geochemistry of the Rio Zone, Bootleg Lake Gold Mine, Creighton area: *in* Summary of Investigations 1992, Saskatchewan Geological Survey, Saskatchewan Energy and Mines, Miscellaneous Report 92-4, p. 138-145.

Ashton, K.E., Hunt, P.A., and Froese, 1992, Age constraints on the evolution of the Flin Flon volcanic belt and Kisseynew gneiss belt, Saskatchewan and Manitoba: Radiogenic Age and Isotopic Studies, Report 5, Geological Survey of Canada, Paper 91-2, p. 55-69.

Bailes, A.H., and McRitchie, W.D., 1978, The transition from low to high grade metamorphism in the Kisseynew sedimentary gneiss belt, Manitoba: *in* Fraser, J.A.,

Bowman, J.R., and Ghent, E.D., 1986, Oxygen and hydrogen isotope study of minerals from metapelitic rocks, staurolite to sillimanite zones, Mica Creek, British Columbia: Journal of Metamorphic Geology, v. 4, p. 131-141.

Boyle, A.P., and Westhead, R.K., 1992, Metamorphic peak geothermobarometry in the Furulund group, Sulitjelma, Scandinavian Caledonides: implications for uplift: Journal of Metamorphic Geology, v. 10, p.615-626.

Brodie, K.H., and Rutter, E.H., 1985, On the relationship between deformation and metamorphism, with special reference to the behavior of basic rocks: *In* Thompson, A.B. and Rubie, D.C., eds., Metamorphic reactions, Advanced in Physical Geochemistry, v. 4, p. 138-179.

Burg, J.P., 1986, Quartz shape fabric variations and c-axis fabrics in a ribbon-mylonite: arguments for an oscillating foliation: Journal of Structural Geology, v. 8, p.123-131.

Burrill, G.H.R., 1987, Mallard Lake gold deposits: Geological Association of Canada - Mineralogical Association of Canada Annual Meeting, Saskatoon, 1987, Field Trip Guide Book 4, p. 32-42.

Card, K.D., Poulsen, K.H., and Robert, F., 1989, The Archean Superior province of the Canadian Shield and its lode gold deposits: Economic Geology Monograph 6, p. 19-36.

Chiarenzelli, J.R., 1989, The Nistowiak and Guncoat gneisses: Implications for the tectonics of the Glennie and La Ronge domains, northern Saskatchewan, Canada: unpublished Ph.D. thesis, the University of Kansas, 229p.

Chiarenzelli, J.R., and Lewry, J.F., 1988, The Nistowiak Gneisses: Evidence of a collisional suture in the Trans-Hudson orogen, northern Saskatchewan: Geological Association of Canada - Mineralogical Association of Canada, Program with Abstracts, v. 13, p. A20.

Chiba, H., Chacko, T., Clayton, R.N., and Goldsmith, J.R., 1989, Oxygen isotope fractionations involving diopside, forsterite, magnetite, and calcite: application to geothermometry: Geochimica et Cosmochimica Acta, v. 53, p. 2985-2995.

Chown, E.H., Daigneault, R., Mueller, W., and Pilote, P., 1995, Geological setting of the eastern extremity of the Abitibi belt: *in* Pilote, P., ed., Metallogenic evolution and geology of the Chibougamau area - from porphyry Cu-Au-Mo to mesothermal lode gold deposits, field trip guidebook, Geological Survey of Canada, Open File 3143, p. 1-30.

Clark, M.E., Carmichael, D.M., Hodgson, C.J., and Fu, M., 1989, Wallrock alteration, Victory gold mine, Kambalda, western Australia: processes and P-T-X_{CO2} conditions of metasomatism: *in* Keays, R.R., Ramsay, W.R.H., and Groves, D.I., eds., The Geology of Gold Deposits: The Perspectives in 1988, Economic Geology, Monograph, v. 6, p. 445-459.

Clayton, R.N., and Epstein, S., 1958, The relationship between $^{18}O/^{16}O$ ratios in coexisting quartz, carbonate, and iron oxides from various geologic deposits: Journal of Geology, v. 66, p. 352-371.

Clayton, R.N., and Epstein, S., 1961, The use of oxygen isotopes in high temperature geological thermometry: Journal of Geology, v. 69, p. 447-452.

Clayton, R.N., and Mayeda, T.K., 1963, The use of bromine pentafluoride in the extraction of oxygen from oxides and silicates for isotopic analysis: Geochimica et Cosmochimica Acta, v. 27, p. 43-52.

Cobbold, P.R., Cosgrove, J.W., and Summers, J.M., 1971, Development of internal structures in deformed anisotropic rocks: Tectonophysics, v. 12, p.23-53.

Colvine, A.C., 1989, An empirical model for the formation of Archean gold deposits: products of final cratonization of the Superior Province, Canada: *in* Keays, R.R., Ramsay, W.R.H., and Groves, D.I., eds., The Geology of Gold Deposits: The Perspectives in 1988, Economic Geology, Monograph, v. 6, p. 37-53.

Colvine, A.C., Fyon, J.A., Heather, K.B., Marmont, S., Smith, P.M., and Troop, D.G., 1988, Archean lode gold deposits in Ontario: Ontario Geological Survey, Miscellaneous Paper 139, 136p.

Coombe, W., 1984, Gold in Saskatchewan: Saskatchewan Energy and Mines, Open File Report 84-1, 134p.

Coombe, W., Lewry, J.F., and Macdonald, R., 1986, Regional geological setting of gold in the La Ronge Domain, Saskatchewan: *in* Clark, L.A., ed., Gold in the Western Shield, Canadian Institute of Mining and Metallurgy, Special Volume 38, p. 26-56.

Corfu, F., Jackson, S.L., and Sutcliffe, R.H., 1991, U-Pb ages and tectonic significance of late Archean alkalic magmatism and nonmarine sedimentation: Timiskaming Group, southern Abitibi belt, Ontario: Canadian Journal of Earth Sciences, v. 28, p. 489-503.

Corfu, F., Krogh, T.E., Kwok, Y.Y., and Jensen, L.S., 1989, U-Pb zircon geochronology in the southwestern Abitibi greenstone belt, Superior Province:

Canadian Journal of Earth Sciences, v. 26, p. 1747-1763.

Cox, S.F., Etheridge, M.A., and Wall, V.J., 1991, Fluid pressure regimes and fluid dynamics during deformation of low-grade metamorphic terranes - Implications for the genesis of mesothermal gold deposits: *in* Robert, F., Sheahan, P.A., and Green, S.B., eds., Greenstone Gold and Crustal Evolution, NUNA Conference Volume, Geological Association of Canada, p. 46-53.

Dallmeyer, R.D., 1974, The role of crystal structure in controlling the partitioning of Mg and Fe^{2+} between coexisting garnet and biotite: American Mineralogist, v. 59, p. 201-203.

David, J., Machado, N., Baikes, A., and Syme, E., 1993, U-Pb geochronology of the Proterozoic Flin Flon Belt, Snow Lake area, Manitoba: Geological Association of Canada, Program with Abstracts, v. 18, p. A-22.

Deines, P., 1977, On the oxygen isotope distribution among mineral triples in igneous and metamorphic rocks: Geochimica et Cosmochimica Acta, v. 41, p. 1709-1730.

Dodson, M.H., 1973, Closure temperature in cooling geochronological and petrological systems: Contributions to Mineralogy and Petrology, v. 40, p. 259-274.

Durocher, K.E., 1997, A study of the P-T-t-fluid evolution of the Glennie Domain, Trans-Hudson Orogen: unpublished Ph.D. thesis, the University of Saskatchewan, Canada, 302p.

England, P.C., and Thompson, A.B., 1984, Pressure-temperature-time paths of regional metamorphism I: Heat transfer during the evolution of regions of thickened continental crust: Journal of Petrology, v. 25, p. 894-928.

Eslinger, E.V., Savin, S.M., and Yeh, H., 1979, Oxygen isotope geothermometry of diagenetically altered shales: Society of Economic Paleontologists and Mineralogists Special Publication 26, p. 113-124.

Etheridge, M., Wall, V., and Cox, S., 1984, High fluid pressures during regional metamorphism and deformation: Implications for mass transport and deformation mechanisms: Journal of Geophysical Research, v. 89, p. 4344-4358.

Farver, J.R., and Giletti, B.J., 1985, Oxygen diffusion in hornblende: Geochimica et Cosmochimica Acta, v. 49, p. 1403-1411.

Fedorowich, J., Stauffer, M., and Kerrich, R., 1991, Structural setting and fluid characteristics of the Proterozoic Tartan Lake gold deposit, Trans-Hudson orogen, Northern Manitoba: Economic Geology, v. 86, p. 1434-1467.

Fedorowich, J., Stauffer, M., Lewry, J., and Kerrich, R., 1995, The age of the Needle Falls shear zone: *in* Hajnal, Z., and Lewry, J., eds., Lithoprobe, THOT Report, No. 48, p. 102-103.

Ferry, J.M, and Spear, F.S., 1978, Experimental calibration of the partitioning of Fe and Mg between biotite and garnet: Contributions to Mineralogy and Petrology, v. 66, p. 113-117.

Fleck, R.J., Sutter, J.F., and Elloit, D.H., 1977, Interpretation of discordant $^{40}Ar/^{39}Ar$ age-spectra of Mesozoic tholeiites from Antarctica: Geochimica et Cosmochimica Acta, v. 41, p. 15-32.

Fortier, S.M., and Giletti, B.J., 1991, Volume self-diffusion of oxygen in biotite, muscovite, and phlogopite micas: Geochimica et Cosmochimica Acta, v. 55, p. 1319-1330.

Fossen, H., and Tikoff, B., 1993, The deformation matrix for simultaneous pure shear, simple shear, and volume change, and its application to transpression/transtension tectonics: Journal of Structural Geology, v. 15, p. 413-425.

Fumerton, S.L., Stauffer, M.R., and Lewry, J.F., 1985, The Wathaman batholith: largest known Precambrian pluton: Canadian Journal of Earth Sciences, v. 21, p. 1082-1097.

Garbutt, J.M., and Teyssier, C., 1991, Prism <c> slip in the quartzites of the Oakhurst Mylonite Belt, California: Journal of Structural Geology, v. 13, p.657-666.

Ghent, E.D., and Stout, M., 1984, TiO_2 activity in metamorphosed pelitic and basic rocks: principles and applications to metamorphism in southeastern Canadian Cordillera: Contributions to Mineralogy and Petrology, v. 86, p. 248-255.

Gilboy, C.F., 1982, Geology of an area around Rottenstone and Dobbin lakes (part of NTS area 74A): Saskatchewan Department of Mineral Resources, Report 193, 68p.

Giletti, B.J., 1986, Diffusion effects on oxygen isotope temperatures of slowly cooled igneous and metamorphic rocks: Earth and Planetary Science Letters, v. 77, p. 218-228.

Giletti, B.J., and Hess, K.C., 1988, Oxygen diffusion in magnetite: Earth and Planetary Science Letters, v. 89, p. 115-122.

Giletti, B.J., Semet, M.P., and Yund, R.A., 1978, Studies in diffusion. III. Oxygen in feldspar, an ion microprobe determination: Geochimica et Cosmochimica Acta, v. 42, p. 45-57.

Giletti, B.J., and Yund, R.A., 1984, Oxygen diffusion in Quartz: Journal of Geophysical Research, v. 89, p. 4039-4046.

Gordon, T.M., Hunt, P.A., Bailes, A.H., and Syme, E.C., 1990, U-Pb zircon ages from the Flin Flon and Kisseynew belts, Manitoba: chronology of Early Proterozoic crust formation at an Early Proterozoic accretionary margin: *in* Lewry, J.F., and Stauffer, M.R., eds., The Early Proterozoic Trans-Hudson Orogen of North America, Geological Association of Canada Special Paper 37, p. 177-199.

Graham, C.M., and Powell, R., 1984: A garnet - hornblende geothermometer: calibration, testing, and application to the Pelona schist, southern California: Journal of Metamorphic Geology, v. 2, p. 13-31.

Greene, D.C., and Schweickert, R.A., 1995, The Gem Lake shear zone: Cretaceous dextral transpression in the northern Ritter Range pendant, eastern Sierra Nevada, California: Tectonics, v. 14, p. 945-961.

Gresens, R.L., 1967, Composition-volume relations of metasomatism: Chemical Geology, v. 2, p. 47-65.

Groves, D.I., 1993, The crustal continuum model for late-Archaean lode-gold deposits of the Yilgarn Block, western Australia: Mineralium Deposita, v. 28, p. 366-374.

Groves, D.I., Barley, M.E., Barnicoat, A.C., Cassidy, K.F., Fare, R.J., Hagemann, S.G., Ho, S.E., Hronsky, L.M.A., Mikuski, E.J., Mueller, A.G., McNaughton, N.J., Perring, C.S., Ridley, J.R., Vearncombe, J.R., 1992, Sub-greenschist to granulite-hosted Archean lode-gold deposits of the Yilgarn Craton: a depositional continuum from deep-sourced hydrothermal fluids in crustal-scale plumbing systems: Geology Department (Key Centre) and University Extension, The University of Western Australia Publication, v. 22, p. 325-337.

Groves, D.I., and Foster, R.P., 1991, Archaean lode gold deposits: *in* Foster, R.P., ed., Gold Metallogeny and Exploration, Blackie, p. 63-103.

Harper, C.T., 1996, La Ronge-Lynn Lake Bridge project: Sucker-Fleming Lake area: *in* Summary of Investigations 1996, Saskatchewan Geological Survey, Saskatchewan Energy and Mines, Miscellaneous Report 96-4, p. 66-78.

Harper, C.T., Thomas, D., and Watters, B., 1986, Geology and petrochemistry of the Star-Waddy Lakes area, Saskatchewan, *in* Clark, L.A., ed., Gold in the Western Shield: Canadian Institute of Mining and Metallurgy, Special Volume 38, p. 57-85.

Harris, L.B., and Cobbold, P.R., 1984, Development of conjugate shear bands during bulk simple shearing: Journal of Structural Geology, v. 7, p. 37-44.

Harrison, T.M., 1981, Diffusion of ^{40}Ar in hornblende: Contributions to Mineralogy and Petrology, v. 78, p. 324-331.

Harrison, T.M., Duncan, I., and McDougall, I., 1985, Diffusion of ^{40}Ar in biotite: Temperature, pressure, and compositional effects: Geochimica et Cosmochimica Acta, v. 49, p. 2461-2468.

He, J., and Roberts, R.G., 1991, Deformation in the Star Lake-McLennan Lake area, La Ronge Domain: *in* Summary of Investigations 1991, Saskatchewan Geological Survey, Saskatchewan Energy and Mines, Miscellaneous Report 91-4, p. 81-84.

He, J., and Roberts, R.G., 1992, Structural setting of lode gold deposits in the McLennan Lake-Star Lake area, northern Saskatchewan. Saskatchewan Energy and Mines, Internal Report, 4 p.

Heaman, L.M., Maxeiner, R.O., and Slimmon, W.L., 1994, 1993-94 U-Pb geochronological investigations in the Trans-Hudson Orogen, Saskatchewan: *in* Summary of Investigations 1994, Saskatchewan Geological Survey, Saskatchewan Energy and Mines, Miscellaneous Report 94-4, p. 96-99.

Hodges, K.V., and Spear, F.S., 1982: Geothermometry, geobarometry and the Al_2SiO_3 triple point at Mt. Moosilauke, New Hampshire: American Mineralogist, v. 67, p. 1118-1134.

Hodgson, C.J., 1993, Mesothermal lode-gold deposits: *in* Kirkham, R.V., Sinclair, W.D., Thorpe, R.I., and Duke, J.M., eds., Mineral Deposit Modeling, Geological Association of Canada, Special Paper 40, p. 635-678.

Hodgson, C.J., and Hamilton, J.V., 1989, Gold mineralization in the Abitibi greenstone belt: End-stage result of Archean collisional tectonics? *in* Keays, R.R., Ramsay, W.R.H., and Groves, D.I., eds., The Geology of Gold Deposits: The Perspectives in 1988, Economic Geology, Monograph, v. 6, p. 86-100.

Hodgson, C.J., and Troop, D.G., 1988, A new computer-aided methodology for area selection in gold exploration: A case study from the Abitibi greenstone belt: Economic Geology, v. 83, p. 952-977.

Hoffman, P.F., 1988, United plates of America, the birth of a craton: Early Proterozoic assembly and growth of Laurentia: Annual Review of Earth and Planetary Sciences, v. 16, p. 543-603.

Hoffman, P. F., 1989, Precambrian geology and tectonic history of North American: *in* Bally, A.W., and Palmer, A.R., eds., The Geology of North America - An Overview, Geological Society of America, The Geology of North America, v. A, p. 447-512.

Hoffman, P.F., 1990, Subdivision of the Churchill province and extent of the Trans-Hudson Orogen: *in* Lewry, J.F., and Stauffer, M.R., eds., The Early Proterozoic Trans-Hudson Orogen of North America, Geological Association of Canada Special Paper 37, p. 15-39.

Holland, T.J.B., and Richardson, S., 1979, Amphibole zonation in metabasites as a guide to the evolution of metamorphic conditions: Contributions to Mineralogy and Petrology, v. 70, p. 143-148.

Hrdy, F., and Kyser, T.K., 1995, Origin, timing, and fluid characteristics of an auriferous event: the Proterozoic Jasper lode gold deposit, Saskatchewan, Canada: Economic Geology, v. 90, p. 1918-1933.

Hudleston, P.J., Schultz-Ela, D., and Southwick, D.L., 1988, Transpression in an Archean greenstone belt, northern Minnesota: Canadian Journal of Earth Sciences, v. 25, p. 1060-1068.

Huebner, M., Kyser, T.K., and Nisbet, E.G., 1986, Stable-isotope geochemistry of high-grade metapelites from the Central zone of the Limpopo belt: American Mineralogist, v. 71, p. 1343-1353.

Ibrahim, M.S., and Kyser, T.K., 1991, Fluid inclusion and isotope systematics of the high-temperature Proterozoic Star Lake lode gold deposit, northern Saskatchewan, Canada: Economic Geology, v. 86, p. 1468-1490.

Jacobson, C.E., 1995, Qualitative thermobarometry of inverted metamorphism in the Pelona and Rand Schists, southern California, using calciferous amphibole in mafic schist: Journal of Metamorphic Geology, v. 13, p. 79-92.

Janser, B.W., 1993, The Star Lake pluton, La Ronge Domain, northern Saskatchewan: petrogenesis of a Proterozoic island-arc pluton: Precambrian Research, v. 70, p. 145-164.

Javoy, M., Fourcade, S., and Allegre, C.J., 1970, Graphical method for examination of $^{18}O/^{16}O$ fractionations in silicate rocks: Earth and Planetary Science Letters, v. 10, p. 12-16.

Kerrich, R., 1983, Geochemistry of gold deposits in the Abitibi greenstone belt: Canadian Institute of Mining and Metallurgy, Special Volume 27, 75p.

Kerrich, R., 1987, The stable isotope geochemistry of Au-Ag vein deposits in metamorphic rocks: *in* Kyser, T.K., ed., Stable Isotope Geochemistry of Low Temperature Fluids, Mineralogical Association of Canada Short Course Handbook, v. 13, p. 287-336.

Kerrich, R., 1989, Geochemical evidence on the sources of fluids and solutes for shear zone hosted mesothermal Au deposits: Geological Association of Canada Short Course Notes, v. 6, p. 129-198.

Kerrich, R, and Fryer, B.J., 1988, Lithophile-element systematics of Archean greenstone belt Au-Ag vein deposits: implication for source processes: Canadian Journal of Earth Sciences, v. 25, p. 945-953.

Kerrich, R., and Wyman, D., 1990, Geodynamic setting of mesothermal gold deposits: An association with accretionary tectonic regimes: Geology, v. 18, p. 882-885.

Knight, J.T., Groves, D.I., and Ridley, J.R., 1993, The Coolgardie Goldfield, Western Australia: district-scale controls on an Archaean gold camp in an amphibolite facies terrane: Mineralium Deposita, v. 28, p. 436-456.

Knipe, R.J., and Wintsch, R.P., 1985, Heterogeneous deformation, foliation development, and metamorphic processes in a polyphase mylonite: *in* Thompson, A.B., and Rubie, D.C., eds., Metamorphic reactions, Advances in Physical Geochemistry, v. 4, p. 180-210.

Kohn, M.J., and Spear, F.S., 1989, Empirical calibration of geobarometers for the assemblage garnet + hornblende + plagioclase + quartz: American Mineralogist, v. 74, p. 77-84.

Krantz, R.W., 1995, The transpressional strain model applied to strike-slip, oblique-convergent and oblique-divergent deformation: Journal of Structural Geology, v. 17, p. 1125-1137.

Krohe, A., 1990, Local variations in quartz [c]-axis orientations in non-coaxial regimes and their significance for the mechanics of S-C fabrics: Journal of Structural Geology, v. 12, p. 995-1004.

Kyser, T.K., 1987, Equilibrium fractionation factors for stable isotopes: *in* Kyser, T.K., ed., Stable Isotope Geochemistry of Low Temperature Fluids, Mineralogical Association of Canada Short Course Handbook, v. 13, p. 1-84.

Kyser, T.K., Fayek, M., and Sibbald, T.I.I., 1992, Geochronologic studies in the La Ronge and Glennie domains: *in* Summary of Investigations 1992, Saskatchewan Geological Survey, Saskatchewan Energy and Mines, Miscellaneous Report 92-4, p. 130-134.

Kyser, T.K., Janser, B.W., Wilson, M.R., and Hattie, I., 1986, Stable isotope geochemistry related to gold mineralization and exploration in the Western Shield: *in* Clark, L.A., ed., Gold in the Western Shield, Canadian Institute of Mining and Metallurgy, Special Volume 38, p. 470-498.

Kyser, T.K., and O'Neil, J.R., 1984, Hydrogen isotope systematics of submarine basalts: Geochimica et Cosmochimica Acta, v. 48, p. 2123-2133.

Kyser, T.K., and Stauffer, M.R., 1995, Petrogenesis and ages of plutons in the Central Metavolcanic Belt, La Ronge Domain: *in* Hajnal, Z., and Lewry, J., eds., Lithoprobe, THOT Report, No. 48, p. 122-130.

Laird, J., 1980, Phase equilibria in mafic schist from Vermont: Journal of Petrology, v. 21, p. 1-37.

Laird, J., and Albee, A.L., 1981, Pressure, temperature, and time indicators in mafic schist - Their application to reconstructing the polymetamorphic history of Vermont: American Journal of Science, v. 281, p. 127-175.

Law, R.D., 1986, Relationships between strain and quartz crystallographic fabrics in the Roche Maurice quartzites of Plougastel, western Brittany: Journal of Structural Geology, v. 8, p. 493-515.

Leake, B.E., Woolley, A.R., Arps, C.E.S., Birch, W.D., Gilbert, M.C., Grice, J.D., Hawthorne, F.C., Kato, A., Kisch, H.J., Krivovichev, V.G., Linthout, K., Laird, J., Mandarino, J.A., Maresch, W.V., Nickel, E.H., Rock, N.M.S., Schumacher, J.C., Smith, D.C., Stephenson, N.C.N., Ungaretti, L., Whittaker, E.J.W., and Guo, Y., 1997, Nomenclature of amphiboles: report of the subcommittee on amphiboles of the international mineralogical association, commission on new minerals and mineral names: Canadian Mineralogist, v. 35, p. 219-246.

Proterozoic Trans-Hudson Orogen of North America, Geological Association of Canada, Special Paper 37, p. 75-94.

Lister, G.S., 1977, Discussion: Cross-girdle c-axis fabrics in quartzites plastically deformed by plane strain and progressive simple shear: Tectonophysics, v. 39, p. 51-53.

Lister, G.S., and Hobbs, B.E., 1980, The simulation of fabric development during plastic deformation and its application to quartzite: the influence of deformation history: Journal of Structural Geology, v. 2, p. 355-370.

Lister, G.S., and Williams, P.F., 1983, The partitioning of deformation in flowing rock mass: Tectonophysics, v. 92, p. 1-33.

Loch, K., 1994, The Jolu gold deposit in northern Saskatchewan: The relationship between the structural history and the thickness and grade of the deposit: Unpublished B.Sc. thesis, University of Waterloo, 46p.

Lucas, S.B., Green, A., Hajnal, Z., White, D., Lewry, J., Ashton, K., Weber, W., and Clowes, R., 1993, Deep seismic profile across a Proterozoic collision zone: surprises at depth: Nature, v. 363, p. 339-342.

Macdonald, R., 1987, Update on the Precambrian geology and domainal classification of northern Saskatchewan: *in* Summary of Investigations 1987, Saskatchewan Geological Survey, Saskatchewan Energy and Mines, Miscellaneous Report 87-4, p. 87-104.

Machado, N., 1990, Timing of collisional events in the Trans-Hudson Orogen: evidence from U-Pb geochronology for the New Quebec Orogen, the Thompson Belt, and the Reindeer Zone (Manitoba and Saskatchewan: *in* Lewry, J.F., and Stauffer, M.R., eds., The Early Proterozoic Trans-Hudson Orogen of North America, Geological Association of Canada Special Paper 37, p. 433-441.

Mandl, G., de Jong, L.N.J., and Maltha, A., 1977, Shear zones in granular material: Rock Mechanics, v. 9, p. 95-144.

Massey, J.A., Harmon, R.S., and Harris, N.B.W., 1994, Contrasting retrograde oxygen isotope exchange behavior and implications: examples from the Langtang Valley, Nepal: Journal of Metamorphic Geology, v. 12, p. 261-272.

Maxeiner, R.O., and Sibbald, T.I.I., 1995, Controversial rocks in the Hebden-MacKay lakes area, southern La Ronge Domain: *in* Summary of Investigations 1995,

Saskatchewan Geological Survey, Saskatchewan Energy and Mines, Miscellaneous Report 95-4, p. 79-85.

McCuaig, A., 1984, Fluid-rock interaction in some shear zones from the Pyrenees: Journal of Metamorphic Geology, v. 2, p. 129-142.

McCuaig, T.C., and Kerrich, R., 1994, P-T-t-deformation-fluid characteristics of lode gold deposits: evidence from alteration systematics: *in* Lentz, D.R., ed., Alteration and Alteration Processes Associated with Ore-Forming Systems, Geological Association of Canada, Short Course Notes, v. 11, p. 339-379.

McCuaig, T.C., Kerrich, R., Groves, D.I., and Archer, N., 1993, The nature and dimensions of regional and local gold-related hydrothermal alteration in tholeiitic metabasalts in the Norseman goldfields: the missing link in a crustal continuum of gold deposits?: Mineralium Deposita, v. 28, p. 420-435.

McNeil, A.M., and Kerrich, R., 1986, Archean lamprophyre dykes and gold mineralization, Matheson, Ontario: The conjunction of LILE-enriched mafic magmas, deep crustal structures, and Au concentration: Canadian Journal of Earth Sciences, v. 23, p. 324-343.

Means, W.D., 1989, Stretching faults: Geology, v. 17, p. 893-896.

Meyer, M.T., Bickford, M.E., and Lewry, J.F., 1992, The Wathaman Batholith: an Early Proterozoic continental arc in the Trans-Hudson orogenic belt, Canada: Geological Society of America Bulletin, v. 104, p. 1073-1085.

Morasse, S., Wasteneys, H.A., Cormier, M., Helmstaedt, H., and Mason, R., 1995, A pre-2686 Ma intrusion-related gold deposit at the Kiena mine, Val d'Or, Quebec, southern Abitibi subprovince: Economic Geology, v. 90, p. 1310-1321.

Murphy, W.L., 1986, Geology and exploration history of the gold mineralization in the Star Lake area, Saskatchewan: *in* Clark, L.A., ed., Gold in the Western Shield, Canadian Institute of Mining and Metallurgy, Special Volume 38, p. 212-220.

Naylor, M.A., Mandl, G., and Sijpesteijn, C.H.K, 1986: Fault geometries in basement-induced wrench faulting under different initial stress states: Journal of Structural Geology, v. 8, p. 737-752.

Nelson, K.D., Baird, D.J., Walters, J.J., Hauck, M., Brown, L.D., Oliver, J.E., Ahern, H.L., Hajnal, Z., Jones, A.G., and Sloss, L.L., 1993, Trans-Hudson Orogen and Williston basin beneath northeastern Montana and northern Dakota: New COCORP deep profiling results: Geology, v. 21, p. 447-450.

O'Neil, J.R., 1986, Theoretical and experimental aspects of isotopic fractionation: *in* Valley, J.W., Taylor, H.P., Jr., and O'Neil, J.R., eds., Stable Isotopes in High Temperature Geological Processes, Mineralogical Society of America Reviews in Mineralogy, v. 16, p. 1-40.

O'Neil, J.R., Clayton, R.N., and Mayeda, T.K., 1969, Oxygen isotope fractionation in divalent metal carbonates: Journal of Chemical Physics, v. 51, p. 5547-5558.

O'Neil, J.R., and Kharaka, Y.K., 1976, Hydrogen and oxygen isotope exchange reactions between clay minerals and water: Geochimica et Cosmochimica Acta, v. 40, p. 241-246.

Pilote, P., and Guha, J., 1995, Metallogeny of the eastern extremity of the Abitibi belt: *in* Pilote, P., ed., Metallogenic evolution and geology of the Chibougamau area - from porphyry Cu-Au-Mo to mesothermal lode gold deposits, field trip guidebook, Geological Survey of Canada, Open File 3143, p. 31-43.

Plyusnina, L.P., 1982, Geothermometry and geobarometry of plagioclase - hornblende bearing assemblages: Contributions to Mineralogy and Petrology, v. 80, p. 140-146.

Poulsen, K.H., 1986, Auriferous shear zones with samples from the Western Shield: *in* Clark, L.A., ed., Gold in the Western Shield, Canadian Institute of Mining and Metallurgy, Special Volume 38, p. 86-103.

Poulsen, K.H., 1989, La Ronge structural studies: *in* Investigations by the Geological Survey of Canada in Manitoba and Saskatchewan during 1984-1989 Mineral Development Agreements, Geological Survey of Canada, Open File Report 2133, p. 50-55.

Poulsen, K.H., Ames, D.E., and Galley, A.G., 1985, Structural studies of gold mineralization in the La Ronge area: *in* Summary of Investigations 1985, Saskatchewan Geological Survey, Saskatchewan Energy and Mines, Miscellaneous Report 85-4, p. 96-98.

Poulsen, K.H., Ames, D.E., and Galley, A.G., 1986a, Gold mineralization in the Star Lake pluton, La Ronge belt, Saskatchewan: a preliminary report: *in* Current Research, Part A, Geological Survey of Canada, Paper 86-1A, p. 205-212.

Poulsen, K.H., Ames, D.E., and Galley, A.G., 1986b, Controls on gold mineralization in the Star Lake Pluton, La Ronge Domain: *in* Summary of Investigations 1986, Saskatchewan Geological Survey, Saskatchewan Energy and Mines, Miscellaneous Report 86-4, p. 139-140.

Poulsen, K.H., Ames, D.E., Galley, A.G., Derome, I., and Brommecker, R., 1987, Structural studies in the northern part of the La Ronge Domain: *in* Summary of Investigations 1987, Saskatchewan Geological Survey, Saskatchewan Energy and Mines, Miscellaneous Report 87-4, p. 107-114.

Poulsen, K.H., and Robert, F., 1989, Shear zones and gold: practical examples from the southern Canadian Shield: *in* Bursnall, J.T. ed., Mineralization and Shear Zones, Geological Association of Canada, short Course Notes 6, p. 239-266.

Ramsay, J.G., 1980, Shear zone geometry: a review: Journal of Structural Geology, v. 2, p. 83-99.

Riedel, W., 1929, Zur Mechanik geologischer Brucherscheinungen: Zb. Miner. Geol. Palaeont. Abh., v. 1929B, p. 354-368.

Robert, F., 1994, Timing relationships between Cu-Au mineralization, dykes, and shear zones in the Chibougamau camp, northeastern Abitibi subprovince, Quebec: *in* Current Research 1994-C, Geological Survey of Canada, p. 287-294.

Robert, F., 1997, A preliminary geological model for syenite-associated disseminated gold deposits in the Abitibi belt, Ontario and Quebec: *in* Current Research 1997-C, Geological Survey of Canada, p. 201-210.

Robert, F., and Brown, A.C., 1986, Archean gold-bearing quartz veins at the Sigma Mine, Abitibi greenstone belt, Quebec: Part I. Geologic relations and formation of the vein system: Economic Geology, v. 81, p. 578-592.

Roberts, R.G., 1987, Archean lode gold deposits: *in* Roberts, R.G., and Sheahan, P.A., eds., Ore Deposit Models, Geological Association of Canada, Geoscience Canada Reprint Series 3, p. 1-19.

Roberts, R.G., 1990, Structural controls on gold deposits in the Star Lake and Island Lake plutons: *in* Summary of Investigations 1990, Saskatchewan Geological Survey, Saskatchewan Energy and Mines, Miscellaneous Report 90-4, p. 58-59.

Roberts, R.G., 1993, The relationship between the gold-bearing quartz veins of the Star Lake and Island Lake Plutons, and the deformation of the Plutons: Saskatchewan Energy and Mines, Open File Report 93-5, 29p.

Roberts, R.G., and Schwann, P.L., 1989, Structural controls on gold deposits in the La Ronge Domain, Saskatchewan: Progress report: *in* Summary of Investigations 1989, Saskatchewan Geological Survey, Saskatchewan Energy and Mines, Miscellaneous Report 89-4, p. 36-40.

Romberger, S.B., 1986, The solution chemistry of gold applied to the origin of hydrothermal deposits: *in* Clark, L.A., ed., Gold in the Western Shield, Canadian Institute of Mining and Metallurgy, Special Volume 38, p. 168-186.

Robin, P-Y.F., and Cruden, A.R., 1994, Strain and vorticity patterns in ideally ductile transpressive zones: Journal of Structural Geology, v. 16, p. 447-466.

Robin, P-Y.F., and Jowett, E.C., 1986, Characterization of superposed Fisher distributions from point density surfaces. Geological Association of Canada, Annual Meeting, Abstract Volume.

Sanderson, D.J., and Marchini, W.R.D., 1984, Transpression: Journal of Structural Geology, v. 6, p. 449-458.

Schaaf, M., and Schwerdtner, W.M., 1992, Structural analysis of McLennan Lake Fault (MLF), La Ronge Domain: Progress report: *in* Lithoprobe Report, THOT report, No. 26, p. 28-39.

Schmid, S.M., and Casey, M., 1986, Complete fabric analysis of some commonly observed quartz c-axis patterns: *in* Hobbs, B.E., and Heard, H.C., eds., Mineral and Rock Deformation: Laboratory Studies, American Geophysical Union, Geophysical Monograph, v. 36, p. 263-286.

Sherlock, R.L., 1993, The geology and geochemistry of the McLaughlin Mine sheeted vein complex, northern Coastal Ranges, California: unpublished Ph.D. thesis, the University of Waterloo, Canada, 309p.

Sibbald, T.I.I., 1978, Geology of the Sandy Narrows (east) area, Saskatchewan: Saskatchewan Department of Mineral Resources, Report 170.

Sibson, R.H., Robert, F., and Poulsen, K.H., 1988, High-angle reverse faults, fluid-pressure cycling, and mesothermal gold-quartz deposits: Geology, v. 16, p. 551-555.

Sinclair, W.D., Pilote, P., Kirkham, R.V., Robert, F., and Daigneault, R., 1994, A preliminary report of porphyry Cu-Mo-Au and shear zone-hosted Cu-Au deposits in the Chibougamau area, Quebec: *in* Current Research 1994-C, Geological Survey of Canada, p. 303-309.

Slimmon, W.L., 1992, Bedrock geological mapping, Hanson Lake-Sturgeon-weir River area (part of NTS 63L-10 and -15): *in* Summary of Investigations 1992, Saskatchewan Geological Survey, Saskatchewan Energy and Mines, Miscellaneous Report 92-4, p. 23-29.

Syme, E.C., 1990, Stratigraphy and geochemistry of the Lynn Lake and Flin Flon metavolcanic belts, Manitoba: *in* Lewry, J.F., and Stauffer, M.R., eds., The Early Proterozoic Trans-Hudson Orogen of North America, Geological Association of Canada Special Paper 37, p. 143-162.

Taylor, G.F., and Appleyard, E.C., 1983, Weathering of the zinc-lead load, Dugald River, northwest Queensland: I. The gossan profile: Journal of Geochemical Exploration, v. 18, p. 87-110.

Taylor, H.P., Jr., 1974, The application of oxygen and hydrogen isotope studies to problems of hydrothermal alteration and ore deposition: Economic Geology, v. 69, p. 843-883.

Taylor, H.P., Jr., 1977, Water/rock interactions and the origin of H_2O in granitic batholiths: Geological Society of London Journal, v. 133, p. 509-558.

Tchalenko, J.S., 1968, The evolution of kink bands and the development of compression textures in sheared clays: Tectonophysics, v. 6, p. 159-174.

Tchalenko, J.S., 1970, Similarity between shear zones of different magnitudes: Geological Society of America Bulletin, v. 81, p. 1625-1640.

Tessier, A.C., and Hodgson, C.J., 1994, Syn-tectonic auriferous quartz-carbonate vein-type orebodies formed by metamorphic remobilization of Au and Cu from pre-metamorphic sulphide lenses at the Portage Mine, Chibougamau, Quebec: implication for crustal recycling of metals and the origin of metal provinces: Geological Association of Canada - Mineralogical Association of Canada Annual Meeting, Program with Abstracts, v. 19, p. 111.

Teyssier, C., Tikoff, B., and Markley, M., 1995, Oblique plate motion and continental tectonics: Geology, v. 23, p. 447-450.

Thom, A., Arndt, N.T., Chauvel, C., and Stauffer, M., 1990, Flin Flon and western La Ronge belts, Saskatchewan: products of Proterozoic subduction-related volcanism: *in* Lewry, J.F., and Stauffer, M.R., eds., The Early Proterozoic Trans-Hudson Orogen of North America, Geological Association of Canada Special Paper 37, p. 163-175.

Thomas, D.J., 1985, Geology of an area around Star Lake: Saskatchewan Energy and Mines, Open File Report 85-6, 83p.

Thomas, D.J., 1986, Bedrock geological mapping, Esmay Lake area: *in* Summary of Investigations 1986, Saskatchewan Geological Survey, Saskatchewan Energy and Mines, Miscellaneous Report 86-4, p. 19-31.

Thomas, D.J., 1988, Bedrock geological mapping, Palf Lake area: *in* Summary of Investigations 1988, Saskatchewan Geological Survey, Saskatchewan Energy and Mines, Miscellaneous Report 88-4, p. 20-25.

Thomas, D.J., 1993, Geology of the Star Lake-Otter Lake portion of the Central Metavolcanic Belt, La Ronge Domain: Saskatchewan Energy and Mines Report 236, 132p.

Thomas, D.J., and Heaman, L.M., 1994, Geologic setting of the Jolu gold mine, Saskatchewan: U-Pb age constraints on plutonism, deformation, mineralization, and metamorphism: Economic Geology, v. 89, p. 1017-1029.

Tikoff, B., and Greene, D., 1997, Stretching lineation in transpressional shear zones: an example from the Sierra Nevada Batholith, California: Journal of Structural Geology, v. 19, p. 29-39.

Tikoff, B., and Teyssier, C., 1994, Strain modeling of displacement-field partitioning in transpressional orogens: Journal of Structural Geology, v. 16, p. 1575-1588.

Tracy, R.J., 1982, Compositional zoning and inclusions in metamorphic minerals: Reviews in Mineralogy, v. 10, p. 355-397.

Tullis, J., 1977, Preferred orientation of quartz produced by slip during plane strain: Tectonophysics, v. 39, p. 87-102.

Van Schmus, W.R., Bickford, M.E., Lewry, J.F., and Macdonald, R., 1987, U-Pb geochronology in the Trans-Hudson orogen, northern Saskatchewan, Canada: Canadian Journal of Earth Sciences, v. 24, p. 407-424.

Walther, J., and Orville, P., 1982, Volatile production and transport in regional metamorphism: Contributions to Mineralogy and Petrology, v. 79, p. 252-257.

Watters, B.R., 1984, Geochemical patterns for metavolcanic rocks of the La Ronge Domain: *in* Summary of Investigations 1984, Saskatchewan Geological Survey, Sask. Energy and Mines, Misc. Rep. 84-4, p. 88-91.

Watters, B.R., 1985, Geochemistry of metavolcanic and plutonic rocks, Star Lake and Waddy Lake areas; *in* Summary of Investigations 1985, Saskatchewan Geological Survey, Saskatchewan Energy and Mines, Miscellaneous Report 85-4, p. 28-34.

Watters, B.R., and Armstrong, R.L., 1985, Rb-Sr Study of metavolcanic rocks from the La Ronge and Flin Flon domains, northern Saskatchewan: Canadian Journal of Earth Sciences, v. 22, p. 452-463.

Watters, B.R., and Pearce, J., 1987, Metavolcanic rocks of the La Ronge domain in the Churchill Province, Saskatchewan: geochemical evidence for a volcanic arc origin: *in* Pharaoh, T.C., Beckinsale, R.D., and Richard, D., eds., Geochemistry and Mineralization of Proterozoic Volcanic Suites, Geological Society of London Special Publication 33, p. 167-182.

Wilcox, R.E., Harding, T.P., and Seely, D.R., 1973, Basic wrench tectonics: American Association of Petroleum Geologists Bulletin, v. 57, p. 74-96.

Yeo, G.M., 1996, Geological investigations in the Scriver Lake area, La Ronge Domain (NTS 73P-16-NE): *in* Summary of Investigations 1996, Saskatchewan Geological Survey, Saskatchewan Energy and Mines, Miscellaneous Report 96-4, p. 79-91.

Zwanzig, H.V., 1990, Kisseynew gneiss belt in Manitoba: stratigraphy, structure, and tectonic evolution: *in* Lewry, J.F., and Stauffer, M.R., eds., The Early Proterozoic Trans-Hudson Orogen of North America, Geological Association of Canada Special Paper 37, p. 95-120.

APPENDIX A

ELECTRON MICROPROBE ANALYSES OF AMPHIBOLE, PLAGIOCLASE, BIOTITE, AND GARNET

Table A-1. Electron microprobe analyses of amphibole associated with the MLTZ

Sample	355	355	358	358	824-1a	824-1b	93-4	93-4	93-2	93-2
Rock type[1]	Mv	Mv	Mv	Mv	Mv	Mv	Gd	Gd	Gd	Gd
Location	Core	Rim	Core	Rim	Rim	Rim	Core	Rim	Core	Rim
Analyses	3	2	3	2	3	4	2	2	2	2
SiO_2	40.49	39.86	45.72	46.03	39.67	39.72	42.26	42.03	41.17	41.14
TiO_2	0.81	0.63	0.33	0.36	0.50	0.55	0.94	0.69	0.84	0.73
Al_2O_3	11.36	11.42	10.25	10.87	12.94	12.76	9.49	9.70	10.24	9.97
FeO	21.44	22.28	17.23	17.56	26.16	26.04	21.68	21.90	21.57	21.45
Cr_2O_3	0.06	0.04	0.23	0.05	0.02	0.05	0.05	0.01	0.04	0.00
MnO	0.27	0.26	0.30	0.24	0.51	0.42	0.43	0.39	0.35	0.38
MgO	8.31	8.98	11.10	10.85	5.00	4.97	9.04	8.80	8.26	8.50
CaO	11.67	10.95	11.05	11.03	11.83	11.65	11.68	11.60	11.59	11.69
Na_2O	1.38	1.22	0.73	0.88	0.92	0.88	1.46	1.44	1.26	1.25
K_2O	1.52	1.35	0.36	0.41	1.42	1.43	1.12	1.09	1.10	1.05
Total	97.31	96.99	97.30	98.28	98.97	98.47	98.15	97.65	96.42	96.16
Numbers of cations on the basis of 23 O										
Si	6.206	6.068	6.709	6.701	6.075	6.111	6.401	6.397	6.350	6.354
Al^{IV}	1.794	1.932	1.291	1.299	1.925	1.889	1.599	1.603	1.650	1.646
Al^{VI}	0.256	0.115	0.480	0.564	0.409	0.423	0.093	0.136	0.210	0.168
Al^{Total}	2.050	2.047	1.771	1.863	2.334	2.312	1.692	1.739	1.860	1.814
Ti	0.093	0.072	0.036	0.039	0.058	0.064	0.107	0.079	0.097	0.085
Cr	0.007	0.005	0.027	0.006	0.002	0.006	0.006	0.001	0.005	0.000
Fe^{3+}	0.726	1.273	0.715	0.623	0.910	0.875	0.752	0.787	0.738	0.797
Fe^{2+}	2.022	1.563	1.399	1.514	2.440	2.475	1.994	2.000	2.045	1.975
Mg	1.899	2.038	2.428	2.355	1.142	1.140	2.041	1.997	1.899	1.957
Mn	0.035	0.034	0.037	0.030	0.066	0.054	0.055	0.050	0.046	0.050
Ca	1.916	1.786	1.737	1.720	1.941	1.920	1.895	1.892	1.915	1.935
Na^{M4}	0.045	0.114	0.103	0.123	0.031	0.043	0.056	0.058	0.045	0.035
Na^{A}	0.365	0.246	0.105	0.125	0.242	0.220	0.373	0.367	0.332	0.339
Na^{Total}	0.410	0.360	0.208	0.248	0.273	0.263	0.429	0.425	0.377	0.374
K	0.297	0.262	0.067	0.076	0.277	0.281	0.216	0.212	0.216	0.207
Total	15.663	15.508	15.136	15.176	15.519	15.501	15.589	15.579	15.548	15.546
Nomencl-ature[2]	Hast	MG-Hast	MG-Hbl	MG-Hbl	Hast	Hast	MG-Hast	MG-Hast	Hast	Hast

1. Abbreviations: Mv, Mafic metavolcanic rock; Gd, Granodiorite; D, Diorite; Pd, Porphyritic diorite.
2. Nomenclature is based on the classification diagrams of Leake *et al.* (1997) (Figure A-1). Eden, Edenite; FE-, Ferro-; Hast, Hastingsite; Hbl, Hornblende; MG-, Magnesio-; Tsch, Tschermakite.

Table A-1. (continued) Electron microprobe analyses of amphibole associated with D_1 deformation

Sample	457	457	7071	7071	7072	7072	GT321	GT321	GT325
Rock type	Mv	Mv	Mv	Mv	Mv	Mv	Pelite	Pelite	Pelite
Location	Core	Rim	Core	Rim	Core	Rim	Core	Rim	Core
Analyses	4	3	3	3	4	2	2	4	3
SiO_2	50.32	43.47	44.62	44.83	45.47	45.54	42.58	41.70	42.82
TiO_2	0.30	0.37	0.33	0.36	0.60	0.60	0.41	0.40	0.35
Al_2O_3	5.08	10.65	10.71	11.04	9.18	9.60	13.12	12.70	13.57
FeO	18.87	22.86	18.34	18.14	17.10	17.29	22.04	20.31	20.63
Cr_2O_3	0.01	0.00	0.18	0.12	0.01	0.04	0.03	0.01	0.00
MnO	0.24	0.29	0.21	0.21	0.27	0.27	0.33	0.44	0.42
MgO	11.73	7.87	11.31	11.26	11.25	11.13	8.31	8.70	8.50
CaO	11.93	11.55	11.08	11.12	11.42	11.60	11.53	11.65	11.57
Na_2O	0.76	1.42	0.90	0.85	1.04	1.13	1.22	1.20	1.26
K_2O	0.06	0.46	0.65	0.56	0.27	0.26	0.37	0.33	0.34
Total	99.30	98.94	98.33	98.49	96.61	97.46	99.92	97.42	99.45
			Numbers of cations on the basis of 23 O						
Si	7.306	6.501	6.508	6.514	6.758	6.721	6.230	6.240	6.272
Al^{IV}	0.694	1.499	1.492	1.486	1.242	1.279	1.770	1.760	1.728
Al^{VI}	0.174	0.377	0.347	0.403	0.365	0.390	0.491	0.478	0.613
Al^{Total}	0.868	1.876	1.839	1.889	1.607	1.669	2.261	2.238	2.341
Ti	0.033	0.042	0.036	0.039	0.067	0.067	0.045	0.045	0.039
Cr	0.001	0.000	0.021	0.014	0.001	0.005	0.003	0.001	0.000
Fe^{3+}	0.382	0.697	0.962	0.932	0.585	0.556	0.975	0.922	0.813
Fe^{2+}	1.909	2.162	1.275	1.273	1.541	1.578	1.722	1.620	1.714
Mg	2.539	1.755	2.459	2.439	2.493	2.449	1.813	1.941	1.836
Mn	0.030	0.036	0.026	0.026	0.034	0.034	0.041	0.056	0.052
Ca	1.856	1.851	1.731	1.731	1.818	1.834	1.808	1.868	1.816
Na^{M4}	0.077	0.080	0.126	0.119	0.097	0.088	0.102	0.071	0.098
Na^{A}	0.137	0.332	0.128	0.121	0.203	0.235	0.244	0.278	0.260
Na^{Total}	0.214	0.412	0.254	0.240	0.300	0.323	0.346	0.349	0.358
K	0.011	0.088	0.121	0.104	0.051	0.049	0.069	0.063	0.064
Total	15.148	15.420	15.233	15.201	15.254	15.284	15.313	15.341	15.323
Nomencl-ature	Mg-Hbl	FE-Hbl	MG-Hbl	MG-Hbl	MG-Hbl	MG-Hbl	Tsch	Tsch	Tsch

Table A-1. (continued) Electron microprobe analyses of amphibole associated with D_1 deformation

Sample	GT325	GT327	GT327	93-42	93-42	93-72	93-72	93-52-1	93-52-1
Rock type	Pelite	Pelite	Pelite	Gd	Gd	Pd	Pd	D	D
Location	Rim	Core	Rim	Core	Rim	Core	Rim	Core	Rim
Analyses	4	2	5	3	2	2	2	3	2
SiO_2	43.60	42.50	43.63	44.74	43.19	48.23	44.28	42.75	43.09
TiO_2	0.47	0.38	0.41	0.64	0.55	0.35	0.43	0.85	0.81
Al_2O_3	11.44	13.09	11.87	9.17	10.12	7.10	9.30	10.97	10.78
FeO	20.14	20.59	20.28	19.77	21.31	18.59	21.05	22.08	21.54
Cr_2O_3	0.03	0.00	0.01	0.02	0.02	0.01	0.02	0.01	0.08
MnO	0.45	0.42	0.42	0.51	0.45	0.56	0.53	0.44	0.43
MgO	9.72	8.63	9.55	9.73	8.05	11.18	9.34	8.39	8.66
CaO	11.59	11.64	11.54	11.86	11.62	11.93	11.89	11.74	11.71
Na_2O	1.15	1.27	1.19	0.97	1.29	0.94	1.10	1.10	1.06
K_2O	0.27	0.31	0.28	0.61	0.94	0.41	0.76	0.81	0.74
Total	98.84	98.81	99.18	98.02	97.54	99.30	98.70	99.14	98.90
				Numbers of cations on the basis of 23 O					
Si	6.397	6.269	6.383	6.672	6.573	7.036	6.599	6.368	6.414
Al^{IV}	1.603	1.731	1.617	1.328	1.427	0.964	1.401	1.632	1.586
Al^{VI}	0.374	0.543	0.427	0.282	0.387	0.255	0.231	0.293	0.304
Al^{Total}	1.977	2.274	2.044	1.610	1.814	1.219	1.632	1.925	1.890
Ti	0.052	0.042	0.045	0.072	0.063	0.038	0.048	0.095	0.091
Cr	0.003	0.000	0.001	0.002	0.002	0.001	0.002	0.001	0.009
Fe^{3+}	0.933	0.853	0.913	0.616	0.461	0.433	0.717	0.810	0.785
Fe^{2+}	1.539	1.687	1.568	1.850	2.252	1.834	1.907	1.941	1.897
Mg	2.126	1.898	2.083	2.163	1.826	2.431	2.075	1.863	1.922
Mn	0.056	0.052	0.052	0.064	0.058	0.069	0.067	0.056	0.054
Ca	1.822	1.840	1.809	1.895	1.895	1.865	1.899	1.874	1.868
Na^{M4}	0.095	0.085	0.102	0.056	0.056	0.072	0.054	0.067	0.071
Na^{A}	0.232	0.278	0.236	0.224	0.325	0.194	0.264	0.250	0.235
Na^{Total}	0.327	0.363	0.338	0.280	0.381	0.266	0.318	0.317	0.306
K	0.051	0.058	0.052	0.116	0.173	0.076	0.144	0.154	0.141
Total	15.283	15.336	15.288	15.340	15.507	15.270	15.408	15.404	15.376
Nomencl-ature	Tsch	Tsch	Tsch	MG-Hbl	FE-Hbl	MG-Hbl	MG-Hbl	FE-Tsch	Tsch

Table A-1. (continued) Electron microprobe analyses of amphibole associated with D_2 deformation

Sample	M2(072)	M2(072)	444	444	93-91	93-90	93-90	450	450
Rock type	Mv	Mv	Gd	Gd	Pd	Pd	Pd	D	D
Location	Core	Rim	Core	Rim	Rim	Core	Rim	Core	Rim
Analyses	2	4	3	2	2	4	2	2	2
SiO_2	41.15	41.52	46.91	45.76	46.68	45.53	44.40	43.62	44.16
TiO_2	0.63	0.48	0.35	0.37	0.39	0.25	0.38	0.93	0.59
Al_2O_3	12.39	11.82	8.45	8.73	8.40	7.98	9.62	9.72	9.70
FeO	23.30	22.54	20.40	20.23	18.01	17.75	19.31	22.52	22.17
Cr_2O_3	0.03	0.07	0.03	0.06	0.02	0.04	0.07	0.00	0.00
MnO	0.31	0.25	0.37	0.37	0.55	0.65	0.69	0.41	0.39
MgO	7.23	7.51	9.75	9.42	10.93	11.36	10.42	7.99	8.00
CaO	11.63	11.70	11.78	11.97	12.26	12.17	11.89	11.76	11.82
Na_2O	1.49	1.44	0.99	1.10	1.06	0.95	1.11	1.03	0.94
K_2O	0.72	0.54	0.57	0.70	0.58	0.52	0.71	0.78	0.71
Total	98.88	97.87	99.60	98.71	98.88	97.20	98.60	98.76	98.48
Numbers of cations on the basis of 23 O									
Si	6.193	6.291	6.884	6.810	6.858	6.780	6.562	6.554	6.635
Al^{IV}	1.807	1.709	1.116	1.190	1.142	1.220	1.438	1.446	1.365
Al^{VI}	0.389	0.400	0.344	0.340	0.312	0.180	0.236	0.273	0.351
Al^{Total}	2.196	2.109	1.460	1.530	1.454	1.400	1.674	1.719	1.716
Ti	0.071	0.055	0.039	0.041	0.043	0.028	0.042	0.105	0.067
Cr	0.004	0.008	0.003	0.007	0.002	0.005	0.008	0.000	0.000
Fe^{3+}	0.832	0.772	0.460	0.408	0.405	0.668	0.783	0.627	0.574
Fe^{2+}	2.101	2.084	2.044	2.110	1.807	1.542	1.603	2.203	2.211
Mg	1.622	1.696	2.133	2.090	2.394	2.522	2.296	1.790	1.792
Mn	0.040	0.032	0.046	0.046	0.069	0.082	0.086	0.052	0.050
Ca	1.875	1.899	1.852	1.909	1.930	1.942	1.883	1.893	1.903
Na^{M4}	0.067	0.054	0.079	0.049	0.037	0.031	0.063	0.057	0.052
Na^{A}	0.368	0.369	0.203	0.269	0.265	0.243	0.255	0.243	0.222
Na^{Total}	0.435	0.423	0.282	0.318	0.302	0.274	0.318	0.300	0.274
K	0.138	0.104	0.107	0.133	0.109	0.099	0.134	0.150	0.136
Total	15.507	15.474	15.310	15.401	15.373	15.342	15.389	15.392	15.358
Nomencl-ature	Hast	FE-Tsch	MG-Hbl	MG-Hbl	MG-Hbl	MG-Hbl	MG-Hbl	FE-Hbl	FE-Hbl

Table A-1. (continued) Electron microprobe analyses of amphibole associated with D_2 deformation

Sample	93-352	93-352
Rock type	D	D
Location	Core	Rim
Analyses	3	1
SiO_2	46.65	45.86
TiO_2	1.07	1.09
Al_2O_3	8.23	8.50
FeO	19.40	19.10
Cr_2O_3	0.03	0.02
MnO	0.40	0.32
MgO	9.70	9.49
CaO	12.02	11.95
Na_2O	0.87	0.87
K_2O	0.85	0.89
Total	99.22	98.09
Si	6.900	6.865
Al^{IV}	1.100	1.135
Al^{VI}	0.333	0.364
Al^{Total}	1.433	1.499
Ti	0.119	0.123
Cr	0.004	0.002
Fe^{3+}	0.217	0.189
Fe^{2+}	2.182	2.202
Mg	2.139	2.118
Mn	0.050	0.040
Ca	1.905	1.917
Na^{M4}	0.051	0.044
Na^{A}	0.199	0.208
Na^{Total}	0.250	0.252
K	0.160	0.170
Total	15.359	15.378
Nomencl-ature	FE-Hbl	FE-Hbl

Table A-1. (continued) Electron microprobe analyses of amphibole associated with D_3 deformation

Sample	445	445	904-6	904-6	93-46	93-46	93-73	93-73	93-74
Rock type	Gd	Gd	Gd	Gd	Gd	Gd	Pd	Pd	Pd
D_{3a}/D_{3b}	D_{3a}	D_{3a}	D_{3a}	D_{3a}	D_{3b}	D_{3b}	D_{3a}	D_{3a}	D_{3b}
Location	Core	Rim	Core	Rim	Core	Rim	Core	Rim	Core
Analyses	2	2	2	3	2	2	1	2	1
SiO_2	46.05	47.68	43.71	44.45	47.57	49.01	47.10	44.87	48.21
TiO_2	0.22	0.24	0.93	0.75	0.19	0.12	0.32	0.43	0.25
Al_2O_3	8.75	7.81	9.38	9.26	7.58	6.97	8.14	9.36	7.37
FeO	18.49	18.17	21.23	20.87	16.08	14.26	17.35	19.65	18.18
Cr_2O_3	0.00	0.02	0.02	0.00	0.05	0.04	0.01	0.02	0.00
MnO	0.37	0.36	0.45	0.55	0.43	0.39	0.64	0.68	0.70
MgO	10.92	11.43	8.74	8.83	12.56	13.66	10.93	9.97	11.44
CaO	12.11	12.04	11.73	11.59	12.33	12.48	12.05	11.68	12.00
Na_2O	0.83	0.67	1.43	1.29	0.73	0.57	0.99	1.13	0.86
K_2O	0.28	0.33	1.04	0.98	0.37	0.17	0.57	0.75	0.40
Total	98.02	98.75	98.66	98.57	97.89	97.67	98.10	98.54	99.41
Numbers of cations on the basis of 23 O									
Si	6.780	6.947	6.584	6.674	6.949	7.098	6.959	6.655	7.002
Al^{IV}	1.220	1.053	1.416	1.326	1.051	0.902	1.041	1.345	0.998
Al^{VI}	0.298	0.287	0.248	0.311	0.253	0.287	0.375	0.290	0.263
Al^{Total}	1.518	1.340	1.664	1.637	1.304	1.189	1.416	1.635	1.261
Ti	0.024	0.026	0.105	0.085	0.021	0.013	0.036	0.048	0.027
Cr	0.000	0.002	0.002	0.000	0.006	0.005	0.001	0.002	0.000
Fe^{3+}	0.680	0.590	0.452	0.426	0.550	0.460	0.302	0.644	0.505
Fe^{2+}	1.598	1.624	2.222	2.194	1.415	1.268	1.842	1.793	1.704
Mg	2.397	2.483	1.963	1.976	2.735	2.949	2.407	2.204	2.477
Mn	0.046	0.044	0.058	0.070	0.054	0.048	0.080	0.085	0.086
Ca	1.910	1.879	1.893	1.865	1.930	1.937	1.907	1.856	1.867
Na^{M4}	0.048	0.064	0.057	0.072	0.038	0.034	0.049	0.077	0.071
Na^{A}	0.189	0.125	0.361	0.303	0.169	0.126	0.234	0.248	0.172
Na^{Total}	0.237	0.189	0.418	0.375	0.207	0.160	0.283	0.325	0.243
K	0.053	0.061	0.200	0.188	0.069	0.031	0.107	0.142	0.074
Total	15.242	15.186	15.560	15.491	15.238	15.158	15.342	15.390	15.246
Nomencl-ature	MG-Hbl	MG-Hbl	FE-Eden	FE-Hbl	MG-Hbl	MG-Hbl	MG-Hbl	MG-Hbl	MG-Hbl

Table A-1. (continued) Electron microprobe analyses of amphibole associated with D_3 deformation

Sample	93-74	93-76	93-78 (228)		93-52	93-52	93-51	93-51
Rock type	Pd	Pd	Pd	Pd	D	D	D	D
D_{3a}/D_{3b}	D_{3b}	D_{3a}	D_{3b}	D_{3b}	D_{3a}	D_{3a}	D_{3b}	D_{3b}
Location	Rim	Rim	Core	Rim	Core	Rim	Core	Rim
Analyses	2	4	3	2	2	3	2	2
SiO_2	45.04	43.88	43.86	43.02	45.08	43.63	47.56	46.98
TiO_2	0.44	0.43	0.41	0.45	0.39	0.39	0.23	0.27
Al_2O_3	9.68	9.01	9.83	10.18	8.87	10.12	8.30	8.48
FeO	20.32	22.64	21.83	22.53	18.70	20.38	14.44	13.89
Cr_2O_3	0.02	0.01	0.03	0.01	0.01	0.00	0.10	0.23
MnO	0.66	0.54	0.55	0.50	0.35	0.37	0.28	0.29
MgO	9.72	7.53	8.21	7.84	9.96	9.09	13.44	13.58
CaO	11.84	11.66	11.72	11.77	11.75	11.61	12.23	11.64
Na_2O	1.25	1.33	1.29	1.33	1.05	1.06	0.52	0.50
K_2O	0.79	0.45	0.81	0.93	0.70	0.93	0.23	0.56
Total	99.76	97.48	98.54	98.56	96.86	97.58	97.33	96.42
Numbers of cations on the basis of 23 O								
Si	6.623	6.699	6.600	6.502	6.791	6.568	6.899	6.870
Al^{IV}	1.377	1.301	1.400	1.498	1.209	1.432	1.101	1.130
Al^{VI}	0.300	0.319	0.342	0.314	0.365	0.362	0.317	0.331
Al^{Total}	1.677	1.620	1.742	1.812	1.574	1.794	1.418	1.461
Ti	0.049	0.049	0.046	0.051	0.044	0.044	0.025	0.030
Cr	0.002	0.001	0.004	0.001	0.001	0.000	0.011	0.027
Fe^{3+}	0.616	0.500	0.547	0.613	0.423	0.629	0.639	0.654
Fe^{2+}	1.882	2.390	2.200	2.235	1.933	1.937	1.113	1.044
Mg	2.131	1.714	1.842	1.766	2.237	2.040	2.906	2.961
Mn	0.082	0.070	0.070	0.064	0.044	0.047	0.034	0.036
Ca	1.865	1.907	1.890	1.906	1.897	1.873	1.901	1.824
Na^{M4}	0.072	0.050	0.059	0.050	0.055	0.068	0.053	0.070
Na^{A}	0.285	0.344	0.318	0.329	0.252	0.241	0.093	0.071
Na^{Total}	0.357	0.394	0.377	0.379	0.307	0.309	0.146	0.141
K	0.148	0.088	0.156	0.169	0.135	0.179	0.043	0.104
Total	15.433	15.432	15.473	15.519	15.386	15.420	15.136	15.152
Nomencl-ature	MG-Hbl	FE-Hbl	FE-Hbl	FE-Hbl	MG-Hbl	MG-Hbl	MG-Hbl	MG-Hbl

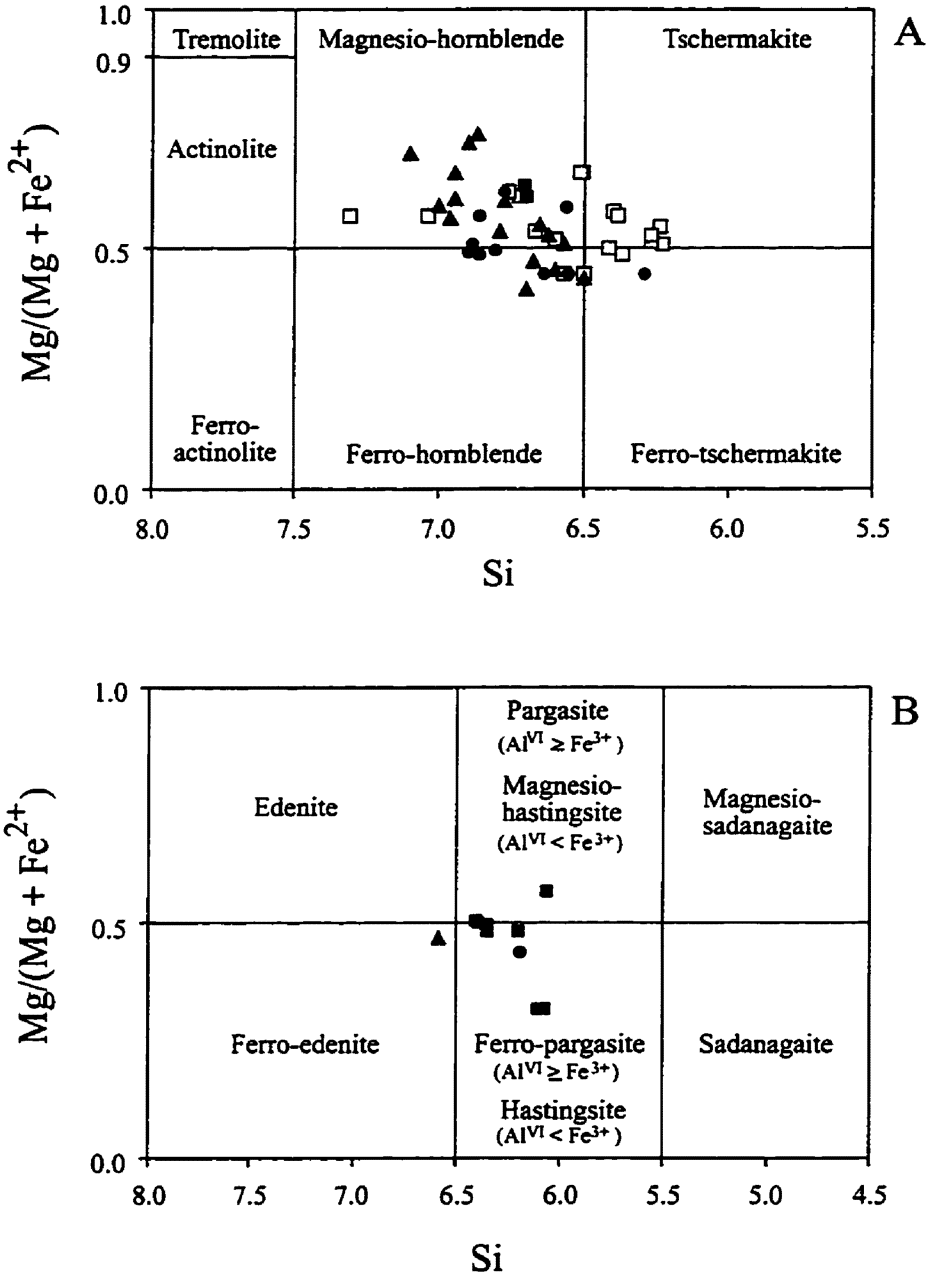

Figure A-1. Classification of calcic amphiboles (Leake *et al.*, 1997). (A) $(Na + K)^A < 0.50$. (B) $(Na + K)^A >/= 0.50$. Open squares, D_1; filled squares, MLTZ; filled circles, D_2; filled triangles, D_3.

Table A-2. Electron microprobe analyses of plagioclase associated with the MLTZ

Sample	355	358	824-1	93-4	93-2
Rock type[1]	Mv	Mv	Mv	Gd	Gd
Analyses	4	3	3	3	5
SiO_2	57.06	53.59	58.74	61.94	60.46
TiO_2	0.01	0.00	0.15	0.00	0.01
Al_2O_3	25.53	28.67	25.91	22.36	23.65
FeO	0.13	0.46	0.09	0.10	0.09
MnO	0.02	0.00	0.04	0.04	0.01
MgO	0.01	0.30	0.02	0.00	0.00
BaO	0.02	0.34	0.00	0.02	0.02
CaO	8.20	8.70	8.34	4.62	5.90
Na_2O	6.06	6.95	6.36	8.14	7.31
K_2O	0.14	0.07	0.06	0.26	0.20
Total	97.18	99.08	99.71	97.48	97.65
	Numbers of ions on the basis of 32 O				
Si	10.483	9.802	10.513	11.227	10.969
Al	5.524	6.176	5.461	4.773	5.053
Ti	0.001	0.000	0.020	0.000	0.001
Fe^{2+}	0.020	0.070	0.013	0.015	0.014
Mn	0.003	0.000	0.006	0.006	0.002
Mg	0.003	0.082	0.005	0.000	0.000
Ba	0.001	0.024	0.000	0.001	0.001
Ca	1.614	1.705	1.599	0.897	1.147
Na	2.159	2.465	2.207	2.861	2.572
K	0.033	0.016	0.014	0.060	0.046
Total	19.842	20.364	19.838	19.841	19.806
Ab	56.7	58.9	57.8	74.9	68.3
An	42.4	40.7	41.9	33.5	30.5
Or	0.9	0.4	0.4	1.6	1.2

1. Rock-type abbreviations are as in Table A-1.

Table A-2. (continued) Electron microprobe analyses of plagioclase associated with D_1 deformation

Sample	457	7071	7072	GT321	GT325	GT327	93-42	93-72	93-52-1
Rock type	Mv	Mv	Mv	Pelite	Pelite	Pelite	Gd	Pd	D
Analyses	4	4	3	4	3	4	4	4	4
SiO_2	57.50	55.92	56.00	56.81	58.03	58.15	61.13	60.67	56.90
TiO_2	0.02	0.01	0.03	0.01	0.02	0.01	0.01	0.01	0.03
Al_2O_3	26.77	27.21	26.79	26.65	26.29	25.95	24.11	24.13	27.25
FeO	0.08	0.15	0.13	0.13	0.02	0.06	0.05	0.05	0.13
MnO	0.01	0.02	0.01	0.02	0.03	0.03	0.01	0.01	0.00
MgO	0.00	0.01	0.01	0.01	0.02	0.01	0.00	0.01	0.00
BaO	0.03	0.01	0.02	0.02	0.01	0.01	0.01	0.01	0.01
CaO	7.17	8.20	8.30	8.16	7.98	7.60	6.08	6.03	8.83
Na_2O	7.44	7.15	6.59	6.23	6.75	6.89	7.62	7.67	6.31
K_2O	0.25	0.15	0.04	0.14	0.11	0.09	0.13	0.08	0.09
Total	99.27	98.83	97.92	98.18	99.26	98.80	99.15	98.67	99.55
				Numbers of ions on the basis of 32 O					
Si	10.366	10.171	10.248	10.342	10.443	10.503	10.932	10.905	10.242
Al	5.683	5.828	5.774	5.713	5.572	5.520	5.077	5.108	5.776
Ti	0.003	0.001	0.004	0.001	0.003	0.001	0.001	0.001	0.004
Fe^{2+}	0.012	0.023	0.020	0.020	0.003	0.009	0.007	0.008	0.020
Mn	0.002	0.003	0.002	0.003	0.005	0.005	0.002	0.002	0.000
Mg	0.000	0.003	0.003	0.003	0.005	0.003	0.000	0.003	0.000
Ba	0.002	0.001	0.001	0.001	0.001	0.001	0.001	0.001	0.001
Ca	1.385	1.598	1.627	1.592	1.539	1.471	1.165	1.161	1.703
Na	2.601	2.522	2.338	2.199	2.355	2.413	2.642	2.673	2.202
K	0.057	0.035	0.009	0.033	0.025	0.021	0.030	0.018	0.021
Total	20.113	20.186	20.027	19.908	19.952	19.948	19.858	19.881	19.970
Ab	64.3	60.7	58.8	57.5	60.1	61.8	68.9	69.4	56.1
An	34.3	38.5	40.9	41.6	39.3	37.7	32.4	30.1	43.4
Or	1.4	0.8	0.2	0.9	0.6	0.5	0.8	0.5	0.5

Table A-2. (continued) Electron microprobe analyses of plagioclase associated with D_2 deformation

Sample	M2(072)	444	93-91	93-90	450	93-352
Rock type	Mv	Gd	Pd	Pd	D	D
Analyses	4	4	5	3	4	4
SiO_2	59.45	60.67	61.21	59.97	58.29	59.91
TiO_2	0.00	0.01	0.01	0.01	0.01	0.02
Al_2O_3	24.14	24.43	23.82	23.52	25.77	24.52
FeO	0.11	0.06	0.07	0.30	0.06	0.03
MnO	0.00	0.00	0.02	0.01	0.03	0.01
MgO	0.01	0.01	0.00	0.02	0.01	0.00
BaO	0.06	0.02	0.02	0.01	0.01	0.01
CaO	7.61	6.34	5.80	5.71	7.98	6.49
Na_2O	7.47	7.57	7.85	6.95	6.90	7.48
K_2O	0.05	0.16	0.14	0.84	0.09	0.11
Total	98.90	99.27	98.94	97.34	99.15	98.58
	Numbers of ions on the basis of 32 O					
Si	10.739	10.854	10.970	10.952	10.505	10.799
Al	5.135	5.147	5.027	5.058	5.470	5.205
Ti	0.000	0.001	0.001	0.001	0.001	0.003
Fe^{2+}	0.017	0.009	0.010	0.046	0.009	0.005
Mn	0.000	0.000	0.003	0.002	0.005	0.002
Mg	0.003	0.003	0.000	0.005	0.003	0.000
Ba	0.004	0.001	0.001	0.001	0.001	0.001
Ca	1.473	1.215	1.114	1.117	1.541	1.253
Na	2.617	2.626	2.728	2.461	2.411	2.614
K	0.012	0.037	0.032	0.196	0.021	0.025
Total	20.004	19.894	19.887	19.840	19.968	19.908
Ab	63.8	67.7	70.4	65.2	60.7	67.2
An	35.9	31.3	28.8	29.6	38.8	32.2
Or	0.3	1.0	0.8	5.2	0.5	0.6

Table A-2. (continued) Electron microprobe analyses of plagioclase associated with D_3 deformation

Sample	445	904-6	93-46	93-73	93-74	93-76	93-78	93-52	93-51
Rock type	Gd	Gd	Gd	Pd	Pd	Pd	Pd	D	D
D_{3a}/D_{3b}	D_{3a}	D_{3a}	D_{3b}	D_{3a}	D_{3b}	D_{3a}	D_{3b}	D_{3a}	D_{3b}
Analyses	4	4	4	4	2	4	4	4	4
SiO_2	60.85	62.90	61.30	61.50	61.65	62.21	63.10	60.18	60.26
TiO_2	0.00	0.01	0.02	0.00	0.01	0.02	0.01	0.01	0.02
Al_2O_3	24.22	22.86	23.56	23.67	23.69	23.31	23.04	23.24	23.57
FeO	0.07	0.07	0.08	0.10	0.13	0.10	0.08	0.03	0.07
MnO	0.02	0.02	0.02	0.00	0.00	0.02	0.01	0.03	0.00
MgO	0.01	0.00	0.00	0.01	0.01	0.00	0.00	0.01	0.00
BaO	0.02	0.01	0.01	0.02	0.04	0.02	0.01	0.01	0.04
CaO	6.09	4.64	5.64	5.62	5.71	5.20	4.77	5.71	5.91
Na_2O	7.78	8.37	8.01	7.85	7.80	8.11	8.48	7.63	7.43
K_2O	0.12	0.19	0.15	0.13	0.15	0.10	0.14	0.12	0.14
Total	99.18	99.07	98.79	98.90	99.19	99.09	99.64	96.97	97.44
				Numbers of ions on the basis of 32 O					
Si	10.892	11.212	11.003	11.014	11.014	11.104	11.189	10.996	10.961
Al	5.106	4.799	4.980	4.992	4.984	4.900	4.812	5.001	5.049
Ti	0.000	0.001	0.003	0.000	0.001	0.003	0.001	0.001	0.003
Fe^{2+}	0.010	0.010	0.012	0.015	0.019	0.015	0.012	0.005	0.011
Mn	0.003	0.003	0.003	0.000	0.000	0.003	0.002	0.005	0.000
Mg	0.003	0.000	0.000	0.003	0.003	0.000	0.000	0.003	0.000
Ba	0.001	0.001	0.001	0.001	0.003	0.001	0.001	0.001	0.003
Ca	1.168	0.886	1.085	1.078	1.093	0.994	0.906	1.118	1.152
Na	2.700	2.893	2.788	2.726	2.702	2.807	2.916	2.703	2.621
K	0.027	0.043	0.034	0.030	0.034	0.023	0.032	0.028	0.032
Total	19.911	19.849	19.910	19.860	19.856	19.851	19.872	19.862	19.835
Ab	69.3	75.7	71.4	71.1	70.6	73.4	75.7	70.2	68.9
An	30.0	23.2	27.8	28.1	28.5	26.0	23.5	29.0	30.3
Or	0.7	1.1	0.9	0.8	0.9	0.6	0.8	0.7	0.8

Table A-3. Electron microprobe analyses of biotite associated with the MLTZ

Sample	355	358	824-1	93-4	93-2
Rock type[1]	Mv	Mv	Mv	Gd	Gd
Analyses	2	2	4	3	4
SiO_2	37.42	36.47	36.23	37.76	37.22
TiO_2	2.56	1.76	2.27	1.60	2.34
Al_2O_3	15.27	16.98	17.40	15.22	15.50
FeO	22.06	20.69	25.59	21.29	21.81
MnO	0.24	0.24	0.31	0.31	0.25
MgO	10.49	14.37	7.63	11.90	11.23
CaO	0.02	0.06	0.16	0.01	0.07
Na_2O	0.06	0.20	0.08	0.09	0.07
K_2O	9.26	5.77	8.86	9.43	9.16
Total	97.38	96.54	98.53	97.61	97.65
Numbers of ions on the basis of 22 O and 0 OH					
Si	5.640	5.404	5.475	5.660	5.588
Al^{IV}	2.360	2.596	2.525	2.340	2.412
Al^{VI}	0.350	0.367	0.572	0.347	0.328
Ti	0.290	0.196	0.258	0.180	0.264
Fe^{2+}	2.781	2.564	3.234	2.669	2.738
Mn	0.031	0.030	0.040	0.039	0.032
Mg	2.357	3.174	1.719	2.659	2.513
Ca	0.003	0.010	0.026	0.002	0.011
Na	0.018	0.057	0.023	0.026	0.020
K	1.780	1.091	1.708	1.803	1.754
Cations	15.610	15.489	15.580	15.725	15.660
Fe/Fe+Mg	0.540	0.450	0.650	0.500	0.520
Mg/Fe+Mg	0.460	0.550	0.350	0.500	0.480

1. Rock-type abbreviations are as in Table A-1.

Table A-3. (continued) Electron microprobe analyses of biotite associated with D_1 deformation

Sample	457	7071	7072	GT321	GT325	GT327	93-42	93-72	93-52-1
Rock type	Mv	Mv	Mv	Pelite	Pelite	Pelite	Gd	Pd	D
Analyses	4	2	3	2	4	3	4	4	4
SiO_2	35.97	35.37	34.34	37.12	36.88	36.90	37.70	37.26	37.56
TiO_2	1.89	2.41	2.42	1.93	1.99	1.95	2.10	1.44	1.65
Al_2O_3	16.73	16.58	16.86	16.33	16.16	16.12	16.58	16.25	16.24
FeO	23.74	21.63	22.14	20.73	20.26	21.59	21.50	19.56	23.88
MnO	0.12	0.05	0.09	0.14	0.18	0.18	0.37	0.43	0.27
MgO	9.70	13.85	14.55	11.48	11.68	11.35	10.63	12.15	9.45
CaO	0.15	0.09	0.08	0.06	0.22	0.48	0.04	0.03	0.01
Na_2O	0.22	0.18	0.15	0.14	0.15	0.12	0.07	0.06	0.05
K_2O	8.21	5.78	4.45	8.82	8.39	7.85	9.33	9.18	9.44
Total	96.73	95.94	95.08	96.75	95.91	96.54	98.32	96.36	98.55
Numbers of ions on the basis of 22 O and 0 OH									
Si	5.480	5.314	5.193	5.578	5.574	5.560	5.601	5.607	5.633
Al^{IV}	2.520	2.686	2.807	2.422	2.426	2.440	2.399	2.393	2.367
Al^{VI}	0.482	0.248	0.195	0.468	0.450	0.421	0.502	0.487	0.501
Ti	0.217	0.272	0.275	0.218	0.226	0.221	0.235	0.163	0.186
Fe^{2+}	3.025	2.718	2.800	2.605	2.561	2.721	2.671	2.462	2.995
Mn	0.015	0.006	0.012	0.018	0.023	0.023	0.047	0.055	0.034
Mg	2.203	3.102	3.280	2.572	2.632	2.550	2.354	2.726	2.113
Ca	0.024	0.014	0.013	0.010	0.036	0.077	0.006	0.005	0.002
Na	0.065	0.052	0.044	0.041	0.044	0.035	0.020	0.018	0.015
K	1.596	1.108	0.858	1.691	1.618	1.509	1.768	1.762	1.806
Cations	15.627	15.520	15.477	15.623	15.590	15.557	15.603	15.678	15.652
Fe/Fe+Mg	0.580	0.470	0.460	0.500	0.490	0.520	0.530	0.470	0.590
Mg/Fe+Mg	0.420	0.530	0.540	0.500	0.510	0.480	0.470	0.530	0.410

Table A-3. (continued) Electron microprobe analyses of biotite associated with D_3 deformation

Sample	445	904-6	93-46	93-73	93-74	93-76	93-78	93-52	93-51
Rock type	Gd	Gd	Gd	Pd	Pd	Pd	Pd	D	D
D_{3a}/D_{3b}	D_{3a}	D_{3a}	D_{3b}	D_{3a}	D_{3b}	D_{3a}	D_{3b}	D_{3a}	D_{3b}
Analyses	4	4	4	4	2	4	4	4	4
SiO_2	37.39	37.67	38.24	37.46	37.79	36.78	37.59	37.07	37.92
TiO_2	2.18	1.59	1.72	1.67	1.53	1.98	2.32	1.69	1.66
Al_2O_3	16.04	15.63	17.26	16.24	16.38	16.33	16.34	15.89	16.38
FeO	21.96	21.47	18.37	19.88	20.44	23.23	22.42	20.02	18.11
MnO	0.28	0.34	0.29	0.44	0.43	0.36	0.38	0.27	0.21
MgO	10.48	11.89	12.96	11.31	11.52	10.15	10.28	11.15	12.07
CaO	0.01	0.04	0.01	0.03	0.01	0.02	0.00	0.02	0.03
Na_2O	0.06	0.05	0.08	0.08	0.04	0.08	0.05	0.10	0.09
K_2O	9.33	8.91	9.68	9.16	9.08	8.79	9.58	9.14	9.24
Total	97.73	97.59	98.61	96.27	97.22	97.72	98.96	95.35	95.71
	Numbers of ions on the basis of 22 O and 0 OH								
Si	5.608	5.633	5.580	5.646	5.643	5.543	5.583	5.651	5.689
Al^{IV}	2.392	2.367	2.420	2.354	2.357	2.457	2.417	2.349	2.311
Al^{VI}	0.441	0.386	0.546	0.529	0.524	0.441	0.441	0.504	0.583
Ti	0.246	0.179	0.189	0.189	0.172	0.224	0.259	0.194	0.187
Fe^{2+}	2.755	2.685	2.242	2.506	2.553	2.928	2.785	2.552	2.272
Mn	0.036	0.043	0.036	0.056	0.054	0.046	0.048	0.035	0.027
Mg	2.343	2.651	2.819	2.541	2.565	2.280	2.276	2.534	2.700
Ca	0.002	0.006	0.002	0.005	0.002	0.003	0.000	0.003	0.005
Na	0.017	0.014	0.023	0.023	0.012	0.023	0.014	0.030	0.026
K	1.785	1.700	1.802	1.761	1.730	1.690	1.815	1.777	1.769
Cations	15.625	15.664	15.659	15.610	15.612	15.635	15.638	15.629	15.569
Fe/Fe+Mg	0.540	0.500	0.440	0.500	0.500	0.560	0.550	0.500	0.460
Mg/Fe+Mg	0.460	0.500	0.560	0.500	0.500	0.440	0.450	0.500	0.540

Table A-4. Electronic microprobe analyses of garnet

Sample	GT321	GT321	GT325	GT325	GT327	GT327
Location	Core	Rim	Core	Rim	Core	Rim
Analyses	2	5	2	5	2	5
SiO_2	37.68	37.33	37.30	37.12	37.28	37.34
TiO_2	0.05	0.03	0.06	0.04	0.03	0.01
Al_2O_3	21.58	21.92	21.85	21.70	22.17	21.58
FeO	29.93	28.03	27.99	27.73	30.07	27.22
MnO	5.72	6.65	6.45	6.63	5.98	6.50
MgO	2.90	2.63	2.75	2.56	2.81	2.52
CaO	3.99	5.31	4.33	5.13	4.36	5.15
Total	101.85	101.90	100.73	100.91	102.70	100.32
			Formulae based on 12 oxygens			
Si	2.967	2.932	2.964	2.945	2.910	2.978
Al^{IV}	0.033	0.068	0.036	0.055	0.090	0.022
Al^{VI}	1.968	1.960	2.008	1.973	1.948	2.005
Ti	0.003	0.002	0.004	0.002	0.002	0.001
Fe^{2+}	1.971	1.841	1.860	1.840	1.963	1.816
Mg	0.340	0.308	0.326	0.303	0.327	0.300
Mn	0.381	0.442	0.434	0.446	0.395	0.439
Ca	0.337	0.447	0.369	0.436	0.365	0.440
Alm	0.651	0.606	0.622	0.608	0.644	0.606
Gross	0.111	0.147	0.123	0.144	0.120	0.147
Pyrope	0.112	0.101	0.109	0.100	0.107	0.100
Spess	0.126	0.146	0.145	0.147	0.130	0.147
Mg/Fe	0.173	0.167	0.175	0.165	0.167	0.165

APPENDIX B

MAJOR AND TRACE ELEMENT CHEMISTRY AND NET COMPOSITION

Table B-1. Major and trace element chemistry of deformed and least deformed rocks related to the McLennan Lake Tectonic Zone, the D_2 structures, and the D_3 gold-bearing shears.

Notes:

1. Rock-type abbreviations: D, diorite; G, granite; Gd, granodiorite; Pd, porphyritic diorite.
2. Rock fabric abbreviations: P, least deformed precursor; Pm, protomylonite; M, mylonite.
3. Analytical techniques: (1) Major elements were analyzed by XRF-F and trace elements by XRF-F, INAA and ICP while Au by FADCP at XRAL Laboratories (2) Major elements were determined by XRF-F at McGill University; trace elements were measured on a Perkin Elmer Sciex Elan 5000 ICP-MS in Department of Geological Sciences, University of Saskatchewan.
4. Major elements are reported in percentage, trace elements in ppm, and gold in ppb.
5. Specific gravity of all specimens were determined using a Beckman Model 930 Air Comparison Pycnometer.

Table B-1. (continued) The McLennan Lake Tectonic Zone

Sample	93-4	93-2	93-2	93-14	93-118	93-117
Rock type[1]	Gd	Gd	Duplicate	Gd	Gd	Gd
Rock fabric[2]	P	M	M	M	P	M
Technique[3]	(1)	(1)	(1)	(1)	(1)	(1)
SiO_2 [4]	59.9	59.2	58.9	55.5	60.4	65.6
TiO_2	0.78	0.80	0.83	0.86	0.77	0.56
Al_2O_3	17.0	17.2	17.1	18.6	16.5	15.7
Fe_2O_3	5.92	6.44	6.42	6.63	6.05	5.29
MnO	0.08	0.08	0.09	0.09	0.08	0.10
MgO	2.40	2.80	2.78	2.07	2.61	1.80
Cr_2O_3	<0.01	0.01	0.01	<0.01	0.01	0.02
CaO	4.29	5.19	5.22	5.58	4.16	5.27
Na_2O	4.26	4.00	3.98	4.76	4.12	3.59
K_2O	3.96	3.18	3.19	3.18	3.84	1.12
P_2O_5	0.30	0.35	0.36	0.51	0.34	0.15
LOI	0.50	0.80	0.75	0.70	0.70	1.10
Total	99.39	100.05	99.63	98.48	99.58	100.30
Li						
B						
Rb	142	137	134	90	157	43
Sr	490	464	461	635	537	287
Y	16	18	18	19	21	<10
Zr	321	271	283	223	364	149
Nb	20	19	19	12	21	<10
Ba	914	875	863	954	904	587
Sc	11.3	11.4	10.6	12.6	10.3	8.9
Cr	120	150	140	110	160	230
Cs	5	7	6	<3	7	3
La	49	54	53	52	51	14
Ce	85	98	100	91	98	30
Nd	30	40	40	40	40	10
Sm	5.7	6.5	6.5	6.3	6.8	2.6
Eu	0.9	1.9	1.7	2.5	1.1	0.9
Tb	<0.5	0.6	0.5	<0.5	0.7	<0.5
Yb	2.0	1.8	1.9	2.2	2.2	1.4
Lu	0.33	0.31	0.30	0.33	0.33	0.23
Hf	8	7	6	6	8	4
Th	14.0	9.2	9.3	3.8	14.0	2.5
U	5.0	4.8	4.5	2.3	6.3	1.7
Co	9	12	12	10	12	8
Ni	17	25	25	11	23	11
Cu	66.4	78.6	78.2	44.9	64.8	29.6
Zn	56.8	44.0	44.1	54.1	55.4	40.9
Mo	<1	4	5	<1	3	<1
Pb	3	4	3	5	4	<2
Au	7	24	27	4	13	2
Ag	0.03	0.03	0.03	<0.02	0.04	<0.02
S.G.[5]	2.759	2.793		2.788	2.752	2.759

Table B-1. (continued) D_2 structures

Sample	93-90	93-91	443	450
Rock type	Pd	Pd	D	D
Rock fabric	M	M	M	M
Technique	(1)	(1)	(1)	(1)
SiO_2	50.0	55.3	56.8	53.7
TiO_2	0.54	0.59	0.61	0.67
Al_2O_3	19.1	16.2	18.2	19.0
Fe_2O_3	8.65	10.20	7.79	8.15
MnO	0.22	0.16	0.09	0.11
MgO	4.34	2.28	3.56	4.06
Cr_2O_3	0.03	0.02	0.02	0.01
CaO	7.12	6.99	4.66	6.00
Na_2O	2.85	0.59	4.06	4.19
K_2O	4.33	4.57	2.84	2.65
P_2O_5	0.30	0.29	0.48	0.49
LOI	0.65	1.80	1.10	0.95
Total	98.13	98.99	100.21	99.98
Li				
B				
Rb	73	84	79	67
Sr	591	257	561	635
Y	<10	13	16	15
Zr	63	59	148	138
Nb	<10	<10	10	<10
Ba	5020	1703	897	956
Sc	21	24.6	11.4	13.3
Cr	240	210	170	140
Cs	3	3	3	<3
La	15	11	37	33
Ce	32	27	75	72
Nd	10	10	30	30
Sm	3.2	3.0	5.7	5.9
Eu	1.1	0.8	1.7	1.9
Tb	<0.5	0.5	0.6	0.8
Yb	1.6	2.4	2.0	1.9
Lu	0.28	0.36	0.28	0.29
Hf	1	1	2	3
Th	2.3	2.1	7.2	3.4
U	1.1	1.2	1.9	1.3
Co	17	20	21	17
Ni	38	11	38	36
Cu	73.8	133.0	75.9	59.6
Zn	115.0	89.7	73.2	50.0
Mo	<1	<1	<1	<1
Pb	<2	<2	4	<2
Au	3	7	2	5
Ag	<0.02	0.02	<0.02	<0.02
S.G.	2.877	2.904	2.782	2.821

Table B-1. (continued) D_3 Rod shear

Sample	93-52-1	93-52	93-51	93-42	93-42	93-44	93-46
Rock type	D	D	D	Gd	Duplicate	Gd	Gd
Rock fabric	P	Pm	M	P	P	Pm	M
Technique	(2)	(2)	(2)	(2)	(2)	(2)	(2)
SiO_2	55.7	55.4	54.9	61.0		61.6	62.1
TiO_2	0.72	0.69	0.65	0.33		0.32	0.31
Al_2O_3	18.6	18.3	17.1	18.9		18.5	17.6
Fe_2O_3	7.46	7.86	8.17	5.10		4.52	4.88
MnO	0.124	0.115	0.119	0.094		0.083	0.088
MgO	2.90	3.71	4.79	2.02		1.69	1.92
Cr_2O_3	0.01	0.01	0.03	<0.01		<0.01	<0.01
CaO	6.11	5.51	6.39	4.94		3.86	4.25
Na_2O	3.99	4.03	3.79	4.90		4.83	4.16
K_2O	3.37	3.19	2.89	2.78		3.20	3.52
P_2O_5	0.43	0.42	0.39	0.19		0.17	0.22
LOI	0.74	0.83	1.42	0.62		1.02	0.72
Total	100.11	100.05	100.65	100.81		99.73	99.80
Li	26	39	25	32	24	25	25
B	56	33	18	16	20	19	18
Rb	107	107	86	73	72	75	76
Sr	576	807	732	747	764	553	428
Y	26	23	20	12	12	12	16
Zr	201	93	142	80	53	114	202
Nb	12	11	11	5	5	6	9
Ba	1003	793	621	937	939	1178	1049
Sc	15.4	15.1	17.9	8.1	8.3	6.7	9.0
Cr	77	106	276	36	30	30	36
Cs	4	4	3	3	3	3	3
La	48	40	38	24	23	24	34
Ce	94	83	80	43	44	46	66
Nd	45	39	41	19	19	21	29
Sm	7.2	6.7	6.6	3.0	3.1	3.5	4.6
Eu	1.7	1.7	1.7	1.1	1.1	1.0	1.2
Tb	0.8	0.8	0.7	0.4	0.4	0.3	0.5
Yb	2.7	2.2	1.9	1.2	1.1	1.3	1.4
Lu	0.42	0.31	0.25	0.15	0.17	0.19	0.21
Hf	5	3	4	2	1	3	5
Th	8.7	4.0	3.9	4.5	4.8	9.8	8.6
U	4.4	3.0	1.8	1.6	2.1	3.1	2.9
Co	23	25	28	15	15	14	15
Ni	34	48	73	20	20	13	20
Cu	54.7	65.2	84.3	48.9	49.6	57.3	80.1
Zn	88.0	80.7	80.0	54.9	55.1	33.9	23.3
Mo	3	1	1	1	<1	<1	1
Pb	17	14	12	14	14	7	6
Au	1	28	51	4		39	204
Ag							
S.G.	2.805	2.827	2.833	2.791		2.718	2.733

Table B-1. (continued) D_3 Rod shear and MacLeod Main shear

Sample	93-72	93-73	93-74	93-4	904-6	904-7
Rock type	Pd	Pd	Pd	Gd	Gd	Gd
Rock fabric	P	Pm	M	P	Pm	M
Technique	(1)	(1)	(1)	(1)	(1)	(1)
SiO_2	58.2	58.8	54.6	59.9	59.9	61.9
TiO_2	0.61	0.59	0.59	0.78	0.74	0.76
Al_2O_3	16.2	16.3	19.2	17.0	16.4	16.8
Fe_2O_3	7.00	7.22	9.72	5.92	5.84	5.69
MnO	0.16	0.17	0.18	0.08	0.08	0.04
MgO	3.18	3.06	1.45	2.40	2.41	2.77
Cr_2O_3	0.02	0.02	<0.01	<0.01	0.02	0.01
CaO	5.98	6.21	6.64	4.29	3.96	2.29
Na_2O	4.32	3.85	3.27	4.26	4.47	2.64
K_2O	1.92	2.23	2.94	3.96	4.13	5.10
P_2O_5	0.23	0.22	0.35	0.30	0.30	0.37
LOI	0.60	0.70	0.60	0.50	1.00	1.45
Total	98.42	99.37	99.54	99.39	99.25	99.82
Li						
B						
Rb	36	50	57	142	129	268
Sr	997	850	956	490	507	332
Y	15	15	18	16	21	19
Zr	137	131	81	321	371	423
Nb	<10	<10	<10	20	20	21
Ba	922	941	1400	914	797	1490
Sc	15.3	15.2	21.9	11.3	9.4	12.6
Cr	190	200	130	120	200	120
Cs	<3	<3	<3	5	4	8
La	20	21	12	49	49	42
Ce	41	42	28	85	94	80
Nd	20	20	10	30	30	30
Sm	4.0	4.0	3.2	5.7	6.5	4.9
Eu	1.1	1.1	1.3	0.9	1.1	0.8
Tb	0.5	0.5	0.6	<0.5	0.7	0.5
Yb	1.8	1.7	2.7	2.0	2.0	1.5
Lu	0.29	0.28	0.43	0.33	0.31	0.22
Hf	3	3	1	8	8	10
Th	2.6	2.4	2.2	14.0	15.0	17.0
U	2.6	2.1	1.1	5.0	5.6	7.7
Co	11	12	15	9	12	17
Ni	12	14	5	17	22	42
Cu	55.6	83.8	194.0	66.4	119.0	520.0
Zn	64.0	161.0	138.0	56.8	61.2	71.7
Mo	2	1	<1	<1	7	4
Pb	<2	5	<2	3	4	7
Au	2	23	76	7	21	771
Ag	<0.02	0.05	0.14	0.03	0.12	4.22
S.G.	2.819	2.822	2.889	2.759	2.756	2.767

Table B-1. (continued) D_3 James-Roxy shears

Sample	93-29	93-28	93-26	93-41	93-39	93-38
Rock type	G	G	G	G	G	G
Rock fabric	P	Pm	M	P	Pm	M
Technique	(2)	(2)	(2)	(2)	(2)	(2)
SiO_2	69.9	68.9	70.7	69.4	70.1	70.5
TiO_2	0.27	0.26	0.25	0.25	0.24	0.24
Al_2O_3	15.3	15.1	14.9	15.3	15.8	15.6
Fe_2O_3	2.47	2.85	2.35	2.13	2.11	2.22
MnO	0.05	0.04	0.03	0.04	0.05	0.04
MgO	1.11	1.01	0.95	0.98	0.77	0.79
Cr_2O_3	0.01	0.01	0.01	<0.01	0.01	0.01
CaO	2.48	2.18	1.40	2.76	2.17	2.05
Na_2O	4.39	3.38	2.65	4.34	3.97	3.35
K_2O	3.66	4.63	5.12	3.60	3.67	4.01
P_2O_5	0.10	0.10	0.09	0.09	0.09	0.07
LOI	0.42	1.16	1.31	0.70	0.79	1.25
Total	100.19	99.61	99.78	99.54	99.76	100.15
Li	42	26	22	22	13	15
B	10	6	26	7	12	23
Rb	120	128	127	93	93	96
Sr	468	391	277	510	292	285
Y	7	7	6	7	4	7
Zr	115	114	117	121	52	111
Nb	10	7	9	8	3	7
Ba	1000	995	928	1147	1160	1189
Sc	4.4	4.4	4.3	4.0	2.8	3.9
Cr	59	54	56	43	60	51
Cs	2	2	3	1	2	2
La	27	24	30	22	20	25
Ce	43	40	53	38	30	33
Nd	13	14	18	15	13	15
Sm	1.9	2.0	2.5	2.0	1.9	2.2
Eu	0.5	0.6	0.6	0.6	0.5	0.6
Tb	0.2	0.2	0.2	0.2	0.2	0.2
Yb	0.6	0.7	0.7	0.6	0.5	0.7
Lu	0.11	0.10	0.10	0.10	0.09	0.09
Hf	4	4	3	4	4	3
Th	10.0	8.5	9.4	8.1	6.5	8.2
U	10.3	2.9	5.9	1.8	1.5	2.5
Co	6	9	7	6	3	5
Ni	13	14	12	11	6	10
Cu	3.4	11.6	143.0	2.0	6.3	69.8
Zn	44.9	32.6	53.4	24.7	16.5	46.5
Mo	1	1	1	<1	1	<1
Pb	17	32	86	12	12	23
Au	1	373	447	2	48	326
Ag						
S.G.	2.675	2.676	2.664	2.670	2.665	2.662

Table B-2. Net composition of deformed and least deformed rocks related to the McLennan Lake Tectonic Zone, the D_2 structures, and the D_3 gold-bearing shears (grams/100cc for major elements, grams/cubic metre for trace elements).

Notes:

1. Rock-type abbreviations are as in Table B-1.
2. Rock-fabric abbreviations are as in Table B-1.

Table B-2. (continued) The McLennan Lake Tectonic Zone

Sample	93-4	93-2	93-14	93-118	93-117
Rock type[1]	Gd	Gd	Gd	Gd	Gd
Rock fabric[2]	P	M	M	P	M
Si	77.3	73.4	64.9	77.7	87.3
Ti	1.29	1.27	1.29	1.27	1.30
Al	24.8	24.2	24.6	24.0	23.7
TFe	12.70	13.30	12.90	12.90	11.70
Mn	0.17	0.16	0.17	0.17	0.22
Mg	4.00	4.48	3.12	4.33	3.09
Ca	8.46	9.84	9.98	8.18	10.70
Na	8.72	7.87	8.84	8.40	7.58
K	9.07	7.01	6.61	8.77	2.65
P	0.36	0.41	0.56	0.41	0.19
O	126	121	112	126	135
Li					
B					
Sc	31.2	30.3	31.5	28.3	25.3
Cr	331	398	275	440	655
Co	25	32	25	33	23
Ni	47	66	28	63	31
Cu	183.0	209.0	112.0	178.0	84.3
Zn	157.0	117.0	135.0	152.0	116.0
Rb	392	364	225	432	122
Sr	1350	1230	1590	1480	817
Y	44	48	48	58	
Zr	886	719	558	1000	424
Nb	55.2	50.4	30.0	57.8	
Mo				8	
Cs	14	19		19	9
Ba	2520	2320	2390	2490	1670
La	135	143	130	140	40
Ce	235	260	228	270	85
Nd	83	106	100	110	29
Sm	15.7	17.2	15.8	18.7	7.4
Eu	2.5	5.0	6.3	3.0	2.6
Tb				1.9	
Yb	5.5	4.8	5.5	6.1	4.0
Lu	0.91	0.82	0.83	0.91	0.66
Hf	22	19	15	22	11
Au	0.019	0.064	0.010	0.036	0.006
Pb	8	11	13	11	
Th	38.6	24.4	9.5	38.5	7.1
U	13.8	12.7	5.7	17.3	4.8
FV	1.00	0.97	0.90	1.00	1.04
Vol. change		-3%	-10%		4%
Immobile element		Ti	Ti, Sm Yb		Ti, Al

Table B-2. (continued) D_2 structures

Sample	93-72	93-90	93-91
Rock type	Pd	Pd	Pd
Rock fabric	P	M	M
Si	76.7	74.7	75.7
Ti	1.03	1.03	1.04
Al	24.2	32.3	25.1
TFe	15.30	21.50	23.20
Mn	0.35	0.55	0.36
Mg	5.41	8.37	4.03
Ca	12.10	16.30	14.60
Na	9.04	6.76	1.28
K	4.49	11.50	11.10
P	0.28	0.42	0.37
O	127	138	128
Li			
B			
Sc	43.1	67.1	72.1
Cr	536	767	615
Co	31	54	59
Ni	34	121	32
Cu	157.0	236.0	390.0
Zn	180.0	368.0	263.0
Rb	102	233	246
Sr	2810	1890	753
Y	42		38
Zr	386	201	173
Nb			
Mo	6		
Cs			
Ba	2600	16000	2060
La	56	48	32
Ce	116	102	79
Nd	56	32	29
Sm	11.3	10.2	8.8
Eu	3.1	3.5	2.3
Tb	1.4		1.5
Yb	5.1	5.1	7.0
Lu	0.82	0.90	1.05
Hf	9	3	3
Au	0.006	0.010	0.021
Pb			
Th	7.3	7.4	6.2
U	7.3	3.5	3.5
FV	1.00	1.11	1.01
Vol. change		11%	1%
Immobile element		Ti, Yb Th	Ti

Table B-2. (continued) D_3 Rod shear

Sample	93-52-1	93-52	93-51	93-72	93-73	93-74	93-42	93-44	93-46
Rock type	D	D	D	Pd	Pd	Pd	Gd	Gd	Gd
Rock fabric	P	Pm	M	P	Pm	M	P	Pm	M
Si	73.1	75.5	78.4	76.7	79.1	74.5	79.5	82.2	86.4
Ti	1.21	1.21	1.19	1.03	1.02	1.03	0.56	0.55	0.56
Al	27.6	28.2	27.7	24.2	24.8	29.7	27.9	27.9	27.7
TFe	16.30	17.80	19.40	15.30	16.10	22.10	11.10	10.00	11.30
Mn	0.27	0.26	0.28	0.35	0.38	0.41	0.20	0.18	0.20
Mg	4.92	6.52	8.83	5.41	5.31	2.55	3.40	2.91	3.45
Ca	12.30	11.50	14.00	12.10	12.80	13.90	9.85	7.88	9.04
Na	8.32	8.71	8.59	9.04	8.21	7.08	10.10	10.20	9.18
K	7.86	7.72	7.33	4.49	5.32	7.12	6.44	7.59	8.69
P	0.52	0.53	0.52	0.28	0.28	0.45	0.23	0.21	0.29
O	127	131	137	127	130	130	130	132	138
Li	73	113	76				89	70	74
B	159	97	57				44	54	53
Sc	43.3	44.1	54.6	43.1	43.7	63.9	22.7	19.2	26.9
Cr	216	309	844	536	575	379	100	86	107
Co	66	71	84	31	35	44	43	39	44
Ni	95	140	224	34	40	15	55	38	60
Cu	154.0	190.0	258.0	157.0	241.0	566.0	136.0	164.0	238.0
Zn	247.0	235.0	244.0	180.0	463.0	403.0	153.0	96.8	69.2
Rb	301	311	264	102	144	166	202	213	227
Sr	1620	2350	2240	2810	2440	2790	2080	1580	1270
Y	74	68	61	42	43	53	32	33	47
Zr	564	270	435	386	377	236	224	326	600
Nb	33	32	33				14	17	27
Mo	7	3	2	6	3		1	1	3
Cs	10	10	10				8	8	10
Ba	2820	2310	1900	2600	2710	4090	2620	3360	3120
La	134	117	117	56	60	35	66	68	101
Ce	264	243	243	116	121	82	119	131	197
Nd	128	115	124	56	58	29	52	59	85
Sm	20.1	19.5	20.2	11.3	11.5	9.3	8.4	10.0	13.5
Eu	4.8	4.9	5.1	3.1	3.2	3.8	3.1	2.8	3.4
Tb	2.3	2.2	2.0	1.4	1.4	1.8	1.0	0.9	1.5
Yb	7.6	6.3	5.8	5.1	4.9	7.9	3.2	3.7	4.2
Lu	1.18	0.90	0.76	0.82	0.81	1.26	0.42	0.54	0.63
Hf	14	8	12	9	9	3	6	9	16
Au	0.004	0.082	0.156	0.006	0.066	0.222	0.010	0.111	0.606
Pb	48	42	35				38	19	17
Th	24.4	11.6	12.0	7.3	6.9	6.4	12.6	27.9	25.7
U	12.3	8.7	5.6	7.3	6.0	3.2	4.6	8.9	8.7
FV	1.00	1.03	1.08	1.00	1.02	1.01	1.00	1.05	1.09
Vol. change		3%	8%		2%	1%		5%	9%
Immobile element		Ti, Al Sc, Nb Sm, Eu Tb	Ti, Al Nb, Cs Sm		Ti, Sc,Y Zr, Nd Sm, Eu Tb, Yb Lu, Hf	Ti		Ti, Al Y, Cs La, Tb	Ti, Al

Table B-2. (continued) D_3 James-Roxy shears

Sample	93-29	93-28	93-26	93-41	93-39	93-38
Rock type	G	G	G	G	G	G
Rock fabric	P	Pm	M	P	Pm	M
Si	87.5	88.8	95.8	86.6	91.6	90.4
Ti	0.44	0.43	0.43	0.40	0.41	0.39
Al	21.7	22.0	22.9	21.8	23.5	22.7
TFe	5.14	6.11	5.30	4.42	4.59	4.73
Mn	0.10	0.09	0.07	0.08	0.10	0.08
Mg	1.79	1.68	1.66	1.58	1.30	1.31
Ca	4.74	4.29	2.90	5.27	4.34	4.02
Na	8.71	6.91	5.70	8.60	8.24	6.81
K	8.13	10.60	12.30	7.98	8.52	9.13
P	0.11	0.12	0.11	0.10	0.12	0.09
O	129	130	138	128	134	132
Li	112	71	65	58	37	41
B	28	17	76	20	33	63
Sc	11.6	12.1	12.4	10.5	7.9	10.6
Cr	158	149	162	115	168	140
Co	17	25	21	15	9	14
Ni	36	38	35	31	16	28
Cu	9.2	31.9	415.0	5.3	17.6	191.0
Zn	120.0	89.8	155.0	66.0	46.3	127.0
Rb	321	353	367	247	261	262
Sr	1250	1080	804	1360	818	783
Y	18	18	19	18	19	18
Zr	309	315	339	322	341	305
Nb	26	21	25	22	19	20
Mo	1	1	2	1	2	1
Cs	5	7	7	4	4	6
Ba	2670	2740	2690	3060	3250	3260
La	71	67	88	58	55	69
Ce	115	110	153	100	84	91
Nd	36	38	53	39	37	41
Sm	5.1	5.6	7.3	5.4	5.3	6.0
Eu	1.4	1.5	1.9	1.6	1.4	1.8
Tb	0.5	0.5	0.6	0.5	0.5	0.6
Yb	1.7	1.9	1.9	1.5	1.5	1.8
Lu	0.29	0.28	0.29	0.27	0.25	0.25
Hf	11	11	10	11	11	9
Au	0.003	1.030	1.290	0.005	0.135	0.894
Pb	45	88	249	32	33	62
Th	26.7	23.4	27.2	21.6	18.0	22.6
U	27.6	8.1	17.1	4.7	4.1	6.9
FV	1.00	1.03	1.09	1.00	1.05	1.03
Vol. change		3%	9%		5%	3%
Immobile element		Ti, Al Zr, Tb Hf	Ti, Lu Th		Ti, Sm Tb, Yb Hf	Ti, Sc Y, Tb

Table B-2. (continued) D_3 MacLeod Main shear

Sample	93-4	904-6	904-7
Rock type	Gd	Gd	Gd
Rock fabric	P	Pm	M
Si	77.3	79.7	81.1
Ti	1.29	1.26	1.28
Al	24.8	24.7	24.9
TFe	12.70	12.90	12.40
Mn	0.17	0.18	0.09
Mg	4.00	4.14	4.00
Ca	8.46	8.05	4.58
Na	8.72	9.44	5.49
K	9.07	9.76	11.90
P	0.36	0.37	0.45
O	126	129	128
Li			
B			
Sc	31.2	26.8	35.3
Cr	331	569	336
Co	25	34	48
Ni	47	63	118
Cu	183.0	339.0	1460.0
Zn	157.0	174.0	201.0
Rb	392	367	751
Sr	1350	1440	930
Y	44	60	53
Zr	886	1060	1180
Nb	55	57	59
Mo			
Cs	14	11	22
Ba	2520	2270	4170
La	135	139	118
Ce	235	268	224
Nd	83	85	84
Sm	15.7	18.5	13.7
Eu	2.5	3.1	2.2
Tb			
Yb	5.5	5.7	4.2
Lu	0.91	0.88	0.62
Hf	22	23	28
Au	0.019	0.060	2.160
Pb	8	11	20
Th	38.6	42.7	47.6
U	13.8	15.9	21.6
FV	1.00	1.02	1.01
Vol. change		2%	1%
Immobile element		Ti, Al Nb, La Nd, Yb Lu, Hf	Ti, Al Cr, Nd

NOTE TO USERS

Oversize maps and charts are microfilmed in sections in the following manner:

LEFT TO RIGHT, TOP TO BOTTOM, WITH SMALL OVERLAPS

The following map or chart has been microfilmed in its entirety at the end of this manuscript (not available on microfiche). A xerographic reproduction has been provided for paper copies and is inserted into the inside of the back cover.

Black and white photographic prints (17"x 23") are available for an additional charge.

UMI

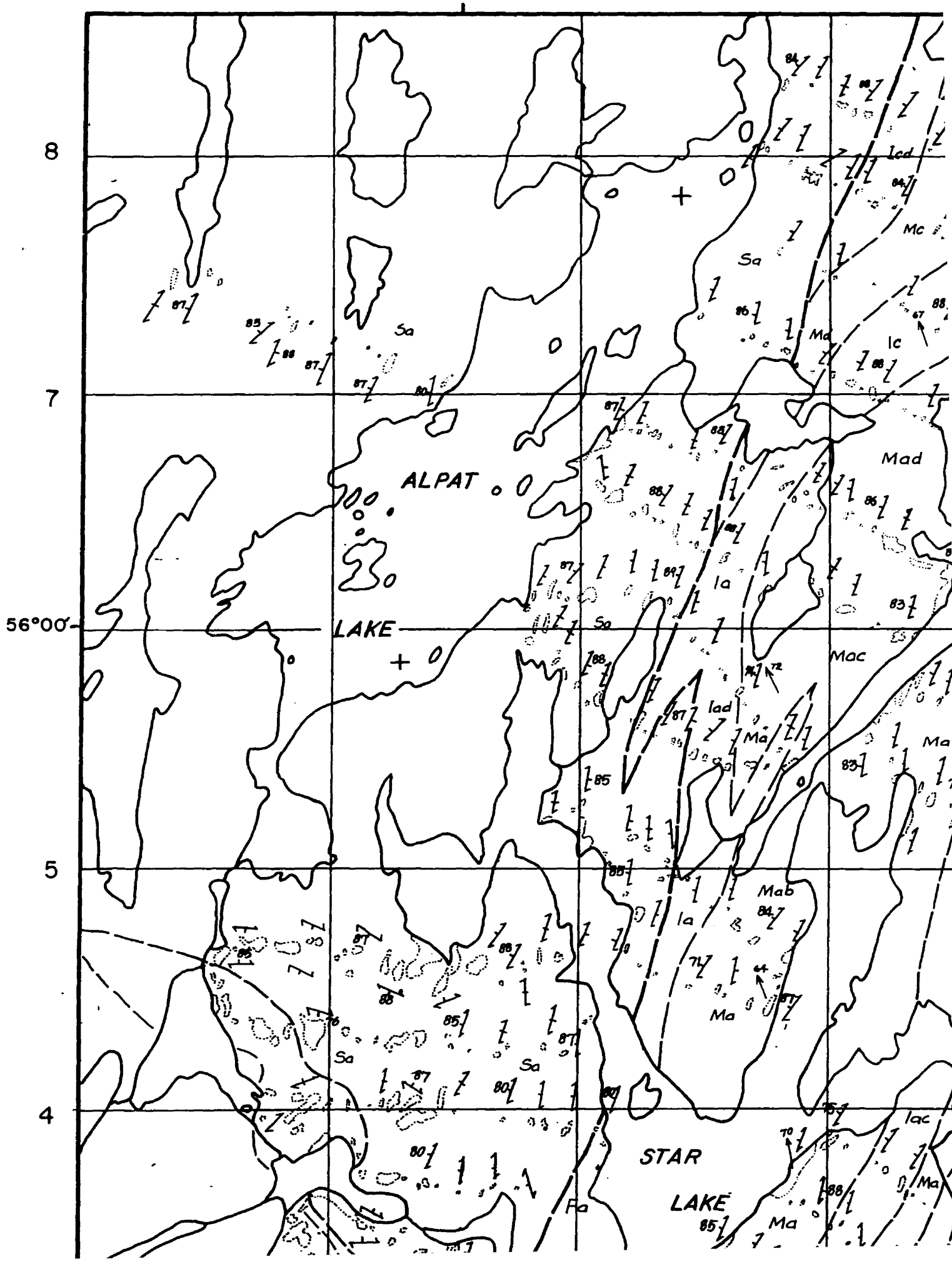
540000m.E.
1
104°20'
2
3
8
7
56°00'
5
4
ALPAT
LAKE
STAR
LAKE
Sa
Mad
Mac
Mab
Ma
Mc
Ic
Iad
Ia
Iac
Fo

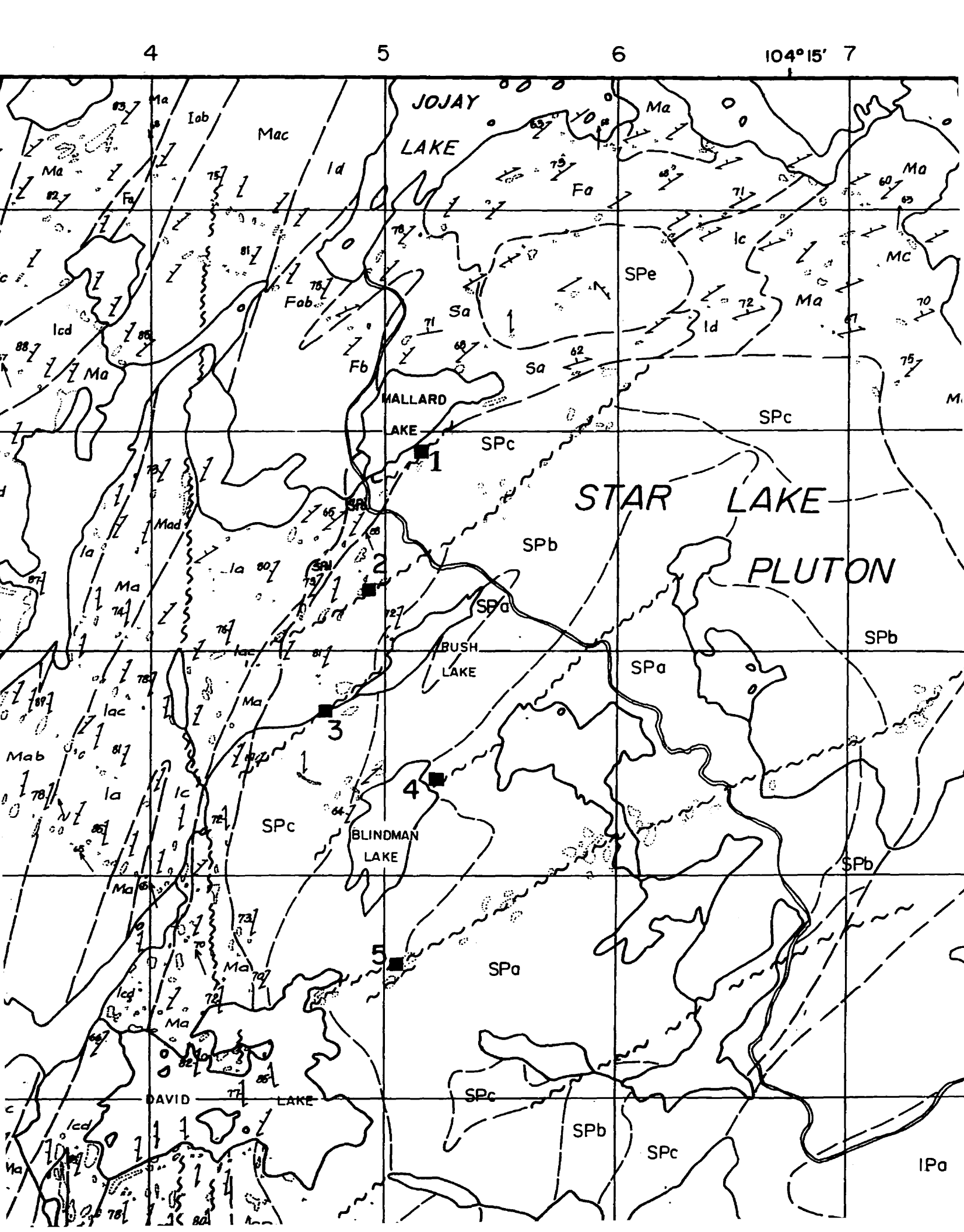
4
5
6
104°15'
7
JOJAY
LAKE
STAR LAKE
PLUTON
MALLARD
LAKE
BUSH
LAKE
BLINDMAN
LAKE
DAVID
LAKE
SPa
SPb
SPc
SPe
Ma
Mac
Mad
Mab
Fa
Fb
Fab
Sa
Ia
Ic
Id
Iab
Iac
Icd
MC
IPa
1
2
3
4
5

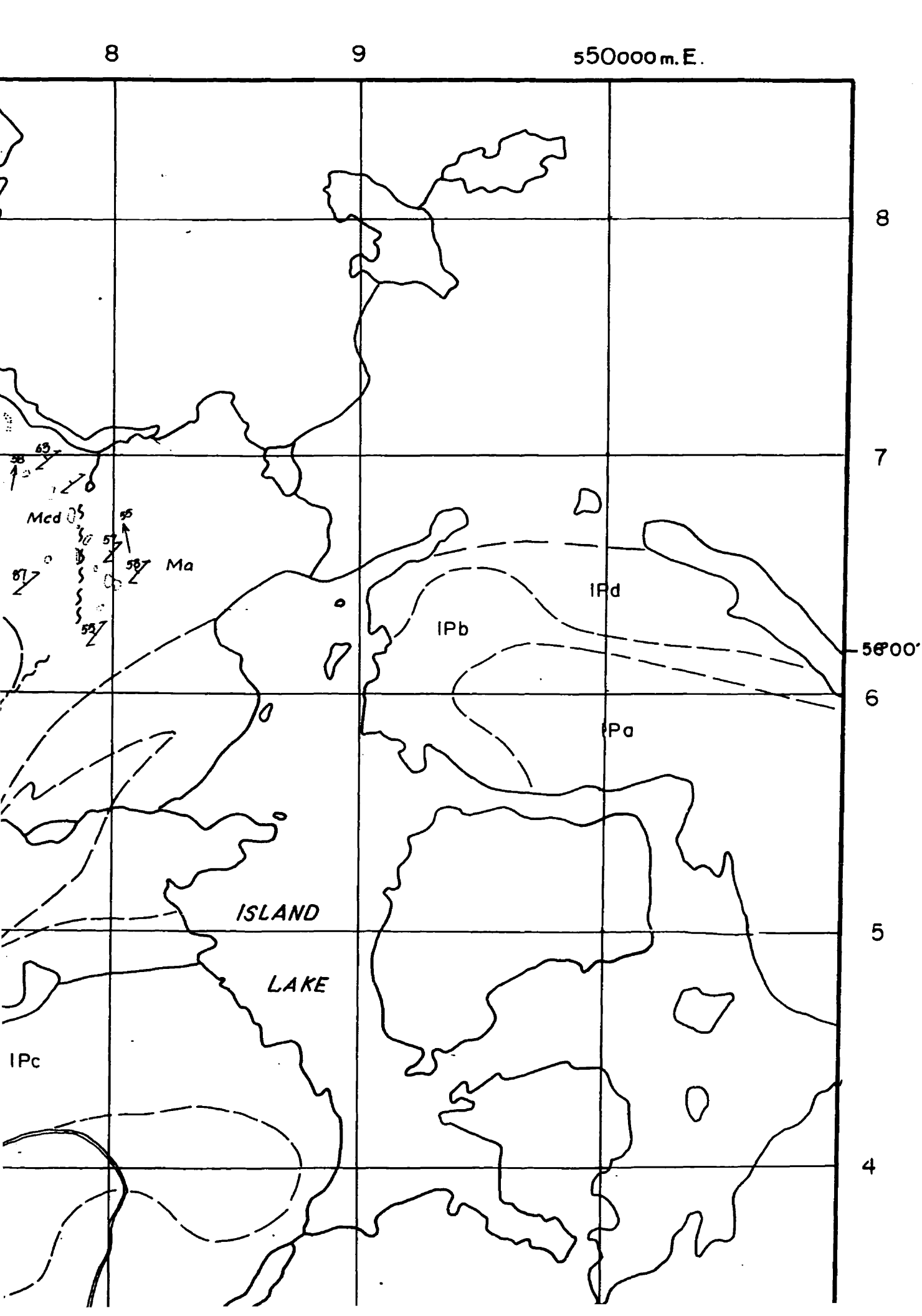
8
9
550000 m. E.
8
7
56°00'
6
5
4
Mcd
Ma
IPd
IPb
IPa
ISLAND
LAKE
IPc

LEGEND

QUATERNARY

Swamp, lake, stream deposits, glacial till and gravel

---------- Unconformity ----------

MINOR INTRUSIVE ROCKS

G — **Granodiorite, quartz monzodiorite:** greenish grey to greyish pink, medium grained, feldspar porphyritic, locally equigranular, massive to weakly foliated; 55 to 70% feldspar, 5 to 15% biotite and hornblende, 5 to 15% quartz, ± epidote, ± magnetite, ± sphene, ± pyrite

B — **Gabbro, pyroxenite, hornblendite:** Gabbro - light grey to greenish grey, medium to coarse grained, inequigranular; 15 to 65% amphibole, 20 to 55% plagioclase, ± pyroxene, ± biotite, ± chlorite. Pyroxenite - greyish green, coarse grained, equigranular, massive, locally weakly foliated; up to 95% augite and actinolite, ± olivine, ± magnetite. Hornblendite - dark grey to greenish black, coarse grained, massive; hornblende, ± biotite, ± chlorite

MAJOR INTRUSIVE ROCKS

Star Lake Pluton (after Thomas, 1985; Ames et al., 1987):

SPa — Granite - pink to pinkish grey, medium to coarse grained, porphyritic or equigranular, massive; 20 to 45% plagioclase, 25 to 40% potassium feldspar, 20 to 35% quartz, 5 to 8% biotite, ± hornblende, ± muscovite

SPb — Quartz monzonite, granodiorite - light pink to pinkish grey, medium to coarse grained, equigranular to porphyritic, massive to weakly foliated; 35 to 50% plagioclase, 25 to 45% potassium feldspar, 10 to 15% quartz, 5 to 15% biotite and hornblende, ± epidote, ± magnetite

SPc — Diorite - greenish grey to dark grey, fine to coarse grained, equigranular or porphyritic, weakly foliated; 40 to 60% plagioclase, 15 to 25% hornblende, ± quartz, ± epidote, ± biotite, ± potassium feldspar

SPd — Porphyritic diorite - grey to greenish grey, medium grained, plagioclase porphyritic, weakly to strongly foliated; 35 to 60% plagioclase, 15 to 25% hornblende, ± potassium feldspar, ± quartz, ± epidote, ± biotite

SPe — Gabbro - greenish grey to dark grey, medium to coarse grained, equigranular to porphyritic, locally preserved cumulate texture, massive to weakly foliated; 40 to 70% plagioclase, 25 to 35% hornblende, ± pyroxene, ± potassium feldspar, ± actinolite, ± biotite, ± chlorite

Island Lake Pluton (after Thomas, 1985):

IPa — Granite - pale pink to greyish pink, medium to coarse grained, feldspar porphyritic, massive to weakly foliated; 25 to 45% plagioclase, 25 to 40% potassium feldspar, 10 to 25% quartz, 5 to 10% biotite, ± hornblende, ± epidote, ± magnetite, ± muscovite

IPb — Quartz monzonite, quartz monzodiorite - light grey to pinkish grey, medium to fine grained,

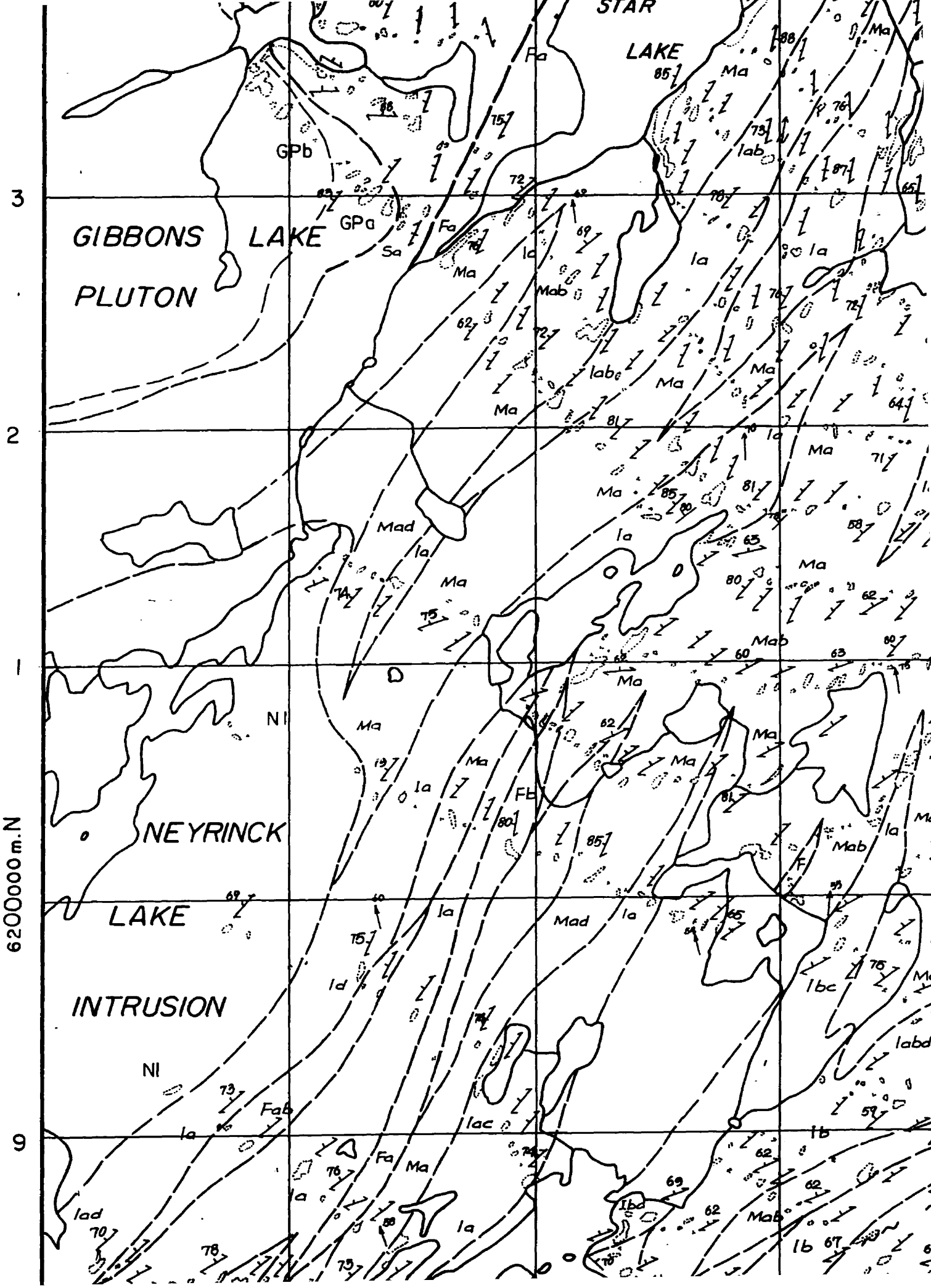
STAR
LAKE
GPb
GPa
GIBBONS LAKE
PLUTON
NEYRINCK
LAKE
INTRUSION
NI
Fa
Sa
Ma
Mab
Mad
la
lab
labc
lac
lad
lb
lbc
Ib
Fab
Id
6200000 m.N
3
2
1
9

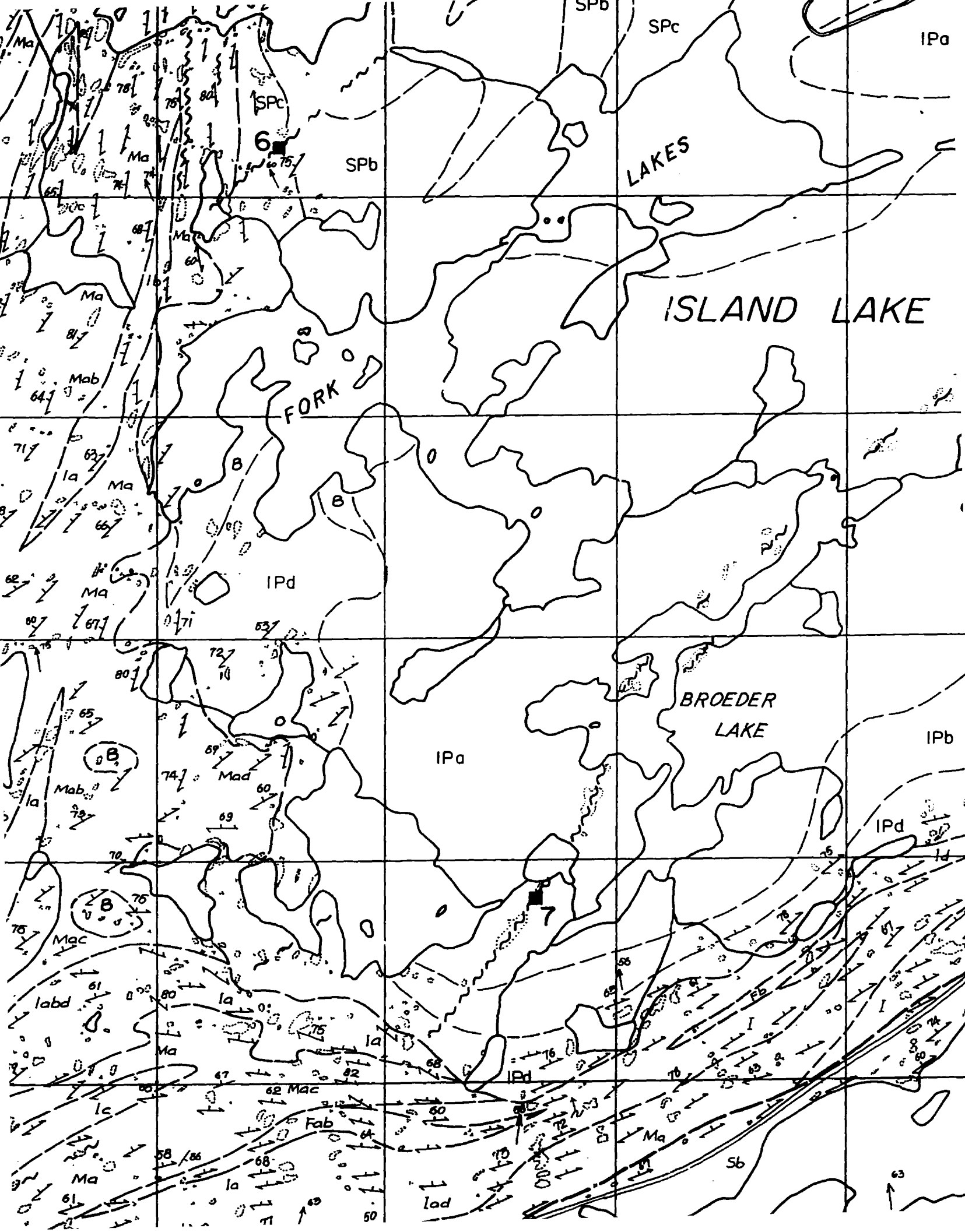
SPb
SPc
IPa
SPc
6
SPb
LAKES
ISLAND LAKE
FORK
IPd
BROEDER
LAKE
IPb
IPa
Mad
IPd
7
Mac
labd
Fab
IPd
Mac
lad
Sb

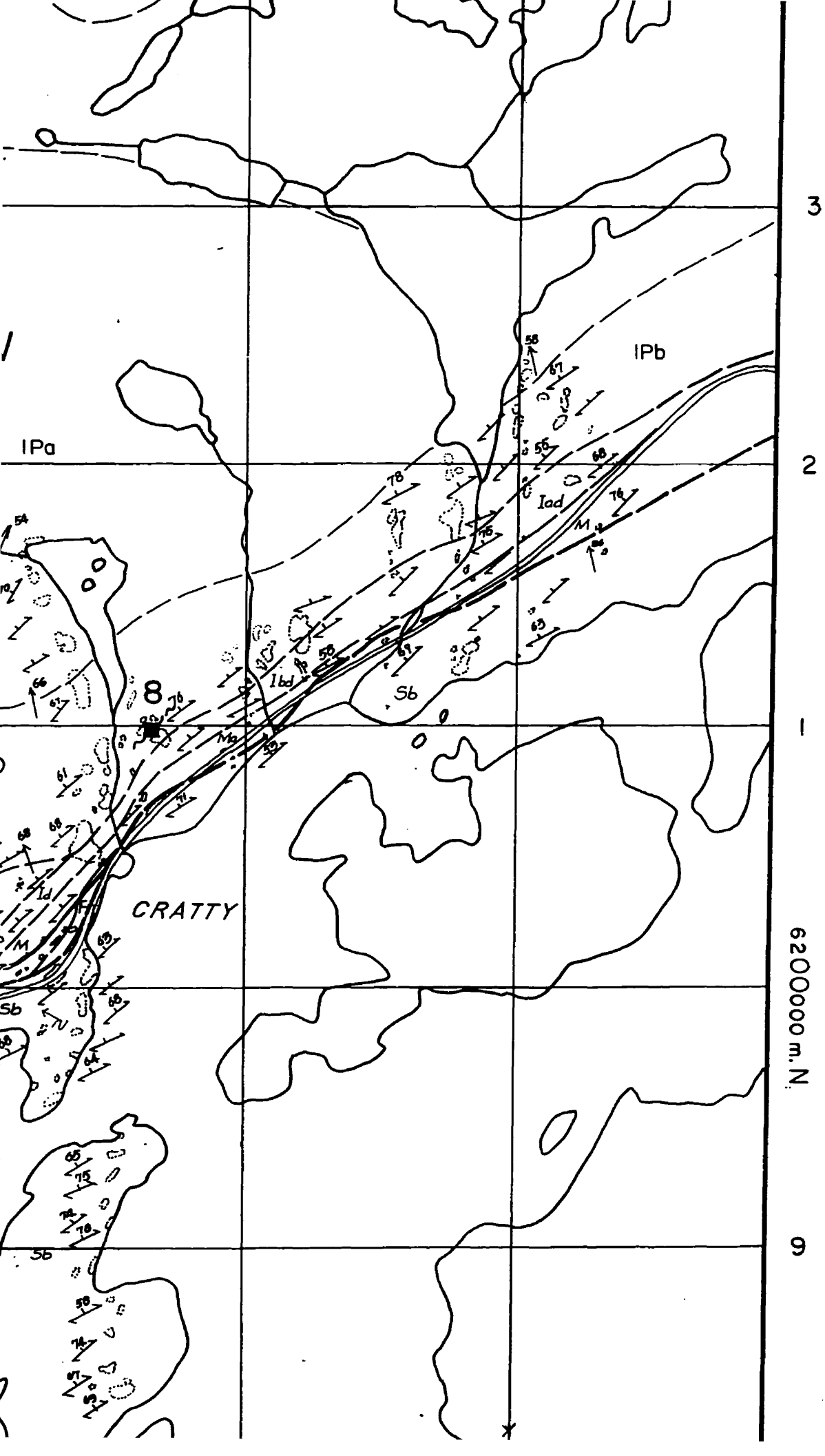

IPb

IPc

IPd

GP

NI

Sb

Sa

M

I

equigranular, weakly to strongly foliated along the southeastern margin of the pluton; 30 to 45% plagioclase, 25 to 35% potassium feldspar, 10 to 25% quartz, ± biotite, ± hornblende, ± magnetite

IPc — Microbrecciated granite - greyish pink, medium to coarse grained, porphyritic, well-developed cataclastic or microbrecciated to weakly foliated; 25 to 45% plagioclase, 25 to 40% potassium feldspar, 10 to 25% quartz, ± biotite, ± hornblende, ± epidote, ± magnetite

IPd — Hybrid quartz monzonite, monzodiorite, intrusion breccia - greyish pink, medium to fine grained, massive to weakly foliated, with intrusion breccia up to tens of centimeters in diameter; 30 to 45% plagioclase, 25 to 35% potassium feldspar, 10 to 15% quartz, 3 to 10% biotite and hornblende, ± epidote, ± magnetite

GP — **Gibbons Lake Pluton** (after Thomas, 1985): GPa, quartz diorite; GPb, quartz monzodiorite, granodiorite; pale pinkish grey to grey, medium to coarse grained, porphyritic, massive to well foliated; 55 to 70% plagioclase, 5 to 25% potassium feldspar, 10 to 25% quartz, 5 to 20% hornblende and biotite, ± epidote, ± carbonate, ± magnetite

NI — **Neyrinck Lake Intrusion** (after Thomas, 1985): metagabbro - light to dark grey, greenish black, medium to coarse grained, porphyritic, massive; 50 to 90% plagioclase, 5 to 40 amphibole, ± biotite, ± pyroxene, ± potassium feldspar, ± chlorite

---------- Intrusive Contact ----------

METASEDIMENTARY ROCKS

Sb — **Feldspathic meta-arkoses:** grey, pale pink to light greyish pink, fine to medium grained, equigranular, weakly to strongly foliated; 30 to 55% feldspar (potassium feldspar dominant over plagioclase), 25 to 60% quartz, ± muscovite, ± biotite, ± sillimanite, ± magnetite

Sa — **Pelitic, psammopelitic and psammitic gneiss / schist:** light grey or greenish grey to dark grey, fine to medium grained, equigranular to inequigranular, locally amphibole or garnet porphyritic, locally preserved primary bedding, weakly to well-developed schistosity; 25 to 45% feldspar, 30 to 50% quartz, 5 to 40% biotite and muscovite, ± chlorite, ± amphibole, ± garnet, ± epidote

METAVOLCANIC ROCKS

M — **Mafic metavolcanic rocks** (basaltic, basaltic-andesitic rocks): greenish black or greyish black; 20 to 75% hornblende, 10 to 50% plagioclase, ± actinolite, ± epidote, ± chlorite, ± biotite

Ma, flow - fine to medium grained, equigranular, typically with hornblende porphyroblasts up to 7 mm, weakly to well foliated; local pillow flow, pillows ranging from 35 by 45 cm to 65 by 85 cm, with chilled selvages up to 3 cm wide, weakly deformed

Mb, feldspar porphyritic flow - 10 to 35% subhedral to euhedral plagioclase phenocrysts up to 8 mm long, with altered cores, in a fine grained, equigranular groundmass; weakly to moderately foliated

Mc, volcaniclastic rocks - mainly metatuff breccia and meta-agglomerate, monolithic to heterolithic clasts ranging from 0.5 by 2.5 cm to 35 by 10 cm, poorly sorted, matrix-supported, more felsic than the matrix; locally lapilli and ash metatuff, massive to laminated

I — **Intermediate metavolcanic rocks** (andesitic and dacitic rocks): medium grey to greenish grey; 25 to 60% plagioclase, 10 to 35% biotite and hornblende, 5 to 25% potassium feldspar, ± quartz, ± chlorite, ± actinolite, ± garnet

Ia, flow - fine to medium grained, locally aphanitic, homogeneous and equigranular, massive to schistose, locally quartz amygdaloidal or hornblende porphyroblastic

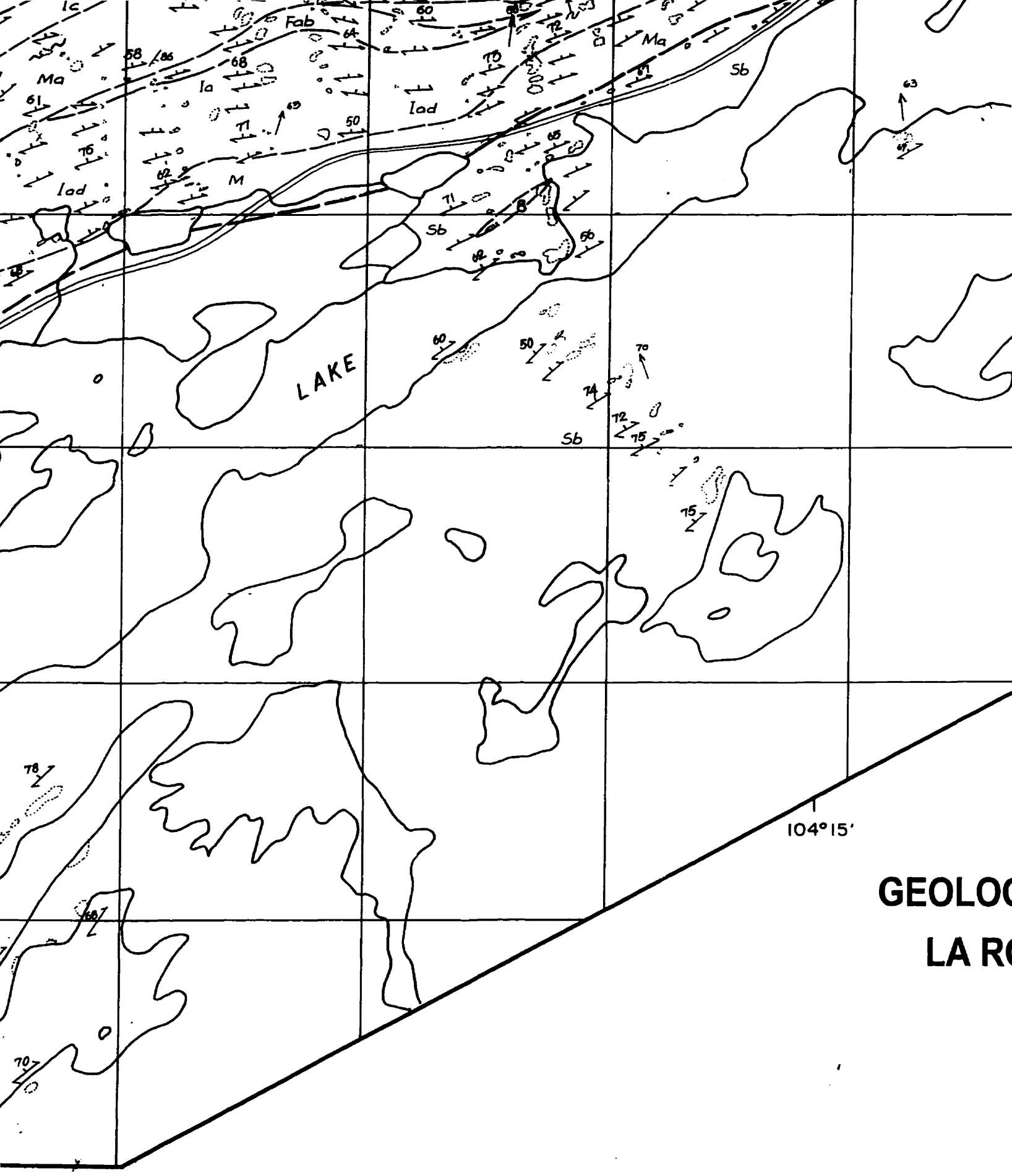

GEOLOG
LA R

GEOLOGY OF THE STAR LAKE-MCLENNAN LAKE AREA, LA RONGE DOMAIN, NORTHERN SASKATCHEWAN

MAPPING BY JIE HE AND ASSISTANTS

Scale 1:20 000

Metres 1000 0 1000 Metres

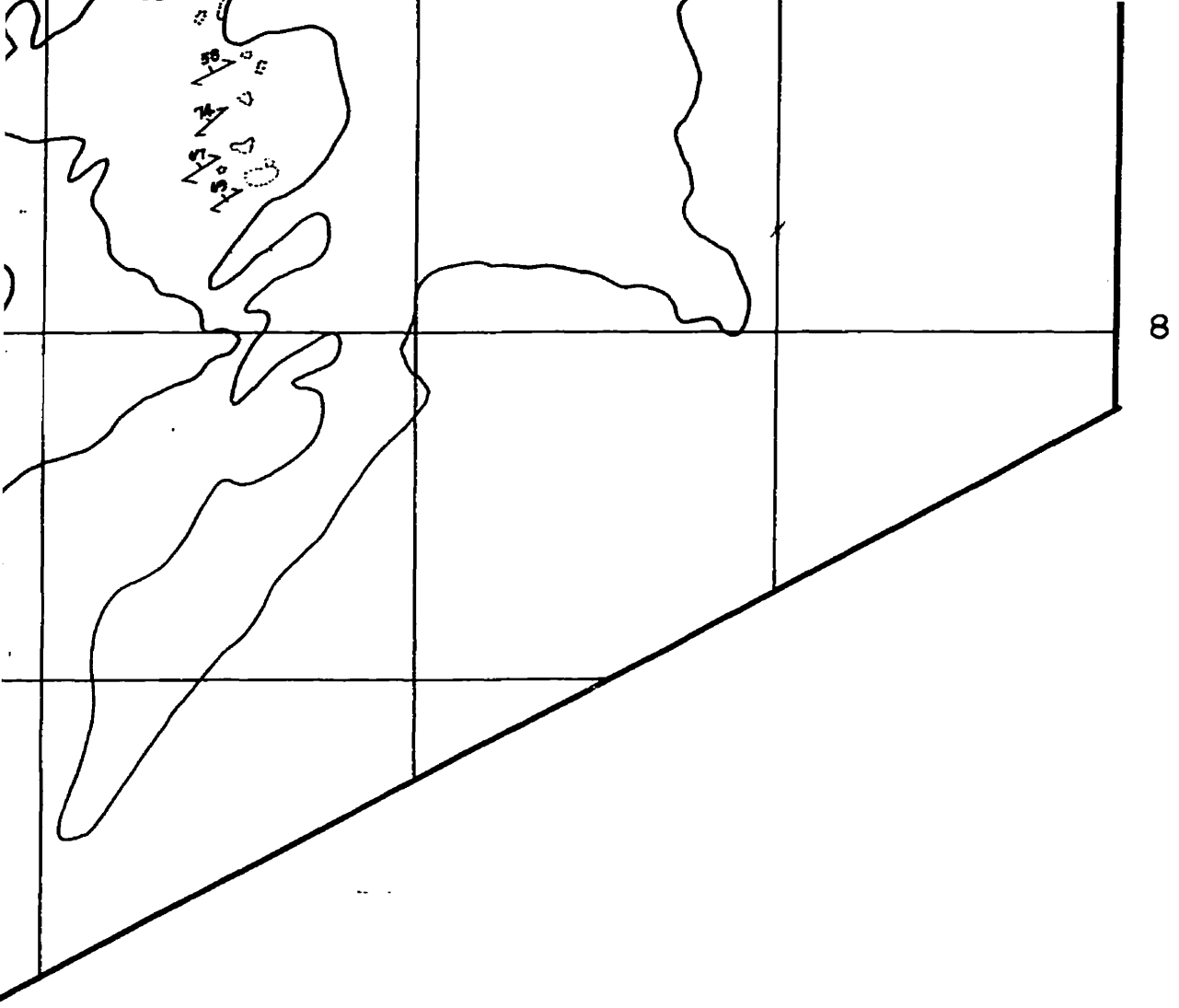

I

F

75

75

65

OF THE STAR LAKE-MCLENNAN LAKE AREA,
GE DOMAIN, NORTHERN SASKATCHEWAN

MAPPING BY JIE HE AND ASSISTANTS

Scale 1:20 000

s 1000 0 1000 Metres

supported, more felsic than the matrix; locally lapilli and ash metatuff, massive to laminated

I — **Intermediate metavolcanic rocks** (andesitic and dacitic rocks): medium grey to greenish grey; 25 to 60% plagioclase, 10 to 35% biotite and hornblende, 5 to 25% potassium feldspar, ± quartz, ± chlorite, ± actinolite, ± garnet

Ia, flow - fine to medium grained, locally aphanitic, homogeneous and equigranular, massive to schistose, locally quartz amygdaloidal or hornblende porphyroblastic

Ib, feldspar porphyritic flow - aphanitic to fine grained, equigranular groundmass; 15 to 30% euhedral plagioclase phenocrysts, 2 to 6 mm long, randomly to moderately oriented

Ic, volcaniclastic rocks - mainly metatuff breccia and meta-agglomerate with unsorted, matrix-supported, heterolithic and felsic fragments up to 30 by 15 cm, weakly to moderately deformed

F — **Felsic metavolcanic rocks** (rhyodacitic and rhyolitic rocks): cream to light grey or greyish brown; 15 to 60% quartz, 20 to 45% potassium feldspar, 15 to 25% plagioclase, 5 to 10% biotite, ± hornblende, ± chlorite, ± epidote

Fa, flow - aphanitic to fine grained, massive to weakly foliated

Fb, volcaniclastic rocks - predominantly lapilli and crystal metatuff, massive to laminated, locally thickly bedded

SYMBOLS

75 — Primary bedding

75 — Foliation with dip

65 — Mineral lineation with plunge

Shear zones

Isoclinal fold with plunge

Lithological boundary

Outcrop

Road

■ **Gold deposits and occurrences**: 1, Decade; 2, Jolu; 3, Rush Lake; 4, Blindman; 5, Star Lake; 6, Tammar; 7, Jasper; 8, MacLeod Main

8

E AREA,

WAN